Neutrino velocity measurement with the OPERA experiment in the CNGS beam

Giulia Brunetti

Institut de Physique Nucléaire de Lyon

Thèse en co-tutelle

avec l'Université Claude Bernard Lyon-I

présentée devant

Alma Mater Studiorum - Università di Bologna

pour l'obtention du

DIPLOME de DOCTORAT

Spécialité : Physique des Particules

(arrêté du 7 août 2006)

par

Giulia BRUNETTI

Neutrino velocity measurement with the OPERA experiment in the CNGS beam

Soutenue le 20 Mai 2011

devant la Commission d'Examen

Jury:	M. F. TERRANOVA	Rapporteur
	M. G. WILQUET	Rapporteur
	M. D. AUTIERO	Directeur de thèse
	M. M. SIOLI	Directeur de thèse
	M. A. DEANDREA	
	M. F. GATTI	

Contents

Introduction **v**

1 Neutrinos **1**

1.1 A Brief History about Neutrinos 1

1.2 Neutrinos in the Standard Model 3

1.3 Experimental Evidence for Massive Neutrinos 5

1.4 Neutrino Masses 10

1.5 Beyond the Standard Model: Lorentz Violation Effects 12

2 Neutrino Velocity Measurements **19**

2.1 SN 1987A 19

2.2 Measurements Performed with Neutrino Beam Experiments 23

2.2.1 MINOS Measurement 24

2.2.2 Potentialities of OPERA in a Neutrino Velocity Measurement 27

3 The OPERA Experiment in the CNGS Beam **33**

3.1 CNGS Beam 33

3.2 CNGS-OPERA Alignment 40

3.2.1 Effect of the Ignorance of the Parent Mesons Decay Point on the TOF 44

3.3 The OPERA Detector 45

3.3.1 Scintillator Target Trackers 48

3.3.2 Magnetic Spectrometers 50

3.3.3 The Data Acquisition System 51

4 Timing System **53**

4.1 Outline 53

4.2 The CERN Accelerators Timing Distribution System 54
4.3 LNGS and OPERA Timing 58
4.4 GPS in Common View Mode 68
4.4.1 Time Transfer with the Septentrio PolaRx2 Receiver and its Calibration 76
4.5 Timing Corrections 81

5 Timing Calibrations 85
5.1 Calibration Measurements at CERN 85
5.2 Calibration Measurements at LNGS 91
5.3 CERN-LNGS Intercalibration Measurements 94

6 Geodesy 97
6.1 Geodesy Measurement at LNGS 99
6.2 Geodesy at CERN 102
6.3 CERN-Gran Sasso Distance Computation 104

7 Event Selection 109
7.1 Generic Selection of On-Time Events in OPERA 109
7.2 Event Selection 110
7.2.1 MC Study on External Events 112
7.2.2 MC Study on Internal Events 114
7.2.3 Selection Algorithm based on the OpCarac Classification . . 117

8 Data Analysis 121
8.1 OPERA Events and Data at CERN 122
8.2 Extraction of the Best Time Shift Value by Using a Likelihood Maximization 128
8.3 Monte Carlo Test 132

9 Results on the Final Data Sample and Extraction of Neutrino Velocity 135
9.1 Data Timing Correction 136
9.2 Distance Correction 136
9.3 Data Analysis Using a Likelihood Maximization 139

9.4 Extraction of the Final Result 143
9.4.1 Systematic Effects 148
9.5 Measurement Result 149

Conclusions **151**

A Timing Corrections **153**

B ITRF/ETRF - International/European Terrestrial Reference Frame **157**

Bibliography **167**

Acknowledgements **173**

Introduction

In this thesis it is presented the measurement of the neutrino velocity with the OPERA experiment in the CNGS beam. The OPERA experiment aims the direct observation of $\nu_\mu \rightarrow \nu_\tau$ oscillations in the CNGS beam, a high energy ν_μ beam produced at CERN.

Previous measurements of the neutrino velocity were performed by other experiments operating on neutrino beams from accelerators like MINOS. However the higher energy of the CNGS beam together with the higher number of interactions in the OPERA detector, a much more sophisticated timing system (composed by cesium clocks and GPS receivers operating in "common view mode"), and a Fast Waveform Digitizer (installed at CERN and able to measure the internal time structure of the proton pulses used for the CNGS beam), allows for a new measurement with a much smaller statistical ($\sim$ 10 ns) and systematical ($<$ 15 ns) uncertainties.

Theoretical models exist foreseeing Lorentz violating effects that can be investigated by neutrino velocity measurements with terrestrial beams: this is discussed in the first two chapters. In the third chapter the CNGS beam as well as the OPERA experiment are described. Details about the timing systems used at CERN and at LNGS and their calibration measurements are given in chapters 4 and 5. A new geodetical survey performed to precisely determine the CERN-LNGS distance is described in chapter 6. In chapters 7 and 8 will be presented the statistical data analysis and the performed MC studies. In the final chapter are reported the results and the extraction of the neutrino velocity. The performed measurement is the most precise one done with a terrestrial neutrino beam.

Chapter 1

Neutrinos

1.1 A Brief History about Neutrinos

The discovery of the continuous spectrum of the electrons emitted in β decay processes by L. Maitner, O Hahn and J. Chadwick in 1914 raised the question of its interpretation. In 1927 - 1930, C. D. Ellis and W. A. Wooster and then L. Maitner and W. Orthman measured the total energy released in the decay by calorimetry and also observed a continuous spectrum. This excluded the possibility that a photon was emitted with the electron.
In 1930 Pauli proposed that a new "radiation" was emitted together with the electron in the decay so that the energy conservation was guaranteed, he called this new particle *neutron*, it should have been neutral and have spin $1/2$ [1] [1] .
When Chadwick in 1932 discovered the neutron as a neutral component of the nucleus with a mass of the order of that of proton, Fermi proposed then in 1933-34 to call the missing particle of the β decay "neutrino" and the continuous spectrum would have been explained assuming that this particle and the electron were

[1] *"Dear Radioactive Ladies and Gentlemen, As the bearer of these lines, to whom I graciously ask you to listen, will explain to you in more detail, how because of the "wrong" statistics of the N and* ^{6}*Li nuclei and the continuous beta spectrum, I have hit upon a desperate remedy to save the "exchange theorem" of statistics and the law of conservation of energy. Namely, the possibility that there could exist in the nuclei electrically neutral particles, that I wish to call neutrons, which have spin 1/2 and obey the exclusion principle and which further differ from light quanta in that they do not travel with the velocity of light. The mass of the neutrons should be of the same order of magnitude as the electron mass and in any event not larger than 0.01 proton masses. The continuous beta spectrum would then become understandable by the assumption that in beta decay a neutron is emitted in addition to the electron such that the sum of the energies of the neutron and the electron is constant.."* Letter to Tubingen conference on 4th December 1930 from Pauli.

simultaneously emitted from the nucleus sharing momentum and energy in the process:

$$n \rightarrow p + e^- + \bar{\nu}_e. \tag{1.1}$$

Fermi postulated that the neutrino mass was zero and that the decay was a 4-bodies point interaction due to a new force: the weak interaction.
All the measurements performed on the recoil of the nucleus during β decays were compatible with the hypothesis that only one neutrino was emitted with the electron, but no direct observation of the neutrino was feasible and it became clear that in order to reach this goal a very abundant source of neutrinos and a very sensitive heavy detectors were needed.

The neutrino experimental discovery was achieved in 1956 in the C. Cowan and F. Reines' experiment through the inverse β decay where an $\bar{\nu}_e$ is captured by a proton: $p + \bar{\nu}_e \rightarrow n + e^+$ [2]. The detector was exposed to the Savannah River nuclear reactor and was composed by 400 liters of water doped with cadmium chloride used to detect the neutron by largely increasing the neutron capture cross-section. The $\bar{\nu}_e$ from the reactor interacted with the protons of the target yielding a neutron and a positron. The target was surrounded by scintillators that detected the light from the positron annihilation and the neutron capture (the same basic method is used today to observe $\bar{\nu_e}$ in nuclear reactors experiments).

Besides the electron neutrino, after the discovery of the muon in the cosmic rays, the idea that a second type of neutrino could exist brought to the discovery of the muon-associated neutrino: in 1962, the experiment of L. Lederman, M. Schwartz, J. Steinberger and their collaborators used the first accelerator neutrino beam in history, this was produced from a pion beam through the decay $\pi \rightarrow \mu\nu_\mu$. The ν_μ interacted in a target producing muons and not electrons: $\nu_\mu + p \rightarrow n + \mu^-$ [3].

In 1975 M. Perl discovered for the first time the creation of $\tau^+\tau^-$ pairs in e^+e^- collisions at SLAC, adding a third leptonic family to the other two.

Meanwhile a quark-lepton symmetry was proposed, and the quark mixing was described by the CKM (Cabbibo-Kobayashi-Maskawa) matrix: Maki, Nakagawa and Sakata proposed a mixing matrix also for neutrinos. Only the third lepton family was not yet completed. In 1973 neutral currents were discovered at CERN and confirmed at Fermilab. A complete knowledge of weak interactions came after

the discoveries of the W and the Z bosons in 1983 at the CERN SPS $\bar{p}p$ collider; in 1989 the study of the Z^0 boson width at LEP allowed to show that only three lepton families (and then three types of "light" neutrinos with mass less than half the Z^0 mass) exist.

The experimental evidence of ν_τ came in 2001 at Fermilab by the E872 experiment, also known as DONUT (Direct Observation of the Nu Tau), through the selection of the events with the characteristic τ decay tracks produced by charged current (CC) ν_τ interactions with an iron instrumented target. The third lepton family was then completed.

Neutrinos in the Standard Model are described as neutral, spin 1/2 and zero mass particles only interacting through the weak interaction. Precise confirmations of the validity of the SM at low and high energy were experimentally given in the 90's at LEP. Even so, the high energy physics community started turning towards the search for physics beyond the Standard Model, in particular for a non zero neutrino mass and on neutrino oscillations.

1.2 Neutrinos in the Standard Model

The Standard Model (SM) is a mathematical model developed in 1960 as a way to combine the electromagnetic and weak interactions (electroweak theory). Over the years, the strong interaction and the Higgs Mechanism, that give rise to the masses of all the elementary particles in the Standard Model, have been also included in the model. Quantum electroweak and quantum chromodynamics are grouped into an internally consistent theory that describes the interactions between particles in terms of quantum field theory. In the formalism of the field theory a particle is represented by a function ψ called field and each fundamental interaction is described by a Lagrangian invariant under a symmetry group.
The $SU(3)_C \otimes SU(2)_L \otimes U(1)_Y$ gauge symmetry is an internal symmetry that essentially defines the SM. $SU(2)_L \otimes U(1)_Y$ concerns the electroweak sector, L index represents the left chirality of the particles and Y index represents the weak hypercharge ($Y = \frac{1}{2}(q - I_3)$, where q is the electric charge and I_3 the third component of the weak isospin). The $SU(3)_C$ group describes the strong interaction in the quark sector and C is the index used to denote the "color" of the particles.
Fundamental particles (particles without substructure) in the SM are fermions of

spin 1/2 (leptons and quarks) or, in the case of the particles exchanged in the interactions, bosons of spin 1. Fermions are organized in $SU(2)_L$ doublets of left chirality and $U(1)_Y$ singlets of right chirality, they can be represented in three families:

$$\begin{array}{l} 1)\ \binom{\nu_e}{e^-}_L,\ e^-_R,\ \binom{u}{d}_L,\ u_R,\ d_R \\ 2)\ \binom{\nu_\mu}{\mu^-}_L,\ \mu^-_R,\ \binom{c}{s}_L,\ c_R,\ s_R \\ 3)\ \binom{\nu_\tau}{\tau^-}_L,\ \tau^-_R,\ \binom{t}{b}_L,\ t_R,\ b_R \end{array} \tag{1.2}$$

It has to be pointed out that in this representation only left-handed neutrinos exist (and right-handed antineutrinos), the ν_R does not appear, it has not been experimentally observed and its absence assures the zero mass of neutrinos in the SM.

Gauge bosons are defined as force carriers that mediate the fundamental interactions and are in total 12: the photon for the electromagnetic interaction, $W^{\pm}$ and Z^0 for the weak interaction and 8 gluons for the strong interaction. The thirteenth boson is the Higgs boson, that has spin 0 and would explain why the other elementary particles, the photon and gluon excepted, are massive.

Neutrinos, beeing neutral, are sensitive only to the weak interaction and can thus interact by exchanging $W^{\pm}$ (charged-current interactions) or Z^0 (neutral current interactions).

The SM is not, however, a complete theory of the fundamental interactions (it does not include for instance gravity) and assumes massless neutrinos. Beyond the SM, there are different ways to attribute a non-zero mass to neutrinos:

- By adding a neutrino of right chirality ν_R not included in the SM, the Yukawa coupling with the Higgs boson gives rise to a neutrino mass m_D. The corresponding Lagrangian of the Dirac mass is:

$$\mathcal{L}_{m_D} = -m_D \left(\overline{\nu_L}\nu_R + \overline{\nu_R}\nu_L\right). \tag{1.3}$$

  The leptonic quantum number L is conserved (as well as the leptonic numbers of the families L_e, L_μ and L_τ) and the neutrinos differ from the antineutrinos (they are then called Dirac particles).

- By including a Majorana mass term m_L by coupling a neutrino of left chirality with the Higgs boson. The Majorana Mass Lagrangian is:

$$\mathcal{L}_{m_L} = -\frac{m_L}{2}\left(\overline{\nu_L}(\nu_L)^C + \overline{\nu_L^C}\nu_L\right), \tag{1.4}$$

where ν^C is the charge conjugate of ν and fulfills the condition $\nu^C = \nu$. This term brakes the symmetry U(1) and the leptonic number is not conserved. In this case neutrinos are equivalent to antineutrinos (they are then called Majorana particles). If only the ν_L exist, then neutrinos only can have a Majorana mass.

- By adding a Dirac-Majorana term and assuming the considerations of two first cases, a new Majorana mass term of right chirality m_R is associated to the Lagrangian:

$$\mathcal{L}_{m_R} = -\frac{m_R}{2}\left(\overline{\nu_R}(\nu_R)^C + \overline{\nu_R^C}\nu_R\right). \tag{1.5}$$

If both ν_L and ν_R exist then neutrinos can have both Majorana and Dirac mass components. The general Lagrangian can be written as: $\mathcal{L} = \mathcal{L}_{m_D} + \mathcal{L}_{m_L} + \mathcal{L}_{m_R}$, and the general form for the mass matrix of neutrinos is:

$$\mathcal{M} = \begin{pmatrix} m_L & m_D \\ m_D & m_R \end{pmatrix} \tag{1.6}$$

The values obtained from the diagonalization of the matrix are:

$$m_\pm = \frac{1}{2}\left[m_L + m_R \pm \sqrt{(m_L - m_R)\,2 + 4m_D^2}\right]. \tag{1.7}$$

The so called see-saw mechanism allows describing the lighter mass of neutrinos with respect to the other leptons in the SM by considering $m_L = 0$ and $m_D \ll m_R$, since the two resulting mass terms are then the heavy mass m_+ and the lighter mass m_-:

$$m_+ \simeq m_R, \qquad m_- \simeq \tfrac{m_D^2}{m_R}. \tag{1.8}$$

1.3 Experimental Evidence for Massive Neutrinos

Experiments on neutrino oscillations have established that, contrary to what assumed in the SM, neutrinos have a mass. These experiments are sensitive to differences of squared masses, but not to the absolute value of the neutrino mass,

and can measure mixing angles [12]. Assuming the simplest description, with three active neutrinos, CPT invariance and no sterile neutrinos, oscillations are due to a mixing between the interactions eigenstates $\nu^{'}$ (ν_e, ν_μ, ν_τ), and the mass eigenstates ν (ν_1, ν_2, ν_3):

$$\nu^{'} = U\nu \tag{1.9}$$

where U is the unitary 3 by 3 mixing matrix, parameterized in terms of three mixing angles (θ_{12}, θ_{23}, θ_{13}) and one phase δ (a non null value of δ would result in CP violation). The following definition can be adopted:

$$U = \begin{pmatrix} 1 & 0 & 0 \\ 0 & c_{23} & s_{23} \\ 0 & -s_{23} & c_{23} \end{pmatrix} \begin{pmatrix} c_{13} & 0 & s_{13}e^{i\delta} \\ 0 & 1 & 0 \\ -s_{13}e^{-i\delta} & 0 & c_{13} \end{pmatrix} \begin{pmatrix} c_{12} & s_{12} & 0 \\ -s_{12} & c_{12} & 0 \\ 0 & 0 & 1 \end{pmatrix} \tag{1.10}$$

where $s_{ij} \equiv \sin\theta_{ij}$ and $c_{ij} \equiv \cos\theta_{ij}$.

The oscillation probability between two neutrino flavours in the two-family approximation can be written in the following form:

$$P(\nu_l \rightarrow \nu_{l'}) = \sin^2(2\theta)\sin^2\left(1.27\frac{|\Delta m^2|\,L}{E}\right) \tag{1.11}$$

where θ represents the mixing angle, L is the distance between the neutrino source and the detector measured in km and E is the neutrino energy measured in GeV. The quantity Δm^2 is then expressed in eV^2. Neutrinos produced in a specific flavour state may then be detected as a different flavour at a distance from the source where the oscillation term is large.

Two different oscillations have been at first measured in solar (ν_e) and atmospheric neutrinos (mostly ν_μ) and later confirmed by experiments on earth. So far the oscillations have been mainly studied through disappearance of the original flavour.

Two types of solar neutrino experiments have been performed: radiochemical experiments (Homestake, Sage, Gallex, GNO) and large Cherenkov experiments (Super-Kamiokande and SNO). The pioneering Homestake experiment opened the "solar neutrino problem" finding nearly 1/3 of the expected ν_e flux from Sun by studying the reaction $\nu_e + {}^{37}Ce \rightarrow {}^{37}Ar + e^-$. In the '90s SAGE and Gallex/GNO

both based on the reaction $\nu_e + {}^{71}Ga \rightarrow {}^{71}Ge + e^-$ observed $\sim$71 SNU[2] over the 130 expected [4]. Superkamiokande studied two channels, the charged-current (CC) $\nu_e + e^- \rightarrow \nu_e + e^-$ and the neutral current (NC) $\nu + e^- \rightarrow \nu + e^-$, using water to detect the Cherenkov light emitted and observed as well a deficit in the expected solar neutrino flux [5]. It was mainly sensitive to ν_e because the CC cross-section is larger and therefore a significant deficit was observed even though the experiment had some sensitivity to NC too. The SNO (Sudbury Neutrino Observatory) detector used a heavy water (D_2O) target 2.5 km underground surrounded by photomultipliers in order to detect the Cherenkov light produced by electrons originated in three reactions: charged-current (CC) ($\nu_e\, d \rightarrow p\, p\, e^-$), neutral current (NC) ($\nu_x\, d \rightarrow p\, n\, \nu_x$), where ν_x can be any of the three flavours, and elastic scattering (ES) ($\nu_x\, e^- \rightarrow \nu_x\, e^-$). It was possible to measure the total flux $\Phi(\nu_x)$ and so to verify the solar model independently of the oscillations. The CC reaction is sensitive only to ν_e, while the NC reaction is equally sensitive to all active neutrino flavours ($x = e, \mu, \tau$), this allowed SNO to determine the electron and non-electron neutrino components of the solar flux. The measured ν_e flux was $\sim$1/3 of the expected and $\Phi_e + \Phi_{\mu\tau}$ was as expected from the Standard Solar Model thus leading to the confirmation of the electronic neutrino oscillation in the other neutrino flavours [6].

Atmospheric neutrinos are produced in the decay of secondary particles, mainly pions and kaons, created in the interactions of primary cosmic rays with the nuclei of the Earth's atmosphere. Although the absolute neutrino flux is rather badly known (predictions from different calculations disagree by $\simeq 20\%$), the ratio R of the numbers of muon to electron neutrinos is known at $\simeq 5\%$:

$$R = \frac{N_{\nu_\mu} + N_{\bar{\nu_\mu}}}{N_{\nu_e} + N_{\bar{\nu_e}}} \simeq 2. \tag{1.12}$$

Neutrino oscillations could manifest as a discrepancy between the measured and the expected value of the ratio R. The Kamiokande-II [7], SuperKamiokande [8], Soudan-2 [9] and MACRO [10] detectors reported energy dependent deficits in the ν_μ fluxes with respect to the predictions and a distortion of the angular distributions. The SK experiment showed a convincing evidence of an up/down asymmetry on the ν_μ flux, a deficit for the up-going ν_μ was found. Since the ν_e data were in

[2]Solar Neutrino Units = 10^{-36} captures per second per absorber nucleus

agreement with the expectations, the observed deficit could be explained in terms of $\nu_\mu \rightarrow \nu_\tau$ oscillations with maximal mixing and $\Delta m^2 \sim 2 \cdot 10^{-3}$. The experiments results of are summarized in table 1.1.

Experiment	R
Soudan-2	$0.68 \pm 0.11_{stat} \pm 0.06_{sys}$
MACRO	$0.74 \pm 0.036_{stat} \pm 0.046_{sys} \pm 0.13_{theo}$ $-1.0 < cos\theta_{zenith} < -0.1$
SK	$R_{sub-GeV} = 0.658 \pm 0.016_{stat} \pm 0.032_{sys}$ $R_{sub-GeV} = 0.702 \pm 0.031_{stat} \pm 0.099_{sys}$

Table 1.1: Results of the atmospheric neutrino experiments.

Reactor neutrino experiments can test either solar or atmospheric oscillations [13], they measure the survival probability $P(\bar{\nu_e} \rightarrow \bar{\nu_e})$ of the electrons antineutrinos emitted by fission reactions in the reactor and travelling for a distance L: for L of the order of about few tens of kilometres the solar region can be studied, for distances that don't exceed few kilometres the parameters of the atmospheric oscillation are involved. The $\bar{\nu_e}$ spectrum is calculated from measurements of β-decay spectra of ^{238}U, ^{239}Pu and ^{241}Pu after fissioning, the reactors can produce about 10^{20} $\bar{\nu_e}$ s^{-1} per nuclear core. Experimentally, one has to compare the observed rate of positrons from the inverse β-decays with the predicted rate. If $\Delta m^2_{sol} << \Delta m^2_{atm}$ and/or θ_{13} is small enough, as it is the case, the solar driven and the atmospheric driven oscillations decouple to a first approximation in the oscillation probability formula $1 - P(\bar{\nu_e} \rightarrow \bar{\nu_e})$.

Two experiment were performed to study the parameter region of the atmospheric neutrino experiments $\Delta m^2_{atm} \sim 10^{-3}$ eV^2: the CHOOZ experiment [14] was located 1050 m away from the Chooz two-reactor nuclear power plant in France, while the Palo Verde experiment [15] used a segmented detector 750 and 890 m away from a 3-reactor nuclear power plant in Arizona. Both experiments measured a ν_e flux in agreement with expectations and thus excluded any $\bar{\nu_e} \rightarrow \bar{\nu_\mu}, \bar{\nu_\tau}$ oscillation in the Δm^2_{atm} region; the CHOOZ experiment also provided the best constraint on the upper limit of the θ_{13} mixing angle.

The KamLAND experiment [16] located in the Kamioka mine in Japan 180 km away from the source sensitive to Δm^2_{sol} studied $\bar{\nu_e}$ disappearance, it reproduced solar neutrino oscillations on Earth and contributed to the measurement of oscillation

parameters, in particular of the Δm^2 value. The solutions found by KamLAND and by the solar experiments agree and the allowed domains in the parameters space largely overlap.

Beams of muon neutrinos can be produced at accelerators allowing *Long Baseline* and *Short Baseline* experiments (depending on the travelled distance L) to study the atmospheric neutrino oscillation. These experiments can look for disappearance of the beam neutrinos or for appearance of a different neutrino flavour in the beam (*disappearance* and *appearance* experiments). The ratio L/E should be the best to reach the oscillation maximum, apart in the special case of τ appearance where this is not compatible with the τ production cross section which requires a high energy beam, in this case the number of τ produced is maximized. Maximizing the oscillation probability at high energy would require baselines measuring in 10000 km.
The K2K experiment [17] used the SK detector as a *Far* detector in combination with a *Near* detector ∼300 m away from the source to study the ν_μ disappearance in the beam produced at the KEK protosyncrotron (PS). The ν_μ spectrum seen by SK was compared with the prediction obtained with the measurements of the near detector (in absence of oscillation) and the atmospheric neutrino oscillation was confirmed at 4σ.
Long-baseline experiments which are now taking data are the MINOS experiment in the USA, described in more details in section 2.2.1, and the T2K (Tokai to Kamioka) experiment which is just starting. It uses the SK detector and neutrinos travel a distance of L∼300 km in order to test the ν_e appearance in the beam produced at the J-Parc PS in Japan. The OPERA experiment is as well a long-baseline appearance experiment designed to prove the $\nu_\mu \rightarrow \nu_\tau$ oscillation in the neutrino beam produced at CERN by detecting ν_τ interactions 730 km away from the source.

Two distinct oscillations need tree neutrino mass eigenstates, at least two neutrinos must be massive while, in principle, the third one could also be massless. The solar neutrino oscillation involves the mass eigenstates m_1 and m_2 (by definition $|m_2| > |m_1|$) so that $\Delta m^2_{sol} = |\Delta m^2_{12}| = m_2^2 - m_1^2 > 0$. For the atmospheric neutrino oscillation, the sign of Δm^2_{atm} is not determined. By convention, it is said to be positive in case of normal hierarchy or negative in case of inverted hierarchy (see fig1.1). When masses are large compared to their differences, the spectrum is

almost degenerate.

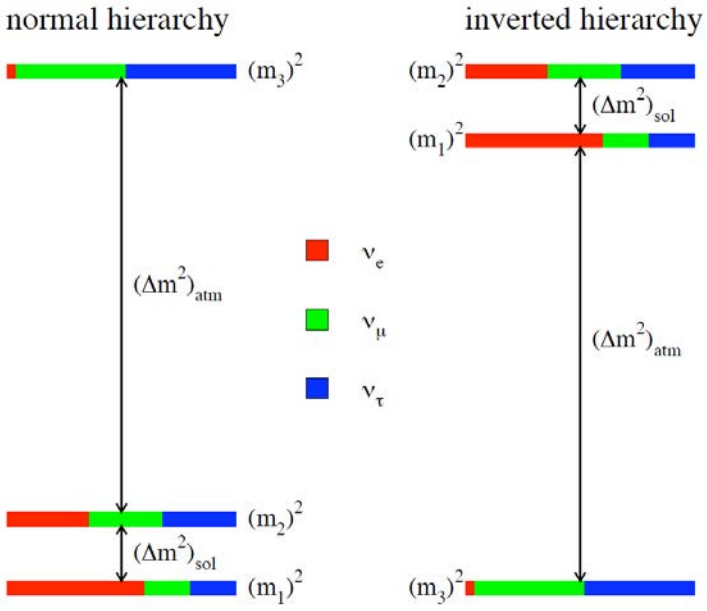

Figure 1.1: *Neutrino mass hierarchy: normal and inverted cases.*

Current data constrain, according to [11]:

$$\begin{array}{ll} \Delta m^2_{sol} = (7.65 \pm 0.20) \cdot 10^{-5} eV^2, & \theta_{12} = 0.32 \pm 0.02. \\ |\Delta m^2_{atm}| = (2.45 \pm 0.11) \cdot 10^{-3} eV^2, & \theta_{23} = 0.45 \pm 0.02. \\ \sin^2 \theta_{13} < 0.050 \ (3\sigma \ bound) & for \ \Delta m^2 \sim \Delta m^2_{atm}. \end{array} \tag{1.13}$$

1.4 Neutrino Masses

Oscillation experiments only measure differences of squared masses and do not provide information about the absolute neutrino mass scale. Limits on that are obtained from the endpoint of the tritium beta decay spectrum, from cosmology and from neutrinoless double beta decay ($0\nu\beta\beta$).

Present techniques for direct measurements of the electron antineutrino mass guarantee a model-independent approach but can only probe the quasi-degenerate region ($|m_i^2| \gg \Delta m^2_{hk}$). The cosmological inferences and neutrinoless double-beta decay are much more sensitive but suffer from a heavy model dependence.

The kinematical analysis of the final region of the beta decay spectrum allows for a direct information on the neutrino mass, the measured parameter is:

$$m_e^2 = \sum_i \left|U_{ei}^2\right|^2 m_i^2. \tag{1.14}$$

The most effective study performed so far is the ^{3}H beta decay endpoint one, by means of electrostatic spectrometers: it has yield an upper limit of the $\bar{\nu_e}$ mass of 2.2 eV [18].

Since neutrino mass affects the evolution of the Universe in some observable ways, a mass constraint can be obtained from the cosmological data such as cosmic microwave background (CMB), galaxy clustering, Lyman-α forest, and weak lensing data. All available data sets are usually combined to obtain constraints on the sum of the neutrino mass species $S_C = \sum m_\nu$. Limits as stringent as 0.2 eV on S_C can thus be obtained. They suffer however from strong dependencies from the used models which tend to spoil their reliability and the comparison with the terrestrial measurements [19]. Assuming just three active neutrino species and considering that the neutrino temperature is $T_{\nu,0}$=1.7×10^{-4} eV, any mass eigenstate heavier than this is non-relativistic at present. The contribution to the universe energy density of all the non-relativistic states is $\Omega_{\nu,i}h^2 = \sum_i m_{\nu,i}/93$ eV, where Ω is the density parameter and h the Hubble parameter in units of 100 km s^{-1}. Cosmology can put a very conservative upper bound on the sum of neutrino masses $\sum m_\nu \lesssim 0.6 - 0.7$ [20].

First suggested in 1935 by M. Goeppert-Mayer, the double-beta decay ($\beta\beta$) is a rare spontaneous nuclear transition resulting from a second order weak interaction in which an initial nucleus (A,Z) decays to a member (A,Z+2) of the same isobaric multiplet with the simultaneous emission of two electrons and two neutrinos:

$$ {}^A_Z X \rightarrow {}^A_{Z+2} X + 2e^- + 2\bar{\nu}. \tag{1.15} $$

This decay is allowed in the SM and well established. Half-lives of many isotopes have been measured, for example the NEMO-3 experiment [21] has measured for the $^{96}Zr \rightarrow^{96} Mo + 2e^- + 2\bar{\nu}$ an half-life $T^{2\nu}_{1/2} = [2.35 \pm 0.14(stat) \pm 0.16(syst)]\, 10^{19} yr$. The 0-neutrino mode ($\beta\beta(0\nu)$):

$$ {}^A_Z X \rightarrow {}^A_{Z+2} X + 2e^- \tag{1.16} $$

which violates the lepton number by two units and occurs if neutrinos are their own antiparticles. It is one of the most powerful way to test neutrino properties: it can exist only if neutrinos are Majorana particles and it allows then to fix constraints on the neutrino mass scale [22]. The rate of $\beta\beta(0\nu)$ is expressed as:

$$\left[T_{1/2}^{0\nu}\right]^{-1} = G^{0\nu}\left|M^{0\nu}\right|^2 |\langle m_\nu \rangle|^2 \tag{1.17}$$

where $G^{0\nu}$ is the phase space integral, $|M^{0\nu}|^2$ is the nuclear matrix element and $\langle m_\nu \rangle$ is a linear combination of the neutrino masses, the connection between the neutrino mixing matrix and $\langle m_\nu \rangle$ is known to be:

$$\langle m_\nu \rangle = \sum_{k=1}^{3} \left|U_{ek}^{L}\right|^2 m_k e^{i\Phi_k}, \tag{1.18}$$

where U_{ek} are the elements of the first row of the mixing matrix, m_k are the three neutrino mass eigenvalues, and Φ_k is related to Majorana CP phases. The experimentally available information in $\beta\beta(0\nu)$ decays are those carried by the daughter nucleus and the two emitted electrons. Different signatures depend therefore on the number of such information which are actually measured: sum of the electron energies, single electron energy and angular distributions, identification and/or counting of the daughter nucleus. Progress has been obtained during the last years also in improving $\beta\beta(0\nu)$ halflife limits for a number of isotopes. The best results are still maintained by experimental investigation of ^{76}Ge (Heidelberg-Moscow and IGEX) but two other experiments have recently reached comparable sensitivities: NEMO3 at LSM and CUORICINO at LNGS[3] [23]. A very controvertial evidence for a $\beta\beta(0\nu)$ signal has been claimed and recently confirmed [24] by a subset of the Heidelberg-Moscow collaboration at LNGS with $T_{1/2}^{0\nu} = 2.23^{+0.44}_{-0.32} \times 10^{25}$ y.

1.5 Beyond the Standard Model: Lorentz Violation Effects

If the mass of the neutrino is assumed to be $\sim$ eV/c^2, the neutrino relativistic velocity v should satisfy the limit $\frac{|v-c|}{c} < 10^{-19}$, which is clearly beyond experimental measurements feasible today. However, exotic theories have been proposed with Lorentz violation effects that allow velocities different than the speed of light, some of these with a limit $\frac{|v-c|}{c} < 10^{-4}$ at neutrino energies of a few GeV. Terrestrial neutrino beams could measure an effect of this magnitude.
The Lorentz violating models all imply a change in the energy-momentum dispersion relationship.

[3]Laboratori Nazionali del Gran Sasso - *Gran Sasso National Laboratory, Italy*

In [25] a model is investigated in which the effect of small extra dimensions, universal with respect to all particles, can be connected with the gravitation recoils of the propagation of neutrino in the spacetime vacuum-foam. It leads to the effect of diminishing the neutrino velocity at high energies. In this effect the energy dependence of the "effective" metric is the main deviation from space-time Lorentz invariance: in the perturbed metric one finds a retardation in the propagation of an energetic photon/fermion:

$$(\delta c/c) \sim (E/M) \quad \text{or} \qquad (\delta c/c) \sim \left(E/\widetilde{M}\right)^2, \tag{1.19}$$

where M or $\widetilde{M}$ is a high mass scale characterizing quantum fluctuations in space-time foam.
For a massless particle the relation between the energy E and the momentum p becomes:

$$E^2 = c^2 \cdot p^2 - 2cE(\vec{p} \cdot \vec{u}), \qquad |\vec{u}| \sim E/M \ or \ \left(E/\widetilde{M}\right)^2. \tag{1.20}$$

The sensitivities of the effect for neutrino velocity deviation from the speed of light ($\Delta\beta$) and for neutrino velocity differences ($\Delta\beta_{12}$) has been reported in [25] for existing and possible experiments in the $\delta\beta = E/M$ and $\delta\beta = E^2/\widetilde{M}^2$ hypothesis. In general $\Delta\beta_{12} \leq \Delta\beta$, an example is reported in section 2.1.

A toy model which assumes Lorentz violation effects on right-handed neutrinos only is presented in [26], where also the sensibility of longbaseline neutrino experiment to these effects is exploited. Neutrinos occupy a special seat in the SM: in fact, the left-handed lepton doublets can be paired to the Higgs doublet to form an operator invariant under the gauge symmetries of the SM. This means that this operator can be coupled to a singlet fermionic operator and generate a mass for the neutrino. The standard ways are to couple it to a fermion field, the right-handed neutrino, via a small Yukawa coupling, or to couple it to itself in a dimension 5 operator that generates a Majorana mass for the neutrino (thus violating lepton number conservation). The latter can be obtained in the see-saw scenario as a result of the integration of a heavy right-handed neutrino. However the nature of the neutrino mass term is fairly unknown, therefore, it may be that the right-handed neutrino is not a simple fermionic field. One interesting possibility is that

the right-handed neutrino is part of a conformally invariant sector of the theory[4]. This is possible in the case of a sector that does not carry any of the quantum numbers of the SM, in particular does not transform under gauge transformations. Therefore, one of the bound states of the conformal sector, say ψ_R, can play the role of the right handed neutrino. The right-handed neutrinos appear to be the best candidates for an object of a quasi-conformal sector (*un-neutrinos*[5]): their Yukawa couplings to the Higgs are suppressed at low scales giving rise naturally to a small Dirac neutrino mass which breaks the conformal invariance. The same kind of model is also reported in [27], where right-handed neutrinos make part of a strongly coupled conformal field theory and acquire an anomalous dimension ($\gamma < 1$) at a large scale Λ. It is presented an alternative and natural way to obtain small neutrino masses assuming right-handed neutrinos with large anomalous dimension and coupling to SM fields through irrelevant operators. Moreover if lepton number is not conserved in the conformal theory an irrelevant Majorana mass operator for right-handed neutrinos appears and dimension-five couplings between the leptons and Higgs are present. The usual dispersion relation $E^2 - p^2 = m^2$ can be parameterized including Lorentz violating effects as follows:

$$E^2 - p^2 \pm \frac{E^{2+\delta}}{M^\delta} = 0, \tag{1.21}$$

with the violation parameter $\delta > 0$ and E$\ll$M (the mass scale parameter). In terms of an effect on the propagation velocity that implies:

$$\beta = \sqrt{1 \pm \frac{E^\delta}{M^\delta}} \sim 1 \pm \frac{E^\delta}{2M^\delta}. \tag{1.22}$$

Let us assume ν_R scaling with dimension d_R under the transformation:

$$x^\mu \to \frac{1}{\epsilon} x^\mu, \quad p^\mu \to \epsilon p^\mu \quad \Rightarrow \quad \nu_{L,R} \to \epsilon^{d_{L,R}} \nu_{L,R}, \tag{1.23}$$

[4]A conformal field theory (CFT) is a quantum field theory that is related to conformal symmetries, *i.e.* a symmetry under scale invariance and special conformal transformations, together with the Poincaré group (symmetry including translations, rotations and boosts).

[5]Unparticle physics is a theory that conjectures matter that cannot be explained in terms of particles using the SM, because its components are scale invariant. The idea of unparticles comes from supposing that there may be "something" that does not necessarily have zero mass but is still scale-invariant, with the same physics. This "something" is unlike particles, and described as unparticle [28].

the action for neutrinos must be invariant under scaling transformations:

$$S = \int dx^4 - i\overline{\nu}_L \gamma^\mu \partial_\mu \nu_L - i \left(\frac{p^2}{\Lambda^2}\right)^{-\frac{\alpha}{2}} \overline{\nu}_R \gamma^\mu \partial_\mu \nu_R, \tag{1.24}$$

where $\alpha/2 = \gamma$. For the right neutrino term it yields $\epsilon^{-4}\epsilon\epsilon^{-\alpha}\epsilon^{2d_R} = 1$, hence $d_R = \frac{3+\alpha}{2}$. The formalism is valid for $\frac{3}{2} < d_R < \frac{5}{2}$, so $0 < \alpha < 2$ can be considered. For massive neutrinos the action is:

$$S = \int dx^4 - i\overline{\nu}_L \gamma^\mu \partial_\mu \nu_L - i \left(\frac{p^2}{\Lambda^2}\right)^{-\frac{\alpha}{2}} \overline{\nu}_R \gamma^\mu \partial_\mu \nu_R + m_D(\overline{\nu_R}\nu_L + \overline{\nu_L}\nu_R). \tag{1.25}$$

By finding the propagator pole we obtain:

$$p^2 = (m_D^2 \Lambda^{-\alpha})^{\frac{2}{2-\alpha}} = m_\nu^2 \quad \Rightarrow \quad \alpha = 2\frac{logm_D - logm_\nu}{log\Lambda - logm_\nu}, \tag{1.26}$$

with m_D the Dirac mass and Λ the characteristic scale of the 5-dimensions model ($x_5 = \frac{1}{\Lambda}$). A conformal see-saw with m_D=100 GeV, m_ν=1 eV, $\Lambda = 10^{19}$ GeV yields then to α=0.8. This value is well contained between the limits presented for the α parameter.

The Lorentz violation effects appear only in this warped extra dimension where only right handed neutrinos propagate, whereas the SM (and so left handed neutrinos) continues to be described in the classical way (see figure 1.2).

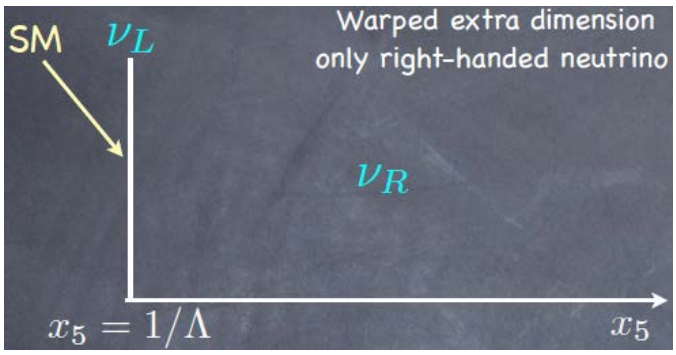

Figure 1.2: *Only the right-handed neutrinos can propagate in the extra dimension whereas the SM is described in the classical way*

After integrating over x_5 the action, the denominator of the propagator can be expanded as follows:

$$\Sigma(p^2) \sim (\frac{p^2}{\Lambda^2})^{-\frac{\alpha}{2}} + c(\frac{E}{\Lambda})^\beta, \tag{1.27}$$

this is one way to model the Lorentz violating operator: it is assumed that one of the subleading terms in the expansion of Σ only depends on the energy (and not on the invariant p^2). The parameter β should be greater than -2γ for the expansion to be consistent. The new dispersion relation is:

$$p^2 - m_\nu^2 + \frac{2c}{2-\alpha}\frac{m_\nu^{2+\alpha}E^\beta}{\Lambda^{\alpha+\beta}} = 0 \qquad \begin{cases} \delta = \beta - 2 \\ M = \left(\frac{2-\alpha}{2c}\frac{\Lambda^{\alpha+\beta}}{m_\nu^{2+\alpha}}\right)^{\frac{1}{\beta-2}} \end{cases} \tag{1.28}$$

As example, by simulating a typical set of neutrino events, and calculating the time of flight between Fermilab and Soudan, one can analyse the case of the MINOS experiment. In figure 1.3 is presented the plot obtained for the α parameter as a function of $logM$ by evolving 50k events with a time resolution of 40 ns, and counting the number of neutrinos that arrive later that the bunch time of 9.7μs.

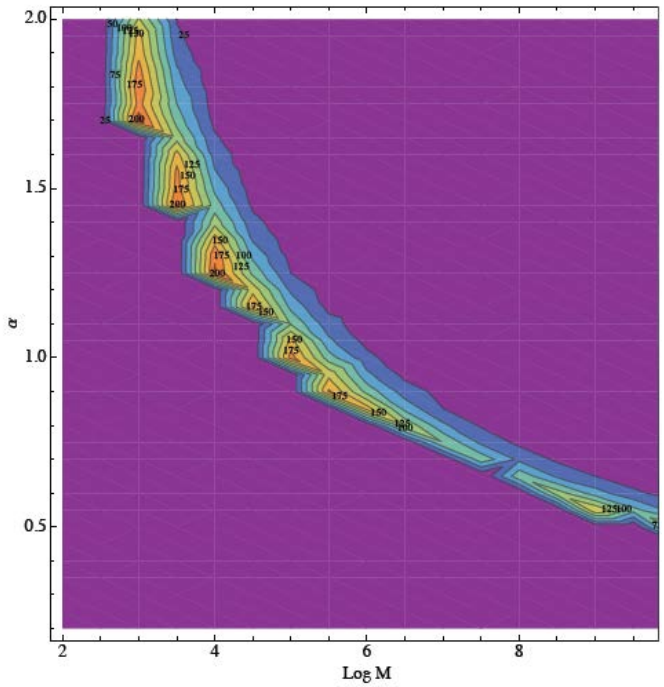

Figure 1.3: *α parameter as a function of $logM$ by evolving 50k MINOS simulated events with a time resolution of 40 ns, and counting the number of neutrinos that arrive later that the bunch time of 9.7 μs. The numbers in the plot correspond to the variuos values of the contour lines.*

The presented theoretical model proposes a very general parameterisation with two parameters: a mass scale and an exponent. OPERA can place strong bounds at mass scale values $M > 10^4$ GeV, and be competitive with supernova neutrinos bounds ($M > 10^{10}$ GeV for $\delta = 1$, $M > 10^4$ GeV for $\delta = 2$) [33].

If there is a deviation of v_ν from the speed of light, the model does not exclude

a priori either $v_\nu > c$ or $v_\nu < c$, since both possibilities are allowed.
It should be pointed out that since in the theoretical model presented here the Lorentz violating effects depend on the neutrino energy, if there is a deviation of the neutrino velocities from the speed of light, necessarily also a spread of the neutrino velocities must exist. The differences of neutrino velocities should be smaller than the $\Delta\beta = v_\nu/c - 1$ effect.

In the following chapter the existing measurements on the neutrino velocity will be presented, in particular the theoretical Lorentz violation model described here is applied to the case of the SN1987A measurements.

Chapter 2

Neutrino Velocity Measurements

2.1 SN1987A

In table 2.1 are listed the neutrinos from the type II supernova SN1987A detected by the Kamiokande II, IMB and Baksan detectors, the times, energies and corresponding errors on energies are given.

By comparing the arrival times of neutrinos and photons from SN1987A [29], a sensitivity of $|v - c|/c \leq 10^{-8}$ was achieved, for neutrinos of the energies in tab.2.1. The considerations made in [29] did not refer to a dispersion in the neutrino velocity but to a direct comparison between the speed of light and the speed of neutrinos.

Despite different authors try to treat differently dispersion ($\Delta\beta_{12}$) from shift ($\Delta\beta$) they are related and one cannot treat them separately. In [25] the SN1987A data are used for estimates of differences in the neutrino velocities too, given the time shift $|\Delta\beta| < 10^{-8}$. It is said that because the 12.4 s experimental duration of the neutrino pulse is compatible with the expected duration of the neutrino emission during the supernova gravitational collapse it is reasonable to take this value as an upper limit for the $\Delta\beta_{12}$ estimate with the average neutrino energy ∼10 MeV:

$$\Delta\beta_{12} < \Delta T/T_0 = 12.4/4.5 \cdot 10^{12} = 2.8 \cdot 10^{-12}, \tag{2.1}$$

where $T_0 = 150000$ light years.

It should be stressed that, comparing to the SN1987A results, the OPERA

Event	t_i (s)	E_i (MeV)	σ_i (MeV)
Baksan			
1	$\equiv$0.0	12.0	2.4
2	0.435	17.9	3.6
3	1.710	23.5	4.7
4	7.687	17.6	3.5
5	9.099	20.3	4.1
IMB			
1	$\equiv$ 0.0	38	7
2	0.412	37	7
3	0.650	28	6
4	1.141	39	7
5	1.562	36	9
6	2.684	36	6
7	5.010	19	5
8	5.582	22	5
Kamiokande II			
1	$\equiv$ 0.0	20	2.9
2	0.107	13.5	3.2
3	0.303	7.5	2.0
4	0.324	9.2	2.7
5	0.507	12.8	2.9
6 (omitted)	0.686	6.3	1.7
7	1.541	35.4	8.0
8	1.728	21.0	4.2
9	1.915	19.8	3.2
10	9.219	8.6	2.7
11	10.433	13.0	2.6
12	12.439	8.9	1.9
13 (omitted)	17.641	6.5	1.6
14 (omitted)	20.257	5.4	1.4
15 (omitted)	21.355	4.6	1.3
16 (omitted)	23.814	6.5	1.6

Table 2.1: *Data from SN1987A. There are 5 data points identified by Kamiokande II as background in previous investigations and then omitted. The relative arrival time in each experiment with respect to the others are not known, so times are given setting t=0 for the first event.*

experiment can perform an experimental measurement on the neutrino velocity in controlled and known conditions, which is not the case of the SN data, moreover given the energy dependence, a $\delta\beta/\beta$ limit has no more universal validity and in particular the SN limit of 10^{-8} is not directly applicable to CNGS where the neutrino energy is 3 orders of magnitude larger. Indeed, in general the effect in

the dispersion relation increases with energy. For instance in the Lorentz Violation (LV) effects ([26]) depend on $\left(\frac{E}{M}\right)^{\delta}$ and it is possible with the CNGS beam to investigate LV effects at a much higher energy, that cannot be visible in the supernova data case and that are not directly comparable due to the much smaller energy.

The model presented in [26] has been used to analyse effects related to the dispersion which test the dependence of neutrino velocities from their energies. Following the results obtained in [30], events falling below the energy threshold 7.5 MeV have been excluded as background. Since LV effects are energy dependent it is worth noticing that the energy measured at the detector is not the energy of the incoming neutrino, but that of the charged lepton resulting from the largely dominant process [30]:

$$\bar{\nu}_e + p \rightarrow e^+ + n \tag{2.2}$$

The energy of the incoming neutrino is given by the relation $E_\nu = E_l + Q$ (where Q=1.29 MeV is the neutron-proton mass deficit). The relative arrival times in each experiment with respect to the others are not known, thus times are given setting $t \equiv 0$ for the first event of every experiment, and the analysis is conducted independently for every data set. The sign of the overall time shift of neutrino bunches with respect to the Lorentz conserving hypothesis cannot be fixed, since the relative arrival time of the neutrinos with respect to light is known only with poor accuracy. Therefore, the limits for either the superluminal or the subluminal case can be given, but we cannot distinguish between them [31].

The time interval during which neutrinos are produced in a supernova is model dependent (various scenarios are given in [30]), in [26] only the information coming from detected events is considered. The only assumption on the production mechanism taken into account is the energy spectrum at the source, which is rather well established:

$$F \sim E^{\alpha_z} e^{-(1+\alpha_z)E/E_0} \qquad \alpha_z \sim 2 - 5([32]), \tag{2.3}$$

where E_0 and α_z are, respectively, the average energy of neutrinos and a pinching parameter. The numerical results proposed in this section are evaluated assuming $E_0 = 11$ MeV and $\alpha_z = 3$, but it has be checked that the dependence of results on these parameters is negligible in practice.

Limits on LV parameters can be obtained by simulating the evolution of a bunch of neutrinos from the supernova to the detector and measuring the probability that

the time dispersion at the detector predicted by LV parameters is consistent with that actually observed within a given confidence interval. The initial time dispersion of neutrinos can be computed by evolving backward the neutrinos observed in the three experiments considered.

The details on the analysis are given in [26]. If μ is the average of the time dispersion distribution at the detector and σ_L, σ_R are the asymmetric standard deviations, limits on LV parameters can be obtained by requiring that the probability of measuring the observed time dispersion falls within the interval $\{\mu - 2\sigma_L, \mu + 2\sigma_R\}$ of the simulated distribution of time dispersions.

The various steps of a simulation with the Kamiokande II data are presented in figure 2.1: in particular the plot (c) and (d) show respectively the distribution of time dispersions obtained at the detector and the time shift between neutrinos and photons at detector.

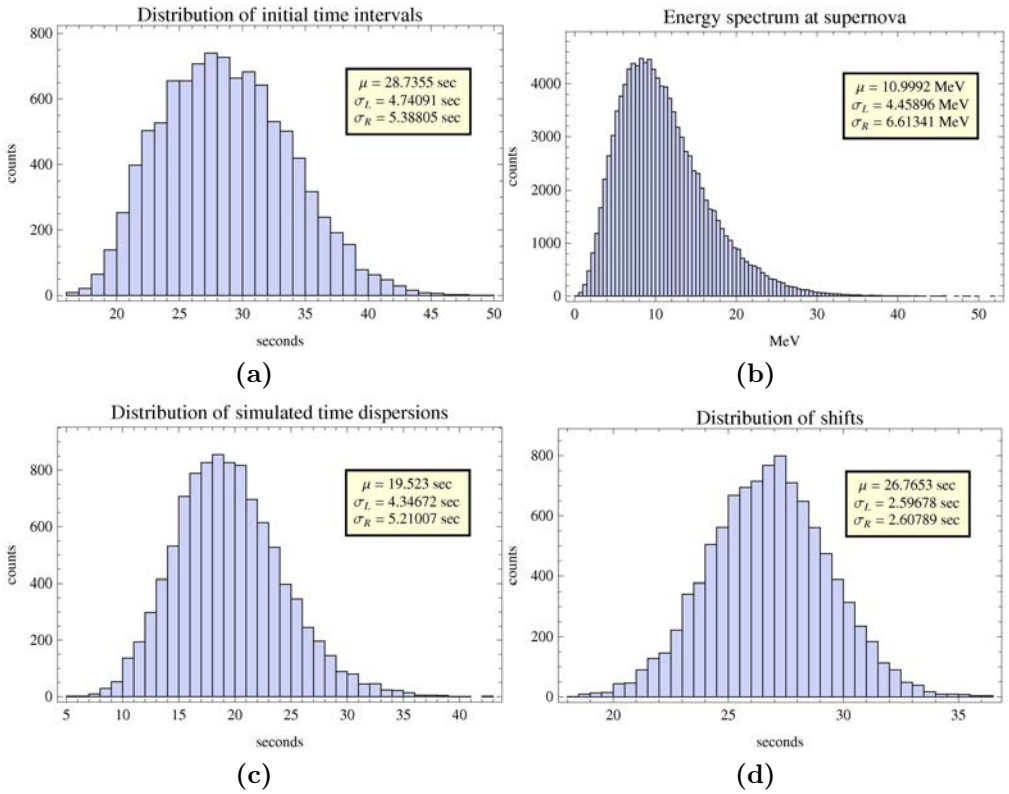

Figure 2.1: *Simulation steps starting with Kamiokande II data with LV parameters $\alpha = 3$, $E_0 = 11$ MeV and $M = 4 \times 10^9$ GeV.*

The results obtained for different scenarios and for each experiment are shown in table 2.2: the average time dispersion of neutrino bunches at supernova (t_{SN}), the average time shift between neutrinos and photons at detector ($\Delta t_{\nu\gamma}$) and lower bounds on the Lorentz Violating mass scale (M_{min}). It is possible to see that

α	t_{SN} (sec)		$\Delta t_{\nu\gamma}$ (sec)		M_{min} (GeV)	
	FN	VN	FN	VN	FN	VN
			Baksan			
0.5	$18.4^{+6.2}_{-5.6}$	$11.7^{+3.3}_{-3.0}$	$43.3^{+6.6}_{-7.0}$	$22.2^{+3.1}_{-3.1}$	5×10^{19}	2×10^{20}
1	$18.0^{+6.5}_{-5.6}$	$13.6^{+4.5}_{-4.0}$	$22.1^{+5.0}_{-4.9}$	$14.4^{+3.1}_{-3.0}$	2×10^{9}	3×10^{9}
1.5	$21.0^{+8.6}_{-6.9}$	$14.5^{+5.4}_{-4.5}$	$19.2^{+5.4}_{-4.9}$	$11.4^{+2.9}_{-2.7}$	5×10^{5}	7×10^{5}
2	$22.3^{+10.7}_{-7.6}$	$15.8^{+6.7}_{-5.2}$	$16.9^{+5.1}_{-4.6}$	$10.3^{+3.1}_{-2.8}$	8×10^{3}	1×10^{4}
			IMB			
0.5	$14.0^{+2.5}_{-2.1}$	$15.1^{+2.7}_{-2.4}$	$20.7^{+2.0}_{-2.2}$	$22.2^{+2.3}_{-2.4}$	5×10^{20}	4×10^{20}
1	$16.8^{+3.0}_{-2.8}$	$16.9^{+3.0}_{-2.7}$	$16.5^{+1.9}_{-2.0}$	$16.3^{+2.0}_{-2.0}$	6×10^{9}	6×10^{9}
1.5	$11.6^{+1.9}_{-1.6}$	$11.6^{+1.9}_{-1.6}$	$10.1^{+0.9}_{-1.0}$	$10.0^{+1.0}_{-1.0}$	2×10^{6}	2×10^{6}
2	$16.8^{+3.7}_{-2.9}$	$16.7^{+3.8}_{-3.0}$	$13.1^{+1.6}_{-1.7}$	$12.9^{+1.6}_{-1.6}$	2×10^{4}	2×10^{4}
			KII			
0.5	$30.4^{+4.5}_{-4.4}$	$37.0^{+6.2}_{-5.9}$	$40.6^{+3.4}_{-3.7}$	$51.4^{+5.2}_{-5.3}$	1.6×10^{20}	9×10^{19}
1	$28.7^{+5.3}_{-4.7}$	$34.8^{+7.1}_{-6.4}$	$26.8^{+2.6}_{-2.6}$	$32.7^{+4.2}_{-3.7}$	4×10^{9}	3×10^{9}
1.5	$27.3^{+6.4}_{-5.1}$	$33.8^{+9.0}_{-7.2}$	$21.7^{+2.3}_{-2.0}$	$26.5^{+4.0}_{-3.1}$	1×10^{6}	8×10^{5}
2	$19.6^{+4.4}_{-3.1}$	$19.7^{+4.5}_{-3.1}$	$15.6^{+1.1}_{-0.8}$	$15.8^{+1.4}_{-0.9}$	2×10^{4}	2×10^{4}

Table 2.2: *Average time dispersion of neutrino bunches at supernova (t_{SN}), average time shift between neutrinos and photons at detector ($\Delta t_{\nu\gamma}$) and lower bounds on the Lorentz Violating mass scale (M_{min}) for different exponent values (α), in the Fixed Number (FN) and Variable Number (VN) hypothesis and for each experimental data set.* Fixed Numbers*: the number of neutrinos in the simulated bunches at the supernova source is the same as the observed one in the considered experiments.* Varying Number*: the number of neutrinos in the simulated bunches at the supernova source varies according to a Poisson distribution centered at 10, in this case, the results are dependent on the choice of the expected number, but it has been checked that varying this parameter in the interval 8,12 the differences remain always within the same order of magnitude.*

the bounds for the mass scales are consistent with similar results obtained in other analysis [33] and the time scales obtained for neutrino production in the supernova ($\sim$10 sec) are consistent with models previously published in the literature [30].

2.2 Measurements Performed with Neutrino Beam Experiments

Man-made neutrino beams are the ideal environment to perform neutrino velocity measurements in a controlled way. Long baseline experiments, being designed to search for neutrino oscillations, allow performing this measurement over long distances and increasing the sensitivity to tiny deviations of the neutrino velocity w.r.t. the speed of light. Measurements prior to those with long baseline neutrino experiments were done in the Fermilab narrow-band beam [35], by comparing

the interaction times of muons and neutrinos [34]. Since in these measurements $|1-\beta_\mu| < 10^{-5}$, this comparison can be considered equivalent to a comparison with the speed of light.
I was found $|\beta_\nu - 1| < 4 \cdot 10^{-5}$ for neutrinos and antineutrinos from pion and kaon decays (the secondaries were produced in 1-ns pulses), in an energy range 30 to 200 GeV and travelling a distance 500 to $\sim$ 900 m, w.r.t. energetic muons.

2.2.1 MINOS Measurement

The MINOS experiment at Fermilab [36] employs a $\sim$3 GeV neutrino beam produced by the NuMI beamline facility (Neutrinos at the Main Injector) in order to search for neutrino oscillations in disappearance mode with a twin detector setup. The neutrino beam is sent through a near detector at Fermilab, and a far detector located 734 km away in the Soudan Mine in northern Minnesota (see figure 2.2). The Near Detector (ND) is foreseen in order to measure the unoscillated neutrino beam and compare the neutrino spectrum to that measured in the Far Detector (FD). The ND can measure as well the time structure of the neutrino beam and

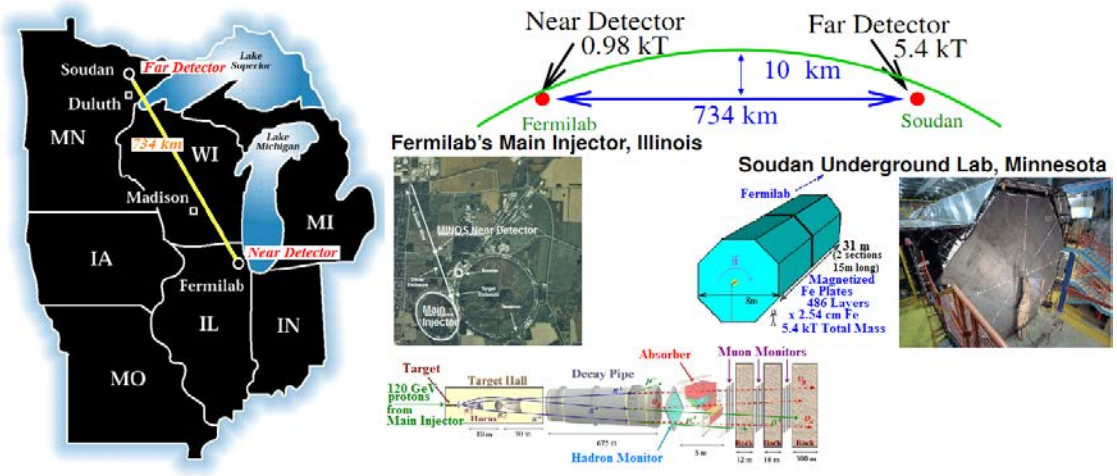

Figure 2.2: *MINOS experiment, near and far detectors location and beamline sketch.*

the beam extraction timing can be referred to the Coordinated Universal Time (UTC)[1]. This measurement can be compared to that at the FD, which will have

[1]The UTC is distributed since the 70s by all national laboratories and broadcast time services, it is derived primarily averaging a large ensemble of cesium oscillator. Cesium oscillators are frequency standards because the SI (International System of Units) second is based on the resonance frequency of the ^{133}Cs since 1971. The International Atomic Time (TAI) is an atomic

the same time structure but delayed by the neutrinos time of flight in between the two detectors.

The intercalibration accuracy of the two measurements is <100 ns. The MINOS detector are steel-scintillator tracking calorimeters, the time of each photomultiplier hit is recorded with a precision of 18.8ns (ND) and 1.6ns (FD). The detector clock are synchronized to two identical Global Positioning System (GPS) receivers to provide absolute UTC. The neutrino beam seen at the ND is composed of 93% ν_μ, 6% $\overline{\nu_\mu}$ and 1% $\nu_e + \overline{\nu_e}$. At the FD, the oscillated neutrino beam is composed at ∼60% by ν_μ, the remaining ν_μ having been transformed into ν_τ (assuming a full mixing $\nu_\mu - \nu_\tau$ oscillation). The Main Injector sends the protons onto a graphite target to generate the neutrino beam by a single-turn extraction. It operates in one of several modes, one spill can have 5 or 6 proton batches resulting in different time structures to be separately analysed. The six batches spill has a duration of 9.7 μs. The ND GPS receiver time-stamps the signal of the magnet used to extract the protons from the main injector and defines the spill's starting time, t_0. The relevant MINOS parameters are summarized in table 2.3.

Parameters	Nominal Values
ND to FD distance,[a] L	734 298.6 ± 0.7 m
Time Of Flight (TOF),[b] δ	2 449 356 ± 2 ns
GPS Receivers	True Time model XL-AK
Antenna fiber delay	1115 ns ND, 5140 FD
Single Events Time Resolution	<40ns
Random Clock Jitter	100 ns, each site
Main Injector Cycle Time	2.2 s/spill
Main Injector Batches/Spill	5 or 6
Spill Duration	9.7 μs (6 batches)
Batch Duration	1582 ns
Gap Between Batches	38 ns

[a] *Distance between front face of the ND and the center of the FD.*
[b] *TOF computed assuming the speed of light.*

Table 2.3: *Relevant MINOS and NuMi parameters as reported in [37]*

The data sample used in the MINOS analysis satisfy some criteria in the ND and in the FD. In the ND the events selection criteria are identical to those of [36]; the events are required to have a total reconstructed energy < 30 GeV, have the vertex contained within 1 m of the fiducial volume and be in time with the spill

scale that conforms as close as possible to the SI definition of the second, the UTC is derived from TAI and differs from it by an integer number of seconds (UTC proceeds as a linear function of TAI).

($\pm \sim 7\mu s$ w.r.t. the spills starting or ending time). The pre-selection of events in the FD requires event times within $\pm 50\mu s$ of the expected arrival time (assuming a massless neutrino). At the FD the 473 accepted events have satisfied one of these three selection criteria: ν_μCC events contained in the fiducial volume, neutrino-induced muons from CC interactions in the rock outside the detector, and NC-like shower events contained in the detector. 258 events out of the selected sample were contained ν_μ or $\overline{\nu_\mu}$ CC events.

The measured time delays with respect to UTC, d_{ND} and d_{FD}, incorporate offsets and delays due to readout time, electronic latency and GPS antenna fiber delays. The related uncertainties are presented in table 2.4.

	Description	Uncertainty (68% C.L.)
A	Distance between detectors	2 ns
B	ND Antenna Fiber Length	27 ns
C	ND Electronics latencies	32 ns
D	FD Antenna Fiber Length	46 ns
C	FD Electronics latencies	3 ns
F	GPS and transceivers	12 ns
G	Detector readout differences	9 ns
Total	(Sum in quadrature)	64 ns

Table 2.4: *Sources of uncertainty in ν relative time measurement.*

The uncertainty on the net correction $|d_{ND} - d_{FD}|$ was determined to be ± 64 ns at 68% C.L. At the ND the time $t_1 = t_{ND} - t_0 - d_{ND}$ was obtained from the time of a neutrino interaction in the detector (t_{ND}) as the time of the earliest hit produced in the scintillator. Similarly, for the FD, $t_2 = t_{FD} - t_0 - d_{FD}$. Both for ND and FD t_0 is the time of the extraction magnet signal.

The ND measures the time structure of the NuMI protons with neutrino interactions as shown in figure (2.3, a). This is described by two probability density functions, related to the 5 or 6 proton batches mode: (PDFs) $P_1^5(t_1)$ and $P_1^6(t_1)$. These PDFs describe as well the expected FD neutrino arrival times distribution, apart from the neutrino time of flight (TOF) computed assuming the light speed and from a degradation due to the uncorrelated jitter of the two GPS clocks, resulting in a time uncertainty of $\sigma = 150$ ns. By taking into account this jitter new PDF P_2^5 and P_2^6 are computed in order to compare to the arrival time of each event in the FD (t_i^2).

The deviation δ from the expected TOF was found by maximizing a log-likelihood

function (that sums each event in the 5- and 6-batch data). The distribution of the measured FD times is shown in figure (2.3, b) together with the predicted distribution for the best fit value $\delta = -126 \pm 32(stat.) \pm 64(sys.)$ ns at a 68% confidence limit.

The neutrino velocity $v = L/(\tau + \delta)$ (where τ is the nominal time of flight) should satisfy

$$\frac{(v-c)}{c} = \frac{-\delta}{\tau+\delta} = 5.1 \pm 2.9(stat. + sys.) \cdot 10^{-5} \quad 68\% C.L. \tag{2.4}$$

for neutrinos of ∼3 GeV. This measurement was the most precise terrestrial neutrino TOF measurement achieved so far. It shows a deviation from the speed of light of about 1.8σ. The corresponding limit at 99% C.L. on the speed of the neutrino is -2.4·$10^{-5} < (v-c)/c < 12.6 \cdot 10^{-5}$. Although this effect is limited by the measurement accuracy, it is at the limit of the region excluded by the previous Fermilab measurements, and it could be still compatible with a null effect; it has motivated the measurement which will be discussed in this thesis. As it will be shown later, if such effect exists, it could be measured with much higher significance by using the CNGS beam and the OPERA detector.

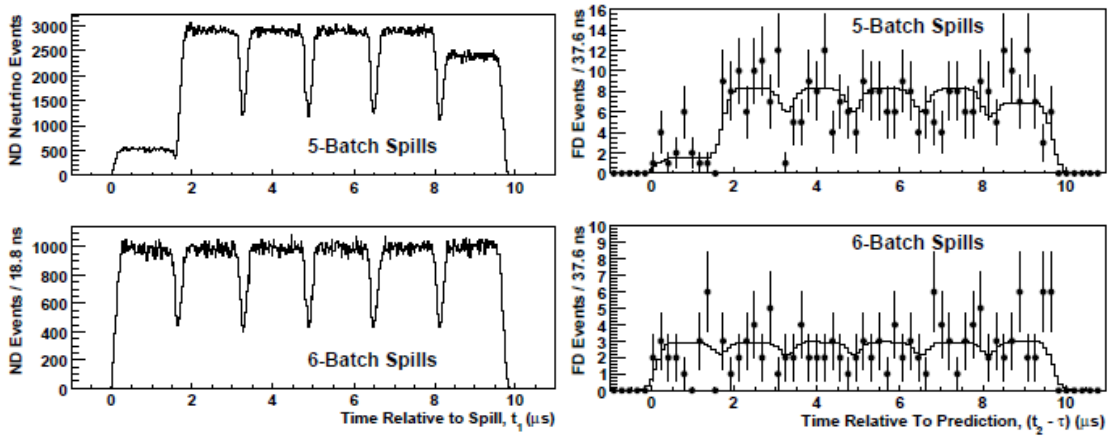

(a) **(b)**

Figure 2.3: *a) Neutrino event time distribution measured at the MINOS Near Detector. The top plot corresponds to events in 5-batch spills $P_1^5(t_1)$ while the bottom plot corresponds to 6-batch spills $P_1^6(t_1)$. b) Time distribution of FD events relative to prediction after fitting the time-of-flight. The top plot shows events in 5-batch spills, the bottom 6-batch spills. The normalized expectation curves $P_2^5(t)$ and $P_2^6(t)$ are shown as the solid lines.*

2.2.2 Potentialities of OPERA in a Neutrino Velocity Measurement

In this section the merit factors which characterize a neutrino velocity mea-

surement performed with the CNGS[2] and OPERA experimental set-up will be presented.

The OPERA experiment allows to perform another neutrino velocity measurement with neutrinos at higher energies (mostly in the 1-30 GeV range with an average neutrino energy of $\simeq$17 GeV) over a distance of 730 km from CERN to LNGS. The OPERA experiment was optimized to search for $\nu_\mu \rightarrow \nu_\tau$ oscillations in appearance mode. Because of kinematical effects resulting from the large mass of the τ lepton (m_τ=1776.8 MeV) on the CC interaction cross-section of the ν_τ, this search requires a high energy beam. The neutrino flux was optimized in order to best match the convolution between the oscillation probability and the cross-section for ν_τ charged current interactions. The neutrino flux expected in Gran Sasso is presented in figure 2.4.

As in MINOS the neutrino pulses are generated at the CERN accelerator complex with a duration of about 10 μs and can be related to the UTC. If the neutrino pulses were instantaneous the deviation w.r.t. the speed of light TOF would simply be $\delta = (t_{FD} - t_{ND}) - TOF$. However since we do not know the exact time, within the proton pulse, of the proton generating the neutrino interaction detected in Gran Sasso by OPERA, the beam timing structure has to be taken into account in the measurement of the TOF. This is done in the case of MINOS by directly measuring the time distributions in the ND. In the case of OPERA a fast waveform digitizer recording (FWD) installed on the proton beam line at CERN allows measuring the pulse timing and plays the same role as the MINOS ND (see figure 2.5). The difference with respect to MINOS is that with the FWD we are able to restrict the timing analysis by selecting only those proton spills that have generated the neutrino interactions seen in the OPERA detector. So with OPERA we can compare the neutrinos arrival time distribution at Gran Sasso precisely with the time distribution of the protons which have generated them and not just with the average time structure. This is important especially if the time structure changes with time. Indeed the spills which correspond to neutrino interactions recorded in OPERA are a very small minority (2.35% of the total number).

The analysis of the 2009 and 2010 OPERA data has been performed using the time information at the starting point (CERN) and at the end point (LNGS).

[2]Cern Neutrinos to Gran Sasso

The proton timing information is referred to the UTC and stored in the CERN database. By using the electronic detectors of the OPERA experiment the CNGS neutrino interactions at Gran Sasso are UTC time tagged as well. The CNGS neutrinos generated at CERN have the same distribution in time of their parent protons. The proton spills have an internal time structure which allows to perform an analysis of the recorded OPERA events that should reproduce the same distribution.

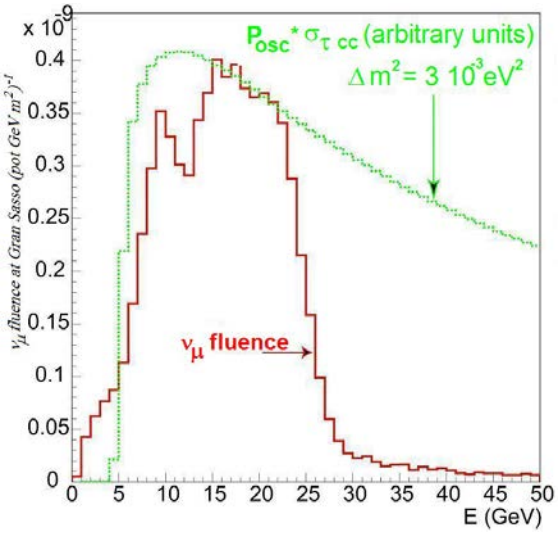

Figure 2.4: *Product of oscillation probability and ν_τ CC cross-section for small Δm^2 and maximal mixing, comparison with the expected ν_μ flux at Gran Sasso, as a function of the neutrino energies.*

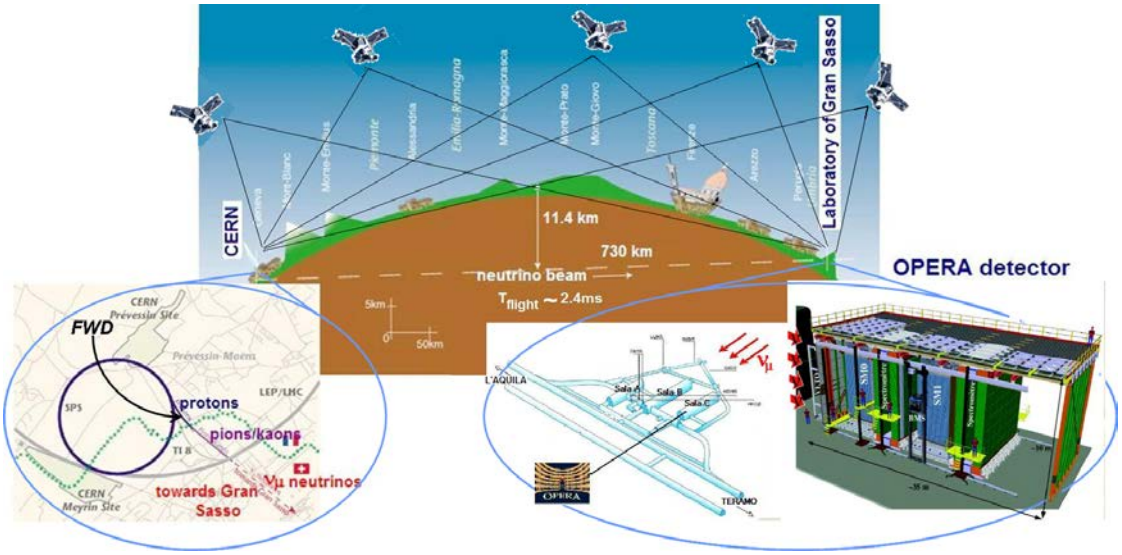

Figure 2.5: *FWD and OPERA detector locations and neutrino beam travel path.*

Compared to the MINOS measurement, the higher energy of the beam, and so the higher number of interactions in the detector (of the order of a few tens of thousands in the 2009 and 2010 runs), allows for a measurement with a much smaller statistical uncertainty. On top of that, the timing system is more sophisticated than that of MINOS, since it was explicitly upgraded in view of the neutrino velocity measurement. This will also reduce systematics by about one order of magnitude.
The accuracy achieved by the OPERA measurement reported in this thesis is of about 10 ns in statistical uncertainty and less than 15 ns in systematical uncertainty. This work implied the study of several aspects which are detailed below:

1. a study of theoretical models concerning Lorentz violation effects and the interpretation of the experimental measurements in terms of the model parameters (as presented in section 1.5 and 2.1);
2. the study and calibration of the CERN and LNGS timing systems (described in chapter 4 and 5):
   a) calibration measurements of the LNGS timing distribution system, from the GPS system to the OPERA detector;
   b) calibration measurements of the timing chain at CERN using a Cesium clock, starting from the GPS system and through the chain until the detector that measures the current of the protons extracted from the SPS;
   c) the timing response simulation of the electronic subdetectors in OPERA;
   d) the study and calibration of the GPS system;
   e) the analysis of the data from the high accuracy timing system: a twin system composed by Cesium clocks and GPS operating in common view mode installed at CERN and at LNGS for high precision timing measurements, the common view mode allows to perform a time transfer between the two sites with 1 ns precision;
3. the geodesy measurements and calculation to precisely determine the distances between the CNGS components and the OPERA detector (chapter 6);

4. the optimization of the events selection criteria in OPERA to reduce the uncertainty related to the neutrino interactions outside the detector volume (chapter 7);
5. the measurement of the delay between the neutrino interactions recorded by OPERA and proton spills of the CNGS beam (chapter 8), including:
   a) the characterization of the CNGS beam time structure and intensity, and the data acquisition from the CERN database;
   b) the analysis of the SPS accelerated proton current, for each single spill extraction related to the OPERA events;
   c) the study of the timing correlation between these spills and the OPERA events;
6. the data analysis and the extraction of the neutrino time of flight (chapter 9), including:
   a) the selection of the final data sample for the neutrino velocity measurement and the statistical analysis to determine the neutrino time of flight, using the correlation between the neutrino interactions seen by OPERA and the time structure of the proton spills at CERN and considering the time transfer corrections between the Cs-GPS systems of the two sites;
   b) the integration of all calibration effects and corrections

In the following chapters the OPERA detector is described as well as the CNGS beam line and the two timing systems.

Chapter 3

The OPERA Experiment in the CNGS Beam

3.1 CNGS Beam

The acceleration of the protons up to 400 GeV/c momentum for the CNGS beam implies several steps performed by the machines belonging to the CERN accelerators chain. The CERN accelerator complex is shown in figure 3.1. Protons of 50 MeV/c are produced by the Linac and transported to the Booster where they are accelerated up to 1.4 GeV. They are then transferred to the PS where they are further accelerated up to 14 Gev/c. The final momentum of 400 GeV/c is reached in the SPS accelerator where protons are injected from the PS. The circumference of the SPS is equivalent to 11 times the PS circumference. This allows filling the SPS circumference by using two PS acceleration cycles, each producing 5 proton batches of the same length as the PS circumference. Protons at the end of each PS acceleration cycle are injected in the SPS by using the Continuous Transfer extraction scheme, that extracts the beam stored in the PS during five turns of the PS circumference. Kicker magnets are used to generate a closed orbit bump around an electrostatic septum which shaves the proton beam in order to produce one batch per turn. During this operation there are proton losses. Because of these losses, protons are not distributed uniformly inside the SPS but are characterized by a density distribution which will result in an internal time distribution at the level of the extracted beam as presented in figure 3.2. The beam contained in the SPS ring and accelerated to 400 GeV/c is then extracted in a spill consisting of

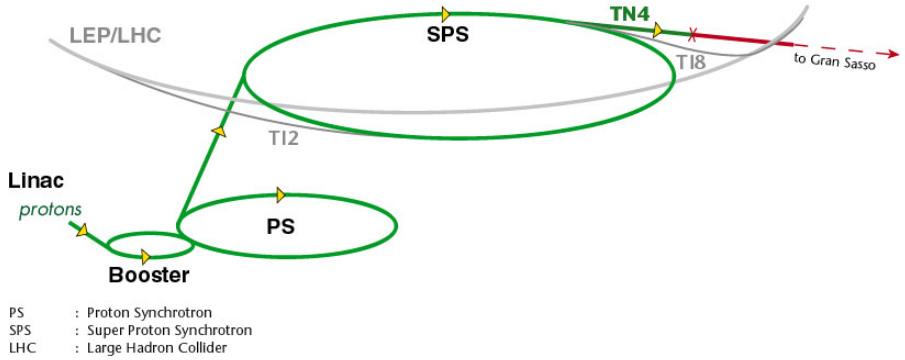

Figure 3.1: *The CERN accelerator complex.*

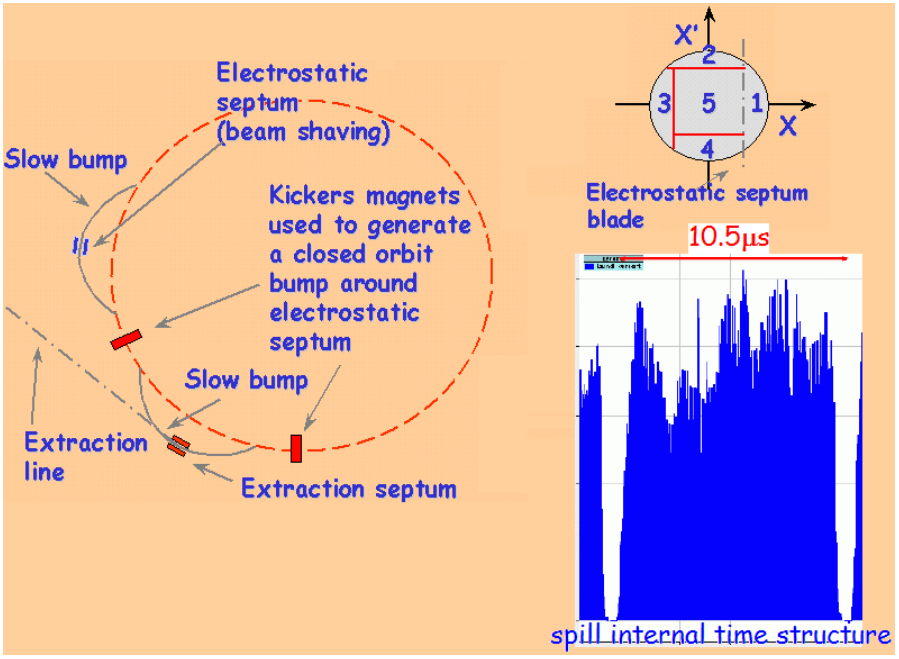

Figure 3.2: *Beam shaving: an electrostatic septum divides the PS proton beam in five parts before they are send to the SPS. During this procedure there are some proton losses so that the resulting spills are not flat.*

two fast extractions of 10.5 μs separated by 50 ms [38],[45]. A complete CNGS cycle, including the two PS acceleration cycles, the SPS acceleration, the CNGS spill and the magnets powering down, lasts 6 seconds. This cycle corresponds to a working-mode of the CERN complex completely dedicated to the CNGS and yields every 6 seconds two neutrino flashes lasting each 10.5 μs and interleaved by 50 ms. This is the simplest neutrino beam timing structure. In the real life the operation of the SPS is most often shared with other users (fixed target experiments, LHC, *etc*) resulting in alternating CNGS cycles with other SPS cycles not producing neutrinos in a more complex structure called supercycle which may

lasts a few tens of seconds. The effect of the supercycle is that the time interval between some of the CNGS spills may last much longer than 6 seconds. A scheme of the CNGS extractions during SPS cycles is shown in figure 3.3.

The time structure within one CNGS cycle is measured by the OPERA experiment as shown in figure 3.4 where two peaks corresponding to the two extractions within the same spill are clearly visible. By comparing the UTC timestamp of the events recorded by the OPERA data acquisition with that of the protons extraction from the SPS it is possible to select the events on time with the CNGS beam. This is done by selecting a window of $\pm$ 20 μs w.r.t. the beginning of the extraction. Then by plotting the UTC time of the events w.r.t. the beginning of the extraction which generated it corrected for the TOF, the time distribution of the extractions lasting 10.5 μs can be well recognized.

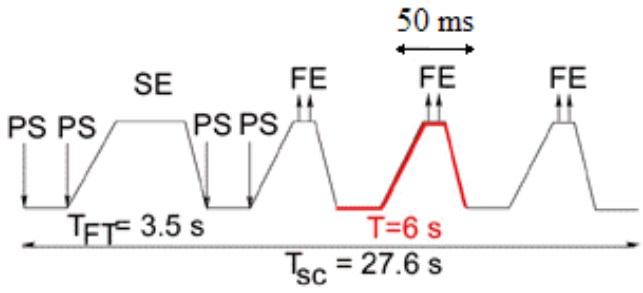

Figure 3.3: *Scheme of CNGS extractions in an SPS cycle, one slow extraction (SE) is followed by 3 cycles with 2 fast extractions separated by 50 ms (FE) for the CNGS.*

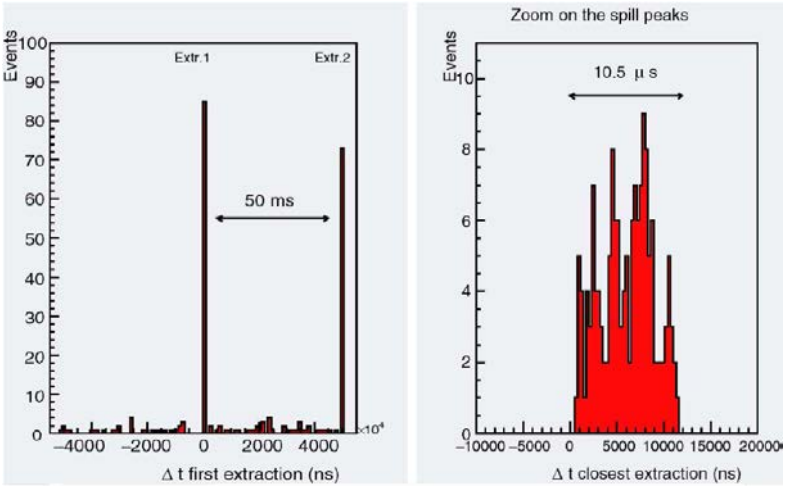

Figure 3.4: *Beam timing structure measured by the OPERA experiment. The events on time with CNGS can be selected using the time information of the GPS systems. On the left the two peaks corresponding to the two fast extractions of protons from the SPS, separated by 50 ms, can be recognized. The events outside the two peaks are cosmic background. On the right is shown a zoom of one peak: the number of the recorded OPERA events in time is contained in a time window of 10.5 μs.*

The protons accelerated in the SPS up to 400Gev/c and extracted from the ring with a kicker magnet are then transported with a dedicated beamline onto a target, made of successive graphite rods. Pions and kaons are produced in the hadronic interactions of the protons on the carbon nuclei. Since neutrinos are produced in the decays of positive mesons, while antineutrinos by negative mesons, the positively charged π/K are energy selected and guided by two focusing lenses, the horn and the reflector, in order to produce the ν_μ beam in the LNGS direction. The effect of the focusing improves by a factor 10 the neutrino flux. These particles are then channelled in a vacuum decay tube 1000 m long where they decay into muons and muon-neutrinos:

$$\text{CNGS target interactions } p + C \rightarrow \pi^+, K^+ \text{ decay in flight} \rightarrow \mu^+ + \nu_\mu \qquad (3.1)$$

The remaining undecaied pions and kaons and the protons that have not interacted in the target, are then absorbed by an hadron stopper. Muons, ultimately absorbed downstream in around 500m of rock, are monitored by two muon detector stations that allow to measure the intensity of the neutrino beam produced, its profile and direction. The CNGS beam line is showed in figure 3.5.
The nominal parameters for the CNGS beam are summarized in table 3.1.

Parameters	Nominal Values
Number of extractions/cycle	2 (50ms apart)
Fast extraction batch length (μs)	10.5
Number of bunches/extraction	2100
Proton intensity/extraction	2.4 10^3
Bunch length (ns) (4σ)	2
Bunch spacing (ns)	5
$\langle E_\nu \rangle$ (GeV)	17
CC interactions $\bar{\nu_\mu}/\nu_\mu$ rate at LNGS	2.1%
CC interactions rate $(\nu_e + \bar{\nu_e})/\nu_\mu$ at LNGS	0.87%

Table 3.1: *CNGS beam parameters*

In figure 3.6 the summary of the cumulated statistics of the OPERA physics runs is presented.

The CNGS proton line is carefully monitored along its 840 m length: the stability of the beam can be verified by measuring its position with 23 Beam Position Monitors (BMP) [39]. The last BMP operates at better than $\pm$0.35 mm accuracy and is mechanically coupled to the CNGS target in order to provide the beam position as seen by the first target rod. Moreover, the beam intensity is

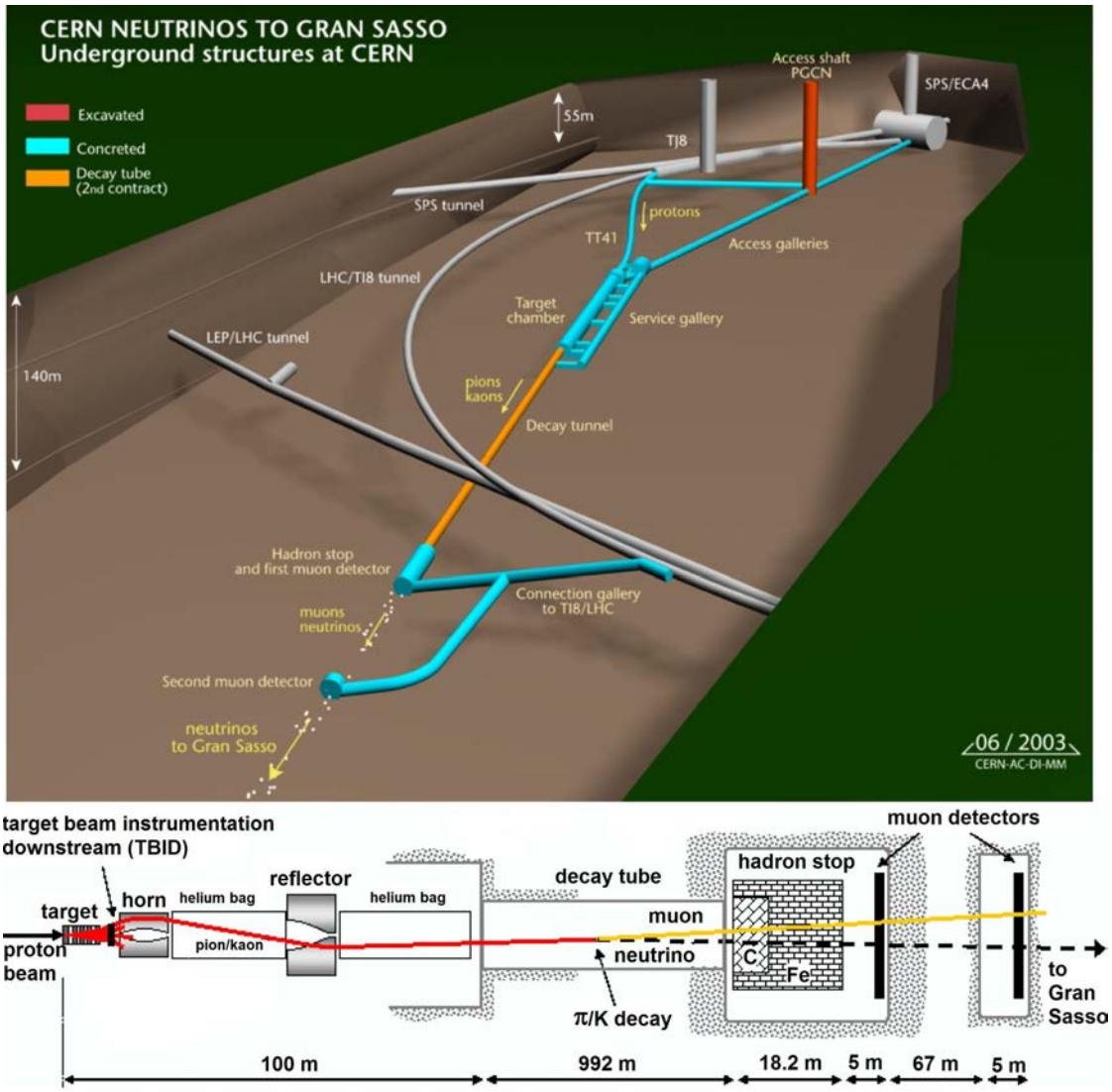

Figure 3.5: *CNGS beam line. Up: scheme of the underground structure at CERN. Bottom: the CNGS secondary beam line: the SPS proton beam interacts in the carbon target, two focusing magnets (the horn and the reflector) deflect the positive pions and kaons. These mesons decay in flight producing muons and ν_μ, two muon monitors at the end of the beam line allow to measure the beam profile. After all the other particles are absorbed, neutrinos continue towards Gran Sasso.*

measured by two Beam Current Transformer (BCT) at the start and at the end of the proton beam line. Beam losses are measured by 18 Beam Loss Monitors (BLM) all along the line. The stability of the protons impact point on the target is excellent: the beam position averaged over several days is within $\sim$50μm r.m.s [40].

The secondary beam line, from the CNGS target to the muon monitors, is instrumented to measure the profile and the intensity of the secondary particles.

Year	Beam days	Protons on target	SPS Eff.	On-time events	Interactions in the bricks
2008	123	1.78×10^{19}	61%	10122	1698
2009	155	3.52×10^{19}	70%	21428	3693
2010	187	4.04×10^{19}	81%	25497	4248

Summary of the OPERA Physics Runs (2008-2010)

Total accumulated statistics: 9.34×10^{19} protons on target

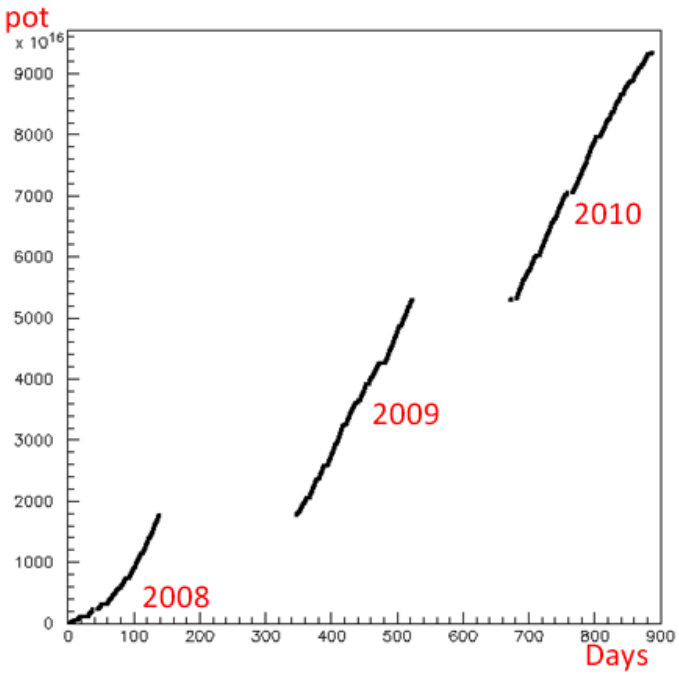

Figure 3.6: *Collected statistics during the OPERA physics runs: the cumulated protons on target for the CNGS are presented.*

A Secondary Emission Monitor may be used to check immediately downstream of the target the efficiency of the conversion of protons into secondaries. A scan across the target position provides information on the best alignment of the proton beam w.r.t. the target. The two muon monitors stations at the end of the CNGS line each have 42 muon detectors assembled in a cross-shape array. The muon intensity and the vertical and horizontal muon profiles can be measured, in order to have an on-line feedback of the neutrino beam quality. Since the two muon stations are separated by 67 m of rock, only muons with an energy above 20 Gev (50 GeV) can reach the first (second) muon station: the first station is then very sensitive to target-horn misalignments, while the second which is sensitive to the most energetic part of the muon spectrum provides information on the proton-target misalignment. A precise alignment of the beam w.r.t. the target and the

horn can be obtained by comparing the muon monitor profiles and the proton scanning at the target [44].

The magnet system focuses positive charged particles with an average energy of 35 GeV while the negative charged secondaries are defocused. Since the first magnet alone is not enough to produce a parallel beam, a second horn called reflector operates 40 m downstream. The working principle of the focusing optics is illustrated in figure 3.7.

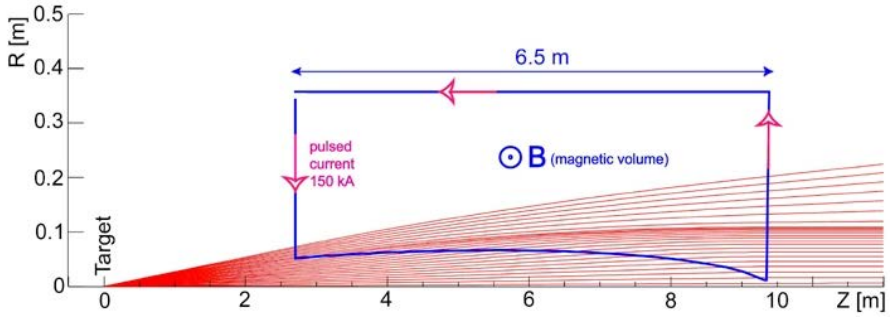

(a)

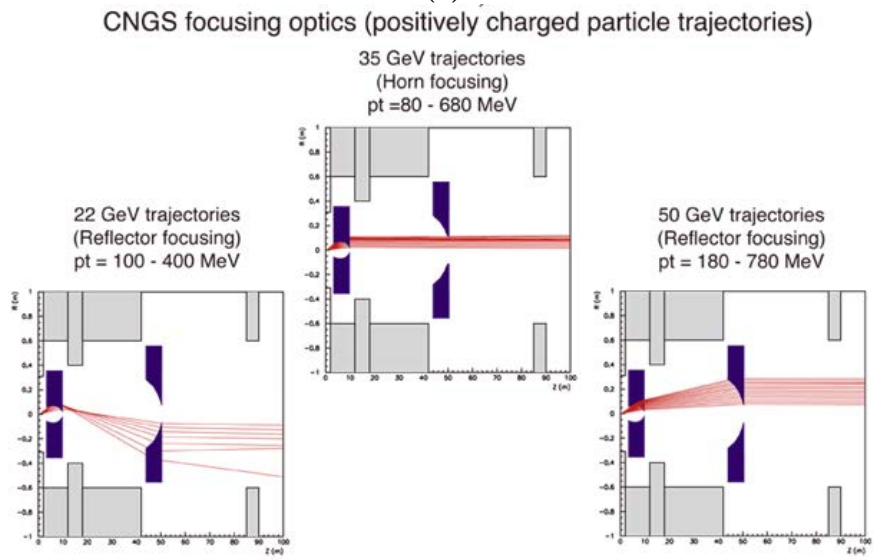

(b)

Figure 3.7: *CNGS focusing optics. a) Horn magnetic field: particles with very small angle at production will never cross the inner conductor into the magnetic volume and will therefore continue in a straight line. Particles with larger production angles travel inside the magnetic volume. Within a given range of angles, these particles all form a parallel beam at the exit of the horn. At even larger production angles, the field in the horn is insufficient and the particles are not deviated enough. b) The resulting beam is illustrated for particles with different energies. For 35 Gev particles (produced with an angle between 2.3 and 19.4 mrad) the horn magnetic field itself produce a parallel beam towards Gran Sasso (second example). At other angles or energies the reflector is also needed.*

Both magnets are toroidal lenses, the magnetic field is within the outer and the

inner conductors, the horn operates with a current of 150 kA and the reflector with 180 kA. The current is not continuous but pulses synchronously with the two beam extractions.
As mentioned, the muon stations are very sensitive to any misalignment between the proton beam, the target and the magnets (for instance an 80 μm parallel beam shift on the target would produce a 5cm shift of the muon profile centroid in the second muon detector station). As a result of the excellent beam position stability on the target also the muon beam stability in the second muon station was very good, i.e. 2.5 mm r.m.s. for the full year 2009 [38]. Also during the 2010 run the CNGS had a good beam position stability on the target: $\sim$50 (90) μm horizontally (vertically). A picture of one muon monitor is shown in fig 3.8, as well as an example of the beam profiles measured by the two muon stations.

The CNGS beam line is fully described using the FLUKA [42] code; this allows performing dedicated MC simulations for the evaluation of the various aspects concerning the beam (as the energy deposition along the beam line, the mechanical stress and so on, up to the muon distributions in the muon monitors and the neutrino energy distributions expected at Gran Sasso). The beam line is described in details from the point of view of its geometry and composition, from the protons impact point up to the hadron stop. Calculations include all what concerns the transport of particles and their interactions with matter.
The FLUKA code is used for the CNGS since it resulted in good agreement with data in past similar neutrino beam experiments at CERN, and the simulation of the CNGS resulted in very good agreement with the secondary beamline data: as presented in figure 3.8 there is an absolute agreement MC/data within 5%(20%) in the first(second) muon monitor [43].

3.2 CNGS-OPERA Alignment

The alignment accuracy of the CNGS beam w.r.t. the OPERA detector is determined by the survey accuracy during the construction of the beam line and its relation with global geodesy and by the monitoring of the beam profiles performed with the instrumentation of the CNGS beam line. This last point just ensures that the beam is operating in conformity with the alignment parameters determined by

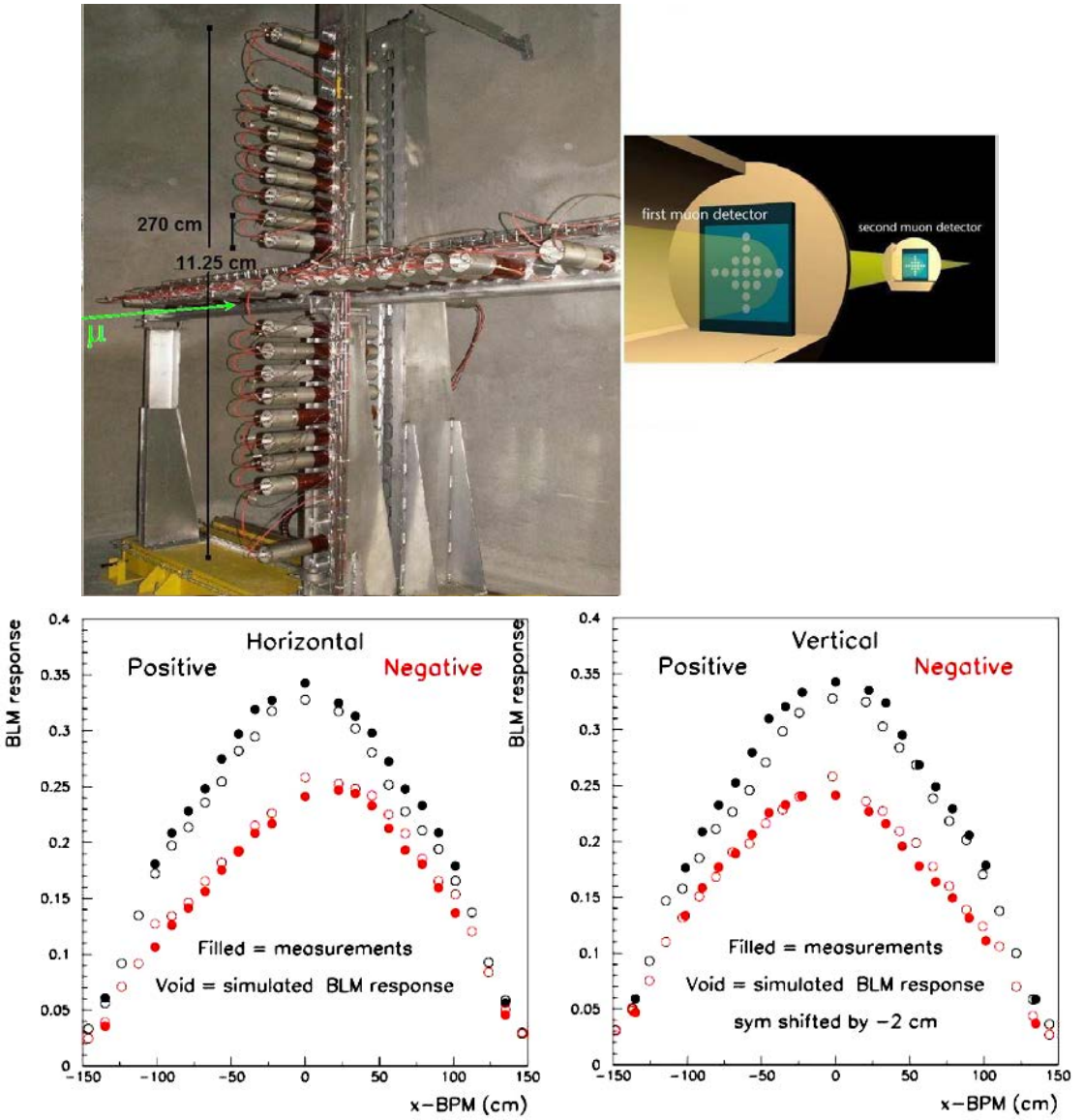

Figure 3.8: *CNGS muon monitors. Top: a picture of one cross-shaped muon monitor of the CNGS. Bottom: beam profiles as measured by the muon detector stations: horizontal and vertical profiles of the beam are plotted (black points) and confronted with the simulations (*A. Guglielmi, TAU08 [43]*), they resulted in good agreement. The profiles for the anti-neutrino CNGS mode (focusing of negative mesons) are also shown (red points), the asymmetry is due to the Earth magnetic field that deflects the positives to left and up and the negatives to right and down, in the 1 km path inside the decay tunnel (Earth magnetic field components calculated in CNGS reference system: $\vec{B}[10^{-5}T]$=(1.59,-4.21,-1.13) with z along the beam direction towards Gran Sasso).*

the global geodesy. In what follows, some simulation results concerning the effects of possible sources of beam misalignment are presented. In figure 3.9 is presented the expected radial distribution for a perfectly aligned ν_μ beam at Gran Sasso [44]: the neutrino beam appears flat (within 5%) over ∼500 m in the radial plane. The beam spread, visible in the radial distribution, is expected due to the transverse

momentum of the neutrinos produced in the mesons decays. The LNGS cavern extends in the same plane over ∼100 m. Given the beam radial distribution, in order to guarantee that the OPERA detector is within the region of the flat neutrino intensity it would be sufficient to establish the beam direction with an accuracy better than 0.5 mrad. The geodesic alignment of the beam line is expected to be one order of magnitude better than this value.

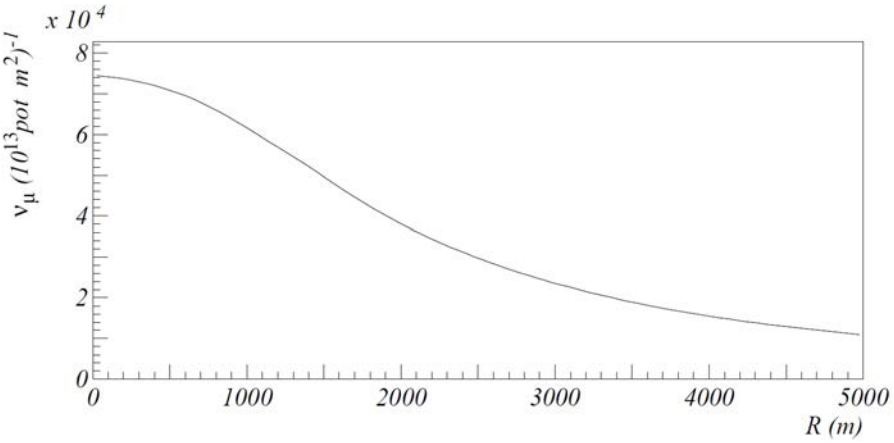

Figure 3.9: *Expected ν_μ radial distribution in Gran Sasso for a perfectly aligned beam [44].*

Simulations were performed to examine how to detect beam deviation or misalignments by monitoring the secondary CNGS beamline. Three independent MC simulations of the CNGS beamline were used, they resulted in very good agreement and indicated that the number of charged current neutrino events detected in Gran Sasso is insensitive to all but extreme misalignments. That is explained mostly by the large diameter of the decay tunnel.
In [44] possible sources of beam errors are studied and the conclusion is that the standard beam monitoring procedures guarantee a beam alignment quality much better than the one which would produce any visible effects at Gran Sasso. The beam is just operating as expected from the global geodesy calculations. The sources of beam errors studied in [44] are the following.

Lateral displacement of the proton beam at the target

With an expected position of the proton beam at the target accurate at better than 0.1 mm, simulations indicate that only displacements larger than 1.0 mm could affect the number of charged-current interactions seen at LNGS. This occurs only if a sizable fraction of protons does not intercept the target. This can be

monitored with the muon monitors at the end of the beam line, which are sensitive to these displacements.

Angular displacements of the proton beam at the focal point

The proton beam is designed to be focused at 50 cm inside the target with a resolution of 0.1 mrad. The number of CC events at Gran Sasso is not very sensitive even in the unrealistic case of 1 mrad of disalignment. The second muon monitor is the most sensitive detector to this distortion and its beam profile was distributed in the opposite direction w.r.t. the beam misalignment.

Change of divergence of the proton beam

The size and the divergence of the beam can be altered by changing the focusing parameters. The case where beam divergency $\sigma_{\theta_{x,y}}$ is doubled and proton beam size $\sigma_{x,y}$ is halved[1] has been studied. The number of events at Gran Sasso is not affected. This can be monitored with the hadron monitor of the CNGS.

Lateral displacements of the magnetic lenses

The case of a misalignment of the horn and the reflector has been studied (the expected position resolution is 0.1 mm). The number of neutrino events at LNGS is sensitive only to a transverse displacement of the horn larger than 6 mm and to a reflector displacement larger than 2 cm. The muon monitors profiles are then dramatically distorted.

Geodesic misalignment of the whole beam system

The case of a huge misalignment of 0.5 mrad of the whole CNGS line w.r.t. the reference Gran Sasso direction was studied (the accuracy of the whole beamline alignment was expected to be 0.05 mrad). This produces a 360 m displacement of the beam axis at LNGS and in a reduction of 2.5% in the number of CC events. To monitor this, the detectors at LNGS are the best suited.

Recently a new campaign of geodetic measurements was performed in order to check the CNGS beam alignment. Its results confirm the original calculations and will be presented more in details in chapter 6.

For what concerns the neutrino velocity measurements, the main effect results from the evaluation of the distance travelled by the particles between the graphite

[1]The reference values at focal point are $\sigma_{\theta_{x,y}} = 0.053$ mrad and $\sigma_{x,y} = 0.53$ mm.

target and the OPERA experiment. This distance depends on the global geodesy measurements but it is rather independent on the beam pointing accuracy. Some second order effects due to the ignorance of the actual decay point of the parent mesons generating the neutrinos seen in Gran Sasso will be discuss in the next paragraph.

3.2.1 Effect of the Ignorance of the Parent Mesons Decay Point on the TOF

OPERA will measure the difference between the real TOF of neutrinos and the TOF expected by assuming that neutrinos and their parents travel at the speed of light. As a matter of fact, it is not possible to know at which point of the tunnel the parent meson decas and generates the neutrino that will interact and interacts at Gran Sasso. In order to compare to the result of the measurement an overall TOF is computed assuming the speed of light from the graphite target down to the interaction point in Gran Sasso. This time is then compared to the one resulting from the OPERA measurement in order to look for a deviation of the neutrino velocity w.r.t. the speed of light. This approximation concerns just a small part of the travelled path ($< 1/730$) and it is a second order effect since, as it will be shown below, also the parent mesons move practically at the speed of light. In order to evaluate the error arising from the uncertainty on the secondaries decay point, a MC study has been performed, starting from the FLUKA code, considering the decays of ν_μ parents π^+, π^-, μ^+, μ^-, K^+, K^-, K_L, K^0 and $\bar{K}^0$. The decay point of these particles along the beam line (the Z axis is aligned with the beam and the target position is taken as origin) has been considered for the calculation of the time difference between the exact and the approximate travel times. In the exact calculation we consider the real parent velocity from the target up to its decay point at a given Z position, and a neutrino travelling with the speed of light from that point up to the interaction point in Gran Sasso. In the approximate calculation, given the ignorance of the decay point, we simply assume the speed of light from the target down to the interaction point.
In figure 3.10 are shown the parent particles populations considered in the simulation, they are mainly pions, and positive muons. In the same figure is also presented the decay points distribution for the secondaries emerging from the CNGS target,

the majority decays inside the 1 km decay tunnel, the mean decay distance is about 450 m. As example, also the energy distribution for pions is shown.
The quantity Δt of equation 3.2 has been calculated for the various neutrino parent particles in order to evaluate the error made by assuming that they travel to position Z along the beam line at the speed of light instead of their true velocity βc:

$$\Delta t = \frac{z}{\beta c} - \frac{z}{c} = \frac{z}{c}\left(\frac{1}{\beta} - 1\right) \approx \frac{z}{c}\frac{1}{2\gamma^2}. \tag{3.2}$$

The resulting distribution of Δt (ns) is shown in figure 3.10, the mean value is $\langle \Delta t \rangle = 1.4 \cdot 10^{-2}$ ns. In general, the error is much less than 0.2 ns; this uncertainty is negligible in the precision on neutrino velocity measurement. In the same figure the 1-β distribution of the parent particles is also presented, it is clear that the particles involved are very relativistic. An example of the anti-correlation between Δt and the neutrino energies is shown as well.
This effect exists also at the Gran Sasso site for neutrino interactions not occurring in the OPERA target. In this case we typically record the arrival time of a secondary muon in the OPERA detector without knowing the real interaction point of the neutrino. This effect will be studied in chapter 7.2.1 and it can be as well neglected within the aimed accuracy of our measurements.

3.3 The OPERA Detector

The OPERA experiment ([46],[45]) is designed for the direct observation of ν_τ appearance from $\nu_\mu \rightarrow \nu_\tau$ oscillations in the ν_μ CNGS beam. The τ is detected via the topological observation of its decay and the kinematical analysis of its production and decay vertices. This needs a very high spacial accuracy of the order of 1 μm which can be obtained with nuclear emulsions as a tracking medium. A hybrid apparatus that combines real-time detection techniques (electronic detectors) and the Emulsion Cloud Chamber technique (ECC) is used. The very high space resolution needed for the decay topology measurement must be achieved over a target mass of the order of about 1 kton in order to have enough interactions and sensitivity to ν oscillations. This target mass can not be build by using only nuclear emulsions. The ECC technique allows to achieve this by interleaving nuclear emulsion films with passive material.
An ECC detector is made of lead plates, the target, alternated with nuclear emul-

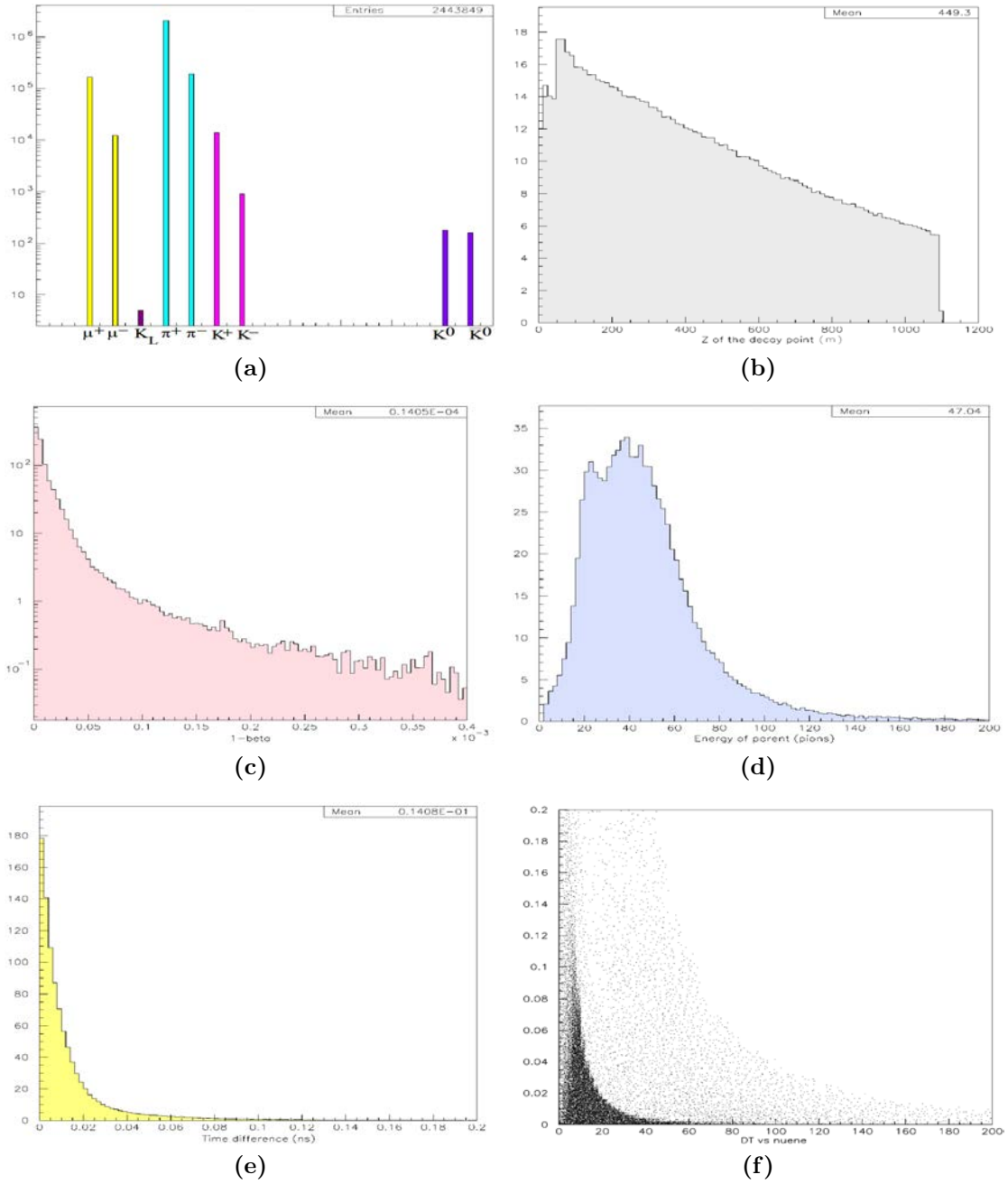

Figure 3.10: *a) The neutrino parent particles used in the MC study. b) The decay point distribution for the secondaries emerging from the CNGS target, the majority of them decay in the decay tunnel. c) The 1-β distribution for the neutrino parent particles. d) Example of π^+ energy distribution (GeV). e) The calculated time difference due to the uncertainty related to the decay point of the parent particles. f) The Δt values (ns) as a function of the neutrino energies (GeV), in the case of π^+ particles.*

sion films, the tracking devices with sub-micrometric accuracy: the basic unit of the OPERA experiment is the "brick", which is made of 56 plates of 1 mm thick lead interleaved with the emulsion films. 150000 of these units have been assem-

bled for an overall mass of 1.25 kton. Electronic detectors complement the ECC bringing real time detection and muon identification capabilities.
In fig3.11 is shown an OPERA brick and a scheme of a ν_τ charged-current interaction in it and as it would appear in the scintillator Target Trackers of the electronic detector. The first ν_τ candidate event of the OPERA experiment is shown in figure 3.12 [47]. It is a candidate for a τ decay in the hadronic channel $\tau \rightarrow \rho + \nu_\tau$.
The OPERA detector is divided in 2 identical units (supermodules), each consisting in 31 walls where the bricks are arranged transversally to the beam direction, interleaved with double layers of plastic scintillators (Target Trackers, TT), followed by a magnetic dipole spectrometer, as illustrated in figure 3.13.

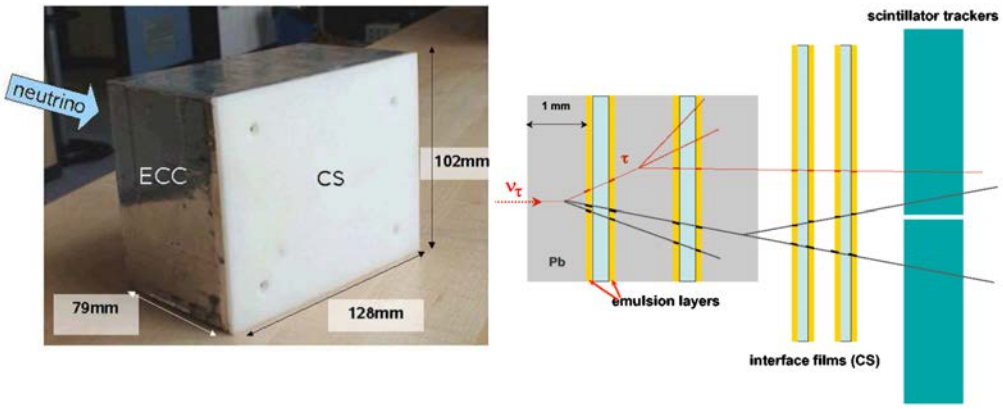

Figure 3.11: *The OPERA brick. On the left: picture of a real brick as produced and inserted in the OPERA walls (CS is the box containing two Changeable Sheets). On the right: Schematic view of a ν_τ charged-current interaction and the decay-in-flight of the final state τ lepton as it would appear in an OPERA brick, in the interface emulsion films (CS), and in the scintillator trackers.*

The electronic detectors trigger the data acquisition, identify and measure the trajectory of charged particles; the spectrometers measure the muon momentum and charge. The iron magnets core are instrumented with bakelite Resistive Plate Chambers (RPC) and complemented with six stations of Drift Tubes (Precision Trackers, PT) which measure the deflection of the charged particles inside the magnetic field. Additional RPC (XPC) layers with readout strips rotated by $\pm 42.6°$ w.r.t. the horizontal are positioned near the first two PT stations, in order to remove left-right ambiguities in the reconstruction of the particle trajectories inside the PT.
The electronic detectors, moreover, are used to define the probability for a brick to contain the neutrino interaction. Then the bricks are extracted from the target according to their probability value. The overall efficiency evaluated on 2009

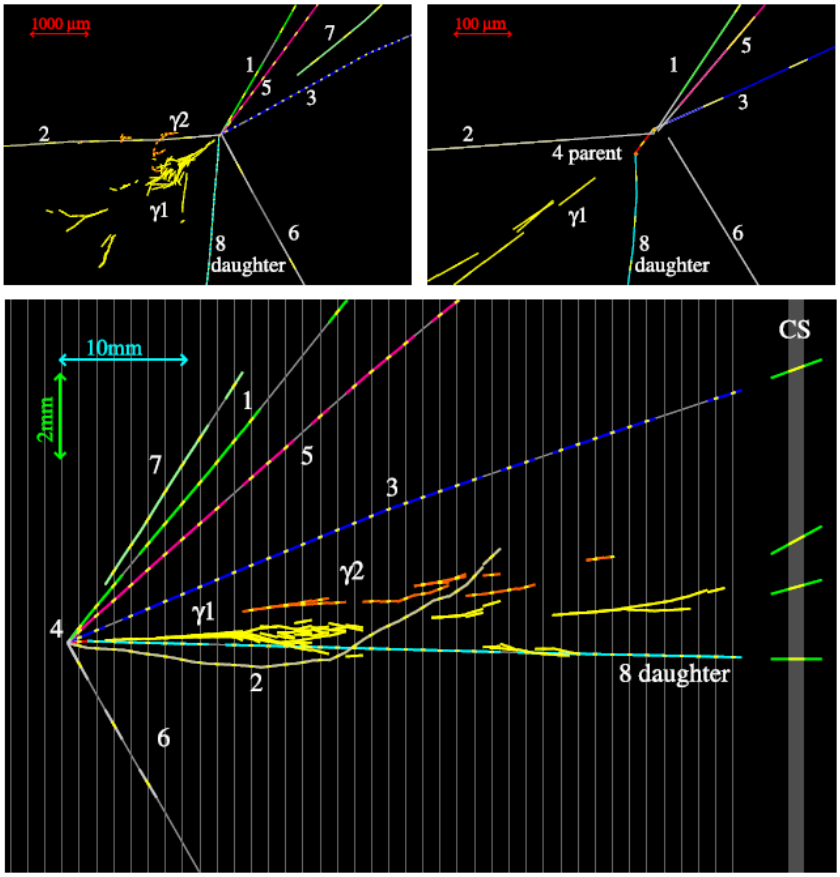

Figure 3.12: *Display of the τ-candidate event [47]. Top left: view transverse to the neutrino direction. Top right: same view zoomed on the vertices. Bottom: longitudinal view. The primary neutrino interaction consists of 7 tracks of which one exhibits a visible kink. Two electromagnetic showers caused by γ-rays have been located that are associated with the event.*

run (taking into account both CC and NC events) in identifying the brick where the neutrino interacts is about 55% considering only the most probable brick. It reaches about 75% considering the first three bricks selected by the electronic detectors.

3.3.1 Scintillator Target Trackers

In between two brick walls there are scintillator walls; each wall is made of a plane of four horizontal modules followed by a similar plane of vertical modules, so that 3D track information is provided [50]. These detectors allow to locate the brick in which neutrino interactions occurred or the entering point in the target of particles generated by neutrino interactions external to the OPERA target.
A module has 64 scintillator strips 6.86 m long, 10.6 mm thick and 26.3 mm wide, read on both sides using Wavelength Shifter fibers (WLS) and multi-anode photo-

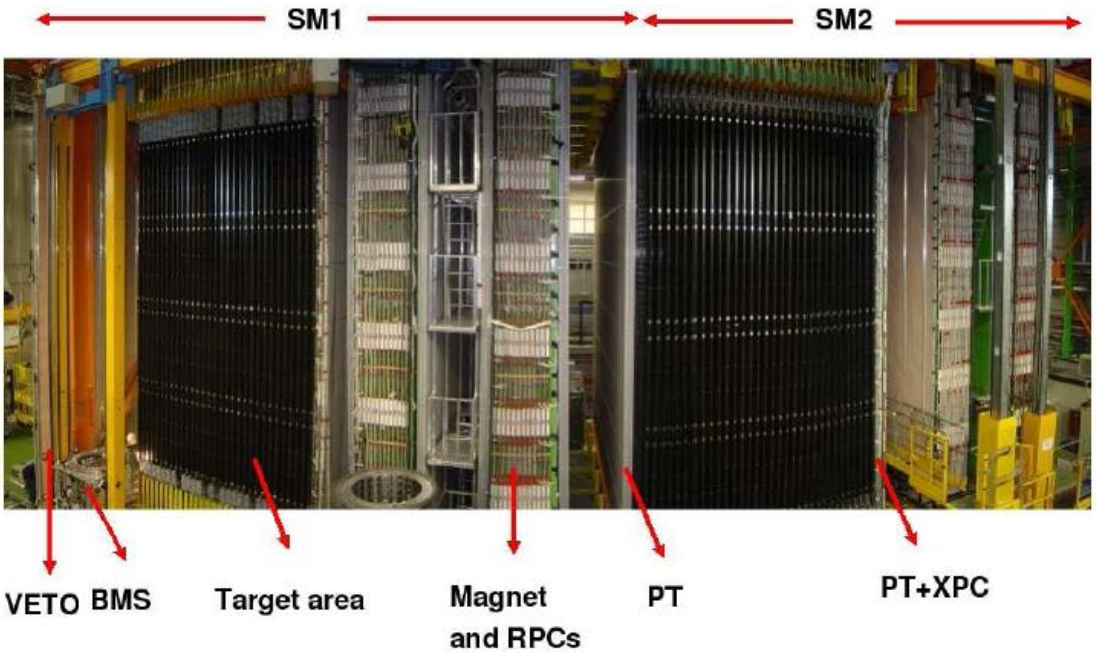

Figure 3.13: *Fish-eye side view of the OPERA detector. The upper red horizontal lines indicate the position of the two identical supermodules (SM1 and SM2). The "target area" is made of walls filled with ECC bricks interleaved with planes of plastic scintillators (TT): the black covers are the end-caps of the TT. Arrows also show the position of the VETO planes, the drift tubes (PT) surrounded by the XPC, the magnets and the RPC installed between the magnet iron slabs. The Brick Manipulator System (BMS) is also visible.*

multipliers (PMT). The ligth signals are read out by 64-channels photomultipliers Hamamatsu H7546 [51] (H8804-mod1). A schematic view of a strip is given in figure 3.14. This detector will be the one mostly use in the timing measurement, which will be presented, given its proximity to the interaction point (see figure 3.15).

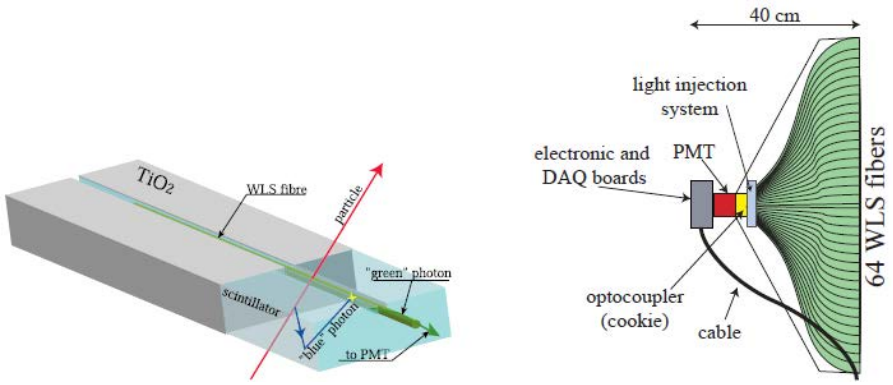

Figure 3.14: *Left: schematic view of a scintillator strip with the WLS fiber. Right: schematic view of a scintillator strip end-cap with the front-end electronics and DAQ board.*

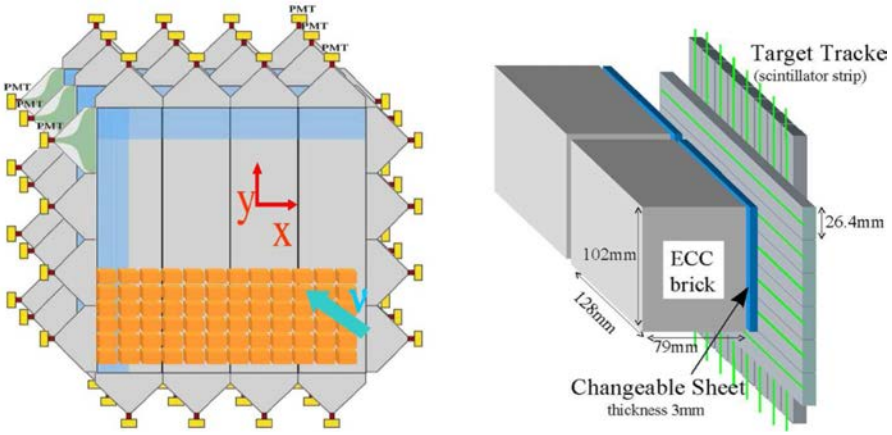

Figure 3.15: *Left: TT planes. Right: brick position w.r.t. the TT planes. The changeable sheet of each brick is located close to a TT plane.*

3.3.2 Magnetic Spectrometers

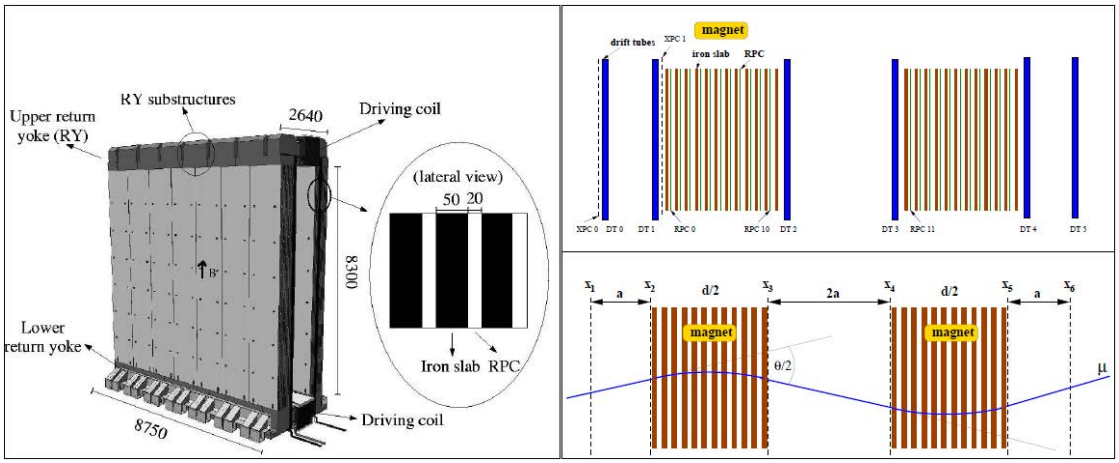

Figure 3.16: *Left: Three dimensional view of one OPERA magnet. Units are in mm. The blow-up insert shows the dimensions of three of the twelve layers of an arm. The height of a slab is given as 8300 mm. Right up: overall scheme of one supermodule. Right bottom: Schematic layout of one half of the muon spectrometer. The six drift tube chambers (PT) are denoted by x1-x6. With three chamber pairs the momentum can be extracted from two independent measurements of the deflection of the charged particle in the magnetic field.*

As illustrated in figure 3.16 each OPERA magnet [55] is made of two rectangular vertical arms built with 12 iron layers interleaved by air for RPC housing. In normal conditions the magnets operate at a current of 1600A. The main task of the RPC system [57] is to reconstruct tracks inside the magnet and perform range measurements of stopping muons. The magnet system is instrumented with two subdetectors: the Inner Tracker and the precision trackers (PT) made of drift tubes. The Inner Tracker includes the RPC tracking system inside each magnet and the XPC, two RPC planes 1 cm upstream and downstream the first and

second drift tubes stations respectively. The Precision Trackers [56], together with the other part of the spectrometers, is used for the muon identification, the determination of the muon charge sign and its momentum. They measure the muon track coordinates in the horizontal plane to track the deflection caused by the two arms of the magnet with opposite magnetic field direction (see figure 3.16). The efficiency on the charge identification is greater than 96% (muon momentum $\in [2.5 \div 45]$ GeV/c) and the resolution on the momentum reconstructed is about 10% at 2.5 GeV/c rising to about 20% at 25 GeV/c.

3.3.3 The Data Acquisition System

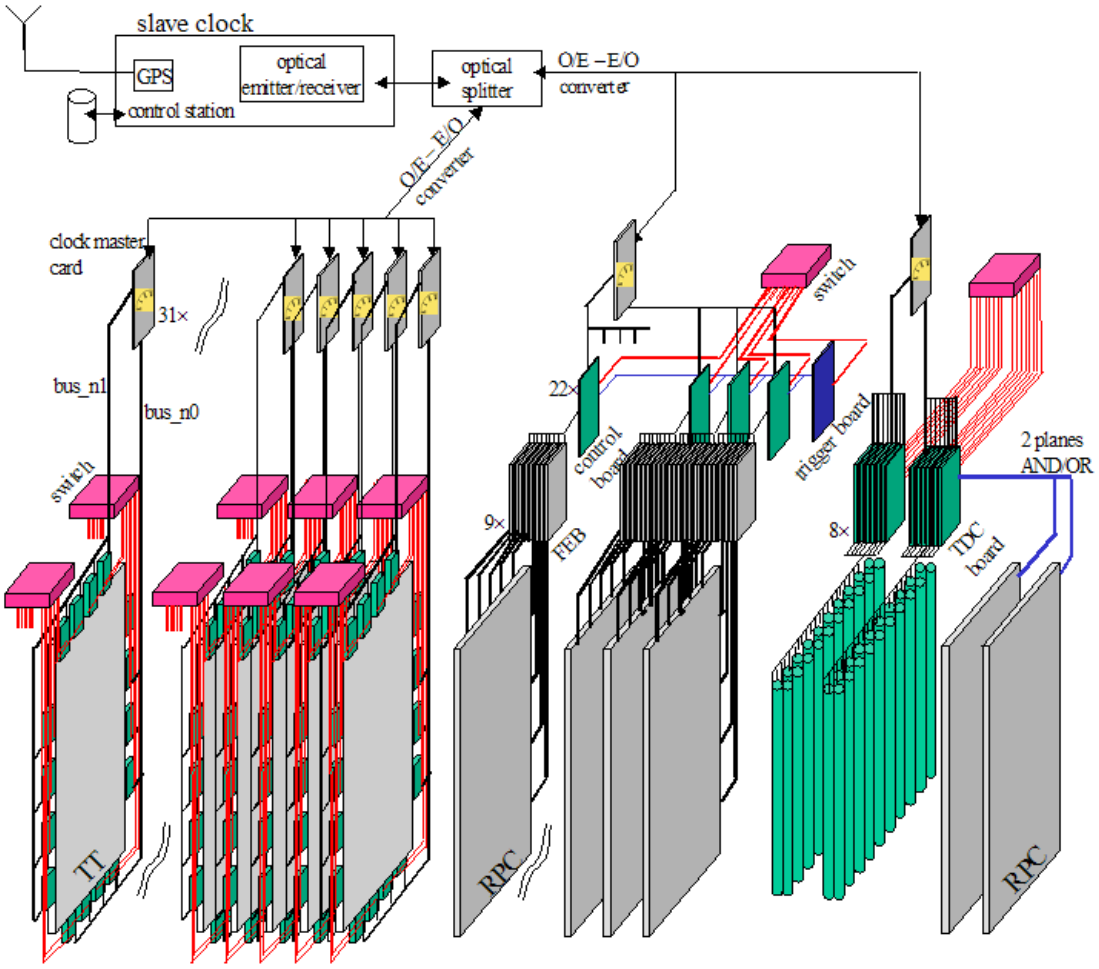

Figure 3.17: *OPERA DAQ scheme [52].*

The data acquisition system [52] of the OPERA experiment is based on the concept of the smart sensor front end units (SFE). Groups of channels of the different

detectors are readout by independent SFE which are self triggering and operate asynchronously associating to the data a timestamp obtained w.r.t. a timing signal distributed to all the units. This signal has a 10 ns quantization and it is related to the UTC. The working principle of the DAQ is presented figure 3.17.
The acquisition process starts at the SFE level, the SFE are connected to two different networks. A standard ethernet network connects the SFE (through switches) to the Event Building WorkStations (EBWS) for the event reconstruction. The smart sensors operate with local processors which acquire the data and output them on the ethernet network after merging with the time stamps. A global clock signal network starts from the GPS slave clock station and through optical fibers sends the optical signal to electric signals converters (0/E) connected to master cards which then deliver the signal to groups of 8 SFE. The event building consists in grouping offline the hits belonging to the same event within a window of 6 μs.
For instance the target tracker planes are made of 2.6 cm wide scintillator strips readout by wls fibers. Groups of 64 wls fibers are readout by multianode photomultipliers which are acquired each one by a SFE. In total, there are 992 SFE for the TT data acquisition (1 SFE per PMT, 2 PMT per module). Further details will be given in chapter 4.3.
The time-ordered hits are processed by the workstations for the event reconstruction as follows:

- The DAQ system looks for timing coincidences of hits in the same TT plane and RPC plane, so that lists of hits for the TT and for RPC planes are produced.
- The DAQ looks for timing coincidences between events in different lists (different TT or RPC planes).
- Finally, a coincidence of 2 consecutive TT planes (XZ and YZ coincidence), or of 3 RPC planes is required. Then, the event is retained if it has at least 10 hits.

Chapter 4

Timing System

4.1 Outline

The measurement of the neutrino time of flight includes corrections of time delays from the various elements of the timing chains operating at CERN and at LNGS. Two twin timing systems composed by an high accuracy GPS (U.S. Global Positioning System) and a Cesium atomic clock were explicitly added at CERN and at LNGS, in addition to the timing system existing already in the two sites. The special GPS receivers at CERN and at LNGS operate in common view mode, a technique used to compare to each other two clocks located in different places which is described in more details in section 4.4. Moreover a DAQ system performs continuously a time comparison between the high accuracy UTC and the local UTC provided by the standard GPS systems on each side. The standard GPS system is used to distribute the UTC time to the LNGS experiments, it is operating since the 1990s and is based on a commercial GPS system with a Rb oscillator, the time accuracy is $\sim$100 ns. Similarly at CERN, the accelerator chain is time stamped with GPS systems, a receiver Symmetricom XLi, with a similar performance. The additional system allows for a precise calibration, which is repeated every second, of the already existing time distribution systems: it allows to improve the inter-calibration among the two sites and the resolution in the measurement of the time difference between the CNGS beam and the OPERA events UTC time tagging.

A schematic view of the whole setup is shown in figure 4.1, a more detailed de-

scription is presented in [49], all the components of the time distribution chains were calibrated by several means, as described more in detail in chapter 5.

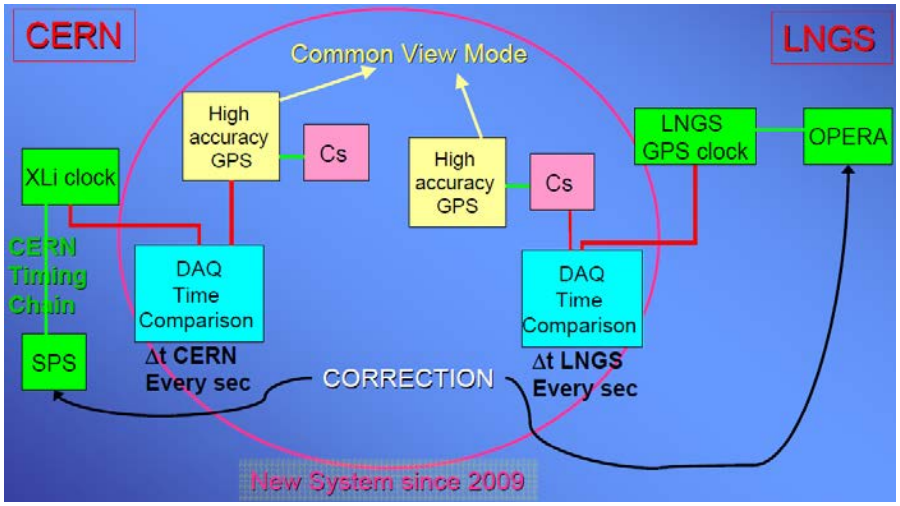

Figure 4.1: *Scheme showing the twin timing systems of CERN and LNGS composed by the existing timing systems and the new high accuracy GPS-Cs clock systems.*

4.2 The CERN Accelerators Timing Distribution System

The CNGS timing system is part of the General Machine Timing (GMT) which distributes the timing information to the entire accelerator complex at CERN including the PS, SPS and LHC. The GMT is based on the UTC. The primary timing source is a GPS receiver Symmetricom XLi which is connected to the GMT. We can consider this GPS as the UTC timing source of CNGS. The XLi receiver is hosted, as other GMT equipments, in the Central Control Room (CCR in Prevessin at CERN), close to the CERN Control Center (CCC), the control room handling the entire CERN accelerator complex. A scheme of the GMT hardware architecture is presented in figure 4.2.
The timing information is treated then in the GMT by a network of nodes:

- Controls Timing Generators (CGT), dedicated CPU nodes which drive each GMT network and run "Timing Events Programs". Timing events include the time sequences: what each accelerator should do as a function of time and in real time coordination with the other parts of the machines complex.

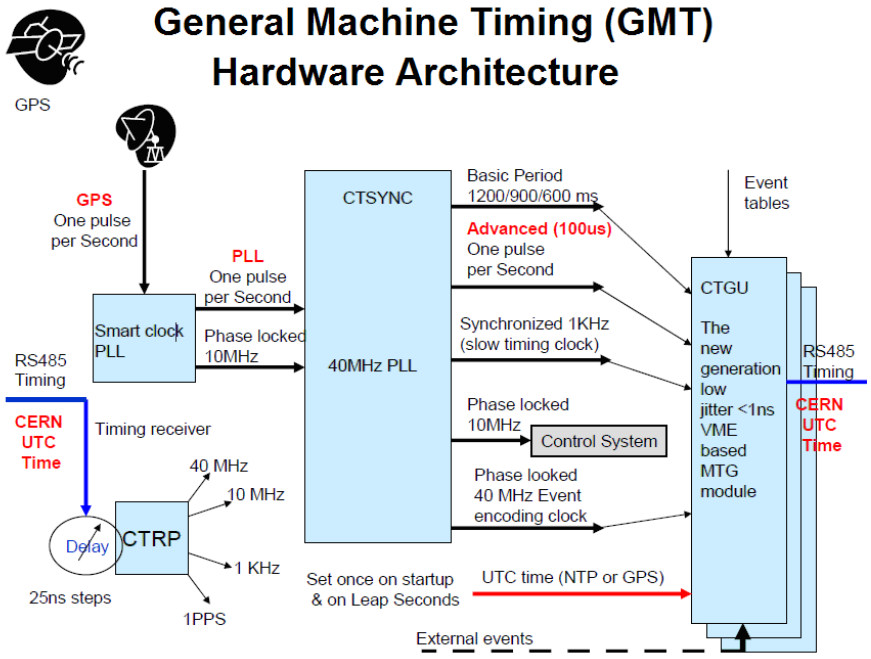

Figure 4.2: *Scheme of the General Machine Timing (GMT) hardware architecture.*

- Control Timing Receivers (CTR) cards which produce pulses and interrupts in response to GMT events and can be used in order to time-tag external signals with respect to the common timing source which is distributed to the entire GMT network.

The CTR cards are available in various form factors, among these, the cards called CTRI, which operate in commercial PC computers, are used in the CNGS time tagging system and also in the accurate timing system which the OPERA collaboration installed at LNGS for the measurement of the neutrino velocity. The software framework handling the GMT network is called FESA (Front-End Software Architecture), it is an object-oriented real-time framework. One of the features handled by FESA is the synchronization over the network which makes possible for the CTR nodes to be synchronized w.r.t. the common GPS source by taking into account in a transparent way the propagation delays of the timing information across the GMT network.

The XLi, the setup with the high accuracy GPS receiver and the Cs clock, and the DAQ that intercalibrates the XLi with respect to the new system, are all installed in the CCR.

The twin high accuracy systems at CERN and at Gran Sasso include in each

site a GPS receiver Septentrio PolaRx2eTR (*Septentrio Satellite Navigation PolaRx2eTR*[1] [61]) operating in common view mode and an atomic cesium clock Symmetricom Cs4000 (Symmetricom Cs4000 [60]). The two systems were installed and commissioned during the summer of 2008 and were fully operative for the 2009 CNGS run. The GPS unit was characterized by the Swiss metrology institute METAS[2].

The data acquisition system which provides the time comparison between the XLi and the Septentrio receiver at CERN is composed by a PC containing a CTRI card. In figure 4.3 is shown a photographic sketch of the CERN setup at CCR including the XLi receiver, the Septentrio, the Cs4000, the DAQ PC with the CTRI card and the various connections.

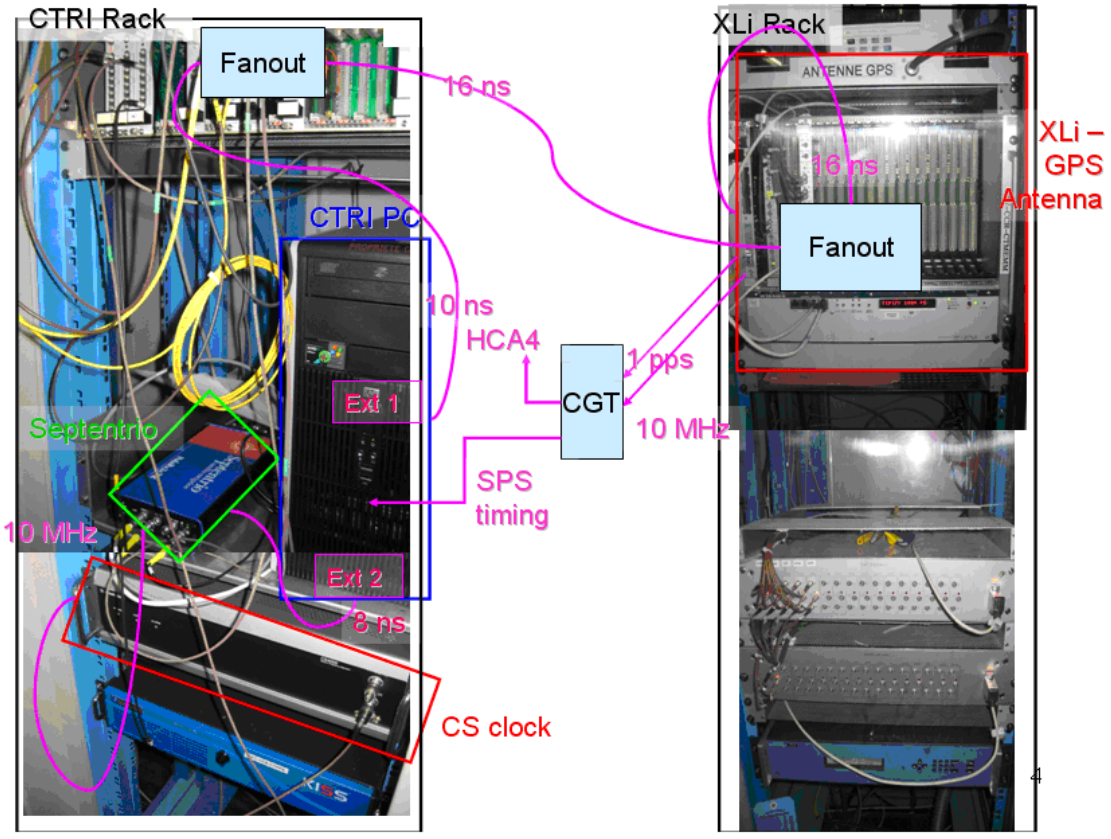

Figure 4.3: *Picture of the DAQ at CERN that provides the time comparison between the XLi and the Septentrio receiver, in this scheme are also presented the connections with the CGT.*

The XLi provides the UTC timing to the CGT which dispatches it to the entire accelerator network and in particular to the CNGS installations underground in the

[1] © 2000-2005 Septentrio nv/sa.
[2] Federal Office of Metrology METAS, Lindenweg 50, CH-3003 Bern-Wabern, Switzerland.

HCA4 hall, in the CNGS access point. The Cs clock can be disconnected from the system and brought around to inject its 1PPS (pulse per second) signal in various point of the chain in order to calibrate the time delays as it was done in January 2010. The calibration measurements that have been performed are presented in chapter 5. A schematic drawing of the setup is shown in figure 4.4.

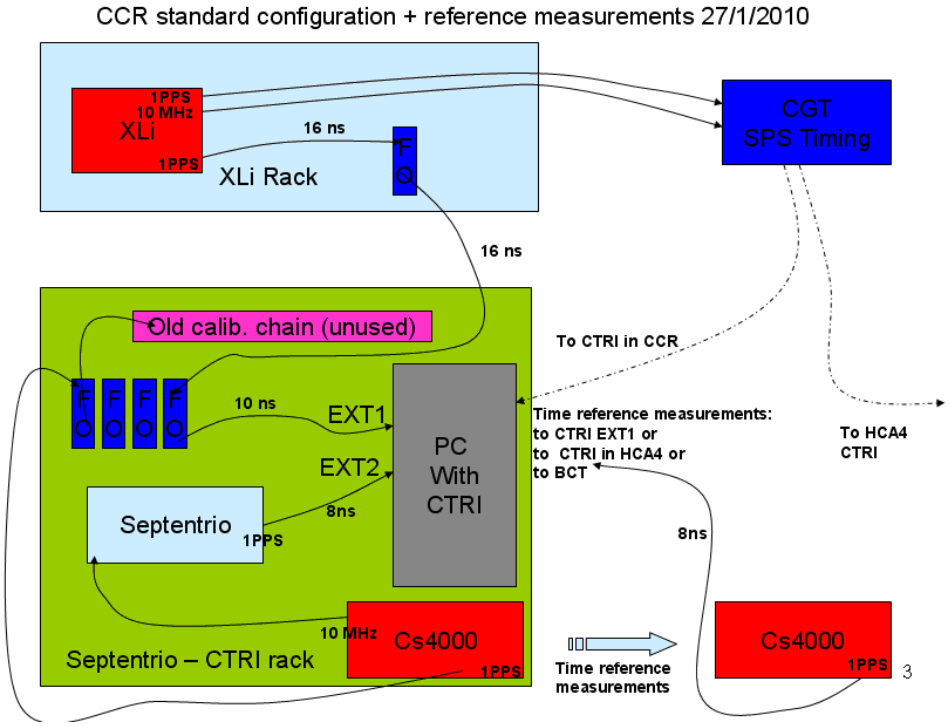

Figure 4.4: *Scheme of the CCR standard configuration and calibration reference setup.*

The CTRI card in the DAQ PC compares every second the 1PPS outputs of the Septentrio and the XLi receivers in order to measure the relative delay among the two signals. The CTRI card is also connected to the CGT so it knows the UTC time and it is able to time-tag both the Septentrio and the XLi signals with respect to the UTC (since the UTC is generated by the XLi itself, its UTC time-tagging provided by the XLi has a constant phase by definition).

The 10MHz signal provided by the Cs4000 is used to feed the Septentrio in the configuration corresponding to normal operation. This ensures high stability of the Septentrio receiver. The Septentrio receiver internally time-tags its 1PPS signal with respect to the UTC time of the GPS satellites constellation. This information is readout as well by the DAQ PC. The Septentrio 1PPS is then sent to the CTRI card for time comparison with respect to the XLi 1PPS signal.

The equipments specific to the CNGS timing are hosted in HCA4. They include a

CTRI card for the time tagging of the kicker signal and the fast waveform digitizer FWD connected to a Beam Current Transformer detector (BCT). The BCT connected to the FWD is called BFCTI400344, it is a transformer that produces an electrical signal proportional to the protons current crossing it, and it is located on the TT41 beam transfer line which brings the protons from the SPS to the CNGS at about 96 m from the CNGS target. The FWD consists in a digital scope card Acqiris DP110 with 1 GS/s sampling rate. Both the CTRI and the FWD cards are hosted in the same DAQ PC.
The result of the kicker signal UTC tagging operated by the CTRI is written in the CNGS database in the variables:

SE.CNGS-BEAM-TIME:GPSTIMING_EXTR1,
SE.CNGS-BEAM-TIME:GPSTIMING_EXTR2,

for the first and second extraction respectively. A general sketch of the underground system and the setup with the DAQ PC with the CTRI and the FWD cards are presented in figure 4.5. The CTRI card generates a replica of the kicker signal received in its input in order to send it to the FWD where it triggers the start of the digitization window. The replica arrives to the FWD with a delay of 26.7 ns which includes the internal CTRI delay plus the cabling.

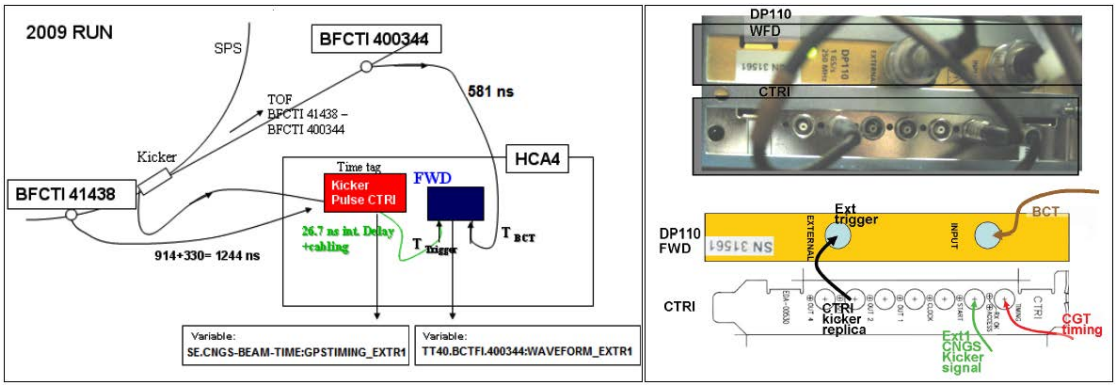

Figure 4.5: *Underground system (left) and setup with the DAQ PC in HCA4 with the CTRI and the FWD cards (right).*

4.3 LNGS and OPERA Timing

A GPS-receiver/Cs clock setup with the DAQ system identical to the one described for the CERN timing system was installed at Gran Sasso in order to intercalibrate the standard LNGS GPS receiver. The LNGS standard timing system

was set-up in 1991. More details about the timing system and its calibration can be found in [49] and will be given in section 5.2.
The OPERA data acquisition system is synchronized with the GPS time. In the external laboratory of LNGS, in the building of Direction, a double ESAT[3] GPS system provides the UTC timing signal to the LNGS experiments underground. This system is disciplined with Rubidium oscillators and it has an accuracy of 100 ns. The two units are called Clock1 and Clock2, normally only one unit is connected to the timing distribution system while the second one is kept as spare. The timing signal is sent underground every ms using a system of mono-modal optical fibers (8 km long). A picture and a scheme of the system are shown in figure 4.6.

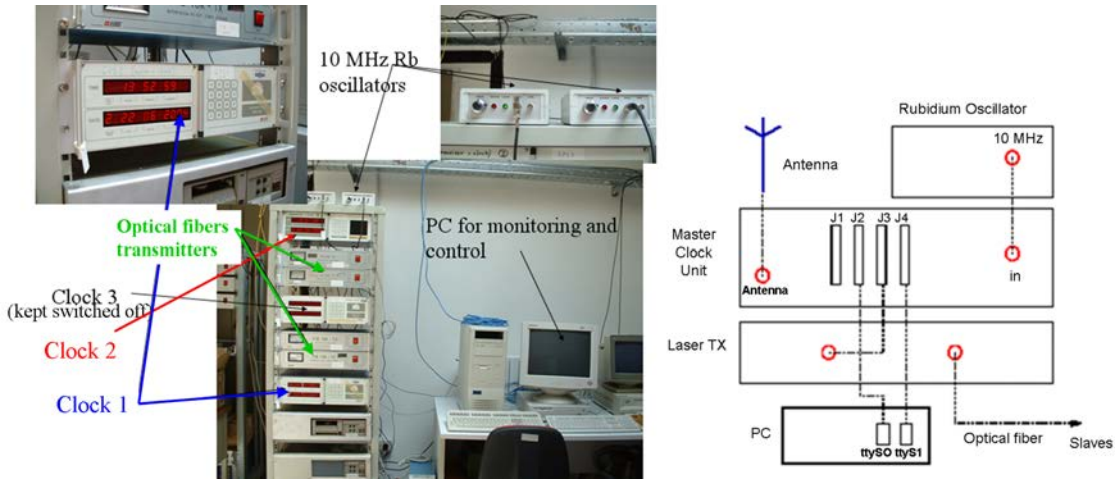

Figure 4.6: *Picture and scheme of the timing system at LNGS*

This fiber arrives in a technical room of the underground laboratory where it is connected to a patch panel, which splits the signal to several fibers going to the various experiments. The signal is transmitted every ms and includes the coding of the date. The leading front of the signal corresponds to the start of the ms. After a short period it starts the transmission of the bits containing the coding of the date and the hour till the ms. This coding implies the transmission of 80 bits. The various experiments are equipped with slave clocks from ESAT (RAD100) which receive the signal from the optical fiber and are able to time-tag an external triggers from the experiments. The slave clocks are readable by the DAQ systems of the experiments, they have 100 ns resolution in the time-tagging.

[3]ESAT srl, Viale A. Gramsci 3, 66020 Paglieta (Chieti), Italy.

OPERA developed its own slave clock which is completely compliant to the format of the input signal but it has a much better performances in terms of the stability of its local clock and it has a time resolution of 10 ns. The figure 4.7 shows a sketch of the ESAT system and the coding of the date.

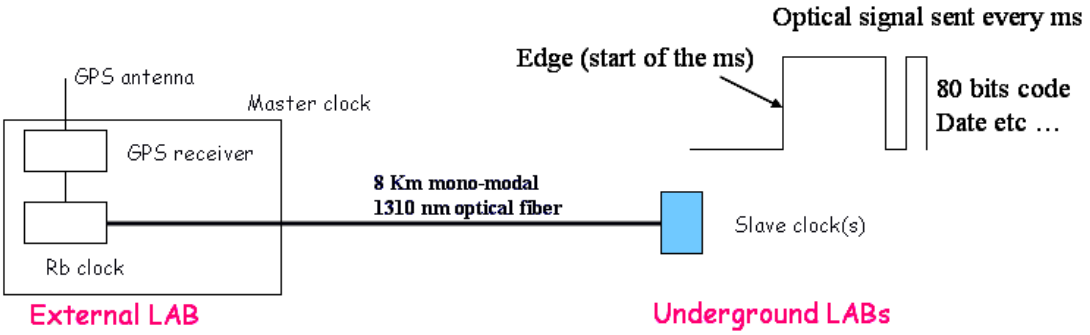

Figure 4.7: *Sketch of the ESAT system and date coding.*

The OPERA slave clock card is also the master of the OPERA DAQ time distribution system to the SFE where data are acquired asynchronously from the various detector units (multianode photomultipliers M64 for the target tracker), time stamped with 10 ns accuracy and output on an Ethernet network. The SFE cards are connected in daisy chains and capable of compensating at the level of the time stamps the signal propagation delays within the chains. The internal delays due to the signal treatment in the slave clock, the propagation to the master clocks down to the last sensor of a chain of 8 SFE, were accurately determined with a set of laboratory measurements and in total amounted to a delay of 4245.2 ns.
The OPERA timing system was designed in 2003 in order to satisfy the basic requirements for the CNGS time synchronization, but given its good performance the system could be used for an accurate measurement of the neutrino velocity.

A detailed sketch of the setup is shown in figure 4.8: a Central Clock unit (PCI board) receives the GPS signal from the external antenna and, acting as slave clock, decodes it before distributing the common clock via another optical link. This link is composed by two optical fibers (one per supermodule) that bring the signal to the O/E cards (*optical to electrical converters*) where it is converted into electrical format. This electrical signal is then distributed to the chain of clock master cards. Each one of these cards sends the clock signal to the DAQ sensors. Each master cards serves 5 TT planes. Each TT plane includes two groups of 8 sensors in daisy chain.

The DAQ timing is organized in cycles of 0.6 s. As soon as a sensor receives the start of DAQ cycle signal, it resets to zero its internal clock counter.

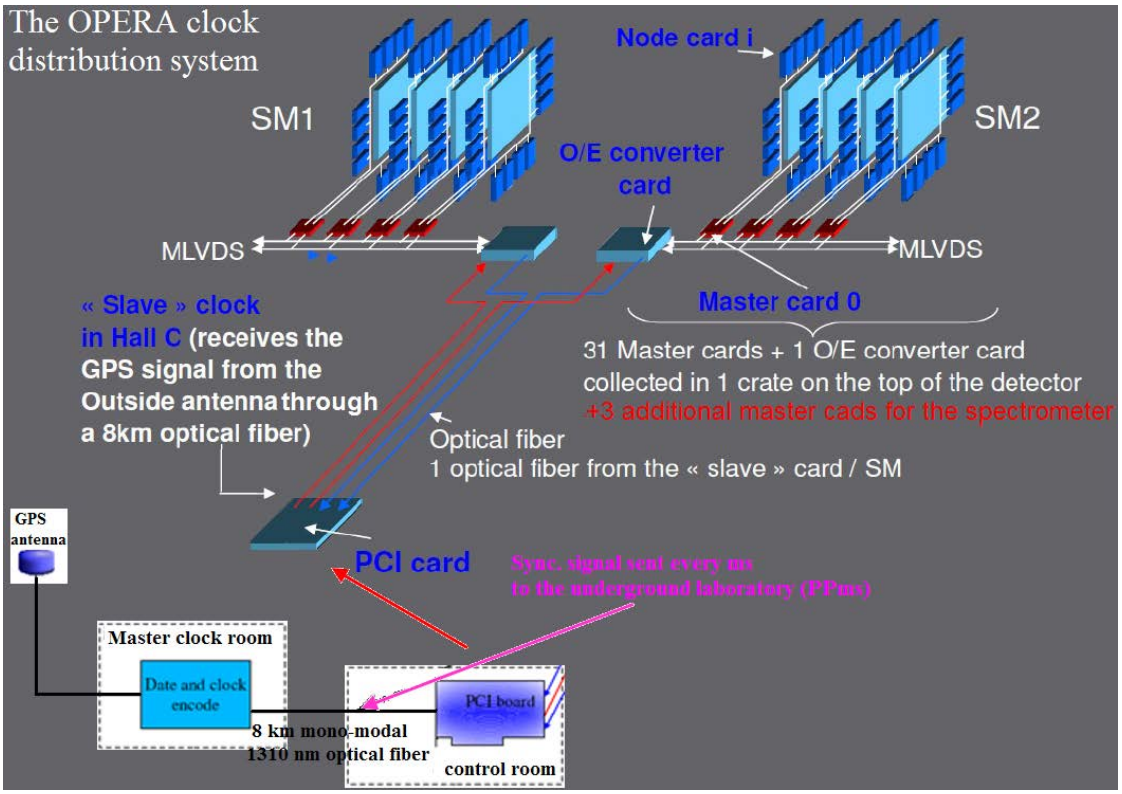

Figure 4.8: *Clock signal distribution to the OPERA electronic detectors: the PCI card receives the signal from the external GPS antenna through an optical fiber. The optical signal is then converted into an electronic signal in the O/E cards and then distributed to the chain of master cards. The last link connects the master cards to the clock unit of each sensor, it is at the level of the sensors that the time stamp is marked.*

Sensors receive from the master cards the start of cycles signals and a 20 MHz clock which is internally converted to 100 MHz in order to produce time stamps with 10 ns granularity. The GPS time recorded each ms by the slave clock is used as a reference for the calculation of the events UTC time stamps, incrementing it by the number of acquisition cycles and the number of 10 ns periods between the arrival of the reset signal and the arrival of the events triggers in the SFE.
A detail of the master cards chain and of the photomultiplier chained sensors of the TT is shown in figure 4.9. Each TT sensor corresponds to a photomultiplier and its readout electronics. In order to synchronize all the sensors the differences related to the cables interconnecting groups of 8 sensors in daisy chain have to be taken into account. Each SFE will start its own DAQ cycles with a delay which depends on the path of the start of cycle signal. The signal coming from the master cards

is dispatched to each plane through the two sides of the detector using two cables, the chained sensors are interconnected by cables of 2m (10 ns of delay), except the sensors at the edge that are connected with a 3m cable (5 additional ns). The delay of 10 ns is automatically compensated at the data-taking level, where all sensors are aligned to the last one in the chain by knowing the position of the sensor in the chain and applying corrections in steps of 10 ns which correspond to one count in the internal time register of the SFE. The delay of 5 ns cannot be compensated by the DAQ given the fact that the data format has a 10 ns quantization, it should be corrected *a posteriori* at the analysis level.

This fact corresponds to a bias due to the first group of 4 sensors in the chain that is undercorrected by 5 ns. However this small correction was not applied in the data processing since the simulation was used in order to estimate the global delay of the readout chain including also this effect (see section 7.2.2). Indeed in the MC simulation the same correction method as in the real DAQ chain is applied so that the effect on the 5 ns undercorrection is represented in the result. One should also note that this bias of 5 ns affects only one side of the target tracker strips (right) while the opposite side is systematically unaffected. This also contributes in reducing the bias.

The way the automatic data corrections are applied corresponds to aligning the time stamps of the 8 sensors on the sensor which is at the end of the chain. This sensor receives the start of cycle signal with a delay of about 75 ns with respect to the first one in the chain. Given the delay on the start of the cycle the UTC time stamp is underestimated by 75 ns. Since all sensors are aligned with respect to this last sensor the OPERA UTC time tags are systematically underestimated by 75 ns.

This bias of 75 ns is then corrected in the TOF calculation by including the 75 ns delay in the DAQ global delay which takes into account all the propagation times in the time distribution chain.

This includes as well the signal path from the PCI card to the O/E converters, the delay from the O/E to the master cards and the delay from the master cards to the first card in the chain. Since these delays are common to all sensors they are not compensated by the DAQ, but treated with an overall offline global DAQ delay correction which amounts to 4245.2 ns. This delay was measured with a laboratory setup reproducing the complete time distribution system down to one

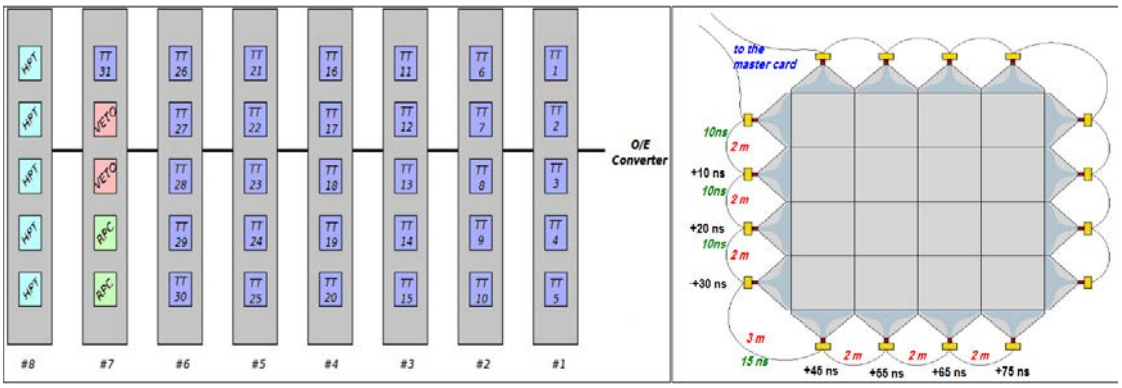

(a) **(b)**

Figure 4.9: *a) Connection scheme of the detector master cards: the TT sensors are connected to 7 different cards (as function of the plane number). There are 0.6 ns between two cards in the chain (this delay is not present for the RPCs since all the sensors are connected to the same master card). b) Clock distribution for the TT: the sensors receive the reset signal one after the other at the 2 sides of the detector. The 2m cable between two sensors introduce 10 ns of delay, this offset is corrected at the data acquisition level as a function of the sensor's number. The cable that connects two sensors at the edge is 3m long and this introduce 5 ns more of delay. It is corrected* a posteriori *at the analysis level since the time data format is 10 ns quantized.*

sensors chain. The only difference with respect to the real setup was the length of the optical fibers of 3.3 m instead of 60 m. The propagation delay measured over 3.3 m was extrapolated to the full length. This dominates the calibration error which is 1.8 ns.

This delay common to all the sensors chains is however affected by additional small local delays since the mastercards are connected in daisy chain and this introduces 0.5 ns of delay in between each pair of cards (*i.e.* 0.5 ns every 5 planes of TT). Furthermore the two last TT planes in the target have an additional cable delay of 5 ns. These corrections are ignored in the data treatment, however their are taken into account in the simulation as well and represented in the readout chain correction evaluated with the simulation.

The way the simulation takes into account all the readout delays is described in details below.

The OPERA detector response to the energy deposition of the particles recorded by the DAQ system is organized in "digits", each digit contains the information about its position (X, Y and Z coordinates) within the detector volume, the deposited energy (number of photoelectrons) and the timestamp. In order to obtain a digitization of the TT signal that simulates as close as possible the real detector response an analysis of the signal propagation in the scintillator strips has been performed as reported in [53] (see the fiber representation figure 3.14).

All the results obtained in the analysis have been integrated in the digitization code of the OPERA software. The photon emission time distribution can be expressed as:

$$F(t) = \frac{1}{\tau_2 - \tau_1}\left[e^{-\frac{t}{\tau_2}} - e^{-\frac{t}{\tau_1}}\right], \tag{4.1}$$

where τ_1 and τ_2 are respectively the decay time constant of the fast scintillation of the scintillator strips and of the fiber. To determine these two values a short fiber and a pulsing N_2 laser (500 ps of resolution) were used, the signal was fitted with the curve of equation 4.1. The result is given in figure 4.10, the time constants correspond to: τ_1 =3.0 ns and τ_2 =6.6 ns. The simulation takes into account the emission of multiple photons and the fact that a trigger is generated on the earliest one, which considerably reduces the delay indicated in the picture.

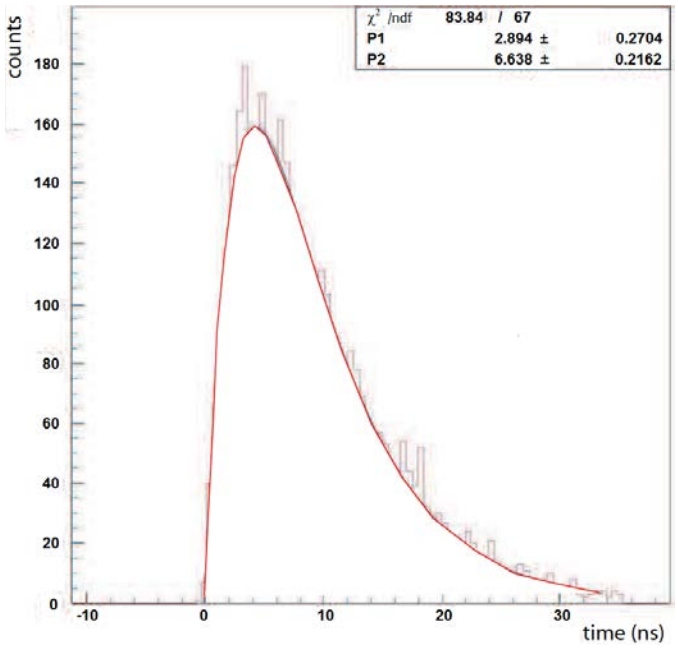

Figure 4.10: *Fit of the signals time dispersion on the PMT signal for laser pulses on a short WLS fiber. Variables P1 and P2 correspond to the time constants τ_1 and τ_2 [53].*

The time dispersion inside the fiber depends on the photon emission angle (see figure 4.11), the signal can be expressed as the convolution of F(t) with a gaussian curve describing the dispersion once the two time constants are known, as in the following equation:

$$\begin{aligned}(G \otimes F)(x) &= \frac{\alpha}{2(\tau_1-\tau_2)} e^{-\frac{x}{\tau_1}+\frac{\sigma^2}{2\tau_1^2}}\left(1 - erf(-\tfrac{1}{2}\sigma(\tfrac{x}{\sigma^2} - \tfrac{1}{\tau_1}))\right) \\ &- \frac{\alpha}{2(\tau_1-\tau_2)} e^{-\frac{x}{\tau_2}+\frac{\sigma^2}{2\tau_2^2}}\left(1 - erf(-\tfrac{1}{2}\sigma(\tfrac{x}{\sigma^2} - \tfrac{1}{\tau_2}))\right)\end{aligned} \tag{4.2}$$

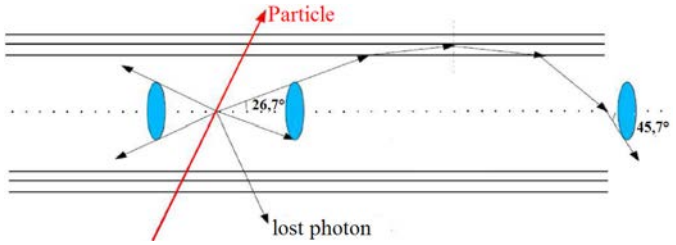

Figure 4.11: *Photon propagation in the fibers.*

The dispersion coefficient σ has been obtained as a function of the travelled distance of the photon by performing several measurements with fibers of different length, the signal was then fitted using equation 4.2 with the free parameters α (normalisation) and σ (dispersion), τ_1 and τ_2 being the values known from the previous measurement. The mean propagation time in the fibers has been found to be 6 ns/m. A linear behaviour between σ and the fiber length (in m) was obtained and the result is $\sigma = 0.16$ ns m^{-1}. These results are shown in figure 4.12.

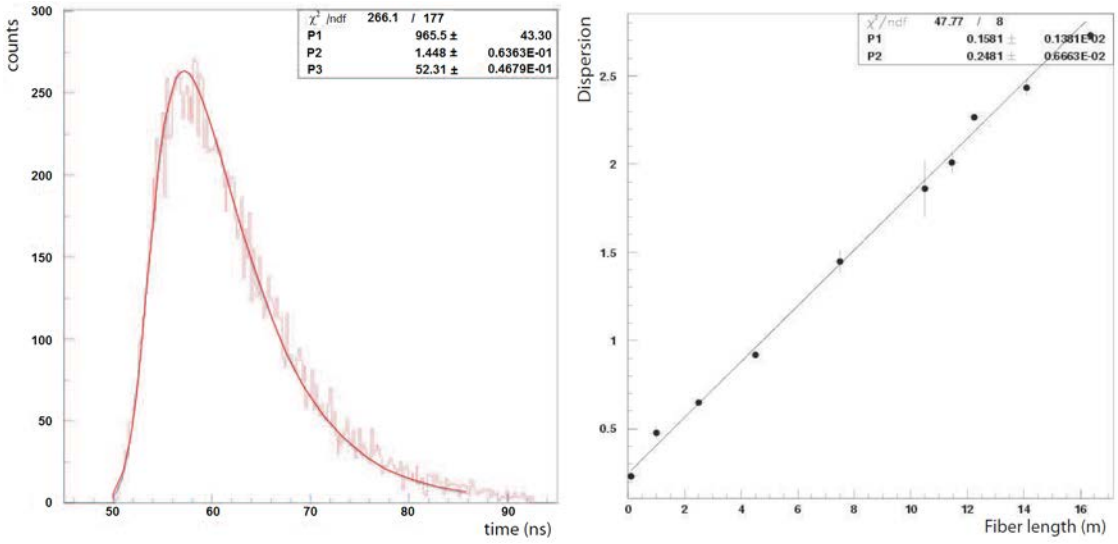

Figure 4.12: *Left: Signal fit for a fiber length of 8.5m. Variables P1 and P2 are respectively the normalisation α and the dispersion σ. Variable P3 represents the electronic offset. Right: time dispersion (ns) versus fiber length. A value of 0.16 ns/m has been fitted [53].*

In the digitization of the target trackers response the transit time constant of the photomultipliers employed in the OPERA detector (Hamamatsu H7546 PMT [51]) is not taken into account. It is of 10.9 ns with a spread of 0.3 ns.

The simulation for the electronics timing consists in two steps: the gain amplification and the trigger. The PMT channel gain (in ADC channel) is chosen for each photoelectron according to the gain fluctuation described by a Gaussian as

can be found in [54], with a mean of 37 (in ADC channel) and σ of 54%. The trigger is produced using the signal of a fast shaper (see figure 4.13 a) that has been parameterized following equation 4.3, derived from measurements presented in [50]. The result is given in figure 4.13 b). The trigger threshold corresponds to a fast shaper output of 1/3 photoelectron. At that moment the time is recorded as signal time-stamp.

$$f(t) = p_1 - \frac{p_2}{t} - \frac{p_3}{t} e^{-\frac{p_4}{t}} \tag{4.3}$$

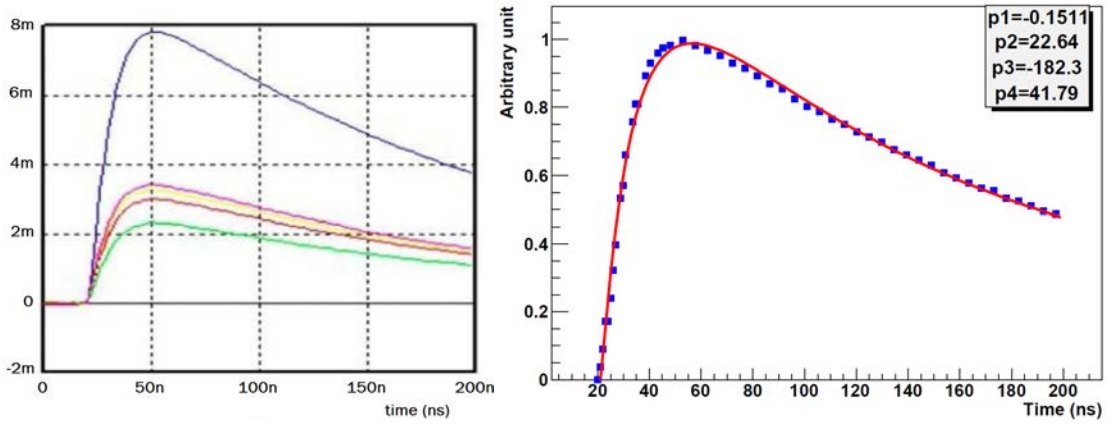

(a) **(b)**

Figure 4.13: *a): Output waveforms measured at the fast shaper for a set of gain correction ranging from 1 to 3. b) Parameterization of the fast shaper. The points come from the measure [50] and the line is the result of the parameterization [53].*

The simulation also takes into account the 5 ns bias for the first 4 SFE in each chain of 8 equipping the TT and the small effects concerning the master cards chains. Another aspect which is simulated concerns the 10 ns quantization of the time which results in an average systematic bias of 5 ns, since the UTC is aligned with the beginning of each 10 ns cycle. This bias is common to the data and the MC simulation and it is therefore taken into account in the analysis.
The simulation of the digitized signals is in good agreement with the real data as can be seen in figure 4.14 the charge ADC for real (red) and for digitized (black) data are shown. The comparison between the reconstructed deposited energy in the TT for real data (red) and for digitized simulated events (blue) is also presented. The timing simulation is also in good agreement with data, as demonstrated by studying the time alignment of different sensors in the reconstruction of muon tracks and the possibility to measure the β of the particles by using the timing system, which has been extensively tested on the data in the search of upwards

going atmospheric neutrinos [48] (see figure 4.15).

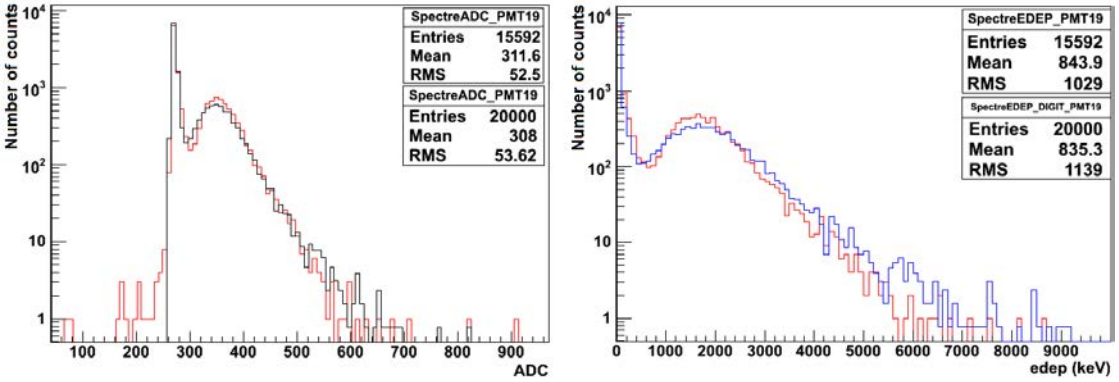

Figure 4.14: *Left: Comparison of the ADC distributions for data (red) an for digitized simulated events (black). Right: Comparison of reconstructed deposited energy for data (red) and for digitized simulated events (blue).*

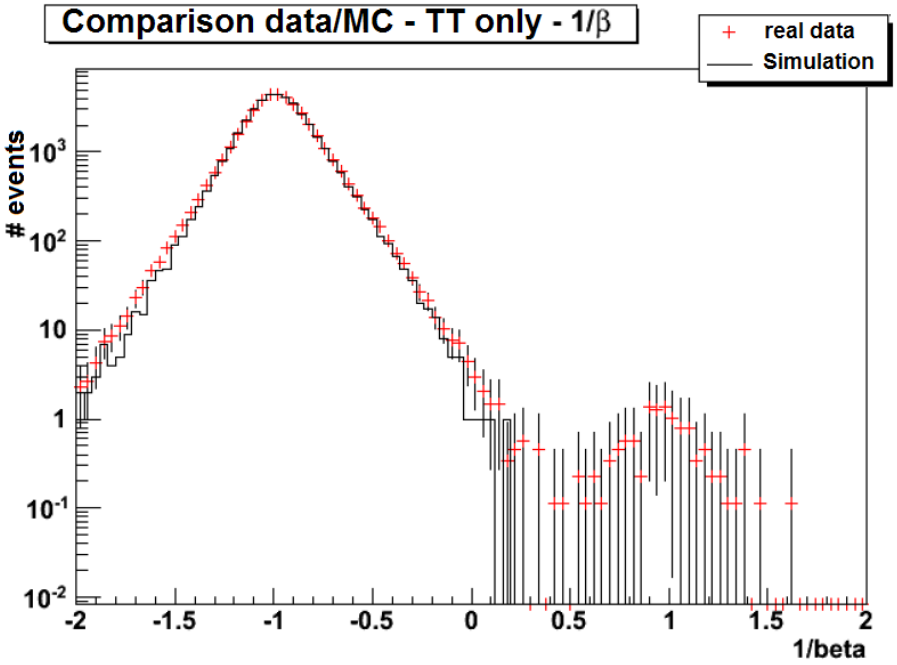

Figure 4.15: *1/β distribution for tracks of at least 3 m length, measured with the TT timing system. The sign of 1/β corresponds to the direction of the particle propagation, positive for the upgoing particles and negative for downgoing particles [48].*

For what concerns the signal propagation in the RPC detectors and their signal digitization, since measurements on the time propagation in the RPC electronic chain were not completed and the calibration of the RPC was not well known at the moment of the measurement of the neutrino velocity, only those events with the earliest digit recorded in the TT for the final data sample were kept.

4.4 GPS in Common View Mode

The Global Positioning System (GPS) provides reliable location and time information anywhere on or near the Earth, when a GPS receiver has an unobstructed line of sight to at least four satellites. The satellites are distributed among six orbital planes, with four satellites per plane. Spare satellites can bring the total number up to 32. Cesium and/or rubidium oscillators operate on each satellite in order to guarantee a clock accuracy at 1 ns level between successive satellites uploads (every 12 hours). The clocks on the satellites are referenced to the Coordinated Universal Time maintained by the US Naval Observatory (USNO), UTC(USNO). The oscillators on the satellites undergo compensations for relativistic effects like second order Doppler shift and gravitation frequency shift.
The satellites continuously broadcast a navigation message at a rate of 50 bits/s over two carrier frequencies: L1=1575.42 MHz and L2=1227.60 MHz. The content of the message includes 3 parts:

a The week number, time within the week and data about the health of the satellite,

b The ephemeris which include the precise orbit of the satellite, they are updated every two hours and generally valid for 4 hours,

c The coarse orbit and status of all satellites in the constellation and data related to the errors corrections. This is typically updated every 24 hours.

Signals are encoded by using a Code Division Multiple Access (CDMA) which foresees unique coding for each satellite in order to distinguish messages from different satellites. The message is encoded with a high rate Pseudo-Random sequence (PRN) which is different for each satellite. The receiver must be able to produce replica of the PRN codes of the 32 satellites in order to match with the incoming code. The measured phase offset between the incoming PRN code and the replica is the GPS range measurement (distance between the satellite and the receiver).
In general, after demodulation and decoding of the PRN sequences GPS receivers can provide a simultaneous determination of the location and time of the receiver. This is done by looking at least at 4 satellites. Each satellite transmits its position

and time. By looking at the propagation time (ranges) of the signals down to the receiver a system of 4 equations with 4 unknowns (the 3 space coordinates and the time of the receiver: x,y,z,t) can be solved (see figure 4.16). This assumes the knowledge of the speed of light and its corrections due to the propagation of the radio signals in the ionosphere and troposphere, where they are slowed down depending on the local refraction index.
The satellites broadcast the ionospheric and tropospheric corrections which reduce the uncertainty on the knowledge of the propagation time of the signals. The range obtained by the measurement of the phase shift between the satellite and the receiver is called pseudo-range and it should be corrected by such effects in order to get the correct range:

$$p = \rho + c(dt - dT) + d_{ion} + d_{trop} + rn, \tag{4.4}$$

where p is the pseudo range, c is the speed of light, ρ is the geometric range to the satellite, dt and dT are the time offsets of the satellite and receiver clocks w.r.t. GPS time, d_{ion} is the delay through the ionosphere, d_{trop} is the delay through the troposphere, and rn represents the effects of receiver and antenna noise. In order to get the best result the correction to the ionospheric conditions must be evaluated locally by using a dual frequency receiver which is able to decode both L1 and L2, these are called MeaSured IonOsphere conditions (MSIO).

If the receiver knows already its location, and this is the typical situation for time transfer applications, the receiver time can be determined just from the observation of a single satellite.

The "Common View Mode" is a simple way to compare to each other two clocks located in different places. In this technique two clock stations, A and B, receive a signal simultaneously from a single transmitter (signal R) and measure the time difference between this received signal and their own local clock. Then data are exchanged offline between the stations A and B. The time difference between clocks A and B is calculated by taking the difference between simultaneous R - A and R - B clock difference measurements. If the travel times to the receivers are exactly equal, then the two receivers can synchronize their clocks with an accuracy that does not depend on the characteristics of the transmitter or the transmission medium. Since the path delay is usually affected by various environmental param-

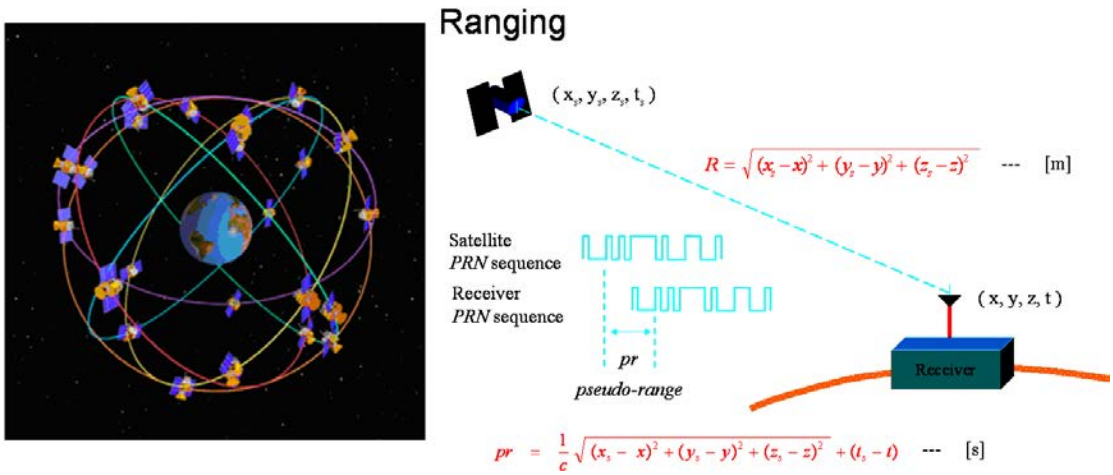

Figure 4.16: *General GPS working principle: the satellites are distributed among six orbital planes, with four satellites per plane. When a GPS receiver has an unobstructed line of sight to at least four satellites it can provide reliable location and time information. Each satellite transmits its position and time. By looking at the propagation time (ranges) of the signals down to the receiver a system of 4 equations with 4 unknowns (the 3 space coordinates and the time of the receiver: x,y,z,t) can be solved.*

eters (such as ambient temperature), the common-view method generally works best if the distance between the receiver stations (the baseline) is small relative to the distance between either receiver and the transmitter (this is typically the case of CERN-OPERA timing systems where the distance between the two receivers is 730 km while the distance to the reference clock is 20200 km (see figure 4.17). This geometry tends to ensure that the delay fluctuations caused by the atmosphere in the two paths will be highly correlated.

Using the high accuracy GPS systems in "common view mode" and exchanging data offline the two sites can be intercalibrated reaching a performance at the level of 1 ns, since the calculations are done by looking exactly at the same satellites from the two stations.

Most of the conventional common-view receivers are designed specifically for time and frequency transfer applications. The receivers are installed in stationary locations with known coordinates to track the same satellites at the same times. They perform the time of arrival measurements between the local reference clock and the received GPS time, these measurements are corrected by the delays in the signal path to produce the difference between the local reference clock and the GPS time (REFGPS). By exchanging data from the remote receivers and differencing the two sets of REFGPS data, the GPS time drops out, and we obtain the time difference between two remote clocks.

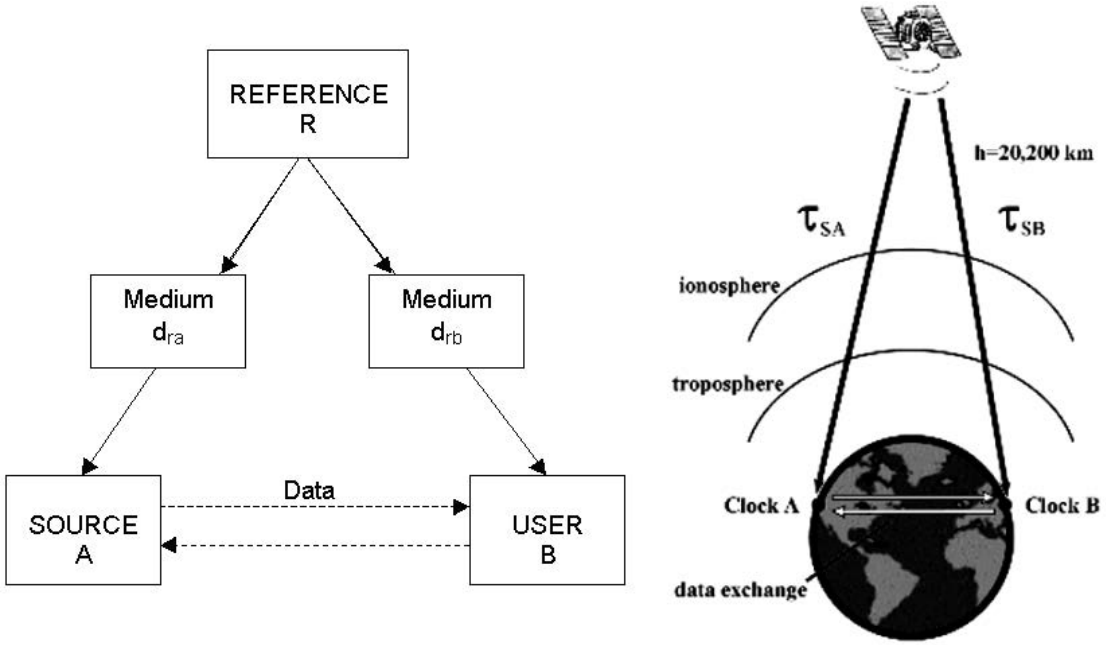

Figure 4.17: *GPS operating in Common View Mode: data are exchanged offline between the stations A and B. The time difference between clocks A and B is calculated by taking the difference between simultaneous R - A and R - B clock difference measurements, here R is the reference signal transmitted by the satellite. The common-view method generally works best if the distance between the receiver stations (the baseline) is small relative to the distance between either receiver and the transmitter (this is typically the case of CERN-OPERA timing systems where the distance between the two receivers is 730 km while the distance to the reference clock is 20200 km).*

The high accuracy GPS information have been stored at CERN and at LNGS during the OPERA run periods and for each day only the data of the common satellites seen by the two sites have been selected. For each satellite the following information are recorded: the satellite ID, the satellite time in *hh:mm:ss* format, later converted in unix time format, and the satellite "reference time" which is the time difference (measured in .1 ns) between the laboratory reference clock and the GPS system time, called *refG* when the "laboratory" site are the LNGS and *refC* in the case of CERN. Afterwards, all the satellites data having the same unix time have been selected and the mean value of *refC* and of *refG* has been calculated for each of these samples of data (usually 6 satellites on average are seen in common by the two sites at the same time and $\sim$ 4 mean values per hour are calculated).

At CERN the SPS time tag is connected to a XLi clock and its 1PPS signal is sent in input to the Ext1 connector of the PC card (CTRI card). The high accuracy Septentrio receiver, connected to the Cs clock signal, sends its 1PPS signal to the Ext2 connector of the CTRI card.
Then, Δt_{CERN}=(Ext2 - Ext1)$_{CERN}$ has been calculated every second.

A similar procedure was used for the LNGS timing logging: the LNGS GPS clock signal is passed as input to the PC card CTRI (in Ext2). The card receives in the Ext1 connector the signal from the Septentrio (which is also connected to the Cs clock).
Again, Δt_{LNGS}=(Ext2 - Ext1)$_{LNGS}$ has been calculated for the logged data every second.
The scheme of these connections is shown in figure 4.18.

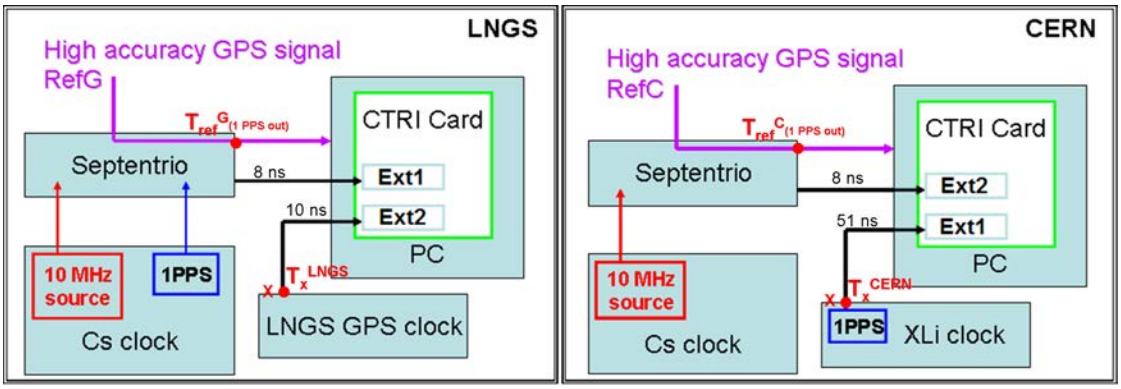

Figure 4.18: *Scheme showing the connections of the new and the old timing systems of CERN and LNGS.*

Now follows the description of how the 1 PPS signals generated by the Septentrio receivers are correlated offline to the GPS time by using the common view mode technique. These data are then combined to those recorded by the two CTRI DAQ systems in order to compute the synchronisation of the LNGS GPS clock and the Xli GPS at CERN.
The Global Navigation Satellite Systems (GNSS) are a set of satellite constellations, transmitting signals anywhere on the surface of the Earth, the GPS system is in one of these constellations corresponding to the US GNSS [4](more details can be found in [49]). The PolaRx is a receiver compatible with the US, Russian, European and Chinese GNSS, which allows to record measurement data (SBF Septentrio Binary files) and convert them in RINEX format (Receiver Independent Exchange Format developed for the easy exchange of the GPS data). This allows the user to post-process the received data to produce a more accurate solution. The final output of a navigation receiver is usually its position, speed or other related physical quantities. However, the calculation of these quantities are based

[4]The currently GNSS in operation are GPS and GLONASS (Russian Global Satellite System) plus Galileo in Europe and Compass in China in development.

on a series of measurements from one or more satellite constellations. The RINEX format is designed to evolve over time, adapting to new types of measurements and new satellite navigation systems.

This format consists basically in six ASCII file types, among these we used the Observation Data Files and the Navigation Message Files. Each file consists of a header section and a data section, the header section contains global information for the entire file. An example of part of one RINEX Observation file and of one RINEX Navigation file is shown in figure 4.19.

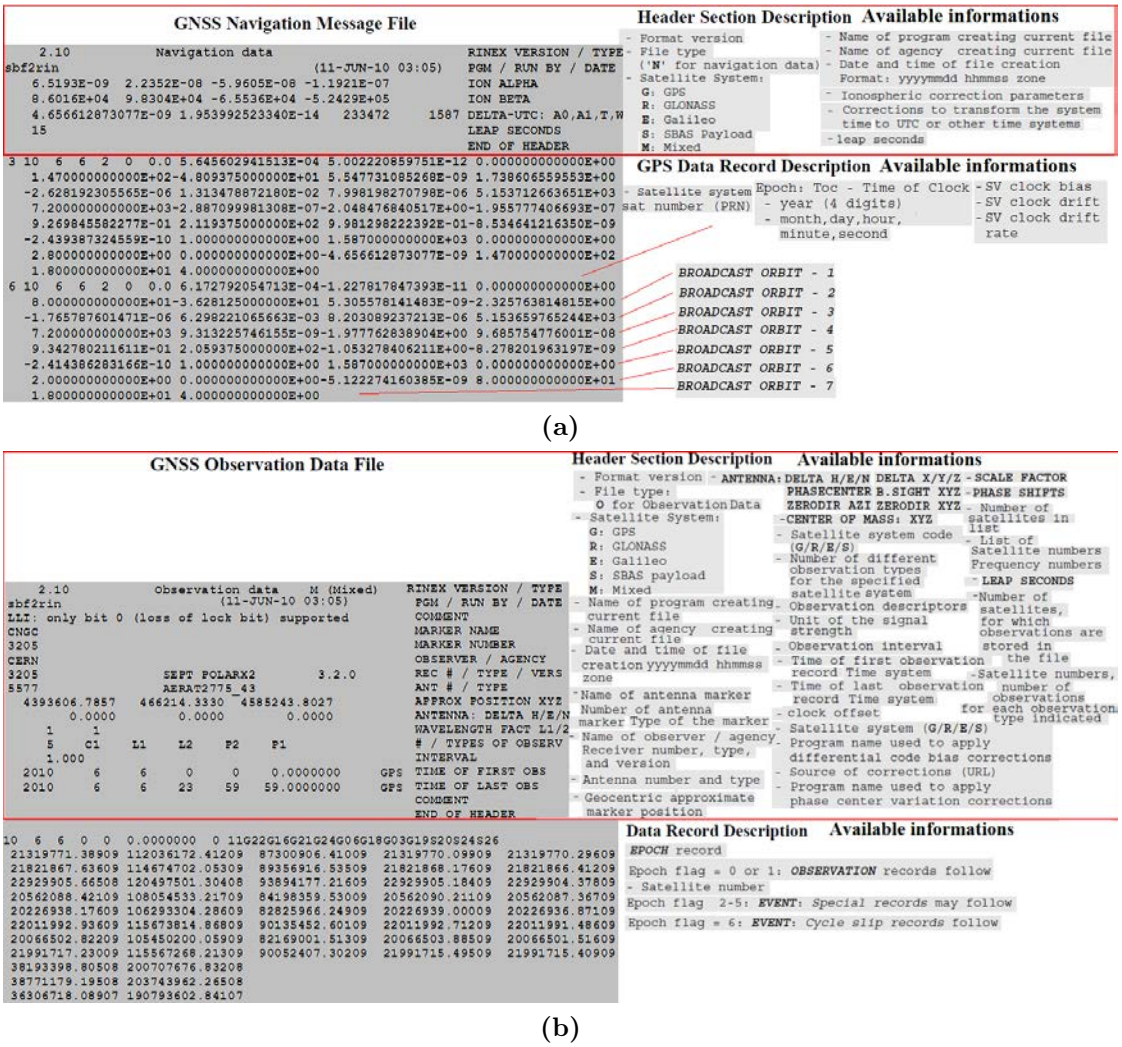

Figure 4.19: *RINEX file format example: a) Navigation Message File description, b) Observation Data File description.*

The two Sepentrio receivers at LNGS and at CERN generate RINEX files which are afterwards converted in the CGGTTS format (CCTF[5] Group on GNSS Time

[5]The Consultative Committee for Time and Frequency

Transfer Standards). An example of a part of a CGGTTS file obtained by the Observation and its relative Navigation RINEX file is presented in figure 4.20, the following table 4.1 explains the information contained in these files useful to select the common satellites seen by CERN and LNGS sites during the OPERA run periods for the timing correction calculation.

CERN CGGTTS file 11-JUN-2010

```
CGGTTS GPS/GLONASS DATA FORMAT VERSION = 02
REV DATE = 2008-08-18
RCVR = SEPT POLARX2 v2.6.0 SN:3205    R2CGGTTS v4.2
CH = 16 (GPS)
IMS = SEPT POLARX2 v2.6.0 SN:3205
LAB = CERN
X = +4393606.61 m (GPS)
Y =  +466214.48 m (GPS)
Z = +4585243.47 m (GPS)
FRAME = ITRF
COMMENTS = RxControl Auto-Generated File
INT DLY =  217.6 ns (GPS P1),  225.7 ns (GPS P2)
CAB DLY =  202.8 ns (GPS)
REF DLY =    2.4 ns
REF = PXTIME
CKSUM = 13
```

PRN	CL	MJD	STTIME hhmmss	TRKL s	ELV .1dg	AZTH .1dg	REFSV .1ns	SRSV .1ps/s	REFGPS .1ns
16	FF	55358	000200	780	322	1830	+1684935	+89	882567
24	FF	55358	000200	780	578	579	-2068816	-19	882576
6	FF	55358	000200	780	815	1107	-5237340	+128	882501
22	FF	55358	000200	780	584	1066	-817605	+58	882588
19	FF	55358	000200	780	522	3016	+1296019	+37	882568
18	FF	55358	000200	780	380	587	+143919	+58	882545
3	FF	55358	000200	780	840	2903	-4784282	-34	882595
16	FF	55358	001800	780	248	1821	+1684957	+102	882553
24	FF	55358	001800	780	510	611	-2068843	-16	882581
6	FF	55358	001800	780	744	1238	-5237212	+140	882508
22	FF	55358	001800	780	586	922	-817588	+31	882595
19	FF	55358	001800	780	592	3041	+1296050	+33	882573
18	FF	55358	001800	780	331	535	+143923	-25	882572
3	FF	55358	001800	780	866	1830	-4784336	-33	882589
24	FF	55358	003400	780	445	646	-2068891	-68	882565
6	FF	55358	003400	780	671	1307	-5237095	+133	882504
22	FF	55358	003400	780	565	790	-817570	-3	882603
19	FF	55358	003400	780	664	3056	+1296070	+10	882567

LNGS CGGTTS file 11-JUN-2010

```
CGGTTS GPS/GLONASS DATA FORMAT VERSION = 02
REV DATE = 2008-08-18
RCVR = SEPT POLARX2 v2.6.0 SN:3206    R2CGGTTS v4.2
CH = 16 (GPS)
IMS = SEPT POLARX2 v2.6.0 SN:3206
LAB = CERN
X = +4585754.09 m (GPS)
Y = +1102187.53 m (GPS)
Z = +4280932.90 m (GPS)
FRAME = ITRF
COMMENTS = RxControl Auto-Generated File
INT DLY =  217.4 ns (GPS P1),  227.0 ns (GPS P2)
CAB DLY =  202.9 ns (GPS)
REF DLY =  245.8 ns
REF = PXTIME
CKSUM = 49
```

PRN	CL	MJD	STTIME hhmmss	TRKL s	ELV .1dg	AZTH .1dg	REFSV .1ns	SRSV .1ps/s	REFGPS .1ns
3	FF	55358	000200	780	755	3030	-5629974	-24	36903
16	FF	55358	000200	780	356	1941	+839246	+20	36878
21	FF	55358	000200	780	226	678	+699254	+27	36839
18	FF	55358	000200	780	408	566	-701790	-46	36837
24	FF	55358	000200	780	602	490	-2914509	-37	36884
19	FF	55358	000200	780	443	3070	+450308	+40	36857
6	FF	55358	000200	780	879	353	-6083020	+123	36820
22	FF	55358	000200	780	663	1061	-1663294	+27	36899
3	FF	55358	001800	780	825	2829	-5630036	-55	36889
16	FF	55358	001800	780	283	1920	+839297	+110	36892
18	FF	55358	001800	780	353	522	-701804	+36	36845
24	FF	55358	001800	780	541	554	-2914538	-41	36886
19	FF	55358	001800	780	511	3091	+450327	+24	36849
6	FF	55358	001800	780	829	1302	-6082888	+200	36831
22	FF	55358	001800	780	654	875	-1663298	+4	36886
3	FF	55358	003400	780	843	2118	-5630076	-27	36897
18	FF	55358	003400	780	293	495	-701838	+97	36834
24	FF	55358	003400	780	481	612	-2914585	-48	36871

Figure 4.20: *CGGTTS file format example (only a part is shown), on the left the file corresponding to the satellites seen by the CERN site and on the right the file corresponding to the satellites seen by the LNGS: the satellite number, the time and the REFGPS information were used to selected the common satellites seen by CERN and LNGS during the OPERA run periods for the timing correction calculation. In red is presented an example of the satellites seen by the two sites at the same hour for the same day, only the satellites that are in common are retained for the calculation.*

Data Category	Meaning
PNR	The satellite vehicle PRN number
CL	The hexadecimal number that corresponds to the Common View class of the track
MJD	The five digit Modified Julian Date of the start of the track
STTIME	hour, minute, and second (in UTC) of the start of the track
REFGPS	The time difference (measured in .1 ns) between the laboratory reference clock and the satellite time, referred to the midpoint of the pass via a linear fit

Table 4.1: *Explanation of the useful information contained in CGGTTS files for the timing correction calculation.*

The guidelines on GNSS Time Transfer Standards (CGGTTS) have been compiled

with the aim of achieving a technique that can transfer time with an accuracy of 1 ns or better. The receiver system consists of a GNSS antenna and receiver, a microprocessor-controller, an input provided for an external frequency reference to be used in all internal oscillator functions, an input provided for an external pulsed signal related to the external frequency standard (1PPS), and possibly an internal time-interval counter. During operation the internal oscillator must remain locked to the external frequency reference. The epoch of the receiver clock can be either:

1. set based on the GNSS signals themselves and continuously monitored against the external pulsed signal using a time-interval counter, or,

2. locked directly to the 1 PPS signal.

Several configurations satisfy these requirements (they are described in [49]), among these, the Septentrio receiver used in the LNGS and CERN timing system is a geodetic-time receiver which directly synchronizes its internal clock on the external clock to be compared. The scheme of a generic geodetic receiver is presented in figure 4.21 a. The user must ensure that the 1PPS epoch is coherent with the frequency reference and maintained sufficiently close to the GNSS time scale to assure proper operation. This kind of receiver cancels the need for a time interval counter and hence provides a final solution REFGPS = UTC(k)-T_{GPS} (see figure 4.21 a) which is less noisy than the solutions obtained with other configurations. The internal reference is obtained either by locking the internal oscillation on the external frequency, or by using directly the external frequency. If the internal oscillator is locked on the external frequency with an enslavement system, then the system should be described in full details by the manufacturer. Furthermore, the way the internal reference clock is obtained from the external 1PPS must also be described by the manufacturer, this is mandatory to have access to the delay between the external clock and the GNSS measurements. The ionosphere-free code (P3) technique was proposed [62] to use the dual-frequency measurements from geodetic receivers for GPS common-view time and frequency transfer applications. The P3 common-view has advantages over conventional common-view (more details are in [49]), resulting in less short term measurement noise. In the case of a P3 CGGTTS file the REFGPS time differences are based on the *ionosphere-free* code P3 which is actually a linear combination of the P1 and P2 codes. Since the propagation delay through the ionosphere is different at the L1 and L2 carrier

frequencies, due to the dispersion of the ionosphere, it is possible to construct a linear combination P3 that compensates for the ionospheric delay variations, hence the name *ionosphere-free* code.
Because the P3 data involve the measurements on both the L1 and L2 frequencies, it is necessary to determine the receiver delay on both frequencies in order to compare the time of remote clocks. Procedures have been developed for absolute calibration of several different types of geodetic receivers, they make measurements between the local reference signal and the received GPS signals on both the L1 and L2 frequencies. Measurements are recorded in the RINEX files. Since the delay through the dispersive ionosphere is proportional to (TEC/f^2), where TEC[6] is the total electron content over the signal path and f is the frequency of the GPS signal, the impact of the ionospheric delay can be cancelled by the linear combination:

$$\mathrm{P3} = \frac{f_1^2}{f_1^2 - f_2^2}\mathrm{P1} - \frac{f_2^2}{f_1^2 - f_2^2}\mathrm{P2} = 2.54\mathrm{P1} - 1.54\mathrm{P2}, \tag{4.5}$$

where P1 and P2 are the code measurements with the GPS signal's propagation time on the frequencies $f_1 = 1575.42$ MHz, $f_2 = 1227.60$ MHz.
For time transfer applications, the receiver hardware delays on L1 and L2 frequencies (INTL1 and INTL2) must be removed from the P1, P2 measurements to generate the P3 data. During the absolute or differential geodetic receiver calibration, INTL1 and INTL2 can be individually determined.

4.4.1 Time Transfer with the Septentrio PolaRx2 Receiver and its Calibration

It is possible to use the GPS receiver PolaRx2 for time transfers, since it is a receiver which provides dual frequency tracking of the GPS signals and it is capable of using the ionosphere free combination P3. Its raw measurements and navigation data can be converted into the RINEX format using a conversion utility provided by Septentrio. Furthermore it accepts in input a 10MHz external frequency and a 1PSS input which make it suitable for time transfer applications. In other words it corresponds to the receiver type illustrated in the previous paragraph (see figure

[6]Today TEC measurements are made mostly using GPS data, since there are a great number of GPS receiving stations able to provide such measurements. TEC values are obtained by pseudo-range and phase observables as $P_2 - P_1$ and $L_1 - L_2$ are proportional to $40.3TEC\left(\frac{f_1^2 - f_2^2}{f_1^2 f_2^2}\right)$.

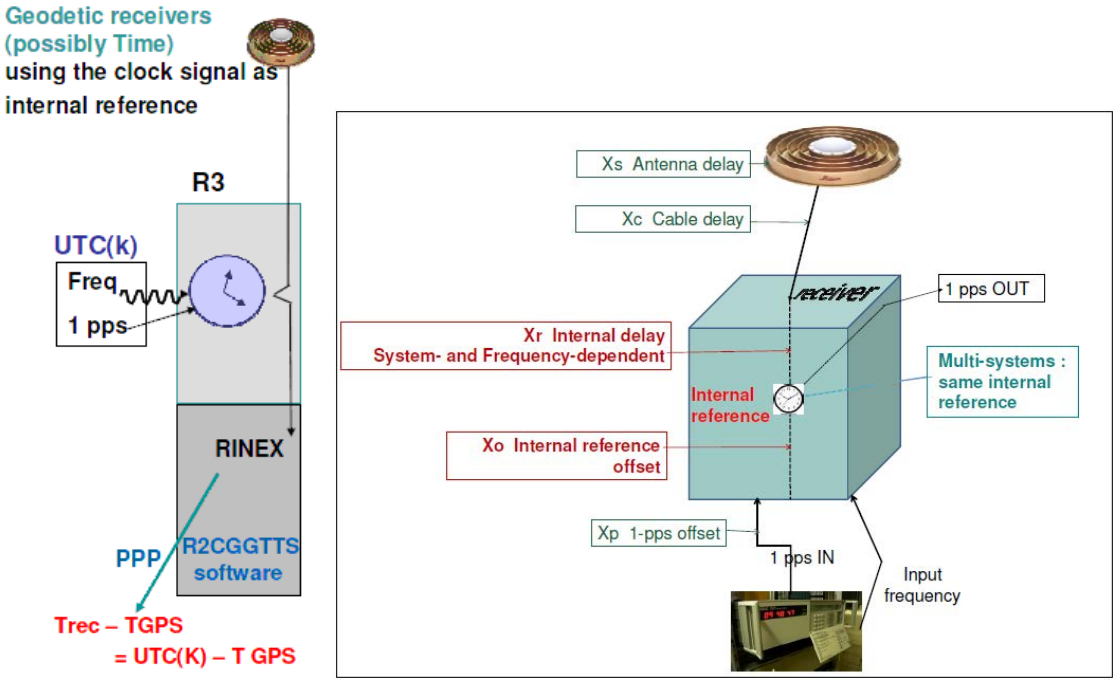

(a) (b)

Figure 4.21: *a) Scheme of the geodetic-time receiver used at LNGS and at CERN. b) Standard set-up of a receiver showing the definition of the different quantities that enter in the calibration.*

4.21 a). The relation between the latching of observations and the external clock can be obtained from the 1PPS output, which is synchronized with the internal clock, or from post-processing. This allows determining, by differential analysis of the code measurements, the internal hardware delays of the receiver. Tests performed with respect to a local time reference linked to USNO showed that the PolaR2x receiver can be used for sub-nanosecond carrier-phase frequency transfer.

When the RINEX data is translated into CGGTTS data for the purpose of GPS P3 common-view time transfer, a number of calibrated delay parameters are used to translate the time comparison node from the antenna reference plane down to a conventional reference location which allows absolute time comparison between the local reference clock and the satellite reference clock. The calibration of the two PolaR2x receivers used at CERN and LNGS was performed by the Swiss Metrology institute METAS.

The calibration includes the time reference source Cesium clock Cs4000 which is associated to each PolaRx2 receiver. The calibration scheme follows a convention[7] where different delays are measured. The calibration information must contain

[7]introduced by G.Petit et al. in 2001

a correct definition of the physical point corresponding to the internal reference clock inside the receiver, i.e. the physical point where the GNSS measurements are made. The information should also contain all the relations between this physical point and the input/output signals, and between it and the point to which the measurements are reported (if it is not the same).
The following calibration quantities are hence defined (a scheme of the calibrated quantities is shown in figure 4.21 b):

- An external timing reference (typically a Cesium clock) sends in input to the receiver its 1PPS signal and an input frequency (10 MHz),
- X0 is the delay between the 1PPS input and the internal reference, XP is the delay between the external time reference and the 1PPS input (cable delay measurement),
- XS and XC are the antenna and cable delays for the GPS signal seen by the antenna to get in the GPS receiver,
- XR is the internal delay between the time at which the GPS time arrives to the receiver and its internal reference, XR will be depending on the frequency, the receiver type and, as well as X0, on the definition of the physical point where the GNSS measurements are made.

The results of the calibrations performed by METAS are reported in figure 4.22 in the standard CGGTTS configuration files of the two PolaR2x receivers.

```
Cggts file 2010 (CERN) GCNGC55.491

CGGTTS GPS/GLONASS DATA FORMAT VERSION = 02
REV DATE = 2008-08-18
RCVR = SEPT POLARX2 v2.6.0 SN:3205  R2CGGTTS v4.2
CH = 16 (GPS)
IMS = SEPT POLARX2 v2.6.0 SN:3205
LAB = CERN
X = +4393606.61 m (GPS)
Y =  +466214.48 m (GPS)
Z = +4585243.47 m (GPS)
FRAME = ITRF
COMMENTS = RxControl Auto-Generated File
INT DLY =  217.6 ns (GPS P1),  225.7 ns (GPS P2)
CAB DLY =  202.8 ns (GPS)
REF DLY =   246.8 ns
REF = PXTIME
CKSUM = 13
```

```
Cggts file 2010 (LNGS) GCNGG55.491

CGGTTS GPS/GLONASS DATA FORMAT VERSION = 02
REV DATE = 2008-08-18
RCVR = SEPT POLARX2 v2.6.0 SN:3206  R2CGGTTS v4.2
CH = 16 (GPS)
IMS = SEPT POLARX2 v2.6.0 SN:3206
LAB = CERN
X = +4585754.09 m (GPS)
Y = +1102187.53 m (GPS)
Z = +4280932.90 m (GPS)
FRAME = ITRF
COMMENTS = RxControl Auto-Generated File
INT DLY =  217.4 ns (GPS P1),  227.0 ns (GPS P2)
CAB DLY =  202.9 ns (GPS)
REF DLY =  245.8 ns
REF = PXTIME
CKSUM = 49
```

Figure 4.22: *Results of the PolaRx calibrations performed by METAS.*

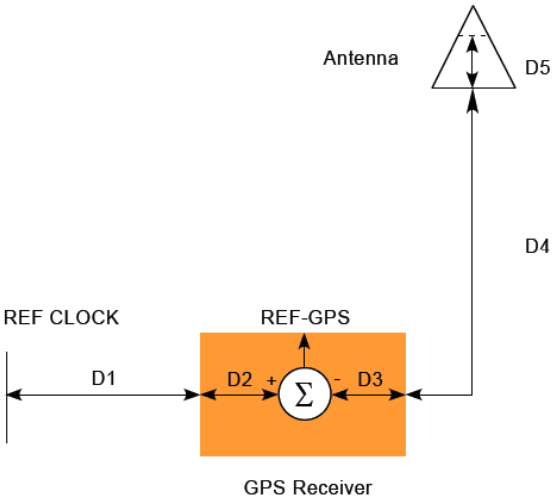

Figure 4.23: *Connection scheme between Reference Clock, GPS receiver and GPS antenna.*

Assuming the connection scheme of figure 4.23, the calibration report of METAS defines the quantities D1, D2, D3, D4 and D5, to be related to the CGGTTS format quantities CAB DLY, INT DLY and REF DLY:

- CAB DLY: is the delay of the coaxial cable that connects the antenna to the receiver. CAB DLY corresponds to XC + XD[8] (Petit et al., 2001, sum of all antenna cables). In the METAS scheme it corresponds to D4.

- INT DLY P1 and INT DLY P2 are the internal delays of the GPS geodetic receiver. There are two internal delay parameters because the P1 and P2 observations are based on two different carrier frequencies, so the propagation delay might be different. In the present version of the CGGTS format INT DLY refers to the sum of the internal delay and the antenna delay. These values are determined by absolute or relative calibration. INT DLY corresponds to XR + XS (Petit et al., 2001). Namely it is the time the GPS signal will take to propagate in the antenna and inside the GPS receiver down to its internal time reference. In the METAS scheme this corresponds to D3+D5. IND DLY P1 = D3(P1) + D5(P1).

- REF DLY is the delay between the local REF clock 1PPS signal and the reference time difference node inside the geodetic receiver. It corresponds to XO + XP (delay between the 1PPS input and internal reference). In

[8]In some configurations it is possible to have another cable connecting the antenna to the receiver after the cable with delay X_C, its delay is called "short cable delay" and labelled as X_D. The total delay due to the cables between the antenna and the receiver amounts then to X_C+X_D

the METAS scheme it is defined as REF DLY = D1 + D2 where D1 is the external part of the REF DLY, *i.e.* the delay between the laboratory reference node of the REF clock and the 1PPS input connector of the GPS receiver. D2 is the internal part of the REF DLY.

In the particular case of the Septentrio PolaRx2eTR receiver we have:

$$D2 = D_i + 8.7 \text{ ns} \tag{4.6}$$

Where D_i is the insertion delay of the Septentrio PolaRx2eTR receiver, i.e. the delay between the 1PPS input signal and the 1PPS output signal. Septentrio specifies that the 1PPS output pulse can be synchronized to what it is called here the time comparison node. Once the synchronization is achieved, the 1PPS output pulse occurs 8.7 ns before the time comparison node.
The values measured by METAS for the LNGS PolaRx receiver are reported in table 4.2.

Measured Quantity		Value
CAB DLY =	D4 =	202.9 ± 0.5 ns
INT DLY(P1) =	D3+D5 =	217.4 ±2 ns
INT DLY(P2) =		227.0 ± 2 ns
D_i =		243.4 ns
D2 =	D_i+8.7 ns =	252.1 ns
D1 =		-6.3 ns
REF DLY =	D1+D2 =	245.8 ns

Table 4.2: *Measurement done by METAS for the LNGS PolaRx receiver.*

Note that the delay D1 depends on a calibration of the 1PPS signal from the reference clock. A negative/positive value of the delay means that the physical 1PPS signal from the reference Cs4000 distribution amplifier leads/lags the calibrated Cs4000 - UTC(CH) time scale.
In the CGGTTS output file, the result REFGPS is the measured time difference:

$$REFGPS = X(CLK) - X(GST), \tag{4.7}$$

in units of 0.1 ns, where X(CLK) is the time of the local REF clock and X(GST) is the estimation of GPS system time broadcasted by the GPS satellite PRN for a given track of duration TRKL started on Modified Julian Day MJD at epoch STTIME.

From a practical point of view the offline analysis of the CGGTS files will take into account the configuration files described above and including CAB DLY, INT DLY P1, INT DLY P2 and REF DLY and generate in the output file a REFGPS value which measures the time difference between the local reference clock and the time of the GPS system brought inside the receiver. As said, the 1PPS output occurs 8.7 ns before the generation of REFGPS. the overall scheme is summarized in figure 4.24.

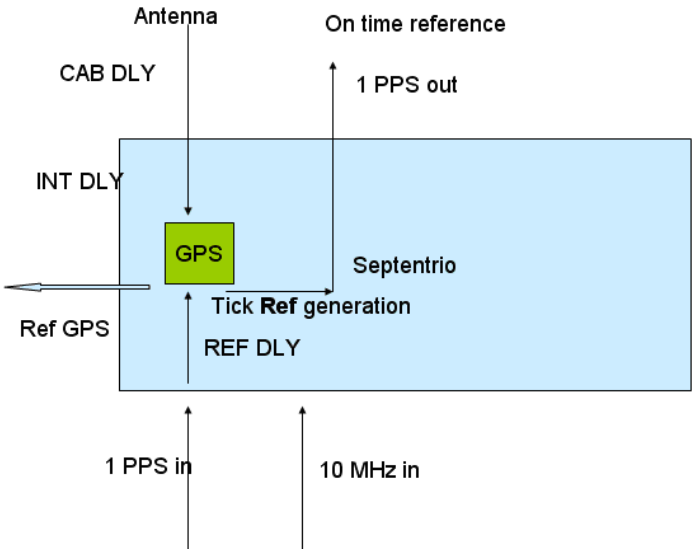

Figure 4.24: *Overall scheme of the PolaRx GPS receiver.*

4.5 Timing Corrections

By using the time comparison values obtained by the data logged to the dedicated PC (Δt_{CERN} and Δt_{LNGS}), the calculated *refC* and *refG* mean values and the time constants determined performing the calibrations of the timing chains described in chapter 5, it is possible to calculate a timing correction value for each OPERA event.

For each OPERA event time t_{OPERA}, the two closest logged values of the two inputs in *Ext1* and *Ext2* were chosen, so that for each one, two values of Δt_{LNGS} and of Δt_{CERN} are available. Using a linear interpolation between them, the Δt_{LNGS} and Δt_{CERN} values corresponding to t_{OPERA} have been extracted. For what concerns the Tref values, both in the CERN and LNGS cases, the two $\langle Tref_C \rangle$ and $\langle Tref_G \rangle$ values before and after t_{OPERA} have been used to compute a linear interpolation corresponding to t_{OPERA}: $Tref_G$ and $Tref_C$. As a result, it is possible to

calculate the timing correction T_X to be applied to the OPERA events, in order to refer the time in both cases at CERN and at LNGS at the point X which is in the "same position" in the two configurations (see figure 4.18):

$$\begin{aligned} T_X^{LNGS} &= Tref_G + d_{LNGS} - \Delta t_{LNGS} \\ T_X^{CERN} &= Tref_C + d_{CERN} + \Delta t_{CERN}, \end{aligned} \tag{4.8}$$

where, as explained, $Tref_G$ and $Tref_C$ are the interpolated GPS reference times, Δt_{LNGS} and Δt_{CERN} are the interpolated (Ext2-Ext1) PC logged values (the Δt sign is due to the fact that in one case the septentrio is connected to the Ext1 of the CTRI card and in the other to the Ext2), d_{LNGS} and d_{CERN} are the cables and Fan Out delays: 2 ns at LNGS and 43 ns at CERN. In appendix A are explained in more details the calculations done comparing with the time scheme in figure 4.18.

An alternative formula was used to calculate T_X^{CERN} for the first part of the 2009 OPERA run data. This is due to the fact that until 30/07/2009 the configuration of the system was different, the 1PPS Cs signal was replacing the signal from the XLi. The correction has been calculated as $T_X^{CERN} = Tref_C + Ext2$ logged value $+const$, where $const$ = (-8 (cable connection) -910876) ns, as derived from the calibration measurements. In this case the linear interpolation was calculated between the two closest value of T_X^{CERN} to find the correction related to t_{OPERA}.

In figure 4.25 are presented the values T_X^{LNGS} and T_X^{CERN} calculated for the 2009 and 2010 OPERA events. It was possible to obtain the correction values for 18683 OPERA events using the LNGS GPS data and for 14684 events using the CERN GPS data during 2009. In 2010 the correction values are 23618(24541) in the case of CERN(LNGS) GPS data. The bands give an idea of the intercalibration stability of the two systems. However this is known at the ns level because the OPERA events will be individually corrected by their corresponding intercalibration value represented in the plot.

Some "strange" values for T_X were obtained for the 2010 data, both for CERN and for LNGS case, as outlined in figure 4.25.

After investigating these cases were identified as follow:

- T_X^{CERN} from 8 October 2010: The XLi at CERN was replaced by one with a newer firmware.

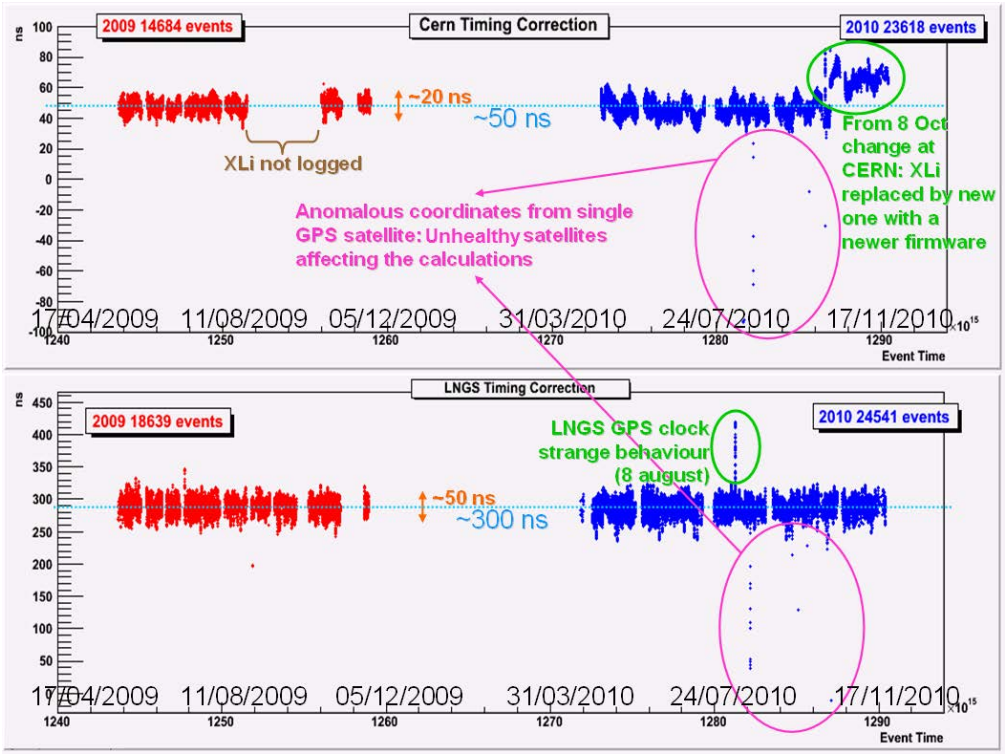

Figure 4.25: *T_X^{LNGS} and T_X^{CERN} calculated for the 2009 (in red) and 2010 (in blue) OPERA events. The missing values of T_X^{CERN} from the end of August to mid October 2009 are due to the XLi data that were not logged at CERN. The "problematic" cases found in the 2010 data were discarded during the selection of the final data sample to be analysed.*

- T_X^{LNGS} on 8 August 2010: strange behaviour of the LNGS GPS clock. The events t_{OPERA} that are in the time window corresponding to this behaviour were discarded during the selection of the final data sample.
- T_X^{LNGS} and T_X^{CERN} simultaneous strange values corresponding to the days of August 19^{th}, September 21^{st} and 28^{th}, and October 14^{th} . Unhealthy satellites signals were found in the same days. This affects the calculation since an anomalous coordinate from a single satellite is reflected in a wrong mean value in the computation of $\langle Tref_C \rangle$ and $\langle Tref_G \rangle$. Also in these cases the corresponding t_{OPERA} events were eliminated from the final data sample. In figure 4.26 is shown one on these cases: the strange *refGPS* values in the CGGTTS file corresponds always to the same satellite, which was sending an unhealthy signal as can be found in the RINEX Navigation file (the health value is reported in the second field of the sixth navigation message records).

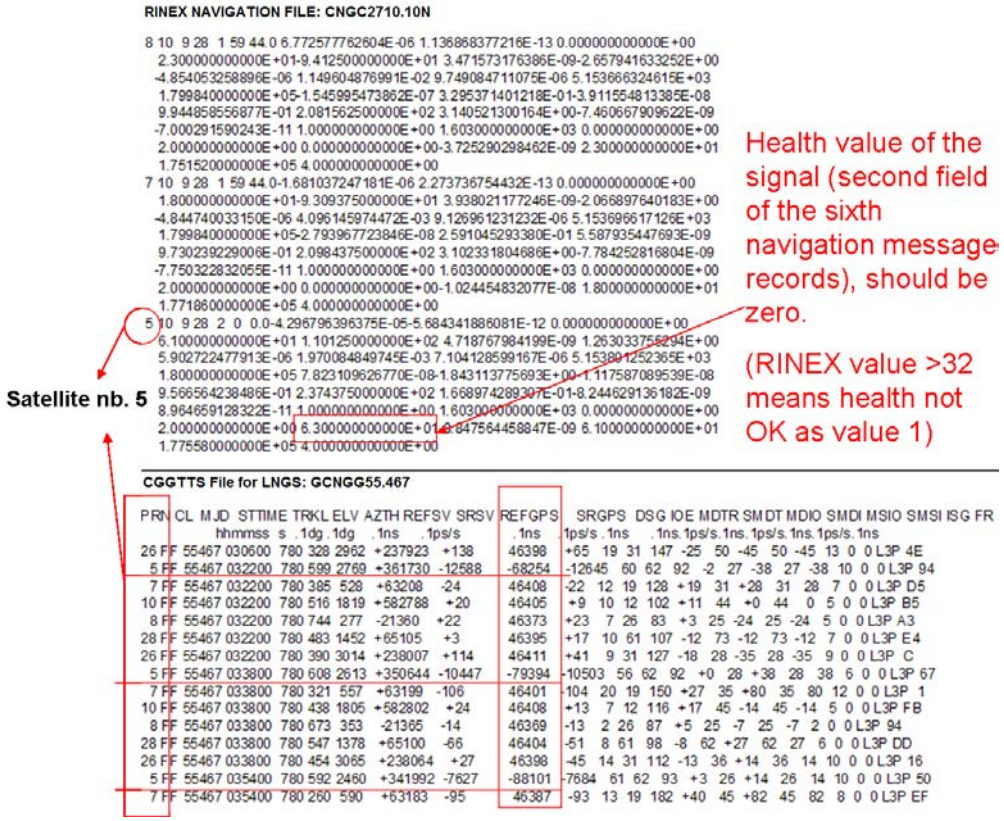

Figure 4.26: *Example of an identified unhealthy satellite which affected the computation of* T_X^{LNGS} *and* T_X^{CERN} *in 2010. The strange* refGPS *value of satellite nb. 5 is due to the unhealthy signal it was sending to the GPS. The corresponding record in the Navigation RINEX file is shown in red and on the bottom is shown the resulting CGGTTS file with strange* refGPS *values for that satellite.*

Chapter 5

Timing Calibrations

5.1 Calibration Measurements at CERN

The kicker signal is not really representative of the real transit time of the proton beam in the machine, since it is generated by the SPS electronics and can have differences at the level of hundreds of ns w.r.t. the protons transit time. For this reason a UTC calibration of the CNGS beam is needed in order to measure independently the real beam transit time and then to correlate it to the UTC time-tag of the kicker signal. The relation between the kicker trigger seen by the CTRI and the real beam time, given by the proton pulse, is established in a different way:

1. The kicker signal time tagged by the CTRI is just a kind of external trigger.

2. This signal is also used to trigger the start of the acquisition window of the FWD.

3. The proton signal is now regularly sampled for each extraction by a different BCT, (BFCTI400344) installed on the CNGS beam line and not in the SPS ring. This signal is sent to the FWD.

4. The CTRI provides the UTC time-tag of the start of the FWD digitization window, then by looking at the acquired waveform, it is possible to know the UTC of each sample of the protons pulse. This is a simple and self-calibrating operation mode.

At CERN the timing chain was re-calibrated in January 2010 taking a series of measurements by using as reference signal the 1 PPS output of a portable Symmetricom Cs4000 cesium clock [60] (more details about the timing system and its calibration measurements in 2006 can be found in [49]). The normal configuration has been already presented in section 4.1 and it is presented in figure 5.1a: the 10 MHz signal from the Cs clock is sent to Septentrio, which is then connected via 8 ns cable to the CTRI card input Ext2 of the PC performing the data acquisition of the Septentrio and of the XLi tagging. The XLi is connected with the input Ext1 of the card through two Fan Out modules and two 16 ns cables. The Xli-GPS antenna sends also 1 PPS and 10 MHz signals to the Central Timing System distributing the SPS timing (labelled CTG). The SPS timing is distributed to the PC card and underground to the HCA4 hall, in the CNGS access point (see figure 5.2), where also the kicker signal is tagged.
The PC allows then to refer the Septentrio and the XLi signals to the CGT signal. The underground configuration of the system is shown in figure 5.3.

The calibration measurements were taken connecting the Cs clock 1PPS output to the various inputs of the instrumentation, always using the same 8 ns cable. The set of measurements is listed here and described more in details below: measurements were first taken in the CCR, then, the Cs4000 powered with car batteries in order to ensure the phase stability of its 1PPS signal, which represents an arbitrary timing reference, was transported to HCA4 in order to inject this reference signal in the CNGS time-tagging electronics. Once the Cs4000 was brought back to the CCR a new measurement was repeated by connecting it to Ext1 of the CTRI. This measurement was just performed as a cross-check of the stability of the Cs and the CGT during the entire calibration operation which lasted about 4 hours.

Measurements in the CCR

The Cs 1 PPS time reference was sent as input to the PC CTRI card in Ext1, disconnecting the XLi cable (see figure 5.1 b). By measuring the Cs clock and the XLi on the same input it is possible to cross-calibrate. Multiple measurements were taken, over a period of a few tens of minutes, and then the average value of the measurements was calculated. The measurements are expressed in terms of UTC time-tags since the CTRI is connected to the GMT. The accuracy of the time-tag is 1/10 of a ns. The stability of the various measurements is at the level

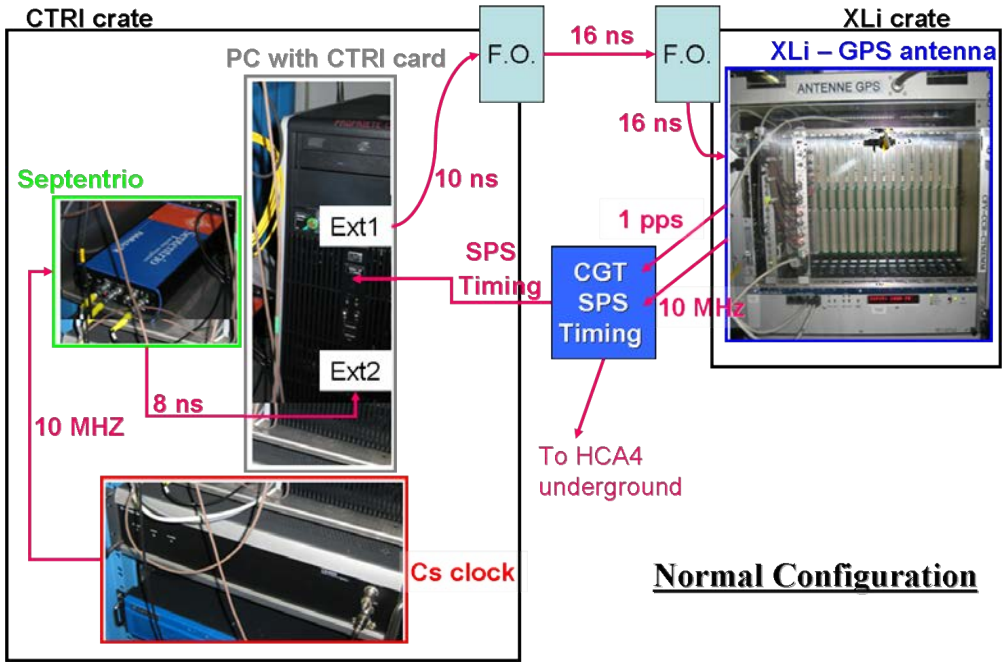

(a)

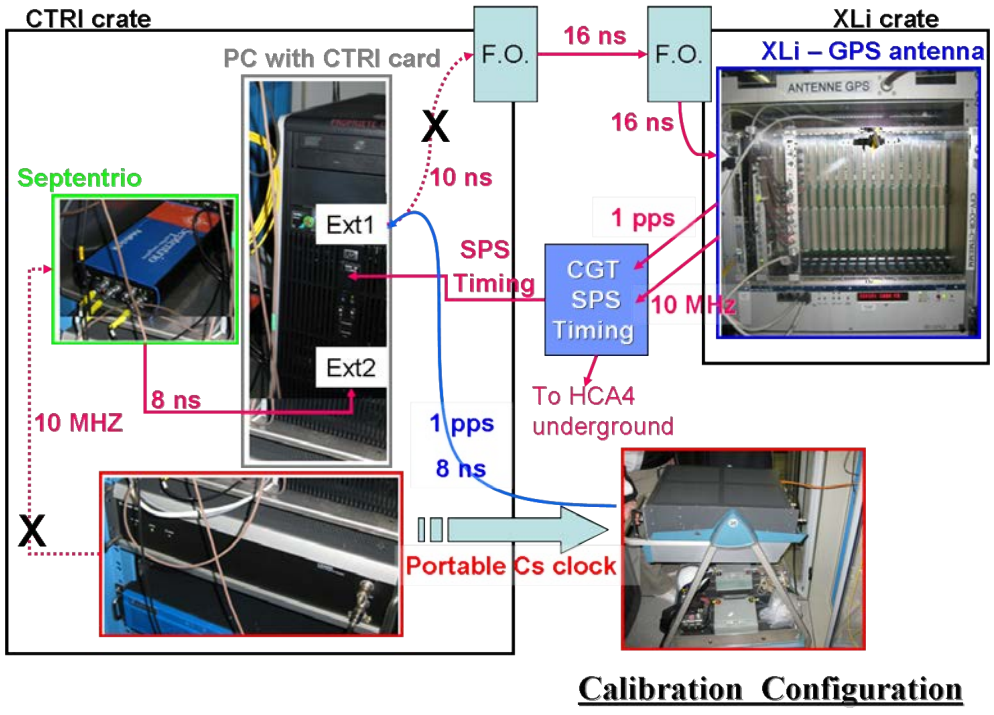

(b)

Figure 5.1: *a) Simplified scheme of the timing chain at CERN, in the normal configuration: the connections between the PC with the CTRI card crate, the XLI-GPS antenna crate and the CGT (Central Timing System) that distributes the SPS timing are shown. b) In the calibration configuration the XLi signal was disconnected and replaced by the Cs 1 PPS reference signal, disconnected from the Septentrio and sent as input in Ext1 of the Pc card.*

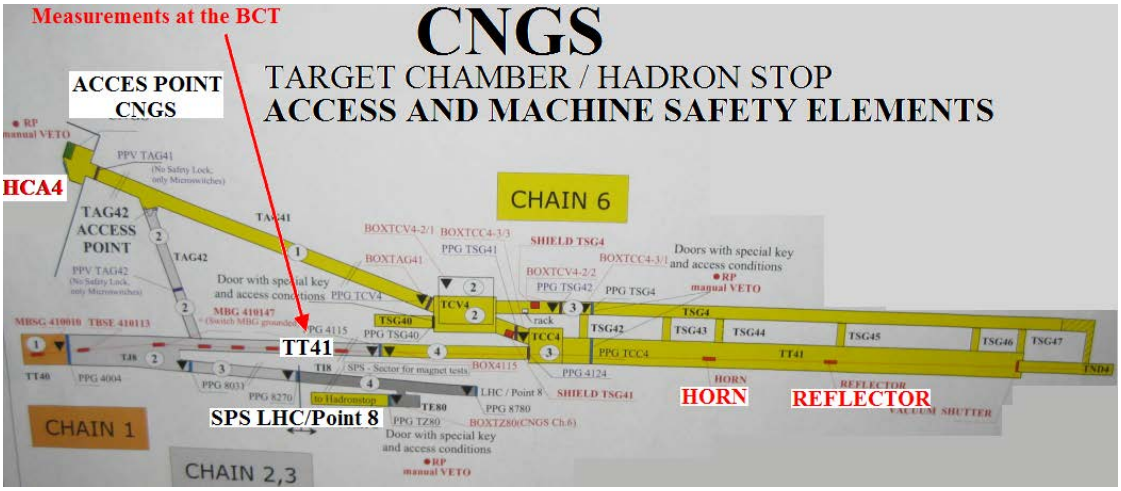

Figure 5.2: *Scheme of the CNGS access point. The calibration measurements were taken in the HCA4 hall and at the BCT located along the CNGS beam line (TT41).*

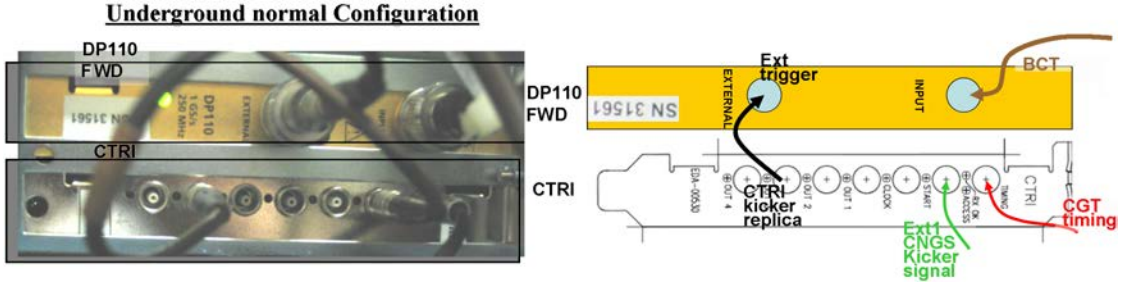

Figure 5.3: *Underground normal configuration at CERN of the timing system. The CTRI card and the FWD card are shown as well as the connections with the BCT, the central timing and the kicker signal.*

of 1 ns over 40 minutes. The results showed that the average values were stable at the level of 3 ns.

Measurements in the HCA4 Hall - Underground

- The Cs reference signal was sent in input to the PC card usually used to time tag the kicker pulse. The kicker cable was disconnected and replaced by the 8 ns cable from the Cs portable clock. Then the 1 PPS signal generated to the CTRI card was sent to a digital scope in order to compare with the 1PPS of the Cs clock. Normally, this 1 PPS output signal from the CTRI card is sent to the external trigger input of the Fast Waveform Digitizer (DP110 FWD card). The scheme is presented in figure 5.4.

The results of these measurements can be summarized as follows:

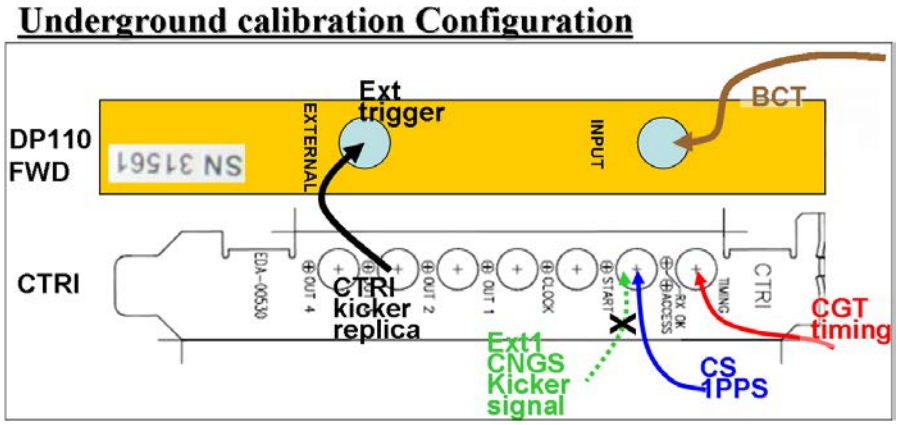

Figure 5.4: *Underground calibration configuration at CERN. The reference signal of the Cs clock was connected with the Ext1 input of the CTRI card, disconnecting the kicker signal.*

1. The Cs4000 signal UTC time-tagged by the CTRI in HCA4 is delayed with respect to the UTC time tagging in the CCR by 10084.8 ns.

2. When the XLi 1PPs is UTC time-tagged by the CTRI in CCR the average measured value is 0.999910927011 s. The XLi is also the source of the UTC used for the time-tagging, so ideally, by considering all delays this number should be 1.0. The difference with respect to 1 is 89073 ns. The cable delays used to connect the XLi to the CTRI have also to be taken into account, they amount to 51 ns (16 ns + 16 ns + 10 ns + 4.5 ns fanout1 + 4.5 ns fanout2). The corrected difference is hence 89073 ns + 51 ns = 89124 ns. This difference should be forced to be zero in order to correct for the delays of treatment of the XLi signals in the GMT timing chain.

3. In order to bring at the level of the XLi 1PPS output the kicker measurement performed in HCA4 one has to take into account the corrections at the previous two points: XLi time = HCA4 time + 10084.8 ns + 89124 ns = HCA4 time + 99208.8 ns. This means that the Time tag in HCA4 is delayed by about 99 μs with respect to the UTC time available at the level of the XLi 1PPS output.

These considerations are summarized in table 5.1.

Delay HCA4 w.r.t. CCR	10084.8 ns
Delay UTC time tag w.r.t. XLI 1PPS	89073 + 2(16+4.5) + 10 ns
Total Correction	99208.8 ns

Table 5.1: *Summary of the calibration measurement results at CERN.*

The default correction value, as measured in past calibrations (August 2006), was

99216 ns. In 2006 the UTC source of CERN timing system was a symmetricom XL-DC GPS receiver disciplined with a Rb clock, and the electronics was located in the hall BA40, one floor above HCA4 ([49]). The result of the calibration is then that the UTC time-tags of the kicker written in the CNGS database should be corrected by 7.2 ns (99216 - 99208.8 ns).

- The Cs signal was then injected in the BCT40034 along the CNGS beam line. By using a digital scope the 1PPS signal of the CTRI was compared with the Cs signal via BCT. The measurement of the delay implied two steps:

  a) The configuration of the CTRI card is changed in order to output a 1 PPS signal synchronous with the CGT. This signal is put in output on the same connector which is normally used in order to generate the replica of the kicker signal. This signal triggers a digital scope and its delay is measured with respect to the 1PPS signal produced by the Cs4000. This delay corresponds to 209.302 ns.

  b) The CTRI 1PPS signal is still used to trigger the digital scope but the Cs4000 is moved to the CNGS beam line and its signal is sent in the calibration input of the BCT40034. The kicker cable normally connected to the input of the CTRI is now connected to the scope. Now the delay of this signal with respect to the trigger which is the same as in the other configuration includes the delays of the BCT cables. The new delay is 790.7 ns.

Since the 1PPS signal generated by the CTRI and used to trigger the scope is stable at better than 1 ns during this period, the delay relative to the cables of the BCT connection amounts to 790.7 - 209.3 = 581.4 ns.
In table 5.2 are presented the conclusions on the calibration measurements performed.

Delay in order to bring the kicker time tag in HCA4 at the level of the XLi 1PPS output	99208.8 ns
Delay of the BCT signal to the FWD in HCA4	581.4 ns

Table 5.2: *Conclusions on the calibration measurements performed at CERN.*

5.2 Calibration Measurements at LNGS

As already mentioned, the LNGS timing system is a twin of the CERN one, it is composed by a GPS receiver Septentrio PolaRx2eTR and a Symmetricom cesium clock Cs4000. A data acquisition system provides the time comparison between the Septentrio receiver and the local clock(s), through the CTRI cards of a dedicated PC. The time-tag of the CTRI card at LNGS has only a relative validity to compare two outputs. The system was installed and commissioned during the summer of 2008 and was fully operative for the 2009 CNGS run, as well as the CERN one. Some sketches/pictures describe the system at LNGS (see figure 5.5).
In 2006 a measurement campaign was organized in order to measure the unknown delay (which will be called $d1$) due to the propagation of the signals through the fibers down to the experiments.
By taking as reference the 1PPS output of the GPS receivers, the measurement was performed with a double path technique:

a) The Clock2 1PPS output (called Hertz) was converted to an optical signal and sent underground with another fibre and reconverted to electrical signal (this delay will be called $d2$). Underground the difference in the propagation delays $d1 - d2$ was measured by comparing the signal coming from $d2$ to the one generated by the slave clock through $d1$.

b) A second measurement consisted in sending back to the GPS room in the external laboratory the signal which had gone through the path $d1$ and compare it to the 1 PPS signal. This measurement allowed to measure the total path $d1 + d2$.

The results of these measurements showed that the propagation delay of the signal distributed underground till the OPERA slave clock was 40993.4 ns. The scheme of the calibrated timing chain and a detail of the first step of the measurement are presented in figure 5.6.

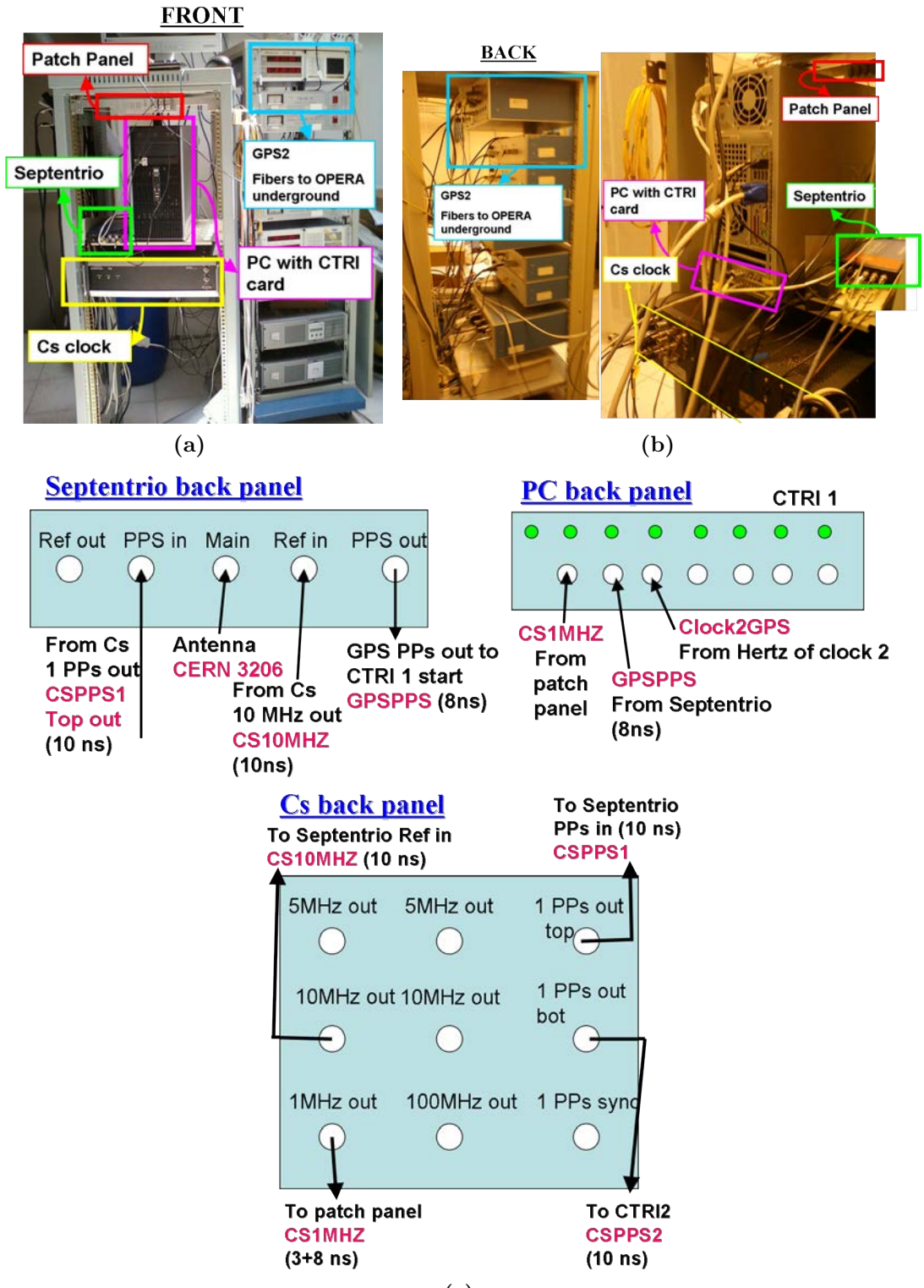

Figure 5.5: *Pictures and sketches of the timing system at LNGS. a) Front panel of the system b) Back panel of the system c) Connection scheme of the Septentrio, PC and Cs clock back panels.*

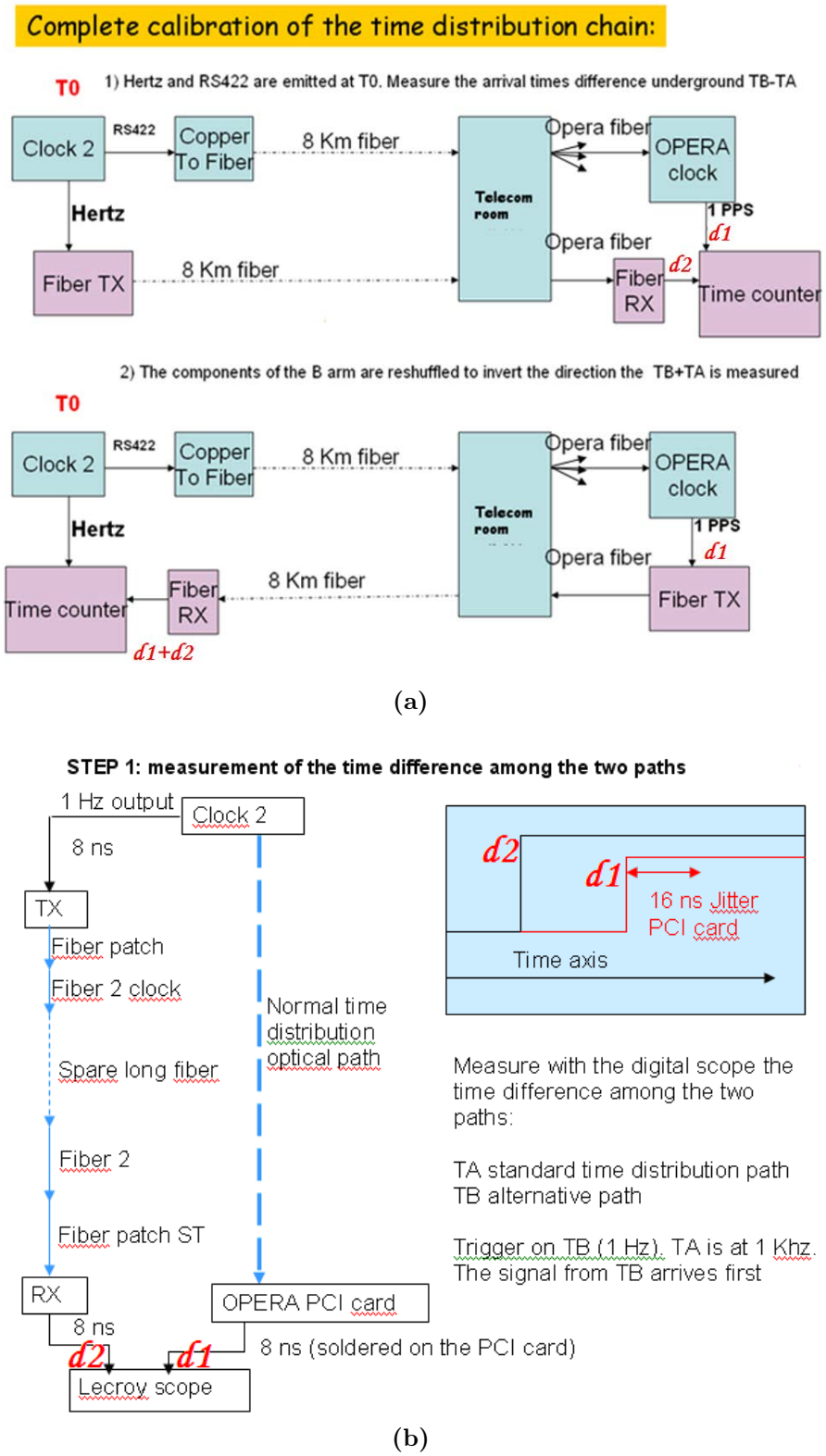

Figure 5.6: *Scheme of the calibrated timing chain at LNGS. The quantity TA corresponds to d1 and TB to d2. a) Scheme of the calibrated timing chain. b) Details of the measurement first step*

5.3 CERN-LNGS Intercalibration Measurements

A first attempt to inter-calibrate the CERN and LNGS sites was performed in March 2006 and lasted about two weeks. At that time the UTC source of the CERN timing system was a Symmetricom XL-DC GPS receiver disciplined with a rubidium clock. That system had an accuracy of 100 ns, similar to the one of the LNGS system. The XL-DC was calibrated by the Swiss metrology institute METAS. It was decided to bring it at LNGS and compare its 1PPS output by using a time interval counter to those of the two LNGS clocks. The antennas of the receivers were within a couple of meters distance, the receivers were operating by looking at the same satellite and in principle should have provided synchronous 1PPS signals, within their accuracies. The result of the measurement showed that there was an offset of 355 in between Clock 2 and the XL-DC, the 1PPS of the XL-DC was coming later. This was due to internal and antenna delays which were not compensated on the LNGS Clock 2. A different offset was measured with respect to Clock 1 showing that the two LNGS clocks were missing of internal compensation of their delays. Once corrected by this offset the relative synchronization between the two clocks was within $\pm$ 23 ns.

A new calibration campaign was performed in July 2007 by bringing from CERN to LNGS the Cs4000. The relative delay with respect to its 1PPS output was measured at CERN, and in various points of the LNGS timing chain. The first result was concerning the direct comparison with respect to the XL-DC receiver at CERN. The phase of the Cs4000 had been measured with respect to the XL-DC before leaving CERN and it was measured again with respect to Clock2 once arrived at LNGS. The two phases were within 424 ns. This result was compatible with the 355 ns from the 2006 measurement, also by taking into account the daily excursions of the GPS clocks, which for the Clock2 1PPS signal with respect to the Cs4000 reference could go up 60 ns (see figure 5.7).

The results from the relative Cs4000, Clock1(2) measurements put in evidence the problem of the daily GPS excursion. It was clear that in order to guarantee a stable and high accuracy inter-calibration among the CERN and LNGS systems it was needed to adopt a much more sophisticated technique consisting in installing a new twin, high accuracy system in the two sites, operating in common view mode and behaving as watchdog in order to correct continuously the erratic behaviour

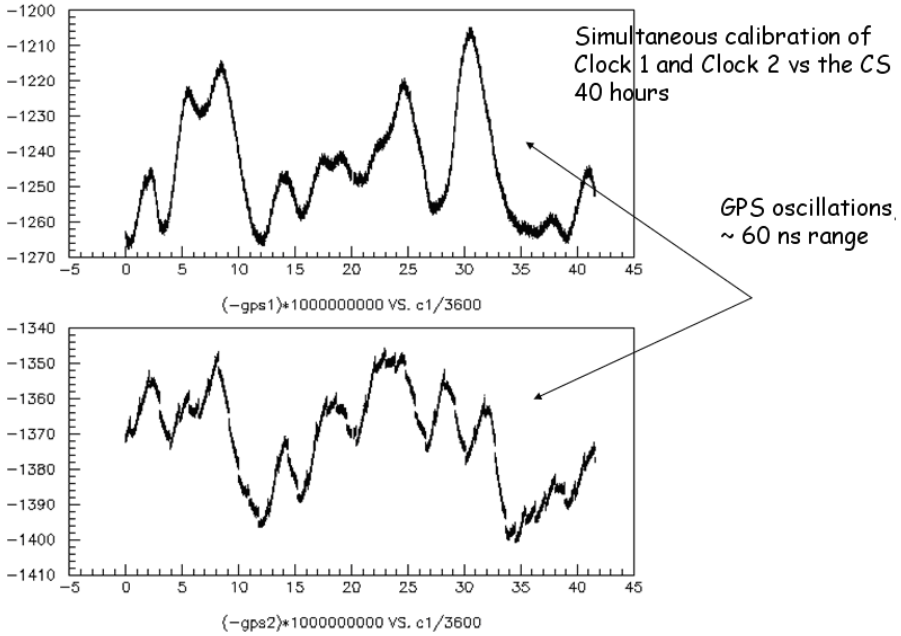

Figure 5.7: *Daily excursions of the GPS clocks, which for the Clock2 1PPS signal with respect to the Cs4000 reference could go up 60 ns.*

of the two local GPS systems, which could not be just replaced from scratch since they were deeply integrated in the operation mode of the two laboratories. An intercalibration accuracy at the 1 ns level is very important for the neutrino velocity measurement.

Chapter 6

Geodesy

An approximate value of the neutrinos TOF from CERN to Gran Sasso was calculated in 2006 on the basis of the known LNGS geodesy, in order to be able to select the OPERA events on time with the CNGS beam (as it will be explained in more details in section 7.1), until 2010, when new geodetic measurements were performed in order to determine the exact distance between the two sites with a much higher accuracy. Before the new geodetic survey, the distance CERN-LNGS was calculated considering the distance of 992.4 m between a BCT used in a calibration measurement performed in order to correlate the kicker time-tag to the beam current and the CNGS graphite target (corresponding to the distance between the beam current transformer BFCT41438 on the SPS ring, close to the kicker, and the CNGS target), and the distance between the target and the OPERA detector which was approximately evaluated on the bases of the measurement of 5 reference points at the underground LNGS. These five points were measured in 1989 at the time of the construction of the laboratory and connected to some external references which underwent GPS measurements in 1998 ([63]). In figure 6.1 are shown the five points (A, B, C, D and E) and the neutrino beam direction, and in table 6.1 are summarized their distances to the CNGS target.
By expressing the points A to E in the CERN reference system it was found that the CNGS beam was centered in the middle of the A-B distance and that the beam angle with respect to the axis of the Hall B was 3.14 mrad.

A new survey of geodetic measurements has been performed in 2010 in col-

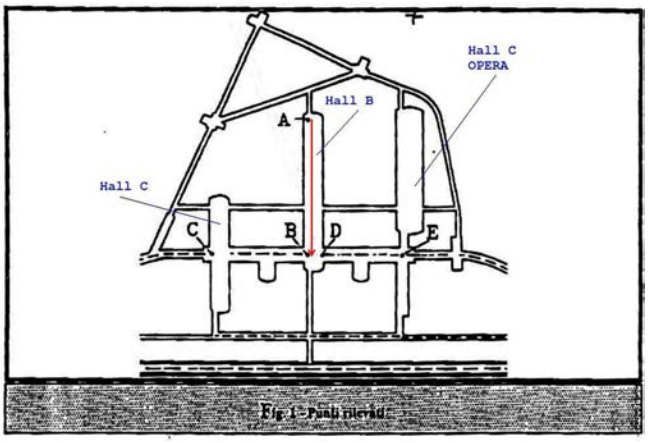

Figure 6.1: *The five reference points at underground LNGS and neutrino beam direction w.r.t. the hall axis.*

Point	Distance (m)
A	730465.4
B	730575.2
C	730575.6
D	730575.2
E	730574.9

Table 6.1: *Distances from CERN measured for the five reference points at underground LNGS.*

laboration with the Rome university geodesy group[1] with the aim of improving the knowledge of the distance between CERN and Gran Sasso in order to compute the distance travelled by neutrinos between the two sites with an accuracy of few decimetres. A complete simulation of the geodetic measurements needed was done by the Rome geodesy group to define how to bring the positions taken with GPS outside the A24 highway tunnel inside the underground laboratory, the goal of the measurements being the characterization of some reference points within the OPERA hall underground. A scheme of the highway tunnel and the LNGS underground laboratories with the OPERA detector hall is shown in fig 6.2. A mixed GPS-terrestrial survey was mandatory due to the underground location of the OPERA detector in order to link external GPS benchmarks to the already existing benchmarks located in the OPERA hall with a high precision traverse along the highway tunnel. The external new GPS benchmarks were chosen to be at the two entrance of the tunnel. The simulation foresaw several positions along the tunnel for the positioning of a LEICA Total Station TS30[64] and several benchmark positions for prisms materialized on the tunnel walls in order to create the traverse along the tunnel and to comply the logistic constraints. In order to bring the external GPS measurements to the OPERA reference system in the laboratories underground, the survey design was driven by some requirements:

- reliability: strong and fast (on-the-field) internal measurement checks,

[1]DICEA (Area di Geodesia e Geomatica), Dipartimento di Ingegneria Civile Edile ed Ambientale, Università Roma La Sapienza.

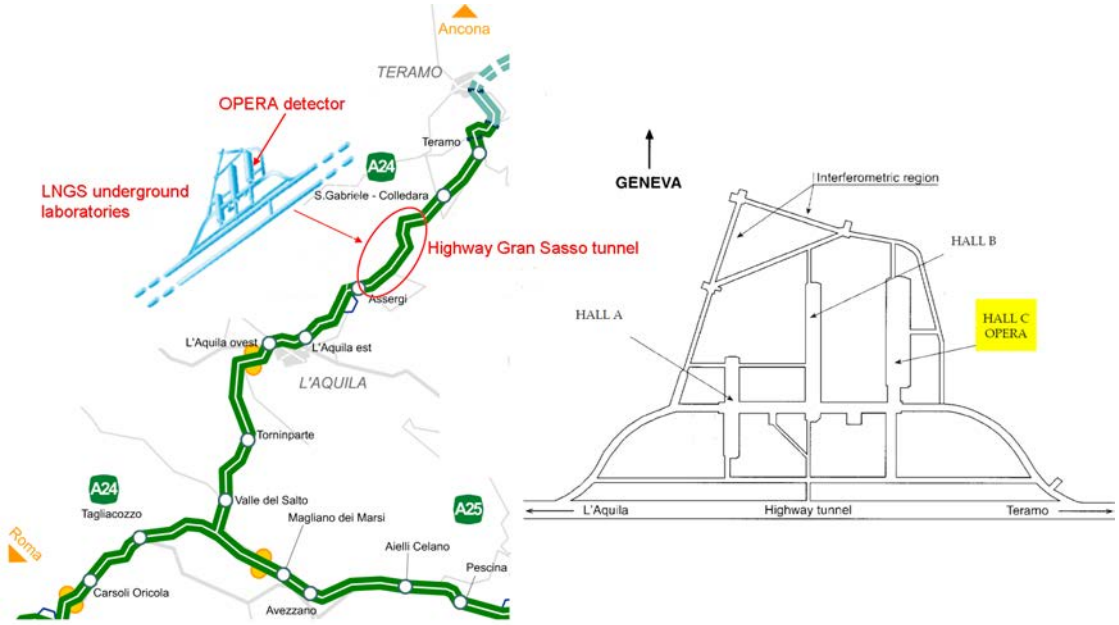

Figure 6.2: *Map of Gran Sasso tunnel and LNGS underground laboratories. The OPERA detector is located in Hall C.*

- logistic constraints:
  - the prisms supports needed to be firmly settled and clearly visible by the LEICA Total Station
  - the visibility conditions should be the best for the total station laser that had to point to the prisms,
  - The traffic could not be completely stopped, only the right lane in the Teramo-L'Aquila direction was available for traversing; a mobile site was used.

A scheme of the geostations along the tunnel, the work site and a total station picture are shown in figure 6.3

6.1 Geodesy Measurement at LNGS

It was agreed to close an highway lane to perform the measurements from 13th to 17th July 2010. Four repetitions were performed for each total station position measurement, this was done for several positions along the tunnel and inside the LNGS underground laboratories. Then a software was used with 3D network adjustment in a local cartesian coordinate system[2] for posterior re-weighing analysis.

[2]CALGE software, developed at Politecnico di Milano

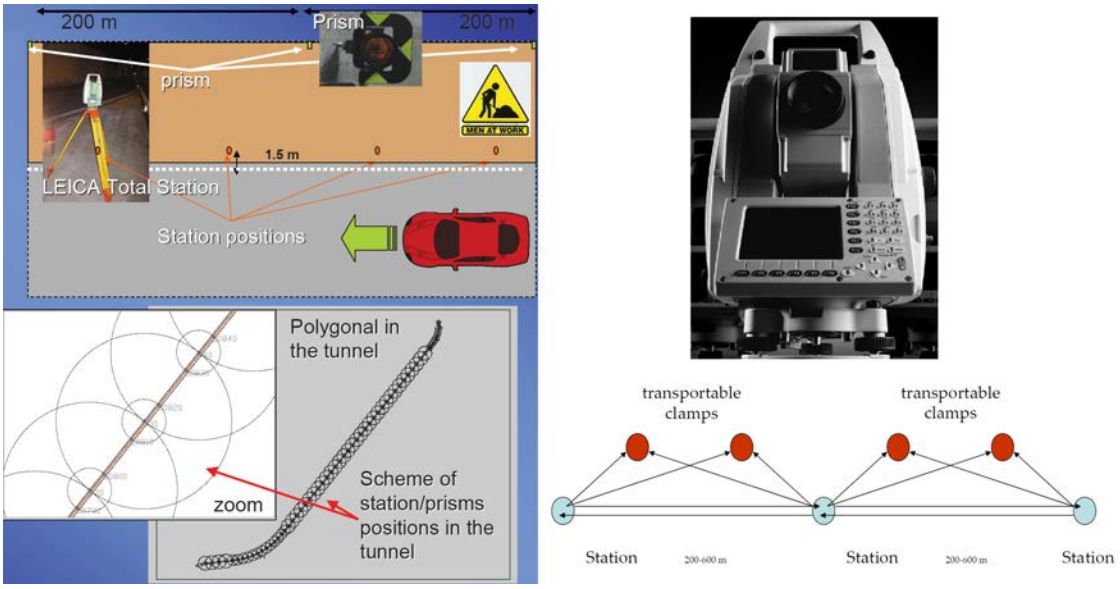

Figure 6.3: *Traverse along the Gran Sasso tunnel. On the left: scheme of the geostations along the highway tunnel, several total station measurement positions were placed in one of the two highway lane, the prism supports were placed close/on the tunnel wall. On the Right: up, the LEICA Total Station TS30 used in the survey. Bottom: scheme of the polygonal made all along the tunnel to create the traverse, the prisms were installed close the tunnel wall and the total station was transported in several positions along the tunnel in the middle between the two highway lanes.*

The precisions obtained are summarised in table 6.2

Observation	Posterior estimated precision
Horizontal direction	5 cc
Zenith angle	12 cc
Distance	0.6 mm

Table 6.2: *Estimated precisions for the LEICA total station measurements (1 cc = 0.0001 gon, 400 gon (centesimal degrees) = 2π rad).*

The measurements were brought inside the LNGS underground hall C where the OPERA detector is located using the laboratories entrance and following the trucks gallery, then the connection with the highway was realized using the bypass in front of Hall B and three fixed benchmarks settled at the exit of the underground LNGS laboratory. In order to achieve an accurate position determination of the detector, some existing OPERA reference points in Hall C were measured by means of a corner cube reflector (LEICA CCR with a precision better than 1 mm) in addition to the LEICA total station and the prisms installed in the laboratory walls. In the OPERA network of reference points the measured positions are called PG1, PG2, PG6, PG7, PG13 and PG14. In figure 6.4 a scheme is depicted of the followed path and the OPERA reference points measured.

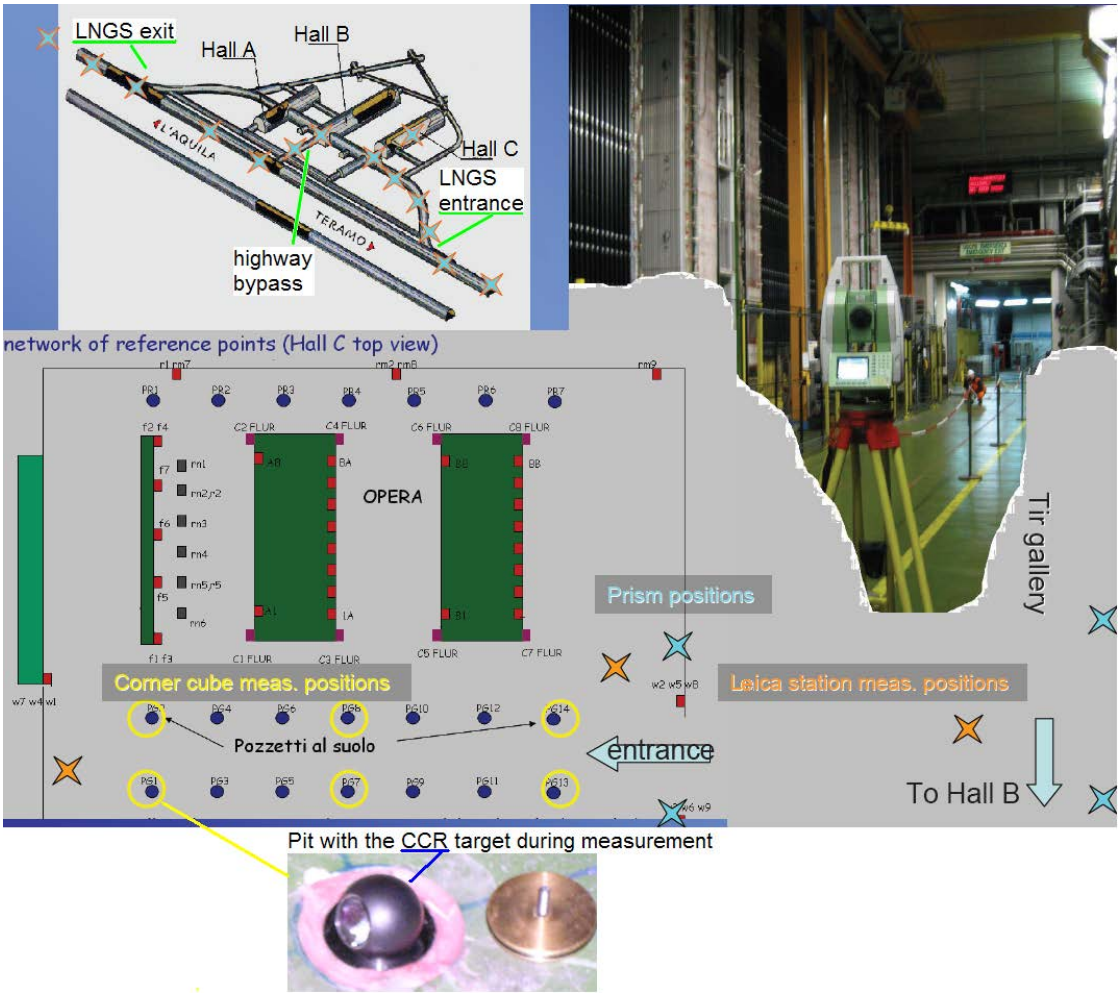

Figure 6.4: *Scheme of the followed path in underground LNGS and the OPERA reference points measured. Top: the followed path in the underground laboratories, from the entrance through the highway bypass to the laboratories exit. On the right a picture of the LEICA total station in the Hall C during the measurements of the OPERA reference points. Bottom: the top view scheme of the OPERA points network. In blue are represented some of the prisms positions on the laboratory walls, in orange some of the total station measurement positions and in yellow the LEICA CCR measurement positions.*

The GPS benchmarks outside the highway tunnel at the two entrance were established in two sessions 7 hours long on September 23rd and 24th 2010. The positions were settled outside the highway lanes close to each entrance requiring to be mutually visible from the very entrance of the tunnel, in order to strength the inside-outside link some additional benchmarks on the tunnel walls were materialized to be eventually visible from inside the tunnel close to the two entrance. Four GPS receivers[3] were used during the measurement session with 1 second

[3] 2 TPS E_GGD/TPSPG_A1 and 2 Leica GX1230 GG / LEIAS10, LEIAX1230GG

sampling interval. The GPS observations were then processed[4] including 3 EPN[5] permanent stations (UNPG-Perugia, UNTR-Terni and MOSE-Roma), the resulting coordinates precisions are:

- East = 2 mm
- North = 2 mm
- Up = 4 mm

in the European Terrestrial Reference Frame 2000 (ETRF2000, epoch 2008.0, see Appendix B). In table 6.3 the resulting positions of the four GPS benchmarks are reported.

Benchmark	X (m)	Y (m)	Z (m)
GPS1	4579518.745	1108193.650	4285874.215
GPS2	4579537.618	1108238.881	4285843.959
GPS3	4585824.371	1102829.275	4280651.125
GPS4	4585839.692	1102751.612	428651.236

Table 6.3: *ETRF2000 (epoch 2008.0, see Appendix B) positions of the four GPS benchmarks.*

A mixed GPS-terrestrial survey adjustment was performed: the Local Cartesian Coordinate System (LCCS) was defined with the origin in position of GPS1 and ellipsoidal East, North and Up as cartesian axes, so that the ETRF2000 GPS positions were transformed into the LCCS. A traverse adjustment constrained on the four GPS benchmarks with proper precision accounting for the geoid undulation was calculated. Finally, the LCCS positions (see table 6.7) and the covariance matrices of the existing benchmarks in the OPERA hall were transformed into ETRF2000. The resulting positions measured in the geodetic survey are shown in figure 6.5, among the six measured positions (PGs) of the OPERA network reference points, four were retained for the global calculation (they are called 5001, 5002, 5005 and 5006 and correspond to PG14, PG8, PG7 and PG13), their resulting ETRF2000 positions as well as the covariance matrix are reported in table 6.4.

6.2 Geodesy at CERN

At CERN the proton beam is transported through the transfer line TT41 to the CNGS target T40. Protons are extracted from the SPS accelerator by a fast

[4]Bernese software v5.0

[5]EUREF (Reference Frame Sub Commission for Europe) Permanent Network, http://www.epncb.oma.be/

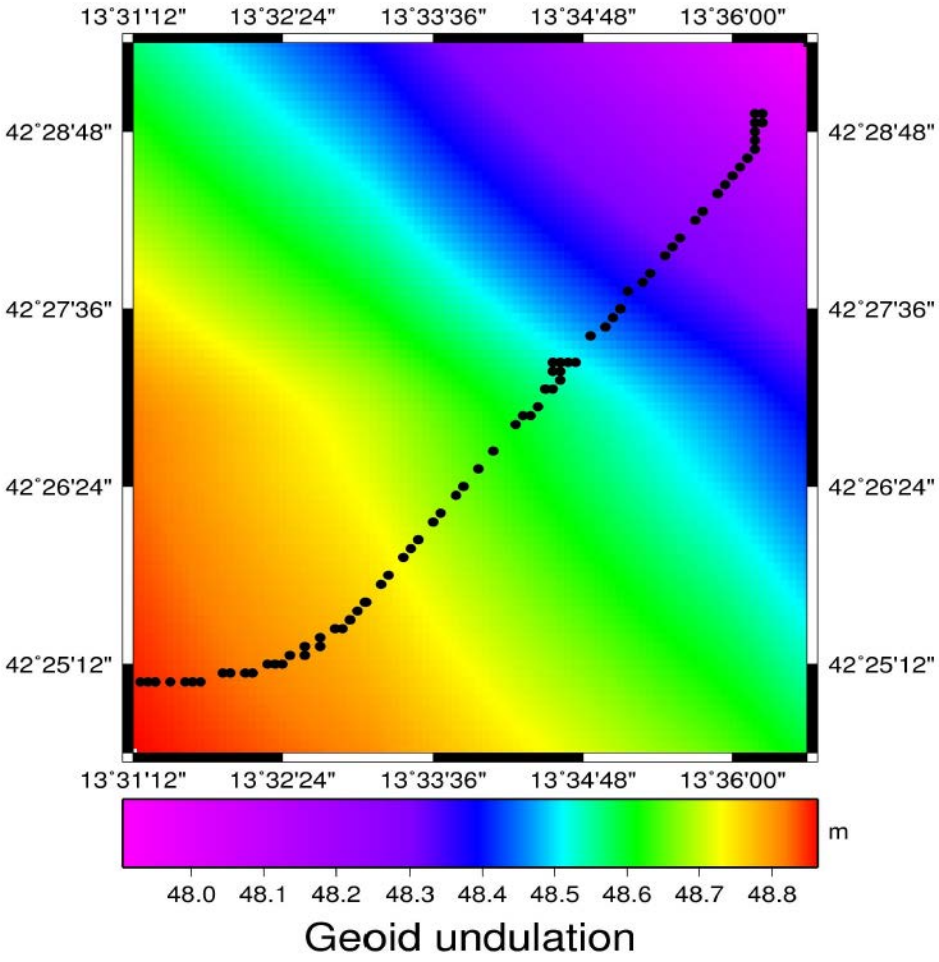

Figure 6.5: *Measured position in the geodetic survey at Gran Sasso.*

Benchmark	X (m)	Y (m)	Z (m)
5001 = PG14	4582171.473	1106530.193	4283594.959
5002 = PG8	4582169.560	1106522.390	4283599.006
5005 = PG7	4582171.539	1106520.975	4283597.248
5006 = PG13	4582173.450	1106528.787	4283593.216

Mean Covariance Matrix (mm^2)				Mean St. Dev. (mm)
X	14037	-8170	-12670	118
Y	-8170	5565	7293	75
Z	-12670	7293	11732	108

Table 6.4: *ETRF2000 positions and precisions of the benchmarks in the OPERA hall.*

extraction system, this extraction system is feeding both the line to LHC (TI8) as well as the TT41 transfer line to the CNGS target. The common part of TI8 and TT41, the first 150 metres from the point of extraction, is called TT40. The target consists of a series of graphite rods, the focal point of T40 is in the CNGS

target after the first rods. The underground structure as well as the CNGS target chamber with the T40 focal point are illustrated in figure 6.6 The coordinates of the T40 focal point given in reference system ITRF97 epoch 98.5 (see Appendix B) with 4 cm accuracy are:

$$\begin{array}{ccc} \text{X (m)} & \text{Y (m)} & \text{Z (m)} \\ 4394369.15 & 467747.94 & 4584236.23 \end{array} \tag{6.1}$$

This point has been then transformed from ITRF97 to ETRF2000 at the same epoch by using the official Boucher-Altamimi transformation (see Appendix B). Afterwards another transformation (with official EPN software) has been performed using for the velocity information the permanent Zimmerwald station (in Bern) in order to obtain the coordinates in ETRF2000 epoch 2008.0. The transformation accuracy was about 5 cm. The results of these transformations are summarized in table 6.5.

Reference	Epoch	X (m)	Y (m)	Z (m)
T40 in ITRF97	1998.5	4394369.15	467747.94	4584236.23
T40 in ITRF2000	1998.5	4394369.14	467747.93	4584236.24
T40 in ETRF2000	1998.5	4394369.32	467747.80	4584236.09
T40 in ETRF2000	2008.0	4394369.33	467747.80	4584236.11

Table 6.5: *T40 coordinates transformations.*

6.3 CERN-Gran Sasso Distance Computation

In table 6.6 are presented the four considered points in the OPERA reference system as measured with the LEICA CCR.

Point	X (cm)	Y (cm)	Z (cm)
PG14	-329.3649	-90.9705	1161.3798
PG8	-328.8763	-90.1183	261.7679
PG7	-628.9908	-91.3842	260.1652
PG13	-628.1278	-91.1725	1159.8059

Table 6.6: *List of the measured points in the OPERA network of reference points.*

The same points measured in LCCS during the geodesy survey at LNGS resulted as in table 6.7.

BY using this information the reference point A1 (the origin of the OPERA reference system) located in the OPERA detector (see figure 6.7) has been expressed

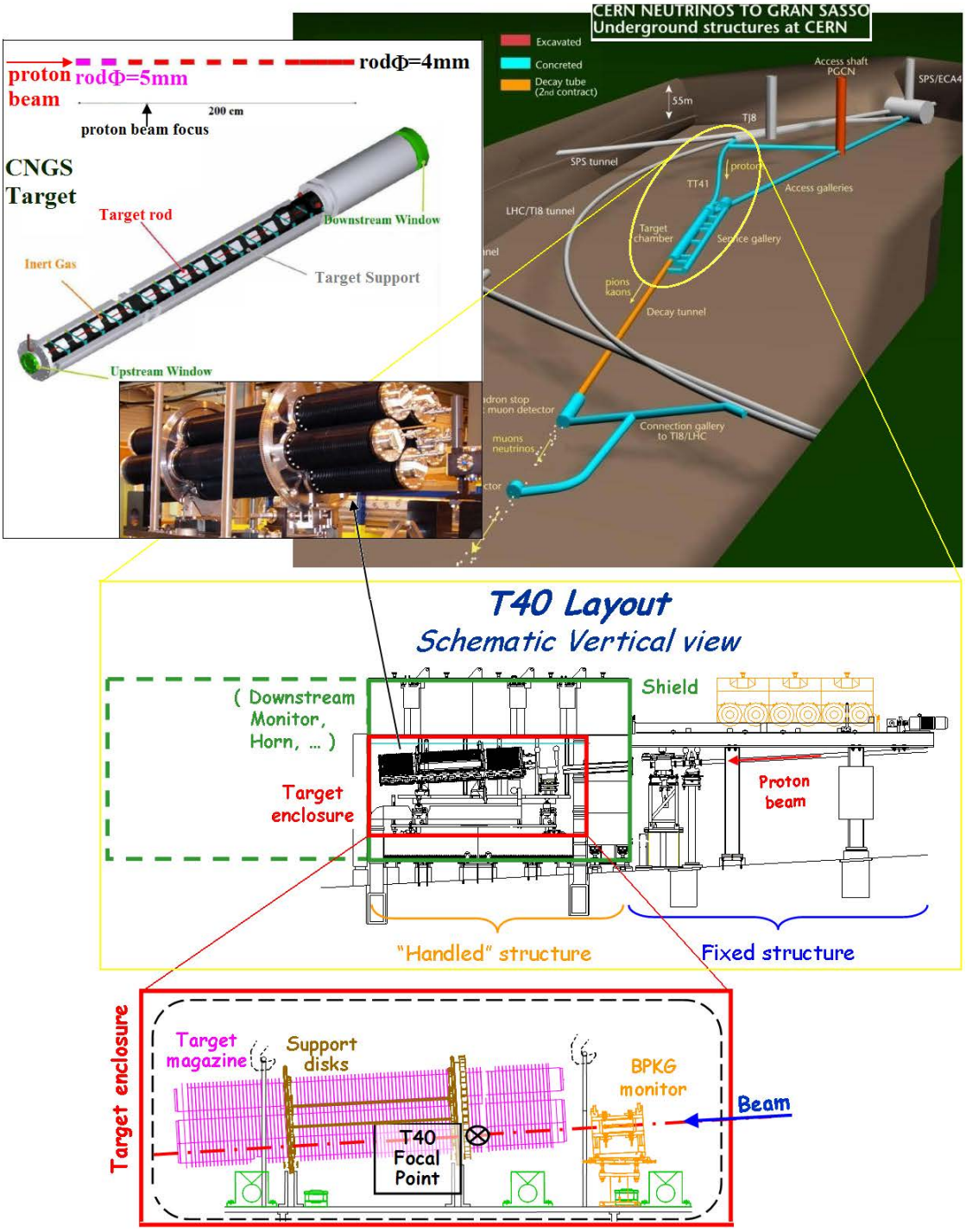

Figure 6.6: *Schematic view of the CERN underground beam lines structure. The protons extracted from the SPS are directed through TT41 line to the CNGS target. The target chamber is situated in T40, the T40 focal point is placed between the rods of the CNGS graphite target. A picture of the CNGS target is presented in the upper part on the left as well as a scheme of the carbon rods. In the bottom part is shown a zoom of T40 where the T40 focal point in the target is indicated.*

Point	East(m)	North(m)	Up(m)
5001	3157.98	-2240.71	74.33
5002	3152.50	-2247.85	74.34
5005	3154.87	-2249.69	74.33
5006	3160.34	-2242.55	74.33

Table 6.7: *List of reference points of OPERA in LCCS during the geodesy measurements at LNGS.*

in the local system by using two independent transformations which were compatible at the level of a tenth of a millimeter as shown in table 6.8.

Transformation	East (mm)	North (mm)	Up (mm)
A1 first	3148299.015	-2247923.985	75240.779
A1 second	3148299.003	-2247923.957	75240.713

Table 6.8: *Reference OPERA point A1 in LCCS. The first and the second transformations are independent and in agreement at the level of tenth of mm.*

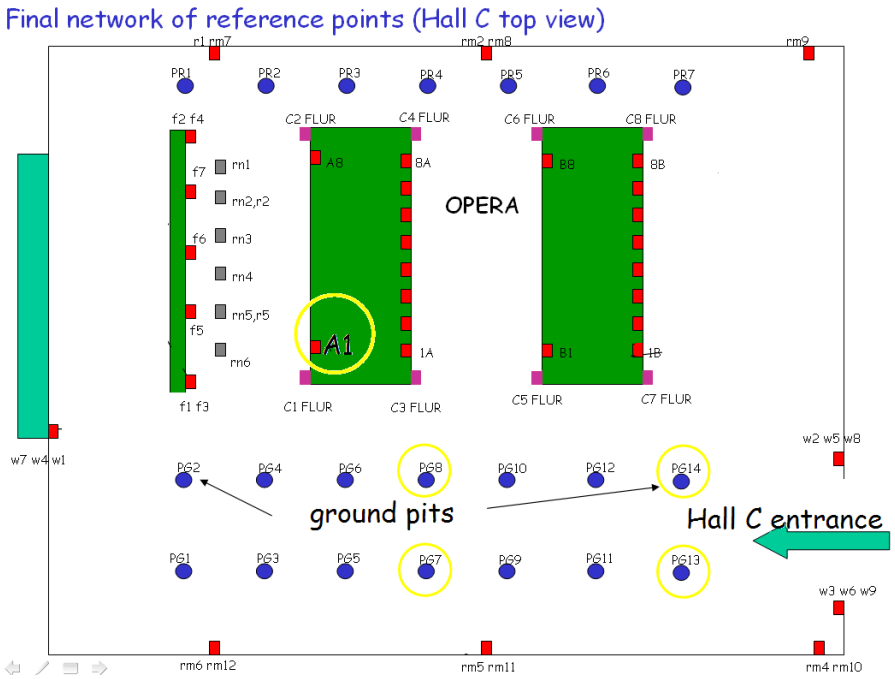

Figure 6.7: *Scheme showing the measured points in the OPERA reference system labelled PG7, PG8, PG13 and PG14 and the reference point A1 in the OPERA detector.*

The coordinates of the point A1 were then transformed in ETRF2000 epoch 2008.0 in order to compute the distance between the reference point at CERN, the focal

point T40 and the reference point A1 in the OPERA detector:

ETRF2000	X (m)	Y (m)	Z (m)
A1 at LNGS	4582167.465	1106521.805	4283602.71
T40 at CERN	4394369.33	467747.795	4584236.11

(6.2)

The resulting distance T40-A1 is then 730534.61 m, with a global accuracy of 20 cm. The distance of the CNGS target to the current transformer BCT (BFCTI400344) is 743.4 m.

The new geodesy measurements linked the reference points on the CNGS line to the OPERA reference system. By expressing these points in the OPERA coordinates it is possible to compute the extrapolation along the beam axis up to the position of the A1 reference point and the beam angles with respect to the OPERA reference frame. In the OPERA reference frame Z is the horizontal coordinate along the beam direction. The frame is right-handed (the X axis is also horizontal and corresponds to the basement of the magnet of the first supermodule, Y is the vertical axis). The XY plane is practically perpendicular to the beam direction. The reference point A1 is the origin of this system.
The result is the following (see figure 6.1):

a The extrapolation of the beam at Z=0 (the A1 reference point) corresponds to X=-86±0.4m and Y=2.6±0.4m. The beam is centered in the Hall B, which is the central Hall of LNGS. This is perfectly corresponding to expectations of the original beam design.

b The beam angle in the XZ plane is -4.4758 mrad which is good agreement with the expectation that the LNGS halls were built aligned with the direction of a future beam coming from CERN. In fact previous verifications based on the old LNGS reference points A-E were indicating that the beam angle with respect to AB (which should be representative of the Hall B axis) was -3.14 mrad. The residual difference with respect to -4.47 mrad comes from the alignment and definition of the Hall C axis with respect to the points AB and the positioning of the OPERA detector with respect to the Hall C axis.

c The beam angle on the YZ plane is 58.113 mrad, as expected from the Earth geometry.

The geodesy measurements, in addition to providing the exact distance between OPERA and the neutrino target, validated the expectations on the good accuracy of the CNGS beam pointing.

Chapter 7

Event Selection

7.1 Generic Selection of On-Time Events in OPERA

The selection of on time events is made in order to tag the OPERA events correlated with the beam activity. This selection is based on loose criteria and on an approximate value of the TOF evaluated in 2006 and the various delays of the timing distribution chain. The selection is based on the time tagging provided by the standard LNGS clock which has an accuracy of about 100 ns. This procedure provides an approximate UTC time corresponding to the start of the spill. The event selection is routinely applied in the on-line OPERA data treatment and it provides a sample of on time events which is the basis of our analysis. The events belonging to this sample are recorded with a time delay value t_{OPERA} referred to the approximate start of the spill. The approximate start of the extraction is computed in the following way:

1. Each extraction is UTC time tagged in the CERN DB thanks to a signal related to the kicker pulse (see chapter 4.1). The variable with the time tag information is called

   SE.CNGS-BEAM-TIME:GPSTIMING_EXTR1
   (SE.CNGS-BEAM-TIME:GPSTIMING_EXTR2),

   for the first(second) extraction. In first approximation it is assumed that the start of the extraction corresponds to this UTC time.
2. This UTC time is corrected by the following factors, in order to take into account the neutrino TOF (assuming the speed of light) and to transport it at the level of the OPERA DAQ system:

a) The TOF from the kicker to OPERA is ∼2.4 ms (2.440.079 ns). This value is calculated considering the neutrinos travel path from the CNGS target to OPERA and velocity c=299.792.458 m/s. The distance from the kicker to the graphite target is travelled by protons of 400 GeV/c that have a β differing from 1 by $3{\cdot}10^{-6}$, which is a negligible effect.

b) The intercalibration between the CERN clocks and the LNGS clocks: 353 ns.

c) The delay due to the fibers that distribute the signal underground: 40993.4 ns.

d) The delays related to the DAQ electronics: 4245.2 ns.

3. The corrected UTC time corresponding to the start of the extraction is subtracted from the UTC time provided by the OPERA DAQ time tag of the event that corresponds to the time of the earliest hit in the OPERA detector. If the difference is within ±20 μs the event is considered on time and attributed at the corresponding CNGS extraction. The event is recorded with the value of the time difference which will be defined from this point onwards as $\Delta tof(data)$

These data will be used in the data analysis (in chapter 8) in order to compute the delay w.r.t. the waveform digitizer data. It is clear that this procedure corresponds just to an approximate evaluation of the delays and the time of flight, however all the analysis procedures are performed by using these data with the intention to apply the precise corrections just at the level of the final result. All the precise corrections will be summarized in a global shift to be applied to the result computed in chapter 8.

7.2 Event Selection

In figure 7.1 is shown the experiment display reproducing the detector horizontal and vertical view of a charged current candidate event recorded by OPERA, the active target area is represented in light gray.

The time stamp of the energy deposition is recorded at the level of the photomultiplier reading groups, with 64 strips belonging to the same plane. The RPC sub-detectors have as well a clock time stamp.

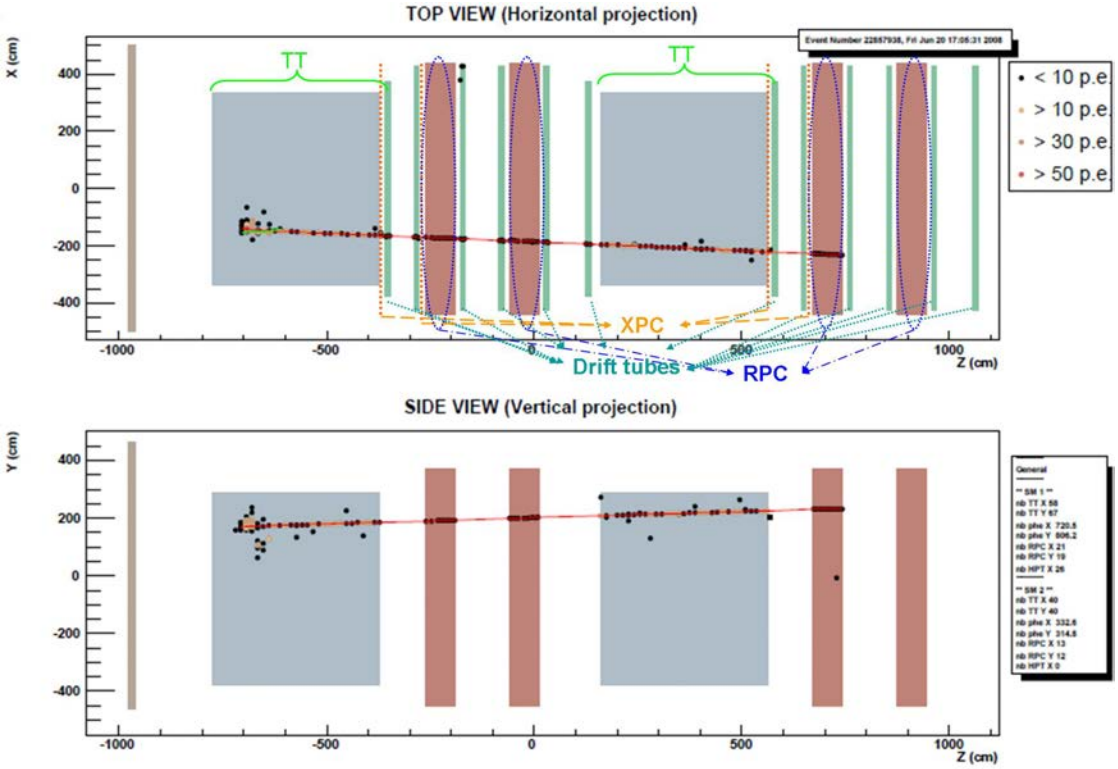

Figure 7.1: *Charged current event as viewed in the experiment display reproducing the detector components in the horizontal and vertical projections. The CNGS beam comes almost horizontally from the left side.*

As shown in the display, particle tracking can be performed (a muon track is reconstructed in red). When a muon three dimensional track is correctly reconstructed and it is crossing the spectrometer, it is then possible to determine its sign by using the information of the trajectory deflection in the magnetic field.
Simulated events have the same digit information as the real events (see chapter 4.3), but in addition also the MC information used to simulate the energy deposition is available and it is organized in "hits". MC hits bring also the information on the "true" interaction time of the particles before effects related to the detector response and the DAQ system.

A MC study has been performed in order to evaluate systematic effects related to the assignment of the events UTC time stamp, and to define the final data sample of the neutrino velocity measurement.

CNGS neutrinos can also interact in the materials surrounding the OPERA detector and then project particles which are detected in OPERA, in this case the travelled path of the particles will be different from a straight line extrapolation joining the earliest detected digit in OPERA to the neutrinos source at CERN.

These interactions in the Hall C of the LNGS ("external" events) have been simulated and analysed to determine the time of flight (TOF) difference with respect to real path of the particle produced by the interaction of a beam neutrino outside the detector volume and detected as a neutrino interaction in the OPERA target in the first hit position. Another contribution to the time resolution comes from the detector response and from the DAQ chain, this effect is fully accounted in the simulation.
The time spread between the earliest hit and the earliest digit of the events has been calculated considering neutrino interactions simulated in the detector volume ("internal" events) in order to evaluate resolution effects.
The OPERA events are reconstructed by a software that includes an offline algorithm (OpCarac) that classifies automatically their typology and disentagles those occurring in the OPERA target from the external ones [58]. A data sample has been extracted over the data collected for the neutrino velocity measurements during the 2009 and 2010 CNGS run periods, taking into account the OpCarac classification.

7.2.1 MC Study on External Events

MC samples of ν_μ CC interactions in the surrounding material of the OPERA detector have been studied in order to evaluate the TOF difference (Δt_{tof}) between the real path of the particle seen in the detector ($t_{particle}$) and the hypothetic path obtained assuming that the earliest hit seen in the detector was generated directly by a neutrino of the beam (t_ν) travelling from the CNGS setup down to the earlies hit point in OPERA, see figure 7.2 a. The MC events studied refer to the LNGS Hall C geometry described in [59], details of the materials surrounding the OPERA detector are presented in figure 7.2 b. The materials that occupy the hall C of LNGS besides the OPERA detector are the Borexino detector and its auxiliary facilities upstream of OPERA and the concrete shielding that covers the rock. A volume of rock having the shape of a cylinder of 35 m radius and surrounding the hall is included in the description. It is extended towards the front and the back of the hall. The number of MC events simulated are summarized in table 7.1, they are interactions in the concrete materials and in the rock volumes sorrounding the detector (these volumes are called SHIELD,ROCKS, ROCS and FOOT as showed in figure 7.2 b).

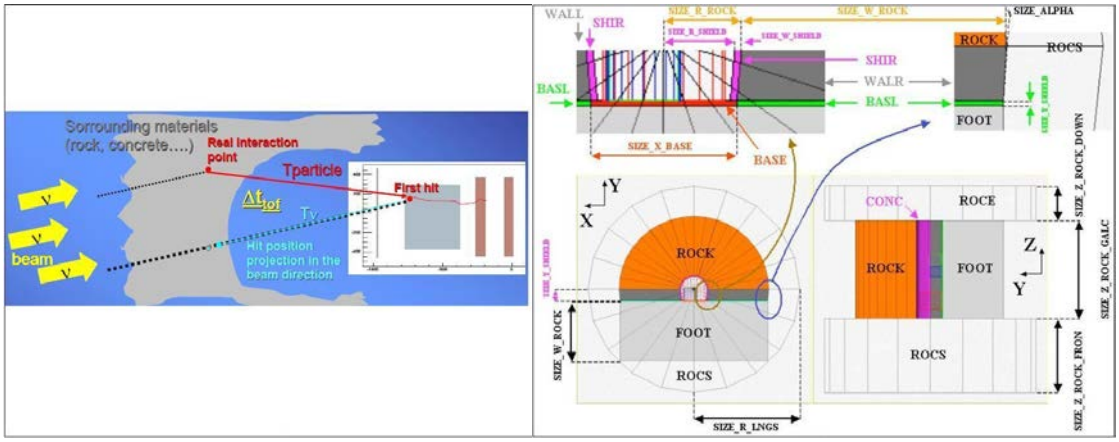

(a) **(b)**

Figure 7.2: *a) Δt_{tof}=t_ν-$t_{particle}$ is obtained considering the projection of the neutrino in the the beam direction and in the particle interaction point x in the detector. b) Front view and rotated side view of rock, base, and shielding volumes.*

The Δt_{tof}=t_ν-$t_{particle}$ has been calculated considering the projection of a neutrino interaction point in the beam direction starting from the earliest hit recorded in the OPERA detector, the CNGS has a tilt of 52 mrad [1] in the vertical projection w.r.t. the OPERA detector, so that the extrapolated positions in the beam direction are:

$$\begin{cases} z_n = z_i, \\ x_n = x_p, \\ y_n = y_p + (z_i - z_p) \cdot \tan(0.052), \end{cases} \tag{7.1}$$

where (x_i, y_i, z_i) is the position of the real neutrino interaction point in the material surrounding the detector and (x_p, y_p, z_p) is the position of the earliest hit recorded in the detector. In figure 7.3 are shown as example the extrapolated interaction points of FOOT and ROCS events.

The Δt_{tof} distributions are obtained considering the time tag of the event's earliest hit in the target trackers or in the RPCs of the detector. In figure 7.4 are shown two examples of the Δt_{tof} calculated: since the mean values are much larger than the 10 ns aimed for the accuracy on the neutrino velocity measurement, as a second step only interactions producing a three dimensional muon track reconstructed by the reconstruction software have been selected. The TOF spread in these cases is less than 10 ns also taking into account the respective RMS values, as presented in figure 7.5. Furthermore, these distributions are obtained considering only the first hit produced by a particle in the target trackers, in order to avoid

[1] The value of the tilt considered is 52 mrad since this calculations were performed before the 2010 geodesy measurements. It was chosen this value from the distribution of the vertical projection angle of the tracks measured in the CS scanning [45].

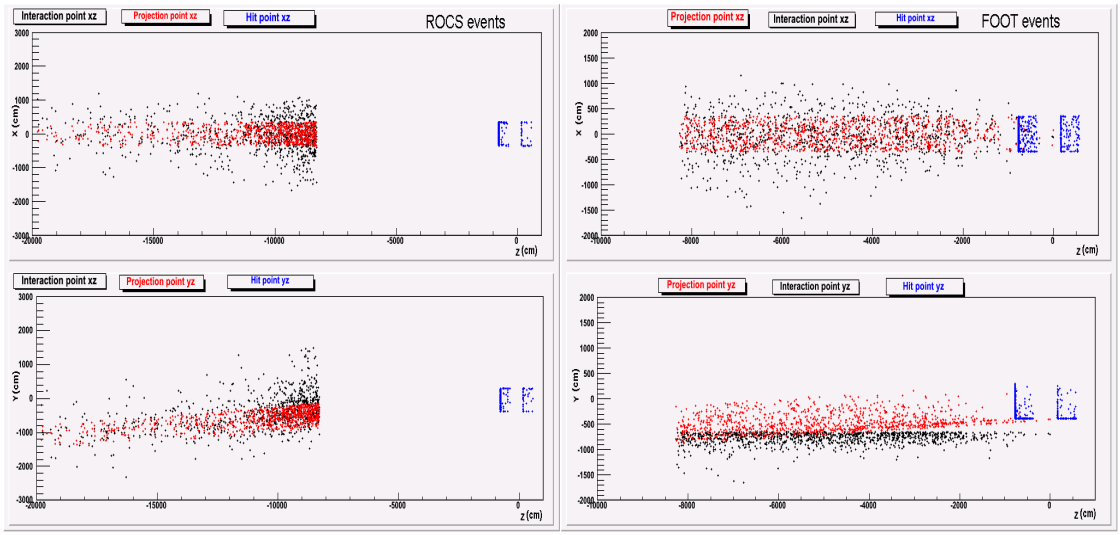

Figure 7.3: *extrapolated interaction points in the beam direction of MC external events. On the left are shown the interactions occurring in the rock surrounding the LNGS Hall C (in black), the corresponding earliest hits in the opera detector (in blue) and their projections in the beam direction (in red). On the right are shown the MC interactions simulated in the base rock of the LNGS Hall C (the color labels are the same).*

the inefficiencies of the RPCs timing, not yet well calibrated. The various MC samples of external interactions were weighed by the known weight values of the corresponding materials (see table 7.1).

MC external interactions	Number of events	Weight
SHIELD (concrete)	11666	0.209039
ROCKS (rock)	248	0.388991
ROCS (rock)	1700	0.873931
FOOT (rock)	1965	0.327635

Table 7.1: *MC events of simulated interactions in the materials surrounding the OPERA detector.*

By taking into account the simulation results of the various sub-samples and their weight in the final selected sample, a systematic error of 2 ns related to the event selection procedure has been estimated.

7.2.2 MC Study on Internal Events

A study on the interactions that occur in the OPERA detector volume has also been performed: 5000 MC ν_μ CC events have been analysed to evaluate the time delay distribution between the earliest hit and the earliest digit of the events in order to correct for this measurement delay the real OPERA data, where only the

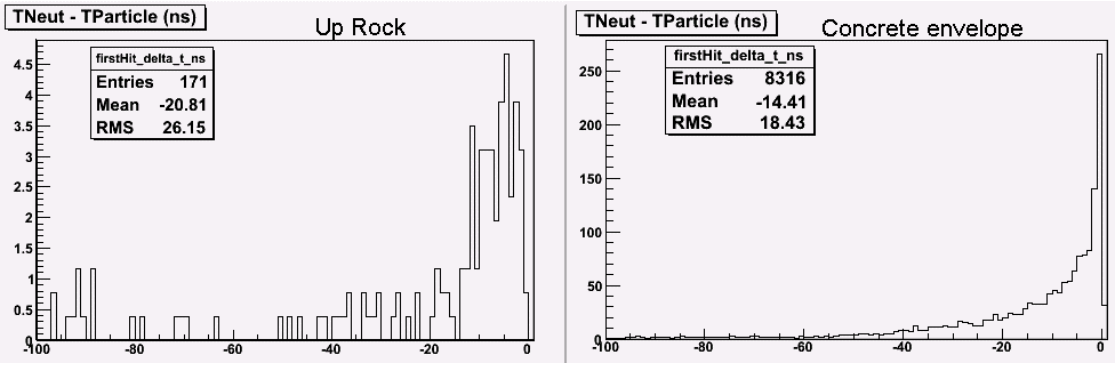

Figure 7.4: *Δt_{tof} distributions for interactions occurred in the materials surrounding the OPERA detector. Left: interactions in the rock volume above the detector, right: interactions in the shielding volume.*

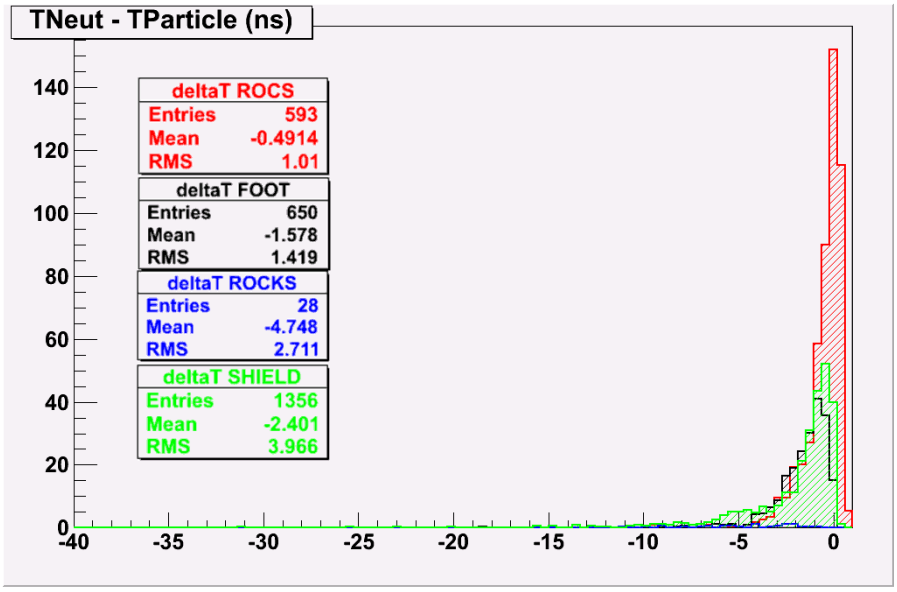

Figure 7.5: *Δt_{tof} distributions for interactions occurred in the materials surrounding the OPERA detector, the events selected have at least one muon track reconstructed in the OPERA detector and the TOF spread is computed considering only the earliest hits in the target trackers.*

digit information is available. The MC takes into account all the effects concerning the light emission, propagation and electronic chain response described in chapter 4.3. The delay was calculated considering the target trackers hits and digits, the first selected hit is not necessarily corresponding to the first selected digit of the event.

The event time for the real data is the time of the first digit recorded by the DAQ, the acquisition cycle is 10 ns quantized, this structure is reproduced in the time spread obtained as shown in figure 7.6.

The simulation takes into account the delays in the time distribution chain in-

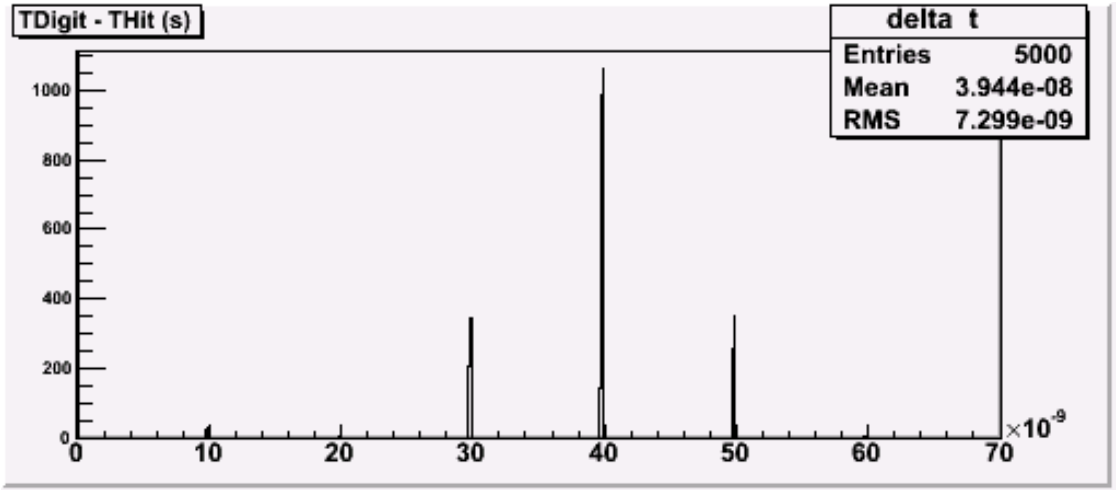

Figure 7.6: *Distribution of the time delay between the first digit and the first hit of the MC interactions in the target trackers of the OPERA detector. The average delay obtained is ∼39 ns with a spread of 7 ns. The MC includes for technical reasons an arbitrary shift of 30 ns which has to be subtracted from this result.*

cluding terms which are not completely compensated by the DAQ system: namely the extra 5 ns cable delay for the sensors around the corner of a plane, the delays in the daisy chain of the master clock cards and the extra cables for the last two planes of each TT. The missing compensation of these timing distribution delays by the DAQ system, in the real data as well in the simulated data brings to the fact that some sensors have their internal clocks not perfectly aligned with respect to the majority of the other sensors and so sligthly anticipating the real time, since they received a delayed synchronization signal. This brings in having in a few cases a negative delay between the measured time of the first hit and the real time the interaction occurred. Since the simulation reproduces completely what happens in the data, the simulation results are used in order to take these effects into account.

The overall delay between the time at which the earliest energy deposition happens in the OPERA detector and the time of the earliest digit corresponds on average to 9.4 ns with a spread of 7 ns. In addition there are 10.9 ns of delay to take into account since the simulation software does not take into account the transit time in the PMT of the target trackers [51].
By considering the result of the simulation and the transit time of the PMT the overall delay due to the response of the OPERA detector is 9.4 + 10.9 = 20.3 ns. This average delay matters in the neutrino velocity measurement, while the spread will just average out on the large sample of events which has been selected.

7.2.3 Selection Algorithm based on the OpCarac Classification

According to the OpCarac algorithm the events on time with the CNGS beam are identified as follows:

- FRONTMUON: events produced by a neutrino interaction outside the detector volume and containing at least one long track left by a penetrating particle and thus compatible with that of a muon. The first hits recorded are in the first two TT planes of the first TT module.
- SIDEMUON: events produced by a neutrino interaction outside the detector volume and containing at least one muon track starting within the target boundaries in the longitudinal coordinate (Z) and within some border areas at the edge of the target in the transverse coordinates (X and Y).
- SPECTRO: events produced by a neutrino interaction in the iron of one of the two spectrometers of the OPERA detector.
- CONTAINED: events with or without muons produced by an interaction in the lead material of the detector (first hits are seen by the TT).
- BORDERSOFTNC: Contained events without reconstructed tracks with the hits centroid near the detector boundaries (X position within 2 bricks distance, Y position within 3 bricks distance).
- NODECISION: All other events not classified in any of the previous types. In particular the following cases: events produced by an interaction neither in the lead nor in the spectrometers iron (typically in the HPTs), NC events with a significant number of hits in some area of the detector not filled with bricks, events with hits only in one of the two projections (X or Y) or events with a track reconstructed with the start point or the end point in different supermodules in the two projections.

Examples of the CONTAINED, FRONTMUON and SIDEMUON topologies are shown in figure 7.7.

For the 2009 run 21440 OPERA on-time events have been considered, and 24371 for the 2010 (see chapter 8.1).
Among these, there is the common view GPS information in 13682 cases for the 2009, and 13679 were found in the on-time events reconstructed with the OPERA reconstruction software. The data sample is extracted starting from these events

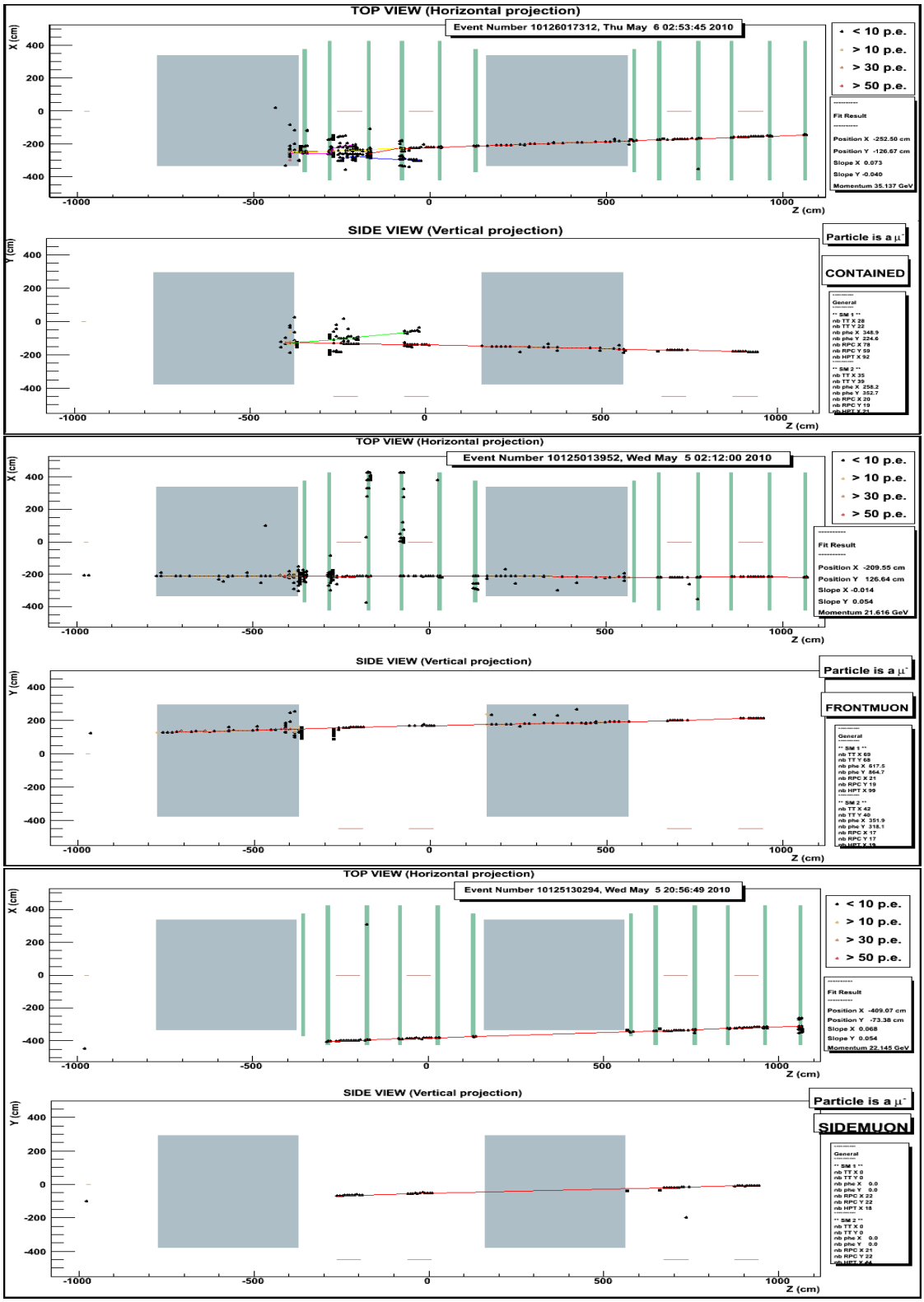

Figure 7.7: *Example of a CONTAINED (top), FRONTMUON (middle) and SIDEMUON (bottom) event, as classified by OpCarac.*

following an algorithm based on the classification of OpCarac as follows.
The high accuracy GPS event time correction is applied on all the CONTAINED events (2246 events in 2009), as well as to other events selected as reported below. The SIDEMUON and the FRONTMUON events are analysed in more detail, taking into account the considerations and the results presented in the section on the MC study on external events. The fraction of events with only RPCs digits (tracks passing only through the spectrometers) are discarded, since the timing calibration is not exactly known at the moment. Besides the OpCarac classification, more severe cuts are applied by the OPERA reconstruction software on the reconstructed tracks to find the associated particle. In particular, it is explicitly required that a 3D track is reconstructed and that it is compatible with that of a muon.
The other types of events are discarded. The number of events for each category is summarized in table 7.2.

The resulting number of the 2009 OPERA events on which is possible to apply time corrections is then 4553.

Among the OPERA events considered in 2010 the selection algorithm retained 8199 events, as summarized in table 7.3, 7693 of these had the common view GPS information.

OpCarac Type	Number of events	Selection
CONTAINED	2246	kept
SIDEMUON	3477	kept in 2307 / 7367 cases
FRONTMUON	3890	(3D μ track)
SPECTRO	1683	discarded
BORDERSOFTNC	245	discarded
NODECISION	2138	discarded

Table 7.2: *Number of events for each OpCarac type analysed, 2009 data sample.*

OpCarac Type	Number of events	Selection
CONTAINED	3844	kept
SIDEMUON	5720	kept in 4355 / 12641 cases
FRONTMUON	6921	(3D μ track)
SPECTRO	2756	discarded
BORDERSOFTNC	418	discarded
NODECISION	4712	discarded

Table 7.3: *Number of events for each OpCarac type analysed, 2010 data sample.*

Then, the events with an incorrect timing correction value (see chapter 4.5), were

discarded, so that the final data sample for the 2010 run is composed by 3830 events for the first extraction and 3827 events for the second extraction.
Also for the 2009 run the data sample was cleaned and the resulting number of retained events is 1931 for the first extraction and 2036 for the second extraction. The OpCarac classification of the final data samples is presented in table 7.4

OpCarac Type	Number of events 2009	Number of events 2010	Number of events 2009+2010
CONTAINED	1956	3590	5546
SIDEMUON	557	1128	1685
FRONTMUON	1454	2939	4393
Total	3967	7657	11624

Table 7.4: *Number of events for each OpCarac type for the 2009 and 2010 final data samples.*

For these samples, about 48% are internal interactions. The complementary events have an uncorrected average bias of about 2 ns, this effect was evaluated with the simulation of external interactions and takes into account both the path differences between a neutrino coming from the target and the real one and the β of the particle emitted in the external interaction. As reported before, the systematic error related to the event selection procedure was evaluated to be within these 2 ns.

Chapter 8

Data Analysis

By comparing the timing information expressed in the Coordinated Universal Time (UTC timestamp) of the events recorded by the OPERA DAQ with the ones of the proton extraction from the SPS it is possible to select the events on time with the CNGS beam.

The internal time structure of the CNGS spills is not flat but depends on how the proton beam is shaved by an electrostatic septum at the extraction from the PS for the injection in the SPS (usually performed in five turns). The SPS RF structure results in bunches of $\sim$2 ns (at 4σ) every 5 ns. The CNGS neutrinos generated by the SPS proton beam will have the same time distribution as the protons. The uncertainty on the knowledge of the decay point of the secondary mesons generating the CNGS neutrinos does not introduce a significant degradation of the time distribution inherited from the protons, as presented in section 3.2.

The sampling window of the Fast Waveform Digitizer is triggered after a known delay by the kicker signal which is time stamped with UTC time. By taking into account all the corrections for the cable delays in the time distribution system at CERN and at Gran Sasso, and the TOF computed assuming the speed of light for the neutrinos, it makes sense to compare the time distributions of the protons and of the events recorded by the OPERA detector. If neutrino propagated with the speed of light the two distributions will coincide within fluctuations. More generally it is possible to compute the probability that the two distributions are identical in shape as a function of the parameter δ, which expresses the deviation

of the neutrino TOF w.r.t. the light TOF.

The disuniformities of the protons time distribution inside the spills can be exploited in the analysis of the recorded OPERA events since this kind of distribution brings more information than a flat distribution. In order to resolve the structure of the proton beam the FWD measures the proton pulse timing with a sampling of 1 ns.

The analysis is done separately for the first and for the second extraction in order to take into account the differences in shape and extraction time between the two. The best estimation of δ is obtained by maximizing a likelihood probability, in this case the data need not to be binned. This method is similar to that presented by the MINOS experiment for their measurement of the neutrino velocity.

8.1 OPERA Events and Data at CERN

The OPERA detector response to the energy deposition of the particles recorded by the DAQ system is organized in "digits" (see chapter 4.3), the UTC timestamp of the events recorded by OPERA (t_{OPERA}) corresponds to the timestamp of the earliest digit of the event.
For each recorded OPERA event it is possible to retrieve exactly the corresponding waveform of the proton pulse that has generated it, the proton time tag (t_{kicker}) is derived from the event time (t_{OPERA}) as below:

$$t_{kicker}=t_{OPERA}\text{-}\Delta tof(data) \text{ - C},$$

where $\Delta tof(data)$ is the event time distance from the closest extraction and C$\sim$2.4 ms, the neutrinos TOF, as already discussed in section 7.1. Since it is not possible to know exactly from which instant inside the proton pulse the neutrino is coming from, the time of flight analysis is performed on a statistical basis by putting together all the selected waveforms in order to obtain a model function of the protons time distribution that can be compared with the OPERA events time distribution. The proton time tag values are stored in the CERN database, as well as the Fast Waveform digitizer data. An example of a proton pulse recorded by the FWD is shown in figure 8.1.

More details about the statistics of these data samples are shown in figure 8.2: the available FWD data are less than the number of the ontime OPERA events because of some malfunctioning of the CNGS data logging and database system.

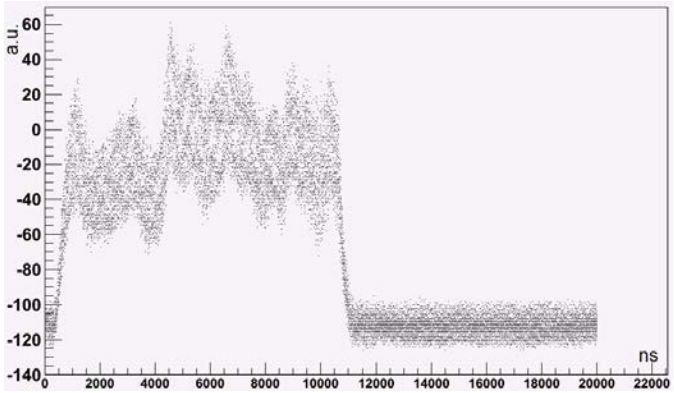

Figure 8.1: *Example of a proton pulse internal time structure as recorded by the FWD.*

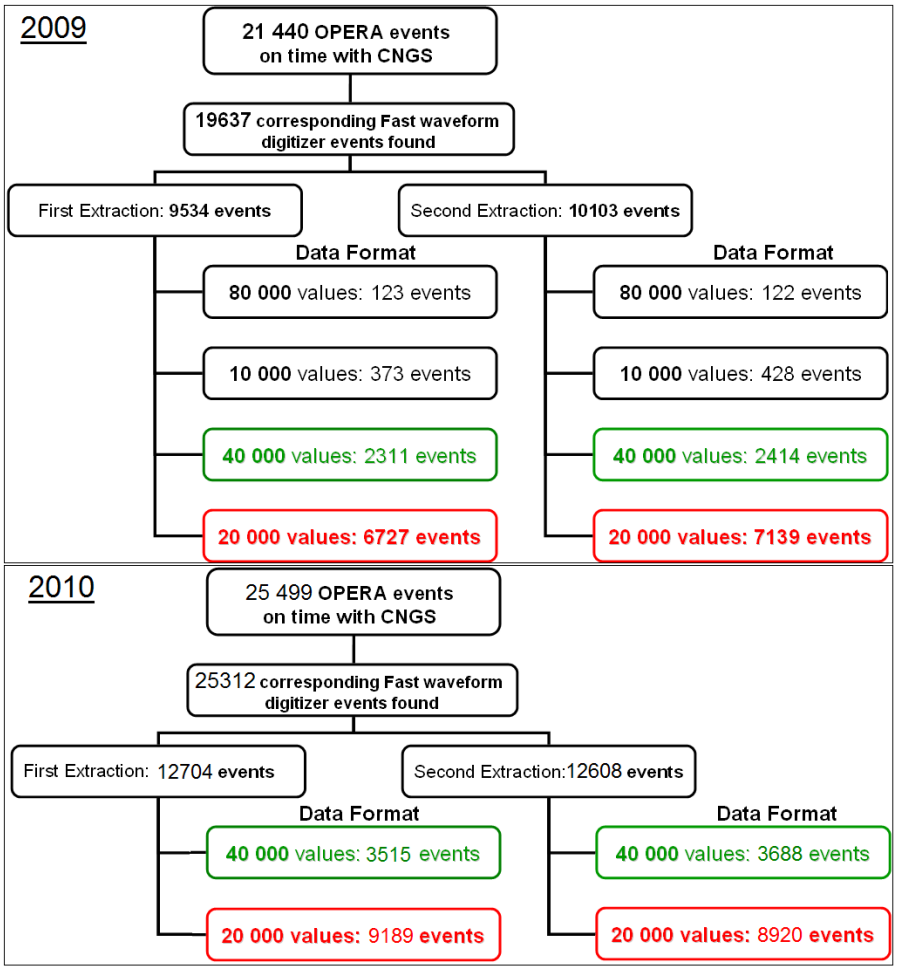

Figure 8.2: *Scheme of the collected statistics, the number of considered OPERA events and the number of events recorded by the FWD digitizer are presented. The data are then separated for the first and the second extraction and for their dataformat. Data with 20000 and 40000 values were used for the analysis, they are highlighted in green and red. Top: summary of the 2009 statistics. Bottom: statistics of 2010.*

Nominally the data variable logged in the CERN database containing the proton pulses as seen by the FWD has 20000 samples. In 2009, 13866 of these cases were

found, but in 245 cases waveforms had 80000 samples, in 801 cases 10000 samples and in 4725 cases 40000 samples. The few cases with 10000 and 80000 samples were due to some wrong data format settings in the FWD at the beginning of the 2009 run and had te be discarded. The data with 40000 samples were found to have both extractions attached together. By knowing the extraction number the waveforms could be split and completely recovered.
In total, 9038 events for the first extraction and 9553 events for the second extraction were used for the analysis. The same considerations are valid for what concerns the 2010 data: 12704 useful events for the first extraction and 12608 for the second one were collected. At the beginning of the 2010 run the setting of the fast waveform digitizer was not appropriate, causing a "saturation" in the logged waveforms, these cases were excluded from the analysis. At the end of the 2010 run some waveforms showed a strange "oscillating" behaviour and were discarded as well from the data sample. An example of each of these cases is shown in figure 8.3.

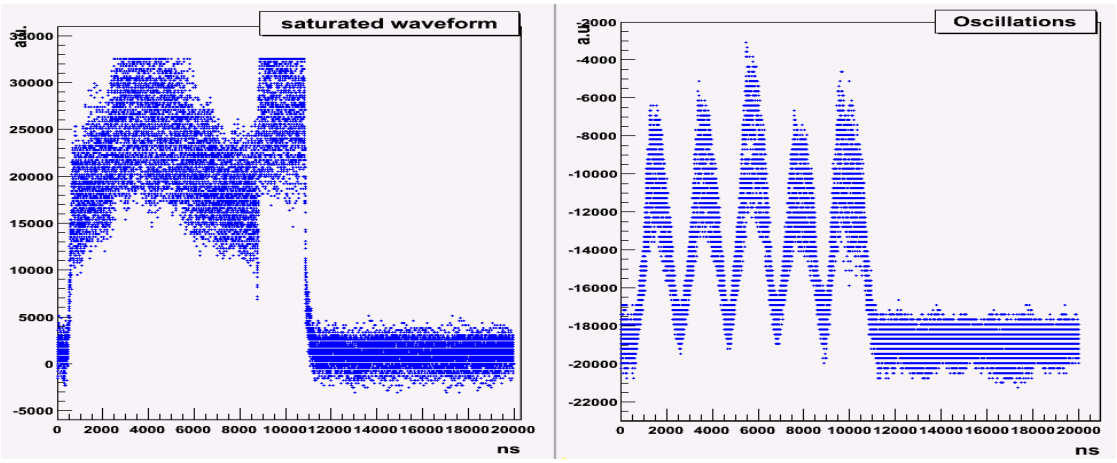

Figure 8.3: *Example of a "saturated" waveform (left), this was due to an erroneous fast waveform digitizer setting at the beginning of the 2010 run. Example of a waveform with a strange "oscillating" behaviour (right), these cases were found at the end of the 2010 run. These problematic waveforms were excluded from the data sample both for the first and for the second extraction.*

At the end, the number of retained waveforms in 2010 is 12240 for the first extraction and 12131 for the second extraction. The statistics of the waveforms retained for the analysis is summarized in table 8.1.

All waveforms are then summed up together separately for the first and for the second extraction in order to take into account the differences between the two in shape and in extraction time. The waveforms resulting from the sums are then

	First Extraction Number of waveforms	Second Extraction Number of waveforms
2009	9038	9553
2010	12240	12131
Total	21278	21684

Table 8.1: *Summary of the number of waveforms retained as data sample for the analysis.*

normalized to the number of corresponding events recorded in OPERA, in order to produce two global waveform functions to be used to analyse the entire OPERA data sample.

The resulting waveform functions however showed an internal oscillating structure which was investigated. By performing a Fourier transform these oscillations were found to correspond mostly to a 30ns/60ns structure, more visible at the edges. In 2010 the oscillation amplitude was larger. This is shown in figure 8.4, were the 2009 and 2010 waveforms functions are plotted as well as a zoom on the rising and falling edges.

In order to eliminate the oscillating internal structure of the waveform functions, which was not caused by the proton beam but that was due to a form of coherent noise synchronous with the beam, a filter has been applied by low-passing frequencies up to 8 MHz. Examples of the results after the filtering are shown in figure 8.5.

A measurement of the cosmic rays rate in a defined time window has been performed in order to evaluate the signal/background ratio in the extraction time window. The probability to have a background event from cosmic rays over 10 ns ris $3.4{\cdot}10^{-8}$ and the cosmic ray background is thus negligible.

For practical reasons a probability has been defined in absence of protons (outside the proton pulse), higher then the natural cosmic background contamination in order to get rid of small fluctuations of baseline of the waveform digitizer which could be misinterpreted as protons signal. This value corresponds to a baseline cut-off at the level of a $4{\cdot}10^{-6}$ threshold in a 10 ns bin. Indeed in the likelihood approach it is important, in the absence of protons, for the waveform to have a value different from zero in order to avoid mathematical divergences. The calculated probability (see equation 8.3), which is the product over all the observed events, would otherwise become zero if just a single event would occur outside the waveform (like it could happen for the cosmic ray background). It has been

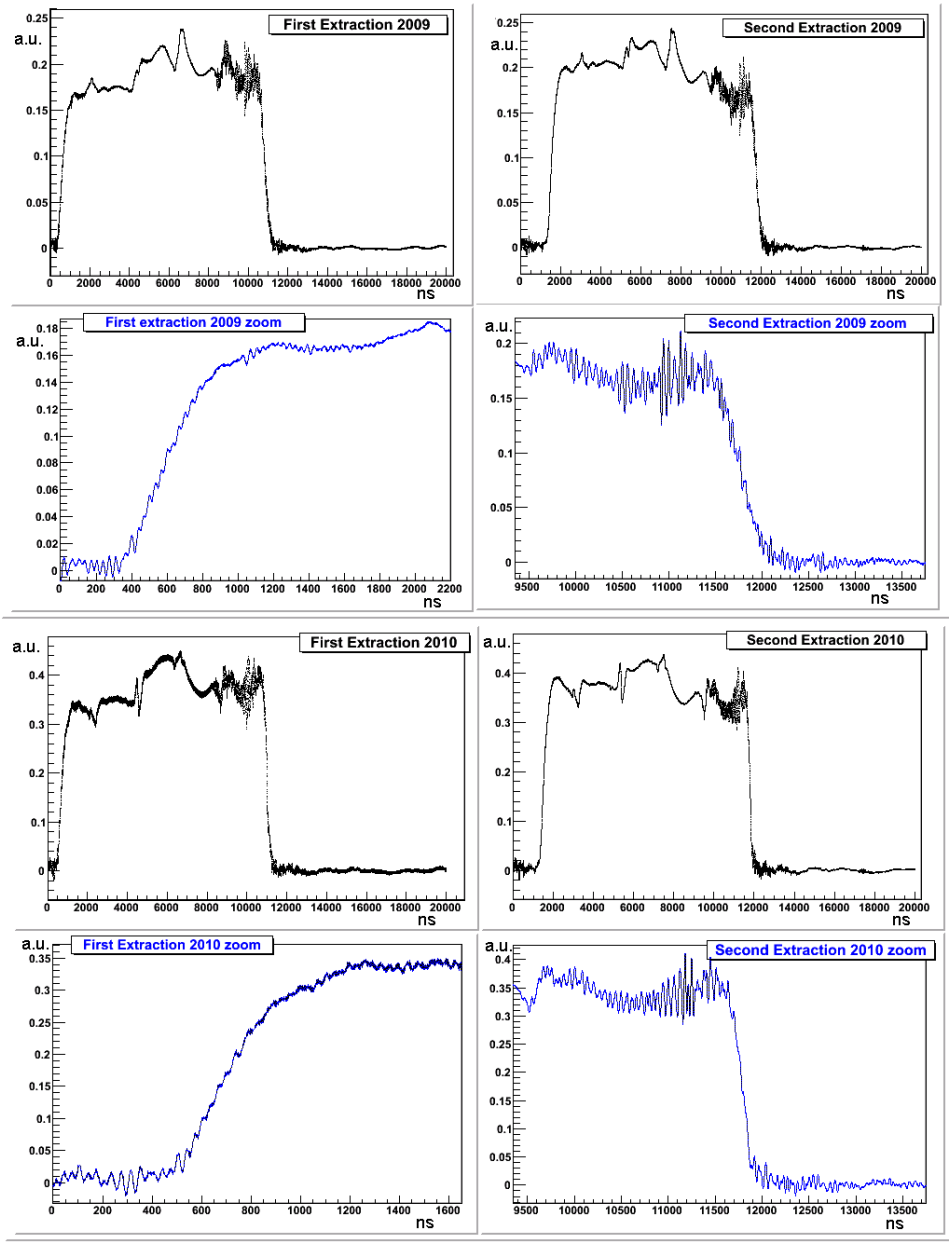

Figure 8.4: *Oscillating structure of the final waveform functions in 2009 (top) and 2010 (bottom) for both the extractions. A zoom of the rising and the falling edges is also shown, where the oscillation structure at 30/60 ns is more visible.*

checked that the value of the cut-off has not effect on the likelihood maximization. The final waveform functions are presented in figure 8.6, the differences between the two extractions are clearly visible, both in the starting time and in the structure of the proton pulses, as well as the fact that these waveforms slightly change with time and are different for the 2009 and 2010 samples.

In all the results which will be shown, the overlay of the waveform function with the neutrino time distribution deliberately does not take into account all the

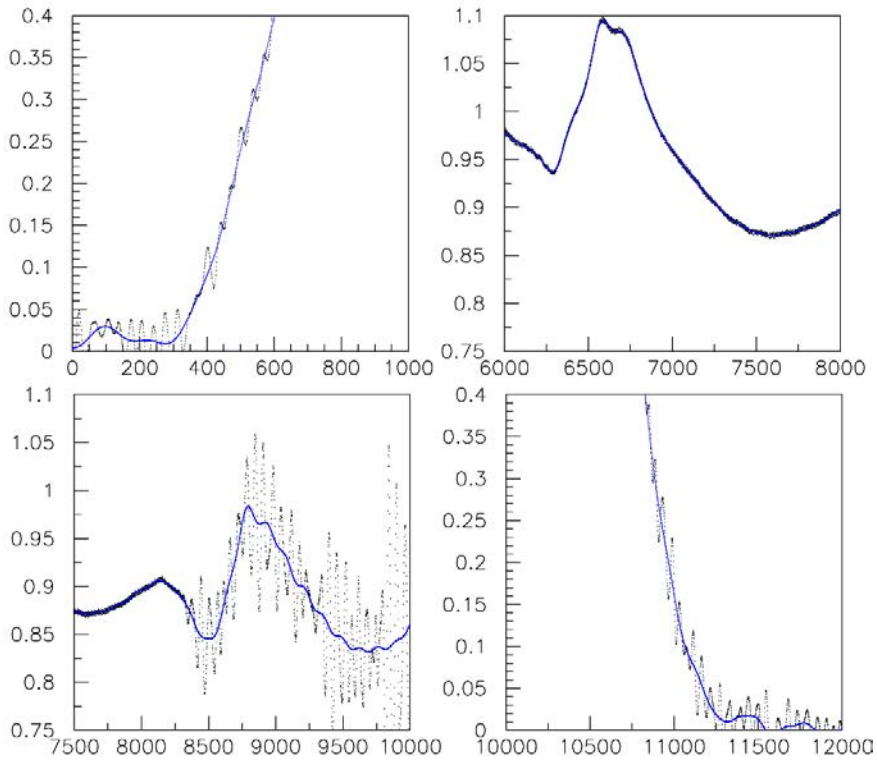

Figure 8.5: *Examples (zoom) of the filtering on the waveform functions, in blue the resulting function is shown while the original data are in black.*

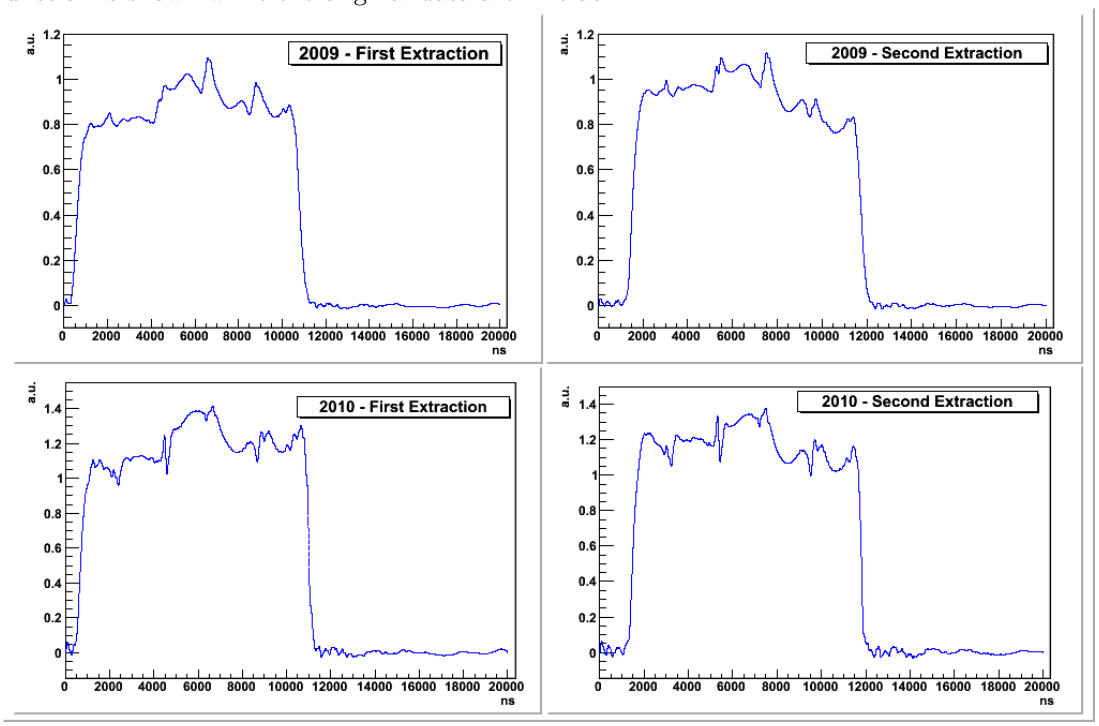

Figure 8.6: *Final waveform functions obtained with the 2009 and 2010 statistics. On the left the first extraction is shown and on the right the second extraction. The baselines show the fluctuations (higher than the cosmic background) which then is cut-off.*

calibration constants so that the determination of the δ parameter is biased by an arbitrary and unknown quantity. Some parts of the calibration chain are not considered in order to keep the analysis blind. Taking into account all the calibration constants, the value of δ will correspond to a deviation from the TOF of the light. The decision to unveil the results is subject to the a priori verification of the internal consistency of all the analysis ingredients and the goodness of each calibration measurement.

8.2 Extraction of the Best Time Shift Value by Using a Likelihood Maximization

The likelihood maximization [66] is a general method that uses the events individually and thus allows performing an unbinned analysis. In general by assuming that the probability density function which describes the data is $f(x|p)$, where x is a measurement and p a parameter (or more generally, a set of parameters, as the method can be extended to the case where more than one parameter fix the *pdf* and must be determined), so that the probability of obtaining x for a given p in the range from x_a to x_b is:

$$P(x) = \int_{x_a}^{x_b} f(x|p)dx, \tag{8.1}$$

the likelihood probability is then defined by:

$$\mathcal{L}(p) = \prod_i f(x_i|p), \tag{8.2}$$

for the given set of data $\{x_i\}$. Thus if we regard $f(x,p)$ as a function of x and p the *pdf* is for constant p while $\mathcal{L}$ is for fixed x. This means that $\mathcal{L}$ is the probability of observing $\{x_i\}$ for the specified p. The maximum likelihood method consits in estimating p by the value $\hat{p}$ that maximizes the likelihood function $\mathcal{L}(p)$.

In this study the likelihood probability $\mathcal{L}$ is a function of the single parameter δ, the time shift $\delta = t_{waveform} - \Delta tof(data)$. It represents the time value that has to be added to the time of the OPERA events time such that their distribution best coincide with the protons waveform. The probability $\mathcal{L}$ is defined as the product over all the observed events of the probabilities to obtain these events, starting from the waveform data:

$$\mathcal{L}(\delta) = \prod_i w(t_{OPERA} + \delta), \tag{8.3}$$

where w is the waveform model function as shown in figure 8.6 and t_{OPERA} our set of data.

It can be shown that, for a large number of experimental observations in the vicinity of the maximum, $\mathcal{L}(p)$ tends to a gaussian distribution of the form:

$$\mathcal{L}(p) = \frac{1}{2\pi\sigma} e^{-\frac{(p-\hat{p})^2}{2\sigma_p^2}}, \tag{8.4}$$

$\hat{p}$ and σ_p are the two unknown to be estimated by maximizing $\mathcal{L}(p)$: they are the best estimation of parameter p and its statistical error. The function $\ell(p) = log(\mathcal{L}(p))$ is then a parabola that may be written as:

$$\ell(p) = P_3 p^2 + P_2 p + const. \tag{8.5}$$

In order to obtain the best estimation of the parameter p corresponding to the maximum of $\ell(p)$, a fit may be performed of $\ell(p)$ following equation 8.5. The values of the parameter $\hat{p}$ and σ_p are given by:

$$\hat{p} = \hat{\delta} = -\frac{P_2}{2P_3}, \qquad \sigma_p^2 = -\frac{1}{2P_3}. \tag{8.6}$$

The relation between $\mathcal{L}$ and ℓ is shown in figure 8.7: the best estimate of the parameter is the one which maximises either $\mathcal{L}$ or ℓ .

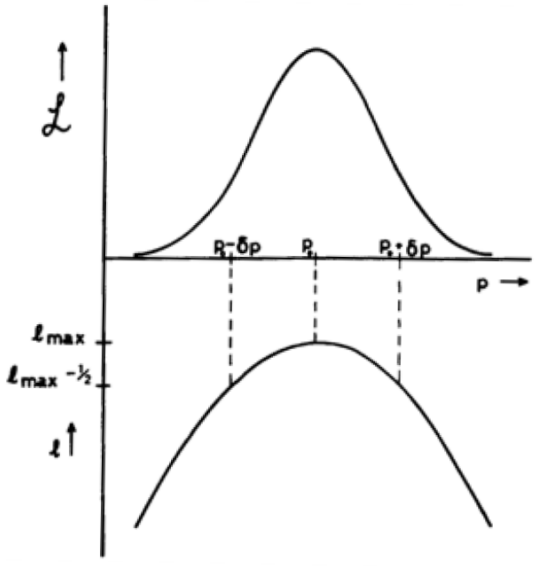

Figure 8.7: *When the likelihood function $\mathcal{L}$ tends to be gaussian, then the ℓ function, the logarithm of the likelihood function, becomes a parabola as a function of parameter* (p) *in the region of the maximum. The best estimate of the parameter* p_0 *is the one which maximises either $\mathcal{L}$ or ℓ. The accuracy δp with which* p_0 *is determined is defined by the condition $\ell(p_0 \pm \delta p) = \ell(p_0) - \frac{1}{2}$. This is equivalent to the statement that δp^2 is the variance of the $\mathcal{L}$ distribution.*

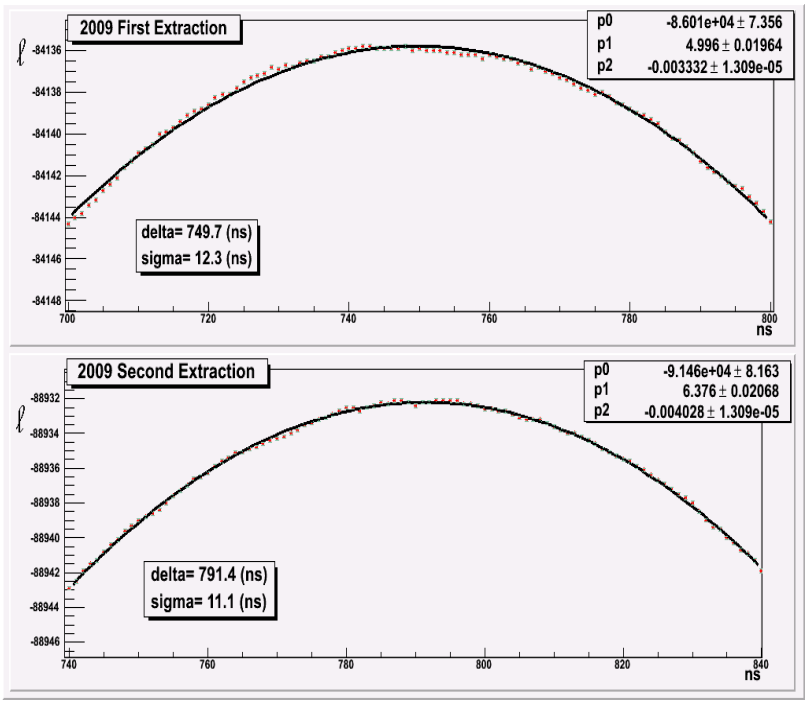

Figure 8.8: *Parabola fit of $\ell(\delta)$ data for the OPERA collected events during the 2009 period of run. In the upper part is presented the plot related to the first extraction: starting from the fit parameters the time shift value obtained is δ=749.7 ns with σ=12.3 ns. In the bottom part is presented the plot related to the second extraction: the time shift value obtained is δ=791.4 ns with σ=12.3 ns.*

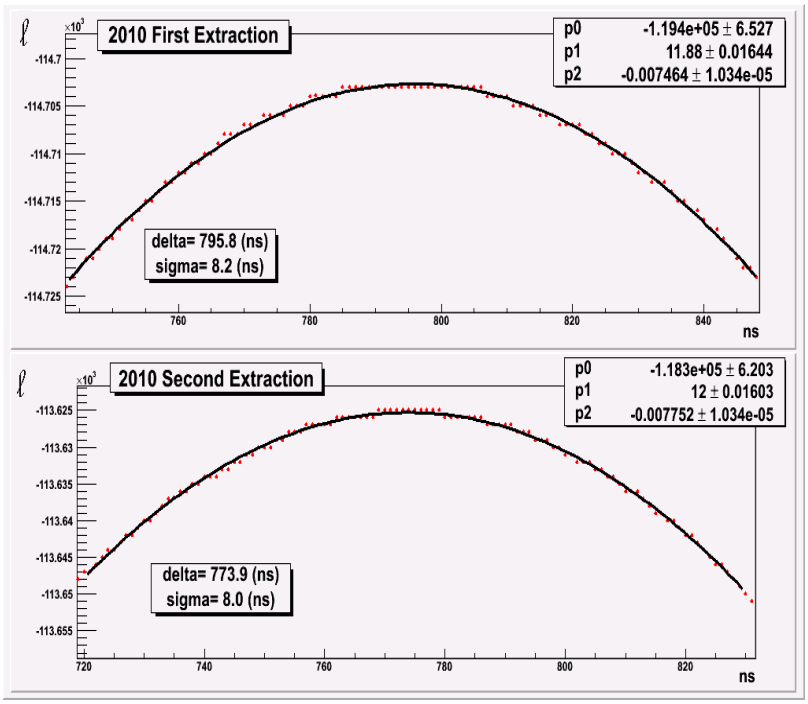

Figure 8.9: *Parabola fit of $\ell(\delta)$ data for the OPERA collected events during the 2010 period of run. In the upper part is presented the plot related to the first extraction: starting from the fit parameters the time shift value obtained is δ=795.8 ns with σ=8.2 ns. In the bottom part is presented the plot related to the second extraction: the time shift value obtained is δ=773.9 ns with σ=8.0 ns.*

Function ℓ is not a parabola over a large range of value, but it can indeed be described as a parabola around the maximum. A scan of function ℓ for many δ values is made in steps of 1 ns and the resulting distribution is fitted with a parabola.
In figure 8.8 and in figure 8.9 are presented the ℓ plots for the two extractions (respectively of the 2009 and of the 2010 OPERA data) and the parabola fit, that results in the δ and σ values reported in table 8.2.

	First Extraction		Second Extraction	
	δ_{best} (ns)	σ (ns)	δ_{best} (ns)	σ (ns)
2009	749.7	12.3	791.4	11.1
2010	795.9	8.2	773.9	8.0

Table 8.2: *δ and σ values resulting from the likelihood maximization.*

The values obtained have been combined together, as it is shown in figure 8.10, and the weighted average of δ is (780.7 ± 4.7) ns.

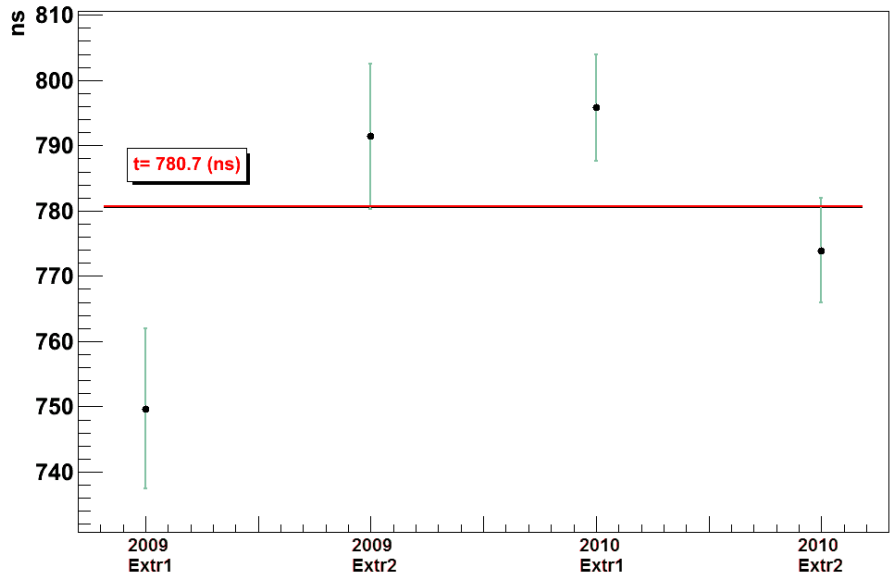

Figure 8.10: *Likelihood results obtained for the global samples combined together. The resulting δ value is 780.7 ns.*

8.3 Monte Carlo Test

In order to check the correctness of the implementation of the likelihood method a MC test has been performed: 100 samples of 7000 "OPERA" events have been generated according to the known waveform functions representing the final sample extracted for the two extractions and considering the 2009 and 2010 data together. A time shift of 800 ns has been introduced in the simulated data w.r.t. the waveform functions.
The likelihood method illustrated in the previous paragraph has been used to determine the values of δ of the two samples, as it would have been done for real data.
In figure 8.11 are shown the total distributions of the generated events for the two extractions. These two global samples have then been split in 100 "opera experiment" equivalent subsamples of 7000 events each.
The distributions of the values of δ obtained from the fit are shown in figure 8.12, the resulting mean values of δ and σ for the two extractions, performing the parabolic fit in a range between 750 and 850 ns are:

$$\begin{array}{rlll} \text{First extraction} & \langle\delta\rangle = 799.7 \text{ ns (rms} = 13.2) & \langle\sigma\rangle = 11.9\text{ns} \\ \text{Second extraction} & \langle\delta\rangle = 800.3 \text{ ns (rms} = 10.1) & \langle\sigma\rangle = 11.0\text{ns} \end{array} \tag{8.7}$$

It can be seen that the procedure is able to retrieve in an unbiased way the known shift and that the spread of its measured value over the different subsamples is compatible with the average measured σ. This test shows that δ and σ as computed with the adopted procedure correspond to the statistical meaning that is attributed them. By considering that the value of σ of both distributions is about 11 ns and that there are 100 entries of δ in each distribution, the error on the two averages $\langle\delta\rangle$ is then $\sim 11/\sqrt{100} \sim 1.1$ ns. The two values of $\langle\delta\rangle$ therefore agree with the true value 800 ns.

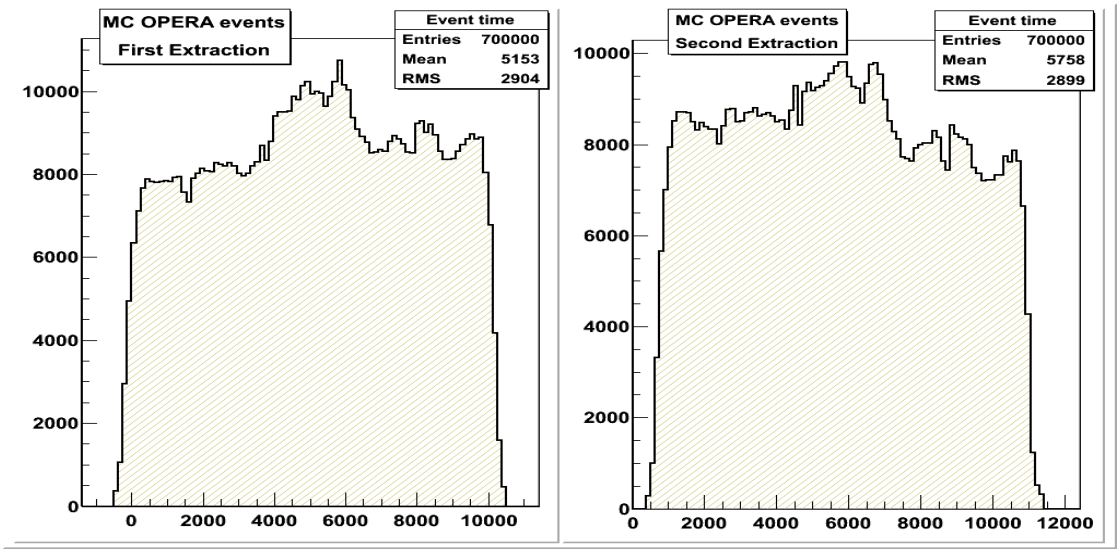

Figure 8.11: *OPERA events generated according to the know waveform functions for the first (left) and for the second (right) extraction. A time shift of 800 has been introduced, 100 samples of 7000 events have been produced.*

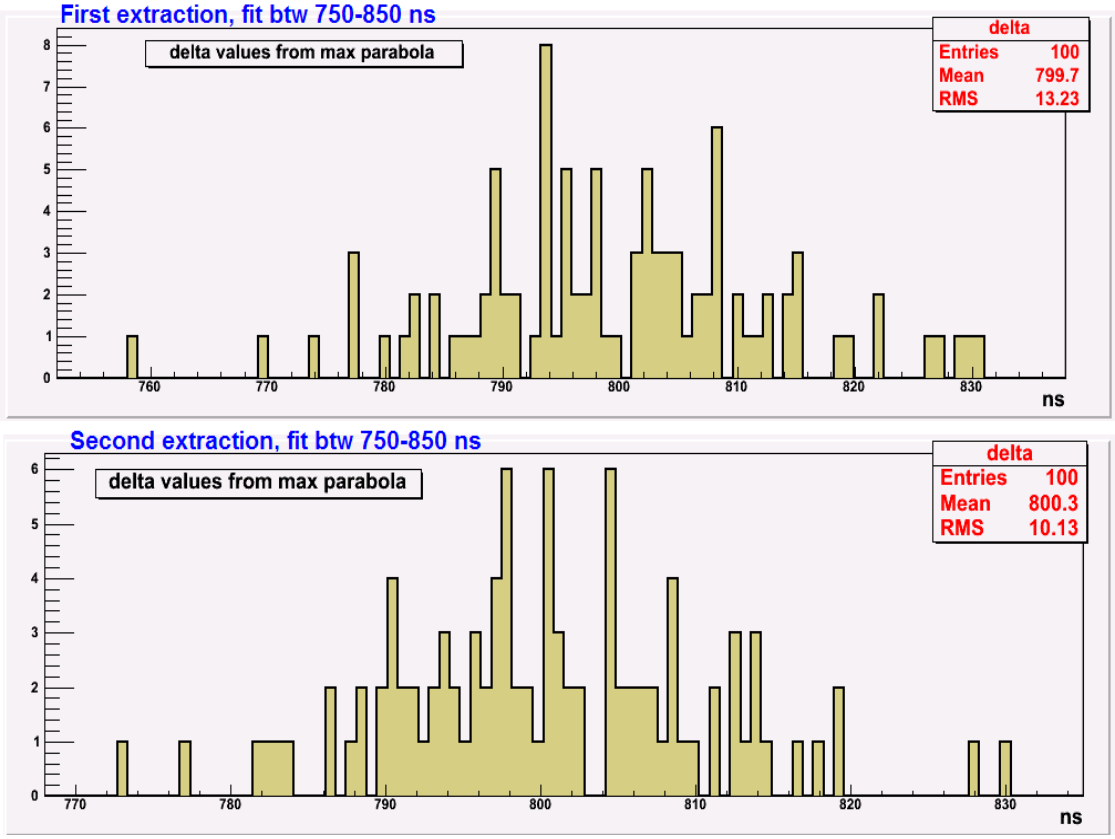

Figure 8.12: *Distribution of the δ values obtained for the 100 MC samples generated with 800 ns of time shift w.r.t the know waveform functions. The parabolic fit has been done in the range 750-850 ns.*

Chapter 9

Results on the Final Data Sample and Extraction of Neutrino Velocity

The final data sample to be analyzed in order to extract the neutrino velocity has been extracted from the global sample of the OPERA events on time with the CNGS beam, and then corrected for different factors, following several steps. A first selection has been made taking into account the considerations explained in chapter 7, on the results of the MC studies on the external events, and implementing a selection algorithm based on the OpCarac classification. Among the retained events a second selection was done choosing only those events for which the timing correction explained in section 4.5 was available both for the CERN timing and for the LNGS timing systems. In total, 3967 events for the 2009 run and 7657 events for the 2010 OPERA run have been selected as final data sample. A global timing correction is then applied to each event. Finally, also a correction on the Z positions of the earliest digit for each event has been applied, in order to evaluate exactly the travelled distance relative to the detection point and not just the origin of the OPERA reference system.

In order to perform the analysis on the final data sample only the waveforms corresponding to the selected OPERA events have been considered, and the model functions have been produced in the same way as explained in section 8.1.

In this chapter the global timing correction and the first digit Z position correction are described. Then the final data sample is analyzed using the likelihood maximization method in order to extract the best value of time shift δ between the OPERA events and the fast waveform digitizer data.

9.1 Data Timing Correction

In order to correct the final data sample, since the OPERA events are UTC time tagged only with an approximate UTC time corresponding to the start of the spill, the time corrections calculated as presented in section 4.5 have been applied. The OPERA event time and the protons time tag at CERN have been both referred to the Cs clocks.
The values considered in the analysis are:

$$\Delta tof(data) = \mathrm{t}_{OPERA} \text{ - } \mathrm{t}_{kicker} \text{ - } (\sim 2.4 \text{ ms}).$$

The calculated correction are:

$$\begin{aligned} T_X^{LNGS} &= Tref_G + d_{LNGS} - \Delta t_{LNGS} \\ T_X^{CERN} &= Tref_C + d_{CERN} + \Delta t_{CERN}, \end{aligned} \tag{9.1}$$

where $Tref_G$ and $Tref_C$ are the interpolated GPS reference times, d_{LNGS} and d_{CERN} are the cables and Fan Out delays, $\Delta \mathrm{t}_{LNGS}$ and $\Delta \mathrm{t}_{CERN}$ are the interpolated (Ext2-Ext1) PC logged values, and as explained in chapter 4, the Cs clock signal is connected in input to the CTRI card Ext1 at LNGS and in input to the CTRI card Ext2 at CERN. The common time correction to be applied to the data is then C=$T_X^{CERN} - T_X^{LNGS}$. Each OPERA event of the final data sample has been corrected by its own C value. The final correction values are shown in figure 9.1, where the events corresponding to the final data sample are highlighted. By zooming over a much smaller period it is possible to find the ∼60 ns oscillation due to the daily excursion of the GPS clocks, as it is shown in the bottom part of figure 9.1, this behaviour was already presented in section 5.3 (see figure 5.7). The twin high accuracy timing system with an intercalibration accuracy at the level of 1 ns is fundamental to perform the neutrino velocity measurement, each OPERA event being corrected by its own time correction value. From this point onwards the analysis on the data sample corrected by the C factor will be referred to the corrected values Δt_C.

9.2 Distance Correction

In order to correctly calculate the effective distance travelled by neutrinos for each event, the distance between the reference point A1 in the OPERA detector

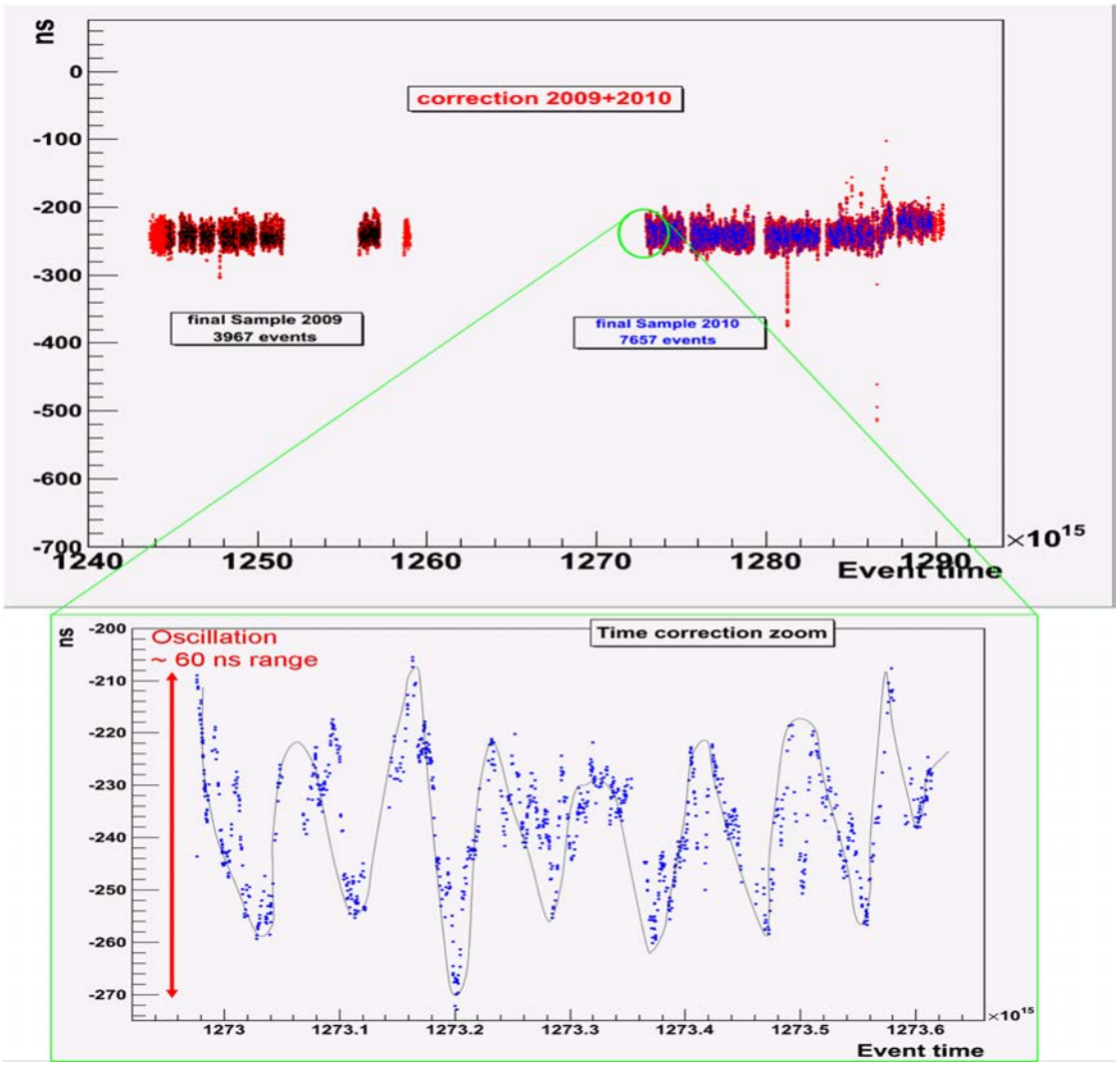

Figure 9.1: *Global timing correction for the final data sample. Up: in black and in blue are shown the events corresponding to the final data sample of 2009 and 2010 respectively. Bottom: By zooming over a smaller period of time the ∼60 ns GPS oscillating behaviour can be seen, it is due to the daily excursions of the GPS clocks.*

and the Z position of the earliest digit whose time correspond to the UTC OPERA event time has been computed for each event. The exact position of A1 has been reported in section 6.3 and can be seen in figure 6.7, this is the point used for the determination of the distance CERN-OPERA. Its Z coordinate in the OPERA detector system as used in the event reconstruction software is z_{A1}=-270.226 cm. The distance used for each event is then corrected by $\Delta z = z_{first\ digit} - z_{A1}$, where $z_{first\ digit}$ is the coordinate of the earliest digit.

The distribution of the Z positions of the first digit for the selected data sample with respect to the A1 position is shown in figure 9.2. The correction to be applied to the event times due to the Δz has been introduced to each event individually.

The data sample containing both the corrections, the one presented in section 9.1 and the one due to Δz, will be called $\Delta t_C^z = \Delta t_C - \left(\frac{\Delta z}{c}\right)$, where $c = 299792458$ m/s.

The transverse (XY) distance of the earliest digit from A1 has not been corrected since the deviation due to this effect would be negligible. For instance considering a Δx distance (it would be the same for Δy) between the first digit position and the A1 position as large as 8 m (which is more than the extension of the OPERA detector), the resulting deviation from the considered L distance on z direction of $\sim$ 730 km would be much less than 1 ns:

$$\begin{aligned} d &= \sqrt{L^2 + \Delta x^2} = L\sqrt{1 + \tfrac{\Delta x^2}{L^2}} \overset{\Delta x \ll L}{\simeq} L\left(1 + \tfrac{1}{2}\tfrac{\Delta x^2}{L^2}\right) \\ \Delta d &= d - L = \tfrac{1}{2}\tfrac{\Delta x^2}{L} = \tfrac{1}{2}\tfrac{64}{730.000} \sim 1.5 \cdot 10^{-4} \text{ ns}. \end{aligned} \tag{9.2}$$

As the maximum likelihood maximization analysis will show, the δ time shift between the OPERA events and the waveform data is affected by a correction of $\sim$ 3 ns due to Δz.

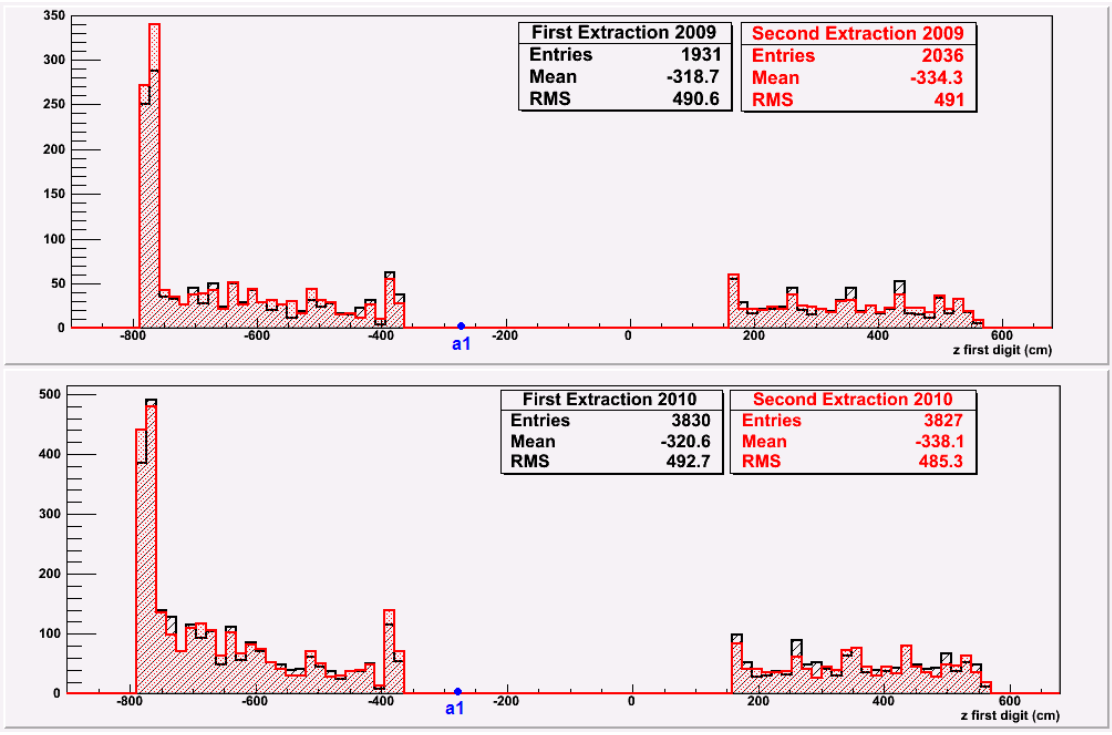

Figure 9.2: *Distribution of the Z positions of the events first digit w.r.t reference point A1 position. The peak around -800 cm is caused by muons produced in interactions in the rock or the material in front of the detector and thus entering the detector from the front.*

In order to cross-check the bias introduced by the z-distribution of the earliest digits, the global data sample has been also studied. In this sample any kind of events are included, for instance all the events classified by OpCarac as "SPECTRO" events are included: in this cases the neutrino has interacted in the OPERA magnets and the earliest digit is recorded by the RPCs, and they are always located downstream w.r.t. A1. The final data sample corresponding to the 2010 data of the first extraction has been compared to the global 2010 data sample of the first extraction, the z distribution of the final data sample digits is shifted by about 140 cm upstream w.r.t. the global data sample, which in terms of TOF results in a reduction of (140 cm/c)=4.7 ns (see figure 9.3). It has been checked that, as expected, this effect was also reproduced by the likelihood maximization analysis on the global data sample.

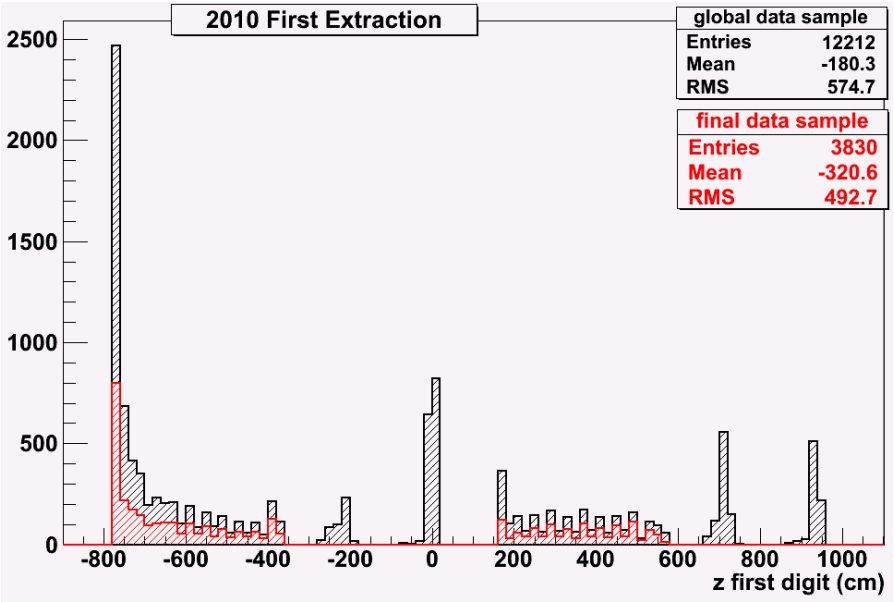

Figure 9.3: *Distribution of the Z positions of the events first digit, for the final (red) and the global (black) data sample of the 2010 first extraction data. The final data sample is shifted by about 140 cm (320.6 - 180.3 cm) upstream w.r.t. the global data sample.*

9.3 Data Analysis Using a Likelihood Maximization

The waveform functions corresponding to the event selected for the final data sample have been used to produce the model functions for the analysis. The resulting functions are presented in figure 9.4, separately for the two years of run

and for the first and the second extraction. In order to combine all the results also a global function for the first extraction and a global function for the second extraction have been calculated for the 2009 and 2010 data together.

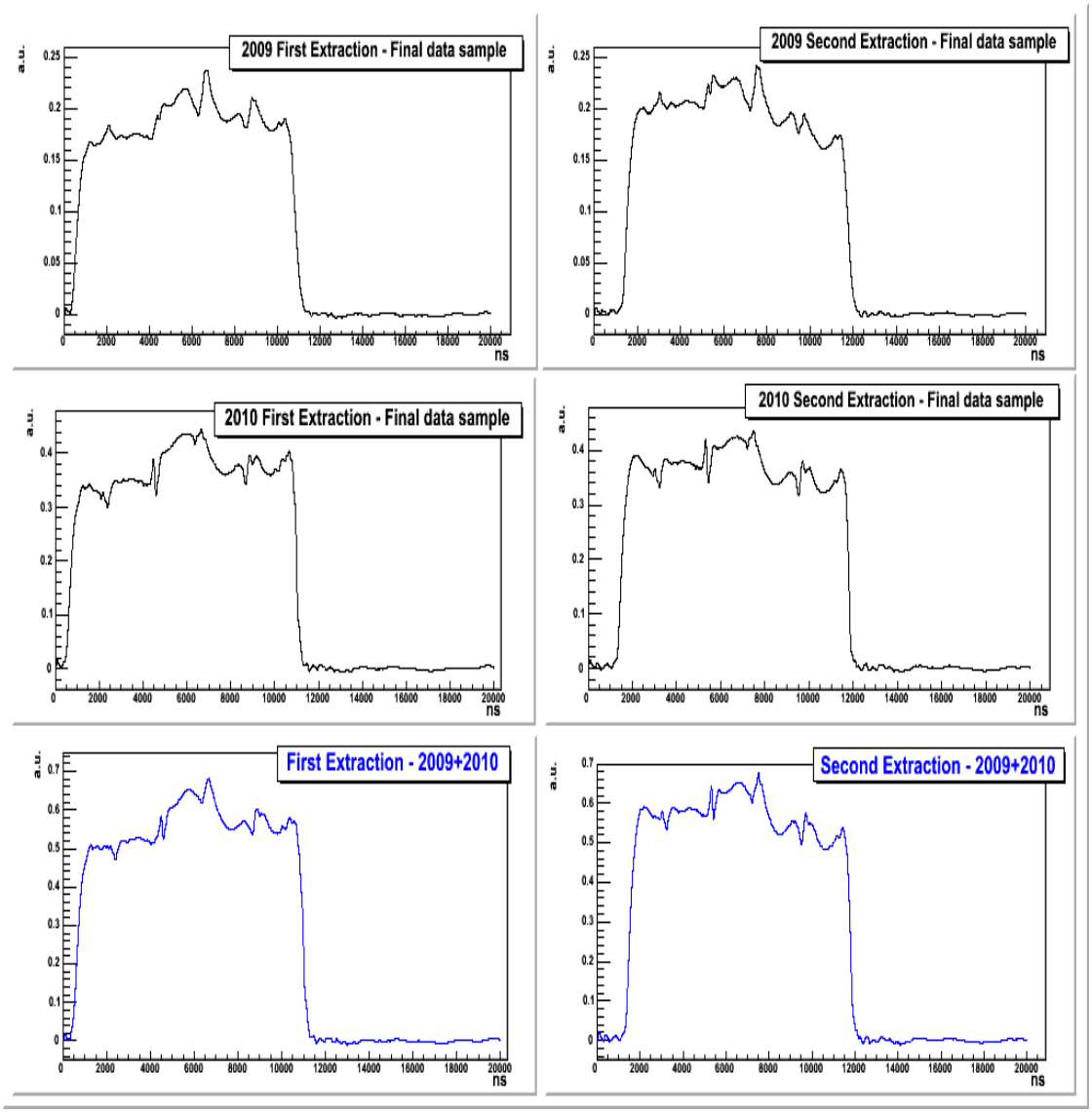

Figure 9.4: *Waveform model functions produced for the analysis of the final data sample. They are shown separately for the two extractions and for the 2009 and 2010 years of OPERA run (in black). Also the global functions for the first extraction and for the second extraction are presented (in blue), obtained with 2009 and 2010 data together.*

The likelihood maximization method has been used (following the procedure explained in section 8.2) to analyse in three steps the final data sample considering the 2009 data together with the 2010 data, *i.e.* 5761 data for the first extraction and 5863 data for the second extraction. First, the $\Delta tof(data)$ values have been analyzed, then the corrected samples Δt_C and Δt_C^z. The $\hat{\delta}$ time shift values that

maximize the $\ell(\delta) = log(\mathcal{L}(\delta))$ function are reported in table 9.1, as well as the corresponding statistical errors. The parabola fit of the likelihood calculated for the Δt_C^z sample is shown in figure 9.5

Sample	First Extraction $\delta_{best} \pm \sigma$ (ns)	Second Extraction $\delta_{best} \pm \sigma$ (ns)
$\Delta tof(data)$	798.4 ± 12.6	815.1 ± 11.7
Δt_C	1035.2 ± 12.9	1055.2 ± 11.4
Δt_C^z	1030.8 ± 13.5	1051.0 ± 11.3

Table 9.1: *Results of the likelihood maximization on the final data samples. The first sample considers the uncorrected data ($\Delta tof(data)$), then the timing correction has been applied (Δt_C), and as a final step also the correction due to the distance between the earliest digit position and the reference point A1 has been considered (Δt_C^z). The samples contain the 2009 data together with the 2010 data, separately for the first and the second extraction.*

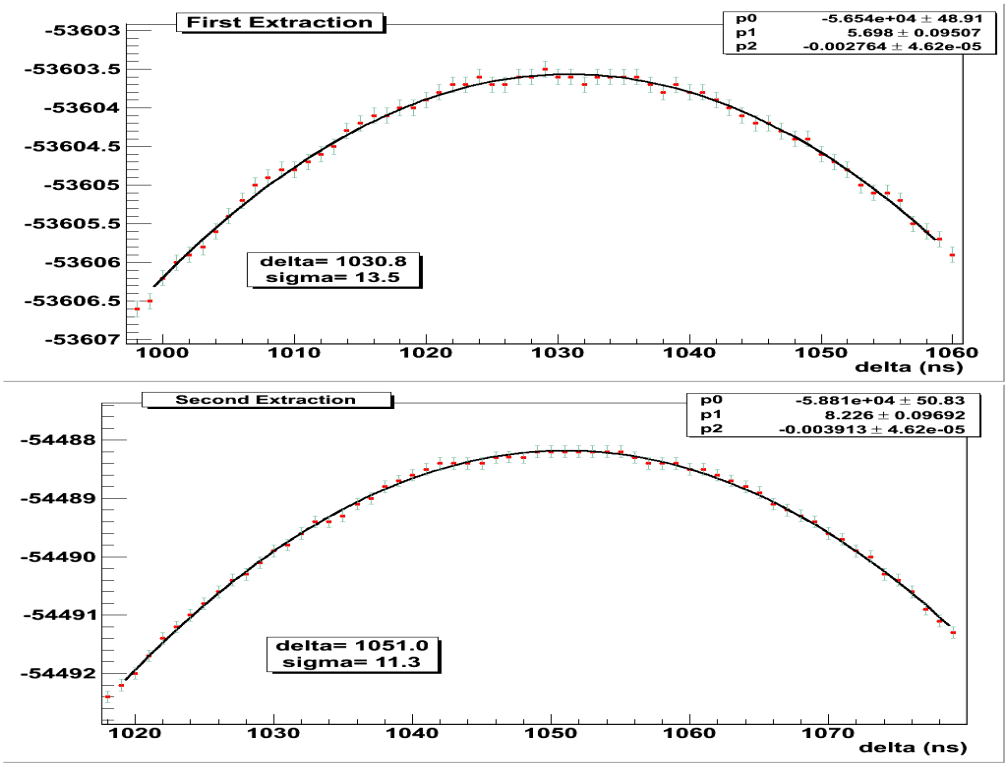

Figure 9.5: *Parabola fit of the calculated $\ell = log(\mathcal{L})$ for the final data sample Δt_C^z. The parabola reaches its maximum for: $\delta_{best}^{First\ extraction}$=1030.8 ± 13.5 ns and $\delta_{best}^{Second\ extraction}$=1051.0 ± 11.3 ns*

The results obtained for the two extractions have then been averaged in order to extract the final time shifts. The results are presented in table 9.2.

Combining the first and the second extraction results, and considering all the cor-

Sample	$\delta_{best} \pm \sigma$ (ns)
$\Delta tof(data)$	807.4 ± 8.6
Δt_C	1046.4 ± 8.5
Δt_C^z	1042.7 ± 8.7

Table 9.2: *δ time shift and σ error obtained combining the first and the second extraction results of the likelihood maximization, presented for the three data samples. The final result is: δ = 1042.7 ± 8.7 ns.*

rections, the δ time shift is:

$$\delta = 1042.7 \pm 8.7 \text{ ns}. \tag{9.3}$$

The parabola fit of the likelihood calculated for the Δt_C^z sample has been performed also for the first and the second extraction separately for the 2009 and the 2010 runs. In table 9.3 are summarized the δ and σ values obtained. This four results are statistically compatible and have been then combined together in order to extract the final time shift, as plotted in figure 9.6, the result is:

$$\delta = 1042.7 \pm 8.1 \text{ ns}, \tag{9.4}$$

which is completely in agreement with the result in 9.3.

	2009 $\delta_{best} \pm \sigma$ (ns)	2010 $\delta_{best} \pm \sigma$ (ns)
First Extraction	1025.8 ± 27.3	1038.5 ± 14.8
Second Extraction	1082.3 ± 20.7	1035.3 ± 12.1

Table 9.3: *δ and σ values obtained for the Δt_C^z sample by maximizing the likelihood probability separately for the first and the second extraction and for the 2009 and 2010 OPERA runs.*

The waveform function of the first and of the second extractions have been superimposed on histograms filled with Δt_C^z data, in figure 9.7 two cases are shown for δ respectively equal to 1042.7 ns and 0 ns: the first one imposes a time shift δ between the OPERA events and the waveform corresponding to the obtained result, δ=1042.7 ns; the second one shows the waveform function and the OPERA events in the case where no time shift is imposed (δ=0 ns). The waveform functions correspond very well to the time distribution of the OPERA events when a time shift of 1042.7 ns is applied whereas there is agreement at all in the second case.

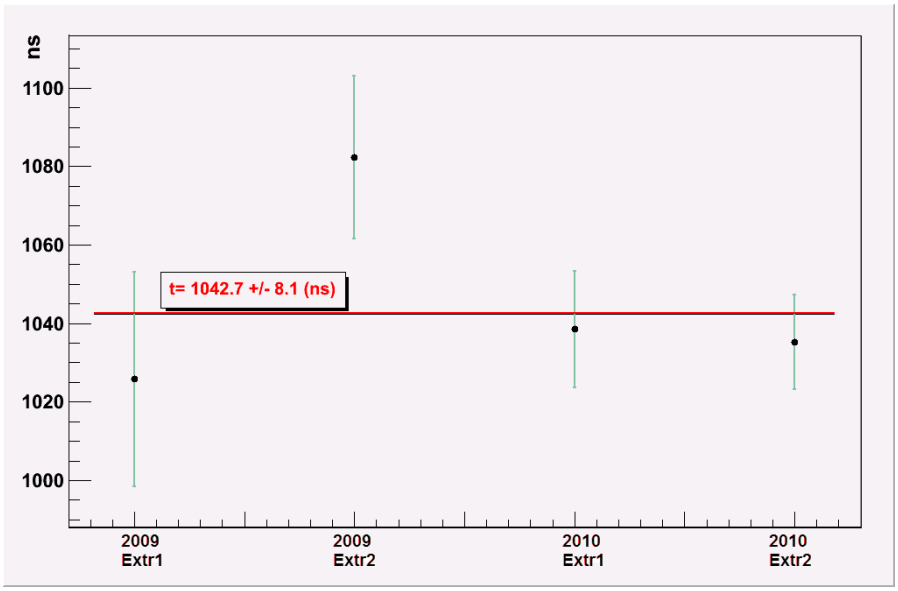

Figure 9.6: *δ time shift value obtained by combining with a linear fit the results of the likelihood maximization on the final Δt^z_C data sample. The result is δ=1042.7 $\pm$ 8.1 ns.*

9.4 Extraction of the Final Result

The twin high accuracy system (composed by the PolaRx, the Cs4000 and the CTRI DAQ) installed at CERN and LNGS and operating in common view mode allows to continuously inter-calibrate, every second, the timing signals present at these two reference points:

a) T_X^{CERN}, the time corresponding to the reference point located at the 1PPS output of the XLi GPS receiver, which is the primary timing source of the GMT timing system at CERN. All timing measurements at CERN are refer to this reference point;

b) T_X^{LNGS}, the time corresponding to the reference point located at the 1PPS output of the GPS Clock2 receiver at LNGS. The timing signal distributed underground is synchronous with the Clock2 output and the UTC time-tags of the OPERA experiment refer to this point.

This intercalibration system based on the common-view mode is more sophisticated than a simple common-view setup. It was designed to time-link reference points of previously existing timing chains. It has to be noted that the absolute UTC calibrations of the XLi or the Clock2 receivers do not really matter in our measurement once their 1PPS outputs, which act as general reference points of

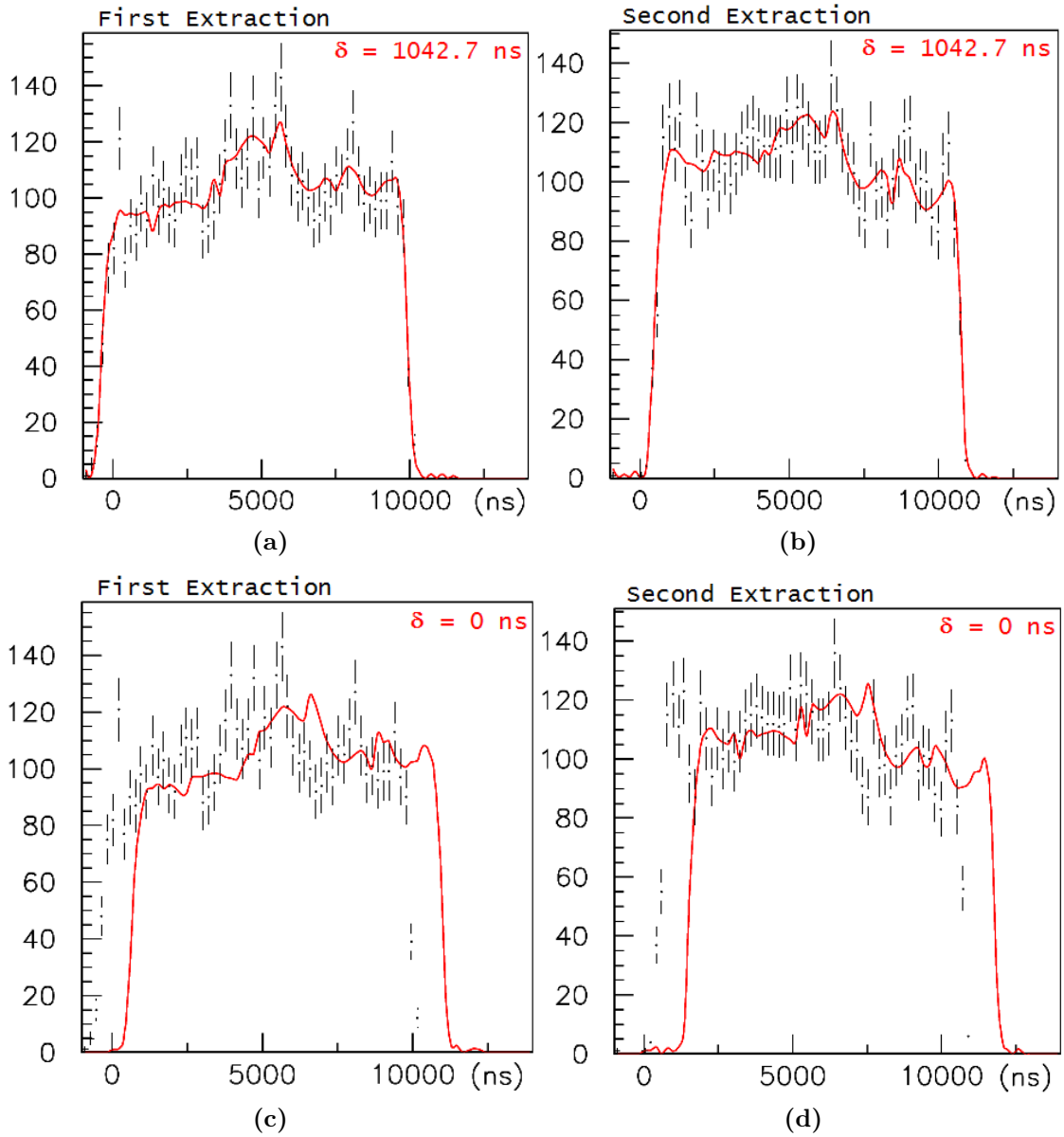

Figure 9.7: *Waveform functions superimposed on the OPERA events of the final data sample Δt^z_C, in the case with a time shift of 1042.7 ns and in the case without time shift. a) First extraction data, the waveform function (red) results in good agreement with the OPERA data (black) if a time shift of 1042.7 ns is applied. b) Second extraction data, as in a) also in this case 1042.7 ns of time shift are imposed and the waveform function corresponds well to the OPERA events. c) First extraction, the waveform function (red) and the OPERA events (black) are plotted together without applying any time shift, it is clear that the function does not correspond to the data. d) Second extraction, as in c) it is clear that the waveform and the OPERA data are not in agreement when no time shift is applied.*

all measurements, are time-linked by the high accuracy twin system. The XLi receiver was calibrated by METAS. The GPS Clock2 at LNGS had never undergone a precise calibration taking into account the antenna cable or internal delays. This

explains also the average offset in between T_X^{CERN} and T_X^{LNGS} measured with the time link.

As previously shown, the data analysis was performed by just using in the TOF calculations the approximate delay corrections and the UTC measurements of the XLi and the Clock2, as normally used for the selection of on-time events in the OPERA detector over a window of 20 μs. This allows to compute the distribution of time differences $\Delta tof(data)$ (tof_{OPERA}-TOF(c)) between the raw measured tof_{OPERA} (t_{OPERA}-t_{kicker}) of the neutrino interaction with respect to the kicker signal and the TOF(c), computed assuming an approximate distance and the speed of light. The distribution of this difference should be normally starting at zero, if all delays are correctly taken into account, and neutrinos travel at the speed of light. It should also be consistent between the two beam extractions. Both conditions are not respected in the data. As it could be seen the distributions corresponding to the two extractions are shifted. This is due to the fact that the real phase of the CNGS beam with respect to the kicker signal is not the same for the two extractions. This phase had to be accurately measured with the FWD, without which a measurement just based on the kicker time tag would not have been sufficient to measure the real TOF of neutrinos.

Then, the real distributions of the proton pulses measured by the FWD, corresponding to each recorded neutrino interaction, have been taken into account. These measurements, referred as well to a trigger based on the kicker pulse, are consistently shifted for the first and for the second extraction as observed for neutrino interactions. A blind treatment of the data has been performed by computing the relative delay of the tof_{OPERA}-TOF(c) distribution with respect to the proton pulse distribution. This analysis, based on a maximum likelihood evaluation of the relative delay (δ) between these two distributions brought to consistent results on the two extractions and for 2009 and 2010 data samples. The value of this relative delay δ should now be zero if all calibration delays are correctly taken into account and if neutrinos travel with the speed of light. If the results are just taken at this level, where one compute the difference (tof_{OPERA}-TOF(c)) and the start of the digitization window of the FWD (which is not properly calibrated with respect to the rest of the chain and the real travel path of particles), the value of the measurement extracted from the maximum likelihood procedure is just arbitrary and not representative of deviations of the neutrino velocity from c. This result

however can be exploited in order to monitor the stability of the data analysis procedure and the consistency among the results of the two extractions and the data samples of 2009 and 2010. While working in parallel on the estimation of the geodesy and the accurate calibration of all the elements of the chain, the data analysis was deliberately finalized in these primitive conditions in order to be unbiased. Just one exception was made by integrating in the data analysis the fine timing corrections provided by the time-link of the twin high accuracy timing systems since they could affect the shape of the events time distribution. The integration of this correction still is not enough in order to extract a result on the neutrino velocity. The followed procedure corresponds to commonly adopted techniques of blind analysis. The "blind box" was opened to look at the final result only once satisfied of the quality of the timing calibration measurements, the geodesy measurements as well as the consistency in the data analysis of the different samples. This moment coincided naturally with the completion of this thesis.
All the missing ingredients will be now put together to extract the result on the deviation of the effective neutrino TOF with respect to that expect by assuming the speed of light. In order to do that, different kind of corrections which were already detailed in the previous chapters, have to be applied:

1. The result of the data analysis by taking into account the raw TOF measurement and the high accuracy time link after merging all data of 2009 and 2010 was δ=1042.7±8.7 ns. The following quantities have been defined:

$$\begin{aligned} &\delta = t_{waveform} - \Delta tof(data), \\ &\Delta tof(data) = tof_{OPERA} - TOF(c), \\ &tof_{OPERA} = t_{OPERA} - t_{kicker}. \end{aligned} \tag{9.5}$$

   The value δ is the time shift to be added to the data distribution in order to superimpose it to the proton pulse. Once all corrections are taken into account, a positive value of δ means that the neutrino pulse anticipates the proton pulse, extrapolated to OPERA assuming the speed of light.

2. TOF(c) needs to be accurately corrected by taking into account:

   a) The final geodesy distance of 730534.61 m between the CNGS target and the point A1 of the OPERA reference system, instead of the 730525

m previously assumed in the TOF calculation.

b) The precise position on the beam line of the BCT connected to the FWD (743.4 m from the target). The raw calculation used in $\Delta tof(data)$ was performed with respect to another BCT at 992.4 m from the target used in 2006 to calibrate the kicker pulse with respect to the real proton pulses.

c) The fact that the old intercalibration (on average 353 ns shift) performed in 2006 between Clock2 and the old XL-DC receiver, used at that time at CERN, is no more valid and it is completely replaced by the time-link which inter-calibrates the XLi and clock2 for each recorded neutrino interaction.

d) The fibers delay correction (40993.4 ns) and the OPERA DAQ delay correction (4245.2 $\pm$ 1.8 ns) are kept unchanged, they should both be subtracted, as already done, from the value of TOF(c).

The old value of TOF(c) assumed in the $\Delta tof(data)$ calculations was 2394488 ns, the new value computed introducing all corrections is 2394042.3, the difference being 445.7 ns. The old TOF(c) value was overestimated, bringing to smaller $\Delta tof(data)$ and consequently larger δ. This correction of 445.7 ns must therefore be subtracted from the uncorrected value of δ=1042.7 ns

3. Corrections in the CERN timing chain: in the chapter describing the calibrations performed at CERN it is explained that the kicker signal time-tagging is directly reported at the level of the 1PPS output of the XLi receiver (XL) by the FESA class which assumes 99216 ns. Given the measurements we performed in 2010, the UTC time-tags of the kicker written in the CNGS database (t_{kicker}) should be corrected by +7.2 ns. In other words the actual time tag was artificially decreased because the FESA class was overestimating the offset.
   Since tof_{OPERA} is computed as t_{OPERA}-t_{kicker} the application of this correction will decrease tof_{OPERA} and decrease $\Delta tof(data)$. So δ will increase correspondingly by 7.2 ns.

4. Corrections to the OPERA events time measurement. By taking into account the MC studies on the simulation of the time response of the detector and the

transit time in the photomultipliers, as declared by Hamamatsu, the time-tag of the events by the OPERA DAQ is actually delayed by 20.3 ns with respect to the time when the products of neutrino interactions or the external particles deposed energy in the OPERA target tracker. Neglecting this effect brings to an overestimation of t_{OPERA}, so to an increase of tof_{OPERA} and $\Delta tof(data)$ and a reduction of δ. When taking this correction into account δ should be increased by 20.3 ns.

5. Given the cable delay, the BCT signal which is acquired by the FWD is delayed by 581.4 ns, this increases $t_{waveform}$ and increases δ. By applying the correction δ should be subtracted by 581.4 ns.

6. The trigger which starts the FWD window is delayed by 26.7 ns w.r.t. the time tag of the kicker signal. This decreases $t_{waveform}$ and decreases δ. The correction will add 26.7 ns to δ.

The final value of δ is:

$$\begin{aligned}\delta(\text{ns}) = \; & 1042.7 - 445.7\ (\text{TOF(c)}) + 7.2\ (\text{CGT}) + 20.3\ (\text{OPERA detector}) \\ & -581.4\ (\text{BCT cables}) + 26.7\ (\text{FWD trigger}) = 69.8\ \text{ns}.\end{aligned} \tag{9.6}$$

9.4.1 Systematic Effects

The study of systematics is still preliminary and the main sources are quoted in table 9.4.
In the timing chain there is still one component which has not been fully calibrated yet. There could be a delay between the calibration input of the BCT and the real signal produced by the proton pulse. This point will be addressed by a precise calibration. For the time being this uncertainty has been conservatively evaluated to 10 ns.
The total systematic error amounts then to 12.4 ns. By combining in quadrature the statistical error with the systematic error the final error is:

$$sys \oplus stat = \sqrt{(8.7)^2 + (12.4)^2} = 15.1\ \text{ns} \tag{9.7}$$

Source	time
Travel path distance (0.2 m)	1 ns
Ignorance of the decay point	< 1 ns
Ignorance of the interaction point	2 ns
LNGS optical fibers calibrations	1 ns
DAQ calibrations	1.8 ns
FESA correction calibrations	1 ns
FWD cable delay calibrations	5 ns
FWD trigger calibration	1 ns
Septentrio calibrations	2 ns ($\times 2$)
Septentrio antenna delay calibration	0.5 ns ($\times 2$)
Opera timing response simulation	3 ns
BCT internal delay calibration	10 ns

Table 9.4: *Main sources of systematic effects.*

9.5 Measurement Result

The result of the performed measurement is that there is a possible deviation of the time of flight of neutrinos with respect to the one expected assuming the light velocity by 69.8 ns $\pm$ 15.1 ns. This result is compatible with the MINOS result within errors.
This would be equivalent to:

$$\frac{v-c}{c} = (2.9 \pm 0.6) \cdot 10^{-5}. \tag{9.8}$$

The preliminary result presented in this thesis is the object of further investigations both from the point of view of the calibration measurements and the data analysis which are currently in progress.

Conclusions

This thesis concerns the measurement of the neutrino velocity with the OPERA experiment in the CNGS beam.

There are different theoretical models that allow for Lorentz violating effects which can be investigated with measurements on terrestrial neutrino beams. The MINOS experiment has performed such a measurement in 2007 finding a deviation in the neutrino time of flight, with respect to the expected time of flight, assuming neutrinos travelling with the speed of light, of 126 ns over a distance of 730 km, with a statistical error of 32 ns and a systematic error of 64 ns.

The OPERA experiment observes as well muon neutrinos 730 km away from the source, the almost pure CNGS ν_μ beam produced at CERN. Since the OPERA experiment aims the direct observation of $\nu_\mu \rightarrow \nu_\tau$ oscillations in the CNGS beam, a higher energy beam w.r.t. that of MINOS is employed. This leads to a significantly higher number of interactions in the detector that allows for a measurement with a much smaller statistical uncertainty.

The timing system was explicitly upgraded in view of the neutrino velocity measurement, allowing for a much smaller systematic uncertainty thanks to a twin high accuracy system at both sites (at CERN and at LNGS) composed by atomic cesium clocks and GPS receivers operating in "common view mode". Thanks to this system a time-transfer between the two sites with a precision at the level of 1 ns is possible.

Moreover, a Fast Waveform Digitizer was installed along the proton beam line at CERN in order to measure the internal time structure of the proton pulses that are extracted from the SPS towards the CNGS target. By comparing the OPERA event time distribution to the time structure of the proton pulses that have generated these events, it is possible to improve the evaluation of the neutrinos time of flight.

The statistical accuracy achieved by the OPERA measurement is about 10 ns and the systematic error, still to be improved, is less than 20 ns. The work described in this thesis concerns all the steps needed to perform the neutrino velocity measurement, in particular I have taken part in:

- the study and calibration of the CERN and LNGS timing systems,
- the timing response simulation of the electronic subdetectors in OPERA,
- the analysis of the data from the high accuracy timing systems,
- the geodesy measurements performed in order to precisely evaluate the CERN-LNGS distance,
- the optimization of the event selection criteria in OPERA,
- the measurement of the delay between the neutrino interactions recorded by OPERA and the proton spills of the CNGS beam,
- the statistical data analysis and the extraction of the neutrino time of flight and the selection of the final data sample for the neutrino velocity measurement.

These studies have been carried out with a blind analysis in order to guarantee the internal consistency and the goodness of each calibration measurement. The result on the neutrino velocity is the most precise measurement so far with terrestrial neutrino beams, it is equivalent to:

$$\frac{v-c}{c} = (2.9 \pm 0.6). \cdot 10^{-5}. \tag{9.9}$$

This is a preliminary result and additional verifications are in progress.

Appendix A

Timing Corrections

The calculated timing corrections to be applied to the OPERA events are:

$$\begin{aligned} T_X^{LNGS} &= Tref_G + d_{LNGS} - \Delta t_{LNGS} \\ T_X^{CERN} &= Tref_C + d_{CERN} + \Delta t_{CERN}, \end{aligned} \tag{A.1}$$

where d_{LNGS} and d_{CERN} are the sum of cables and Fan Out delays, and they are respectively 2 ns at LNGS and 43 ns at CERN. These corrections have been calculated in order to refer the time in both cases at CERN and at LNGS at the same point T_X: as it can be seen in figure A.1, the kicker signal at CERN is connected to this point and at LNGS the OPERA timing signal is referred to this point as well.

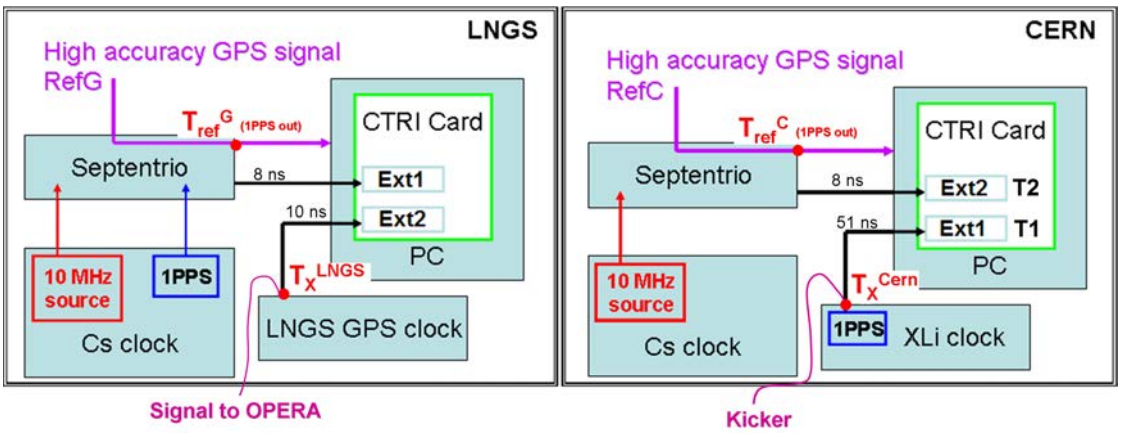

Figure A.1: *Scheme showing the connections of the new and the pre-existing timing systems at CERN and LNGS.*

In the case of the CERN timing system configuration, the XLi is connected to the Ext1 of the PC CTRI card through a path of 51 ns = (16 ns + 16 ns + 10 ns + 4.5 ns fanout1 + 4.5 ns fanout2), as shown in figure 4.4, while the Septentrio is connected directly with a 8 ns cable to the Ext2. By following the two paths up to the point corresponding to the EXT1 input and considering that Tref_C=T(1PPS)-T_{GPS} we can propagate T_{GPS}=T(1PPS)-Tref_C and compare it in the point EXT1 with XLi signal coming from the other path. In doing that it is neglected, as shown in chapter 4.4.1, that the 1PPS out anticipates by 8.7 ns the Tref measurement. This missing correction will not affect the common view measurement since it will be done in the same way at CERN and LNGS and will cancel out.
By assuming $\Delta t_{CERN} = T1 - T2 = (Ext1 - Ext2)$, one can then consider that:

$$(T_X^{CERN})' + 51\mathrm{ns} = -Tref_C + 8\mathrm{ns} + \Delta t_{CERN} = -Tref_C + 8\mathrm{ns} + (T1 - T2). \quad \text{(A.2)}$$

In order to be referred on the T_X point, this yields to:

$$(T_X^{CERN})' = -Tref_C - 43\mathrm{ns} + (T1 - T2). \quad \text{(A.3)}$$

The same considerations are valid for the LNGS timing scheme, whereas the Septentrio is connected with a 8 ns cable to the Ext1 of the PC CTRI card, the LNGS GPS clock2 is connected to the Ext2 with a 10 ns cable. In this case $\Delta t_{LNGS} = T2 - T1 = (Ext2 - Ext1)$, so that:

$$(T_X^{LNGS})' + 10\mathrm{ns} = -Tref_G + 8\mathrm{ns} + \Delta t_{LNGS} = -Tref_G + 8\mathrm{ns} + (T2 - T1), \quad \text{(A.4)}$$

which becomes:

$$(T_X^{LNGS})' = -Tref_G - 2\mathrm{ns} + (T2 - T1). \quad \text{(A.5)}$$

Since the analyzed OPERA events are the $\Delta tof(data)$ values, already corrected for the TOF, in order to apply the timing corrections and be referred to the calculated T_X times, one can consider:

$$\begin{aligned} &\Delta tof(data) = t_{OPERA} - t_{kicker} - TOF(c) \longrightarrow \\ &\Delta tof(data)^{corrected} = t_{OPERA} - t_{kicker} - ((T_X^{CERN}))' - (T_X^{LNGS})') \\ &= t_{OPERA} - t_{kicker} - (T_X^{CERN})' + (T_X^{LNGS})'. \end{aligned} \quad \text{(A.6)}$$

Since all the calculations for the timing corrections presented in the thesis considered in both cases for CERN and LNGS the values Δt=(T2-T1), the correction in A.6 is equivalent to:

$$\begin{aligned} &T_X^{LNGS} = Tref_G + d_{LNGS} - \Delta t_{LNGS} = Tref_G + 2 - (T2 - T1)_{LNGS} \\ &= -(T_X^{LNGS})' \\ &T_X^{CERN} = Tref_C + d_{CERN} + \Delta t_{CERN} = Tref_C + 43 + (T2 - T1)_{CERN} \\ &= -((T_X^{CERN}))', \end{aligned} \tag{A.7}$$

and the final correction applied to the data is ($\Delta tof(data)$+C), where C=$T_X^{CERN} - T_X^{LNGS}$, as reported in section 9.1.

Appendix B

ITRF/ETRF - International/European Terrestrial Reference Frame

The ITRF

Since the Earth is constantly changing in shape, the motion of the Earth's crust must be referenced. A terrestrial reference frame provides a set of coordinates of some points located on the Earth's surface.

The International Earth Rotation and Reference System Service[1] (IERS [65]) has to establish a Terrestrial Reference Frame (TRF), that provides a common reference to compare observations and measurement results from different locations. The International Terrestrial Reference Frame (ITRF) is a set of points with their 3-dimensional cartesian coordinates which realize an ideal reference system: the International Terrestrial Reference System (ITRS). The TRS is a spatial reference system co-rotating with the Earth; in such a system the positions of points anchored on the Earth solid surface have coordinates which undergo (small) variations with time, due to geophysical effects, such as tectonical deformations.
The ITRS definition should fulfill the following conditions:

- it is geocentric, the center of mass being defined for the whole Earth, including oceans and atmosphere.
- the unit of length is the meter. A consistent scale coordinate for a geocentric

[1]The IERS was established in 1987 by the International Astronomical Union and the International Union of Geodesy and Geophysics.

local frame is obtained by an appropriate relativistic modelling.

- its orientation was initially given by the BIH (Bureau International de l'Heure), orientation at 1984.0.
- the time evolution of the orientation is ensured by using a no-net-rotation condition[2] with regards to the horizontal tectonic motions over the whole Earth.

The TRF set of points is a "realization" of the TRS, with precisely determined coordinates in a specific coordinate system.
In the contest of IERS the system is geocentric with the origin close to the geocenter and the orientation is equatorial (Z axis in the pole direction). Nowadays, four main geodetic techniques are used to compute accurate coordinates (the GPS, VLBI, SLR and DORIS). These techniques form a tracking network which is evolving and the available data increase with time: for this reason the ITRF is constantly being updated. The ITRF coordinates are obtained by combination of individual TRF solutions computed by IERS using the mentioned Space Geodesy techniques composed by a network of stations covering the whole Earth. The combination method uses local ties in co-location sites where two or more geodetic systems are operating.
New ITRF solutions are produced every few years to attempt the realization of the ITRS as precisely as possible (in figure B.1 it is shown the ITRS as well as two examples of ITRF).
Since these realizations include station positions and velocities, modelling Earth crust changes, they can be used to compare observations from different epochs. The relationship linking all these solutions are supplied by transformation parameters.

The ETRF

The International Association of Geodesy (IAG) recommended since 1990 to adopt in Europe a reference system related to the ITRS and firmly fixed to the euro-asian tectonic plate: the ETRS89 (European Terrestrial Reference System 89). For each ITRFyy reference (where yy stands for the reference year of the data

[2]The no-net-rotation condition states that the total angular momentum of all tectonic pates should be zero.

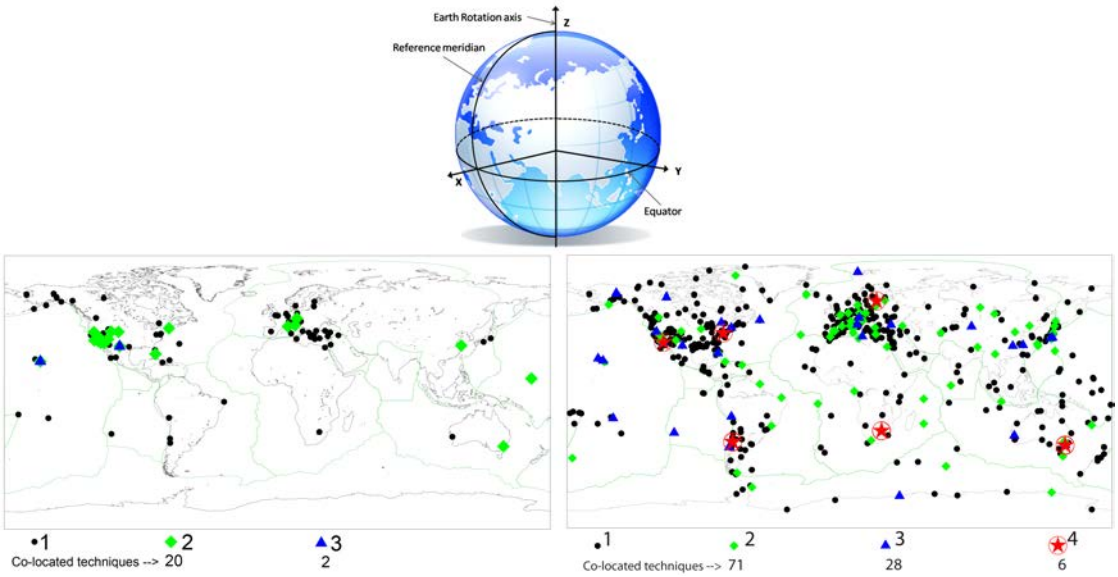

Figure B.1: *ITRS/ITRF. Up: the geocentric Terrestrial Reference System. Bottom: two ITRF examples: ITRF88 (left) and ITRF2008 (right) sites and co-located techniques.*

set) the corresponding ETRFyy is defined.

The ETRF89 and the ITRF89 coincided on 1989.0 (1 January 1989), since then they have deviated because the ITRF follows the continental drift while the ETF remains anchored to the European plate.

The Boucher-Altamimi transformation

The official procedure for the transformation from the ITRFyy to the ETRFyy (and vice-versa) is the one defined by Boucher-Altamimi [65]: one can derive from each annual frame determined by IERS (ITRFyy), a corresponding frame in ETRS, which will be itself labelled ETRFyy.
It consists of 6 parameters linearly depending on time, combined with a linear propagation of the geodynamic velocities that depend on the point position. The detailed specifications to establish ETRFyy are:

1. Selection of points: all points corresponding to sites belonging to ITRF and located in Europe will be selected (occasionally additional markers or points can be added if local eccentricities are available between it and some point already existing in ITRF),

2. Coordinates and velocities. These values are obtained as follows (case 89.0):

a) Computation in ITR, at 89.0:
   $X_{YY}(89.0) = X_{YY}(t_0) + V_{YY}(89.0 - t_0)$,
b) Computation in ETRS at 89.0,
c) Computation of velocity in ETRS.

List of Figures

1.1 Neutrino mass hierarchy 10
1.2 Warped extra dimension where only right handed neutrinos propagate 15
1.3 α parameter as a function of $logM$ by evolving 50k simulated MINOS events 16

2.1 Simulation steps starting with KII data with LV parameters 22
2.2 MINOS experiment, detectors sketch and location 24
2.3 MINOS Data fit 27
2.4 Oscillation probability for the ν_τ CC and expected neutrino flux at Gran Sasso 29
2.5 FWD and OPERA detector locations 29

3.1 Accelerator complex 34
3.2 Beam shaving 34
3.3 Scheme of CNGS extractions 35
3.4 Beam timing structure measured by the OPERA experiment 35
3.5 CNGS beam line 37
3.6 Collected statistics during the OPERA physics runs 38
3.7 CNGS focusing system 39
3.8 CNGS muon monitors 41
3.9 Expected ν_μ radial distribution in Gran Sasso 42
3.10 Resulting distributions of the MC study on the decay point along the CNGS beamline of the neutrinos parent particles. 46
3.11 The OPERA brick 47
3.12 First OPERA ν_τ candidate event 48
3.13 The OPERA detector 49

3.14 Scintillator strip 49
3.15 TT planes and bricks position close to the TT planes 50
3.16 The OPERA magnetic spectrometer 50
3.17 OPERA DAQ scheme 51

4.1 Timing system scheme 54
4.2 Scheme of the General Machine Timing (GMT) 55
4.3 Data acquisition system of the CNGS timing 56
4.4 Scheme of the CCR standard configuration and calibration reference setup 57
4.5 Underground system and setup with the DAQ PC in HCA4 58
4.6 Picture and scheme of the timing system at LNGS 59
4.7 Sketch of the ESAT system and date coding 60
4.8 OPERA timing system scheme 61
4.9 Detector master cards and TT chained sensors 63
4.10 PMT time dispersion 64
4.11 Photon propagation in fibers 65
4.12 Signal dispersion in fibers 65
4.13 Electronics fast shaper 66
4.14 Comparison between TT real and simulated digitized data 67
4.15 $1/\beta$ distribution for the TT 67
4.16 General GPS working principle 70
4.17 GPS operating in Common View Mode 71
4.18 PC system 72
4.19 RINEX file format example 73
4.20 CGGTTS file format example 74
4.21 Scheme of the geodetic-time receiver used at LNGS and at CERN . 77
4.22 Results of the PolaRx calibrations performed by METAS 78
4.23 Connection scheme between Reference Clock, GPS receiver and GPS antenna 79
4.24 Overall scheme of the PolaRx GPS receiver 81
4.25 Timing correction values at CERN and LNGS 83
4.26 Strange T_X values due to unhealthy satellites 84

5.1 Timing chain at CERN, normal and calibration configuration 87

5.2 CNGS access point 88
5.3 Timing chain at CERN, underground normal configuration 88
5.4 Timing chain at CERN, underground calibration configurations . . 89
5.5 Picture and sketches of timing system at LNGS 92
5.6 Scheme of the calibrated timing chain at LNGS 93
5.7 Daily excursions of the GPS clocks 95

6.1 The five reference points at underground LNGS and neutrino beam direction w.r.t. the hall axis 98
6.2 Map of Gran Sasso tunnel and LNGS underground laboratories . . 99
6.3 Traverse along the Gran Sasso tunnel 100
6.4 Scheme of the followed path in underground LNGS and the OPERA measured reference points 101
6.5 Measured positions in the geodetic survey at Gran Sasso 103
6.6 CERN underground structure, CNGS target chamber with the T40 focal point 105
6.7 Reference point A1 in the OPERA detector 106

7.1 Event display 111
7.2 Δt_{tof} 113
7.3 External events, extrapolated interaction points. 114
7.4 Δt_{tof} distributions 115
7.5 Δt_{tof} distributions for reconstructed muon tracks 115
7.6 time delay 116
7.7 CONTAINED, FRONTMUON and SIDEMUON events 118

8.1 Proton pulse internal time structure as recorded by the FWD . . . 123
8.2 Collected statistics 123
8.3 Saturated and “oscillating” waveforms 124
8.4 Oscillating structure of the final waveform functions 126
8.5 Filter on the waveform functions 127
8.6 Waveform functions 127
8.7 Likelihood maximization method 129
8.8 Maximum likelihood 2009 130
8.9 Maximum likelihood 2010 130

8.10 Likelihood results obtained for the global samples combined together 131
8.11 MC generated OPERA events 133
8.12 Distribution of the δ values obtained for the MC samples 133

9.1 Global timing correction for the final data sample 137
9.2 First digit Z positions w.r.t reference point A1 position. 138
9.3 First digit Z positions for the final and the global data samples. . . 139
9.4 Waveform model functions for the analysis of the final data sample 140
9.5 Parabola fit of the calculated $\ell = log(\mathcal{L})$ for the final data sample . 141
9.6 δ time shift obtained by combining the results of the likelihood maximization on final data sample 143
9.7 Waveform functions superimposed on the OPERA events of the final data sample, in the case with a time shift of 1042.7 ns and in the case without time shift 144

A.1 PC system 153

B.1 ITRS/ITRF 159

List of Tables

1.1 Results of the atmospheric neutrino experiments. 8

2.1 Data from SN1987A 20
2.2 Lower bounds on the LV mass scale 23
2.3 MINOS and NuMi parameters 25
2.4 MINOS Uncertainty 26

3.1 CNGS beam parameters 36

4.1 CGGTTS file format explanation 74
4.2 Measurement done by METAS for the LNGS PolaRx receiver . . . 80

5.1 Summary of the calibration measurement results at CERN 89
5.2 Conclusions on the calibration measurements performed at CERN . 90

6.1 Distances from CERN measured for the five reference points at underground LNGS 98
6.2 Total Station measurements estimated precisions 100
6.3 Four GPS benchmarks positions 102
6.4 ETRF2000 positions and precisions of the benchmarks in the OPERA hall 103
6.5 T40 coordinates transformations 104
6.6 List of measured reference points of OPERA 104
6.7 List of reference points of OPERA in LCCS 106
6.8 Reference OPERA point A1 in LCCS 106

7.1 External MC interactions 114
7.2 2009 data sample based on OpCarac classification 119

7.3 2010 data sample based on OpCarac classification 119
7.4 Final data samples OpCarac classification 120

8.1 Statistics of the waveforms retained for the analysis 125
8.2 Likelihood maximization results summary 131

9.1 Results of the likelihood maximization on the final data samples . . 141
9.2 δ time shift obtained combining the first and the second extraction results 142
9.3 δ time shift calculated separately for 2009 and 2010, first extraction and second extraction 142
9.4 Main sources of systematic effects 149

Bibliography

[1] W. Pauli, *On the Earlier and more recent history of the neutrino*, Cambridge Monogr. Part. Phys. Nucl. Phys. Cosmol. 14 (2000) 1-22.

[2] F. Reines and C. Cowan, *The Neutrino*, Nature 178 (1956) 446.

[3] G. Danby, J-M. Gaillard, K. Goulianos, L. M. Lederman, N. Mistry, M. Schwartz, and J. Steinberger, *Observation of High-Energy Neutrino Reactions and the Existence of Two Kinds of Neutrinos*, Phys. Rev. Lett. 9 (1962) 36.

[4] GALLEX collaboration, W. Hampel et al., *GALLEX solar neutrino observations: results for GALLEX IV*, Phys. Lett. B 447 (1999) 127.
SAGE Collaboration, J. N. Abdurashitov et al., *Measurement of the solar neutrino capture rate with gallium metal*, Phys. Rev. C 60 (1999) 055801.
GNO Collaboration, M. Altmann et al., *Complete results for five years of GNO solar neutrino observations*, Phys. Lett. B 616 (2005) 174.

[5] SUPER-KAMIOKANDE Collaboration, J. Hosaka et al., *Solar neutrino measurements in Super-Kamiokande-I*, Phys. Rev. D 73 (2006) 112001.

[6] J. N. Bahcall, *Solar Models: An Historical Overview*, Nucl. Phys. B (Proc. Suppl.) 118 (2003) 77.
J. N. Bahcall, *Solar Neutrinos. I. Theoretical*, Phys. Rev. Lett. 12 (1964) 300.

[7] KAMIOKANDE-II Collaboration, K.S. Hirata et al., *Experimental Study of the Atmospheric Neutrino Flux*, Phys. Lett. B 205 (1988) 416.

[8] SUPER-KAMIOKANDE Collaboration, Y. Fukuda et al., *Evidence for oscillation of atmospheric neutrinos*, Phys. Rev. Lett. 81 (1998) 1562.
SUPER-KAMIOKANDE Collaboration, J. Hosaka et al., *Three flavor neutrino oscillation analysis of atmospheric neutrinos in Super-Kamiokande*, Phys. Rev. D 74 (2006) 032002.
SUPER-KAMIOKANDE Collaboration, K. Abe et al., *A Measurement of Atmospheric Neutrino Flux Consistent with Tau Neutrino Appearance*, Phys. Rev. Lett. 97 (2006) 171801.

[9] SOUDAN-2 Collaboration, W.W.M. Allison et al., *The atmospheric neutrino flavor ratio from a 3.9 fiducial kiloton-year exposure of Soudan 2*, Phys. Lett. B 449 (1999) 137.

SOUDAN-2 Collaboration, M.C. Sanchez et al., *Observation of atmospheric neutrino oscillations in Soudan 2*, Phys. Rev. D 68 (2003) 113004.
SOUDAN-2 Collaboration, W.W.M. Allison et al., *Neutrino oscillation effects in Soudan-2 upward-stopping muons*, Phys. Rev. D 72 (2005) 052005.

[10] MACRO Collaboration, S.P. Ahlen et al., *Atmospheric neutrino flux measurement using upgoing muons*, Phys. Lett. B 357 (1995) 481.
MACRO Collaboration, M. Ambrosio et al., *Measurement of the atmospheric neutrino-induced upgoing muon flux using MACRO*, Phys. Lett. B 434 (1998) 451.
MACRO Collaboration, M. Ambrosio et al., *Measurements of atmospheric muon neutrino oscillations, global analysis of the data collected with MACRO detector*, Eur. Phys. J. C 36 (2004) 323.

[11] A. de Gouvêa, *Current Situation in the Neutrino (and Charged-Lepton) Sector*, CERN-2010-003 4 November 2010, European Strategy For Future Neutrino Physics, pg. 10-20.
M. C. Gonzalez-Garcia, M. Maltoni and J. Salvado, *Updated global fit to three neutrino mixing: status of the hints of $\theta_{13} > 0$*, Journal Of High Energy Physics, Vol. 2010, Number 4, 1-20.

[12] G. Altarelli and F. Feruglio, *Models of neutrino masses and mixing*, New J. Phys. 6 (2004) 106.

[13] T. Lasserre, *Oscillation Parameters with forthcoming Reactor Neutrino Experiment*, CERN-2010-003 4 November 2010, European Strategy For Future Neutrino Physics, pg. 33-40.

[14] CHOOZ collaboration, M. Apollonio et al., *Search for neutrino oscillations on a long base-line at the CHOOZ nuclear power station*, Eur. Phys. J. C 27 (2003) 331;

[15] PALO VERDE Collaboration, F. Boehm et al., *Search for Neutrino Oscillations at the Palo Verde Nuclear Reactors*, Phys. Rev. Lett. 84 (2000) 3764.

[16] KAMLAND Collaboration, T. Araki et al., *Measurement of neutrino oscillation with KamLAND: evidence of spectral distortion*, Phys. Rev. Lett. 94 (2005) 081801.

[17] K2K Collaboration, M.H. Ahn et al., *Measurement of Neutrino Oscillation by the K2K Experiment*, Phys. Rev. D 74 (2006) 072003.

[18] C. Kraus et al., *Final Result from Phase II of the Mainz Neutrino Mass Searching Tritium β Deacay*, Eur. Phys. J. C 40 (2005) 447.
Troitsk Collaboration, M. Lobashev et al., *Direct search for mass of neutrino and anomaly in the tritium beta-spectrum*, Phys. Lett. B 460 (1999) 227.

[19] O. Cremonesi, *Neutrino Masses and Neutrinoless Double Beta Decay: Status and expectations*, CERN-2010-003 4 November 2010, European Strategy For Future Neutrino Physics, pg. 41-50.

[20] S. Hannestad, *The connection between cosmology and neutrino physics*, CERN-2010-003 4 November 2010, European Strategy For Future Neutrino Physics, pg. 85-92.

[21] NEMO-3 Collaboration, J. Argyriades et al., *Measurement of the two neutrino double beta decay half-life of Zr-96 with the NEMO-3 detector*, Nucl. Phys. A 847 (2010) 168.

[22] A. Strumia and F. Vissani, *Neutrino masses and mixings and...*, hep-ph/0606054v2.
S. Pascoli, S.T. Petcov and T. Schwetz, *The Absolute Neutrino Mass Scale, Neutrino Mass Spectrum, Majorana CP-Violation and Neutrinoless Double-Beta Decay*, hep-ph/0505226.

[23] H.V. Klapdor-Kleingrothaus et al. (HM Coll.), *Latest Results from the Heidelberg-Moscow Double-Beta-Decay Experiment*, Eur. Phys. J. A 12 (2001) 147.
C.E. Aalseth et al., *IGEX 76Ge neutrinoless double-beta decay experiment: Prospects for next generation experiments*, Phys. Rev. D 65 (2002) 092007.
A.S. Barabash, *NEMO-3 Double Beta Decay Experiment: Latest Results*, hep-ex/0610025.
K. Lang (NEMO3 coll.), Proc. for the WIN09 conference, Perugia September 2009, Italy.
C. Arnaboldi et al., *Results from a search for the $0\nu\beta\beta$-decay of 30Te*, Phys. Rev. C 78 (2008) 035502.

[24] H.V. Klapdor-Kleingrothaus, *Lessons after the evidence for $0\nu\beta\beta$ decay*, Phys. Scr. T 127 (2006) 40
H.V. Klapdor-Kleingrothaus and I.V. Krivosheina, *The evidence for the observation of neutrinoless double beta decay: the identification of neutrinoless double beta decay events from the full spectra*, Modern Physics Letters A 21 (2006) 1547.

[25] V. Ammosov and G. Volkov, *Can Neutrino Probe Extra Dimensions?*, hep-ph/0008032 ; DFPD-2000-TH-39.

[26] D. Autiero, G. Brunetti, G. Cacciapaglia, A. Deandrea, L. Panizzi, *Long baseline neutrino experiments, SN1987a and Lorentz violations*, to be submitted.

[27] G. von Gersdorff and M. Quiros, *Conformal Neutrinos: an Alternative to See-saw Mechanism*, Phys. Lett. B 678 (2009) 317.

[28] H.Georgi, *Unparticle Physics*, Phys. Rev. Lett. 98 (2007) 221601.

[29] L. Stodolsky, *The Speed of Light and the Speed of Neutrinos*, Phys. Lett. B 201 (1988) 353.
M. J. Longo, *Tests of Relativity from SN1987A*, Phys. Rev. D 36 (1987) 3276.

[30] T.J. Loredo and D. Q. Lamb, *Bayesian Analysis of Neutrinos from Supernova SN1987A*, Phys. Rev. D 65 (2002) 063002.

[31] M. J. Longo, *New Precision Tests of the Einstein Equivalence Principle from SN1987A*, Phys. Rev. Lett. 60 (1988) 163.

[32] M. T. Keil, G. G. Raffelt, and H.-T. Janka, *Monte Carlo study of supernova neutrino spectra formation*, Astrophys. J. 590 (2003) 971. L. Stodolsky, *Neutrino flight times in cosmology*, Phys. Lett. B 201 (1988) 353.

[33] J. Ellis et al., *Probes of Lorentz violation in neutrino propagation*, Phys. Rev. D 78 (2008) 033013.
A. Sakharov et al., *Exploration of possible quantum gravity effects with neutrinos II: Lorentz violation in neutrino propagation*, J. Phys.: Conf. Ser. 171 (2009) 012039.

[34] J. Alspector et al., *Experimental Comparison of Neutrino and Muon Velocities*, Phys. Rev. Lett. 36 (1976) 837.
G. Kalbfleisch et al., *Experimental Comparison of Neutrino, Antineutrino and Muon Velocities*, Phys. Rev. Lett. 43 (1979) 1361.

[35] P. Limon et al., *A Sign Selected Dichromatic Neutrino Beam*, Nucl. Instrum. Methods 116 (1974) 317.

[36] MINOS Collaboration, D.G. Michael et al., *Observation of muon neutrino disappearance with the MINOS detectors and the NuMI neutrino beam*, Phys. Rev. Lett. 97 (2006) 191801.
MINOS Collaboration, P. Adamson, et al., *Search for Active Neutrino Disappearance Using Neutral-Current Interactions in the MINOS Long-Baseline Experiment*, Phys. Rev. Lett. 101 (2008) 221804.

[37] P. Adamson et al., *Measurement of neutrino velocity with the MINOS detectors and NuMI neutrino beam*, Fermilab-Pub-07-153-E, Phys. Rev. D 76 (2007) 7.

[38] http://proj-cngs.web.cern.ch/proj-cngs/
E. Gschwendtner et al., *Performance and operational experience of the CNGS facility*, CERN-ATS-2010-153.

[39] L. Jensens, *Beam Instrumentation for the CNGS facility*, CERN AB-Note-2006-022 (2006).
R. Jones, *CNGS Primary and target instrumentation*, EMDS1 Id 610790.

[40] J. Wenninger, *CNGS and transfer stability in 2007*, CERN-AB-2008-02 (2008).
M. Meddahi et al., *CNGS: Results from Commissioning*, PAC07 Albuquerque, USA, CERN-AB-2007-039 (2007).

[41] J. Serrano et al., *Inter-Laboratory Synchronization For The CNGS Project*, Proceedings of EPAC 2006, Edinburgh, Scotland.

[42] http://www.fluka.org/fluka.php.
http://www.mi.infn.it/∼psala/Icarus/cngs.html.

[43] A. Guglielmi, *CNGS neutrino beam for long base-line neutrino experiments: present status and perspectives*, TAU08 Novosibirsk.

[44] A.E. Ball et al., *CNGS: Effects of possible alignment errors*, CERN-EP-2001-037, CERN-SL-2001-016 EA (2001).
E. Gschwendtner et al., *CERN neutrinos to Gran Sasso: First Beam*, NSS-IEEE06, San Diego, 2006, Report CERN-AB-2007-005 (2007).

[45] R. Acquafredda et al., *The OPERA experiment in the CERN to Gran Sasso neutrino beam*, JINST 4 (2009) P04018.

[46] OPERA Collaboration, M. Güler et al., *An appearance experiment to search for ν_τ oscillations in the CNGS beam: experimental proposal*, CERN-SPSC-2000-028.
OPERA Collaboration, R. Acquafredda et al., *First events from the CNGS neutrino beam detected in the OPERA experiment*, New J. Phys. 8 (2006) 303.

[47] OPERA Collaboration, N. Agafonova et al., *Observation of a first ν_τ candidate event in the OPERA experiment in the CNGS beam*, Phys. Lett. B 691 (2010) 138.

[48] T. Brugiere, *Oscillations des neutrinos sur et hors faisceau: étude des performances du système d'acquisition d'OPERA*, PhD Thesis, (2011).

[49] OPERA Internal Note, to be submitted.

[50] T. Adam et al., *The OPERA experiment target tracker*, Nucl. Instrum. Methods A 557 (2007) 523.

[51] http://www.hamamatsu.com, Hamamatsu R7600-00-M64, http://sales.hamamatsu.com/en/products/electron-tube-division/detectors/photomultiplier-tubes/part-r7600-00-m64.php.

[52] J. Marteau, the OPERA collaboration, *The OPERA global readout and GPS distribution system*, Nucl. Instrum. Methods A 617 (2010) 291.
L. Chaussard et al., *Status report on the OPERA Data Acquisition System*, OPERA Internal Note 31 (2002).

[53] C. Jollet, *Target-Tracker simulation*, OPERA Internal Note 102 (2009).

[54] N. Chon-Sen, *Caractéristiques et suivi du trajectographe éléctronique de la cible OPERA. Etudes des événéments éléctroniques*, PhD Theses, Université de Strasbourg, 2009.

[55] M. Ambrosio et al., *The OPERA magnetic spectrometer*, IEEE Trans. Nucl. Sci. 51 (2004) 975.

[56] R. Zimmermann et al., *The precision tracker of the OPERA detector*, Nucl. Instrum. Methods A 555 (2005) 435.

[57] M. Alviggi et al., *First Results of the cosmic rays test of the RPC of the ATLAS muon spectrometer at LHC*, Nucl. Instrum. Methods A 518 (2004) 79.
M. Abbrescia et al., *Performance of the first RPC station prototype for the CMS barrel detector*, Nucl. Instrum. Methods A 456 (2000) 103.

BABAR collaboration, B. Aubert et al., *The BaBar detector*, Nucl. Instrum. Methods A 479 (2002) 1.
ARGO-YBJ Collaboration, G. Aielli et al., *Layout and performance of RPCs used in the Argo-YBJ experiment*, Nucl. Instrum. Methods A 562 (2006) 92.
A. Bergnoli et al., *Tests of OPERA RPC Detectors*, IEEE Trans. Nucl. Sci. 52 (2005) 2963.

[58] A. Bertolin, N. T. Tran, *OpCarac: an algorithm for the classification of the neutrino interactions recorded by the OPERA experiment*, OPERA Internal Note 100 (2009).

[59] L. Chaussard, *OpGeom: software model of the OPERA detector*, OPERA Internal Note 69 (2005).

[60] http://www.symmetricom.com/products/frequency-references/cesium-frequency-standard/Cs4000/

[61] Septentrio Satellite Navigation, PolaRx2eTR, www.septentrio.com.

[62] P. Defraigne and G. Petit, *Time Transfer to TAI Using Geodetic Receivers*, Metrologia, 40, 184-18 (2003).

[63] Talk given by A. Autiero at LNGS Workshop *Waiting for the neutrino beam*, June 22 (2006).

[64] LEICA geosystems, http://www.leica-geosystems.it/it/index.htm. LEICA TS30, http://www.surveyequipment.com/PDFs/TS30_Technical_Data.pdf

[65] IERS, http://www.iers.org/nn_11216/IERS/EN/IERSHome/home.html.
C. Boucher and Z. Altamimi, *Memo: Specifications for reference frame fixing in the analysis of a EUREF GPS campaign*, http://etrs89.ensg.ign.fr/memo-V7.pdf.

[66] L. Lyons, *Statistics for nuclear and particle physicists*, Cambridge University Press, Cambridge, 1986.
L. Lyons, *Likelihoods*, 2001.

Acknowledgements

First of all I'd like to thank Dario Autiero, who gave me the opportunity to work for my PhD at the IPNL, without him this work would not have been possible. My sincere gratitude for his support and helpfulness, with his great knowledge and devotion to physics he made my PhD a real opportunity to learn, understand and love my work.

Many thanks to Maximiliano Sioli for his help and advice, as well as to the entire Bologna group, for making all these years a wonderful time!

I'd like to thank Gaston Wilquet and Francesco Terranova for having read my thesis and for their useful suggestions, many thanks also to Aldo Deandrea for the friendly collaboration.

I'd like to thank all the friends in Lyon: Elisabetta, Antoine, Timothée, Tiem, Sylvie, Silvano, Silvia, Viola, Luca Panizzi and Luca Pattavina, Abu, Carla and Giacomo! Thanks to you all... the months in Lyon have been the best!

A special thanks to the Rome geodesy group, for making the work time such an enjoyable time. I'd also like to thank all the OPERA collaboration people who helped me and all the other "young" people and friends I met on the way.

Last but not least: Big big and affectionate thanks to my family and to Michele for the loving support and constant presence, they really helped me to overcome all the difficulties.